ABSTRACT

Title of Dissertation:	IMPROVED PREDICTION OF FLAPPING WING AERIAL VEHICLE PERFORMANCE THROUGH COMPONENT INTERACTION MODELING
	John William Gerdes III, Doctor of Philosophy, 2018
Dissertation directed by:	Professor, Dr. Satyandra K. Gupta, Mechanical Engineering, Institute for Systems Research

Flapping wing aerial vehicles offer the promise of versatile performance, however prediction of flapping wing aerial vehicle performance is a challenging task because of complex interconnectedness in vehicle functionality. To address this challenge, performance is estimated by using component-level modeling as a foundation. Experimental characterization of the drive motors, battery, and wings is performed to identify important functional characteristics and enable selection of appropriate modeling techniques. Component-level models are then generated that capture the performance of each vehicle component. Validation of each component-level model shows where errors are eliminated by capturing important dynamic functionality. System-level modeling is then performed by creating linkages between component-

level models that have already been individually validated through experimental testing, leading to real-world functional constraints that are realized and correctly modeled at the system level. The result of this methodology is a system-level performance prediction that offers the ability to explore the effects of changing vehicle components as well as changing functional properties, while maintaining computational tractability. Simulated results are compared to experimental flight test data collected with an instrumented flapping wing aerial vehicle, and are shown to offer good accuracy in estimation of system-level performance properties.

IMPROVED PREDICTION OF FLAPPING WING AERIAL VEHICLE PERFORMANCE THROUGH COMPONENT INTERACTION MODELING

by

John William Gerdes III

Dissertation submitted to the Faculty of the Graduate School of the
University of Maryland, College Park, in partial fulfillment
of the requirements for the degree of
Doctor of Philosophy
2018

Advisory Committee:
Professor Satyandra Gupta, Chair
Associate Professor Sarah Bergbreiter
Professor Hugh Bruck
Professor Jeffrey Herrmann
Professor Norman Wereley

Dedication

This work is dedicated to my family. You have been supportive and encouraging from the beginning and I can’t thank you enough.

Acknowledgements

The broad scope of work demands many acknowledgements of others, without whom I could never have completed my part. For developing code, thanks to Nick Gammon and Duane B for their beautifully written advice and prompt replies. For PCB design and fabrication, thanks to Wosen Wolde and Chris Braun with what at times seemed impossible. For help with the enormous amount of 3D printing required, thanks to Steve Biggs and Jeff Westrich. For help with dyno testing, thanks to Aaron Harrington. Thanks to Wyatt Bucci, Andrew Wood, and Kristen Twigg for help with long hours of experimental work. Thanks to Ania Picard, T'Jae Gibson and Joyce Brayboy for telling the Robo Raven story to the world. Thanks to Chris Kroninger for mentoring me as a student intern many years ago. Thanks to Brian Porter and Howard Carpenter for lending your skills in building many prototypes over the years. Thanks to Elias Rigas, Eric Spero and the rest of ARL for your constant support. Thanks to Drew Wilkerson for some very enthusiastic support and excellent cinematography during flight testing. Thanks to SK for being a tremendous advisor in all my endeavors and sticking with me through all these years. Thanks to Heather for always encouraging me on the long days and late nights. And finally, thanks to Ariel, Luke, Alex, and the rest of the AML gang for everything. You're some of the best people I'll ever know and I'll certainly miss the fun times together. I'm sure you'll accomplish great things in your careers, wherever they take you.

Table of Contents

List of Tables

List of Figures

List of Abbreviations

A	Ampere
A-h	Ampere-hours
AHRS	attitude and heading reference system
CAD	computer aided design
CFD	computational fluid dynamics
DARPA	Defense Advanced Research Projects Agency
DIC	digital image correlation
DoD	Department of Defense
EMF	electromotive force
FEA	finite element analysis
ft	feet
FWAV	flapping wing aerial vehicle
g	grams-force or gravity
GPS	global positioning system
Hz	Hertz
I	Current
I^2C	inter-integrated circuit
ISR	intelligence, surveillance, and reconnaissance
L	inductance
m	meter
N	Newton

PCB	printed circuit board
PIV	particle image velocimetry
PWM	pulse width modulation
R	resistance
rad	radian
rpm	revolutions per minute
RTF	ready to fly
s	seconds
SAPIV	synthetic aperture particle image velocimetry
SPI	serial peripheral interface
UART	universal asynchronous receive transmit
UAS	unmanned aerial system
UAV	unmanned aerial vehicle
V	voltage
VLM	vortex lattice method
W	Watt

Chapter 1: Introduction

1.1 Introduction to UAVs

Unmanned Aerial Vehicles (UAVs) are flying craft spanning a variety of shapes, sizes, and capabilities that operate without a human pilot onboard. Other terms often used include Unmanned Aerial Systems (UAS) which includes associated support equipment like ground control stations, or drones which implies usage of an autopilot but is often misused to describe teleoperated UAVs. Traditionally, militaries have been one of the major operators of UAS, a trend which continues today. Some of the earliest examples of UAVs were developed for the military in the early 20th century [38]. The U.S. Department of Defense uses the size and capability grouping that is shown in Table 1.1 to classify UAS in use across the armed services [39].

Table 1.1: U.S. Army UAS categories

<table>
<tr><th>UAS Category</th><th>Maximum Gross Takeoff Weight</th><th>Normal Operating Altitude (ft)</th><th>Airspeed</th><th>UAS Examples</th></tr>
<tr><td>Group 1</td><td>< 20 pounds</td><td>< 1200 above ground level</td><td>< 100 Knots</td><td>RQ-11B Raven, WASP</td></tr>
<tr><td>Group 2</td><td>21-55 pounds</td><td>< 3500 above ground level</td><td rowspan="2">< 250 Knots</td><td>ScanEagle</td></tr>
<tr><td>Group 3</td><td>< 1320 pounds</td><td rowspan="2">< 18,000 mean sea level</td><td>RQ-7B Shadow</td></tr>
<tr><td>Group 4</td><td rowspan="2">> 1320 pounds</td><td rowspan="2">Any Airspeed</td><td>MQ-1A/B/C, MQ-8B</td></tr>
<tr><td>Group 5</td><td>> 18,000 mean sea level</td><td>MQ-9, RQ-4, MQ-4C</td></tr>
</table>

Examples of the UAS listed in Table 1.1 are depicted below in Figure 1.1 for comparison of scale [4-9]. The military has traditionally been a strong driver of many UAV usage scenarios including intelligence, surveillance, and reconnaissance (ISR) and sensor or payload delivery. Today, consumers of UAVs span government organizations, businesses, academic institutions, and private citizens. These consumers present a diverse set of use cases and requirements.

Figure 1.1: Current DoD UAS. Top row, left to right, Raven, ScanEagle, Shadow, Fire Scout. Bottom row, left to right, Predator, Reaper [4-9].

Drawing inspiration from the traditional military use cases, a variety of applications have emerged relating to photography and videography driven by the needs of journalists [40], realtors [41], filmmakers [42], and many others. UAVs and especially quadcopters have grown increasingly popular with hobbyists and private consumers,

thanks in large part to advances in small, inexpensive, ready-to-fly (RTF) quadcopter systems from companies like Parrot, 3D Robotics, and DJI, shown in Figure 1.2 [43-45].

Figure 1.2: Popular consumer-grade UAVs including the Parrot AR.Drone (left), DJI Phantom (center), and 3D Robotics Solo (right)

User-friendly features including self-stabilization, GPS navigation, and smartphone control have made UAVs more accessible than ever before. A large open-source community combined with a huge commercial market for products related to UAV flight has brought microcontroller-stabilized autonomous flight into the mainstream, with prices in the hundreds of dollars. Military-inspired technology like first-person view goggles and elegantly configured command and control software as shown in Figure 1.3 have greatly reduced the learning curve for flying small UAVs [30, 31].

Figure 1.3: First-person view goggles (left) and the Ardupilot open-source mission planner (right) [30, 31]

Businesses have taken advantage of the capabilities that modern UAVs offer with some creative ideas. Recently, cargo delivery has emerged as a potentially disruptive application for small UAVs, with early trials underway promising delivery times measured in minutes from several major package delivery businesses including DHL and Amazon, as shown in Figure 1.4 [32, 33].

Figure 1.4: Amazon Prime Air delivery system (left) and DHL Parcelcopter (right) [32, 33]

Additional applications include farming [46], disaster relief [47], archaeology [48], search and rescue [49], meteorology, infrastructure inspection, border patrol, law enforcement, and many more that are constantly evolving as new ideas emerge and develop with research and testing [50].

The modern UAV industry continues to grow due to constant innovation and capability improvements by manufacturers. Market projections for UAVs vary widely, but all suggest rapid growth to billions of dollars by 2020 [51, 52]. UAVs are a versatile technology that have already demonstrated widespread benefits across many use cases. Hence, UAVs are deserving of research and development efforts to maximize the breadth and depth of these benefits to as many consumers as possible.

The research conducted in this dissertation is focused on the smaller end of Group 1 UAS listed in Table 1.1, colloquially referred to as hand-launched. To maintain a

relevant scope of discussion, the remainder of this chapter will focus on this size scale. While many of the applications previously discussed span all the Groups of Table 1.1, the unique design challenges associated with the usage of small UAVs necessitate a specialized discussion.

1.2 Motivation for Flapping Wings

In general, the majority of modern UAVs may be classified into two primary categories, airplanes and rotorcraft. Airplanes rely on a propeller to provide thrust that overcomes drag and drives a wing through the air. This generates lift that overcomes weight. Deflecting control surfaces create asymmetric drag, resulting in control of the aircraft. Rotorcraft instead rely on one or several rotors composed of blades rapidly spinning in a disk-shaped volume to provide vertical thrust that overcomes weight. This rotor disk may be tilted forward, backward, left, or right to provide control, or in the case of a multirotor vehicle, differences in rotor thrust may be used to provide control.

These two styles of flight offer some distinct advantages and disadvantages, which naturally result from the physics of the style of flight. Airplanes tend to be much more effective at reaching high speeds and altitudes, lifting large amounts of weight, and remaining aloft for long periods of time. While this makes airplanes ideally suited to flying high, far, and fast, it also means that airplanes require more space to take off, climb, maneuver, and land. Rotorcraft suffer a large penalty in efficiency because of

the direct thrust-based strategy used to generate lift. However, rotorcraft excel in low-speed maneuvers, hovering, obstacle avoidance, and flight in cluttered environments. While there are some man-made ideas on how to bridge this gap by using multi-mode flight or tilting rotors [53], a third option is suggested by nature, flapping wing flight.

Flying animals including birds, bats, insects, and others are capable of an enormous flight envelope spanning many shapes, sizes, and capabilities. Animals offer a versatile compromise between airplanes and rotorcraft by providing a combination of excellent maneuverability and long flight endurance. Common Ravens, *Corvus Corax* are capable of inverted flight, rolls, and flips, and have a broad distribution around the world due to their adaptability [54-56]. Hummingbirds can hover and even fly backwards, yet can also migrate across the Gulf of Mexico in a non-stop flight [57]. Some birds have even been observed in flight at altitudes in excess of 6,000m [58]. Hence flapping wing aerial vehicles (FWAVs), sometimes also called ornithopters (after the Greek 'ornitho' for bird), may be able to combine many useful capabilities in a single platform. In addition, some unique benefits arise that are particular to flapping wings. Since there are no rapidly spinning propellers or rotor blades, the danger of FWAVs to nearby people or property is significantly reduced. Low flapping rates result in greatly reduced noise relative to propellers and rotors. Since flapping wings are a nature-inspired approach to flight, FWAVs may have a realistic appearance that provides excellent stealth.

Clearly, flapping wing flight offers a wide range of capabilities, and FWAVs may benefit tremendously from an understanding of flapping wing flight. Many researchers have studied the techniques used by birds, leading to a large body of general knowledge explaining animal flight [59, 60]. Allometric scaling and corresponding energetic requirements have been thoroughly studied by researchers, revealing scaling laws that govern flapping wing flight [58, 61-72]. Furthermore, detailed aerodynamic models have revealed the important physical phenomena that explain avian flight [73-76]. Variations in morphology lead to many useful behaviors observed in flying animals. Furthermore, within each species, adjustments to the specific flapping motions and wing shapes provide adaptability and robustness to changes in the environment or flight requirements.

1.3 Motivation for Independent Wing Control

Flying animals use highly deformable wings to achieve a wide range of shapes for control of aerodynamic forces. In addition to using passive strategies like tail deflection, flying animals maneuver by altering their flapping gait in multiple degrees of freedom, [59, 77-79]. This strategy enables rapid maneuvering and flight stability in confined spaces, which are useful for disturbance rejection and obstacle avoidance. Researchers have shown pigeons are capable of aggressive obstacle avoidance maneuvers by harnessing significant asymmetry in the wingbeat kinematics and wing shapes [80]. Changing flight requirements such as added mass cause animals to adjust

many flight parameters including the stroke asymmetry, tail and body inclination, flight speed, and flapping rate [71]. Clearly, FWAV researchers may benefit from an understanding of avian flight, but challenges persist as evidenced by the large gap between animal flight performance and current FWAVs [81, 82]. It is therefore important for researchers to develop FWAVs capable of adjustments to both flapping and tail kinematics to enable the study of bio-inspired flight.

1.4 Goal and Scope

The goal of this dissertation is to develop a modeling and simulation framework that offers improved performance prediction accuracy while maintaining reasonable tractability. If this goal is accomplished, future efforts in design of flapping wing aerial vehicles may be facilitated since the predictive framework offered here will provide sufficient data throughput across many operational characteristics while retaining acceptable accuracy to trust the results. This goal will be accomplished by building component models that are validated with experimental data. Next, a technique for establishing a reasonable operational parameter space will be presented. More in depth modeling will then be set up by composing the component models into a system-level model that includes key constraints arising due to the component model linkages. Due to the breadth of flight styles that are possible with flapping wings, the scope will be limited to avian-scale vehicles that exhibit slow cruising flight with Reynolds number

of $O(10^5)$. Several research and capability gaps will be addressed by this dissertation as follows:

i. *Improved accuracy for component-level modeling:* The overall dissertation goal of providing a suitable blending of tractability and accuracy is challenging because the lower fidelity modeling approaches that are needed to keep tractability reasonable suffer from a significant amount of simplifying assumptions that create predictive inaccuracies and reduce the scalability of the approach. To address this challenge, experimental techniques have been developed that provide suitable information to populate component models for the motors, wings, and battery. These techniques have been designed to highlight the dynamic features of each component that interact to constrain overall system functionality, which is essential to achieving acceptable modeling accuracy. Flapping wing aerial vehicles are inherently dynamic systems, and by capturing this dynamic behavior at the component-level to reduce errors, a baseline is established for improved modeling accuracy.

ii. *Efficient determination of feasible operational parameters for flapping wing aerial vehicles:* Performance modeling of FWAVs is challenging because many parameters need to specified correctly that describe the characteristics of the design and how it is operated. In cases where little or no data is available from an existing design, it can be prohibitively difficult to ensure that a model is set up in a way that is reflecting the real conditions encountered in flight and thus is providing realistic estimates of flight performance. To avoid this problem, a

modeling approach from biology is adopted based on Vortex Ring Theory. The mathematics of this modeling approach are set up in such a way that the feasibility of the flight is enforced by balancing the predicted forces and calculating the trim conditions simultaneously, while requiring no specification of coefficients of lift and thrust by the wings. In addition, the method is computationally inexpensive and provides results in a few seconds. Thus, the approach offers a method to efficiently estimate reasonable operational parameter spaces, for example to support new design efforts where there is little to no data available from flight testing.

iii. *Improved scalability and accuracy for aerodynamic modeling*: In the strip theory aerodynamic modeling approach, correct specification of wing motion is essential to achieving predictive accuracy. By linking component models that are derived from experimental characterization, predictive accuracy of wing motions is improved due to realistic constraint application. The resulting lift and thrust projections and power requirements for flight are more accurate and scale with improved realism when compared to flight testing results, which is a natural result from enforcing constraints that prevent feasibility violations at the component modeling level. This approach relies on easily observable properties of vehicle components, and is therefore extensible to accommodate changes to vehicle components, since the constraints that are determined by component-level performance modeling will automatically ensure feasibility is maintained.

iv. *Improved estimate of system-level measures of performance*: System-level measures of performance are simulated by first building up from experimental characterization to component models, then linking all component models into a vehicle-level prediction framework that contains component-level constraints that update throughout the simulation. The result of this approach is to improve the accuracy of vehicle-level predictions including lift and endurance by accounting for the interactions within the vehicle system that result from instantaneous component constraints and gradually diminishing performance associated with battery discharge. The interconnected simulation framework enables exploration of the time history of changing operational characteristics, rather than a simple snapshot of performance, since the structure of component-models and constraints is maintaining appropriate linkages to continually enforce feasibility.

Chapter 2: Literature Review

2.1 Review of Flapping Wing Aerial Vehicles with Adjustable Wing Control

Several FWAV platforms have been developed to investigate flight with adjustable wing control. Maneuvering and control are made possible by altering the force production asymmetrically through changing kinematics. One of the smallest examples of this concept is called the RoboBee, developed at Harvard University's School of Engineering and Applied Sciences. RoboBees are small, tailless, insect-like flying vehicles that maneuver with adjustments to wingbeat kinematics, shown in Figure 2.1 [83]. Several experiments and simulations have demonstrated the effectiveness of the wing-based maneuver and control strategy [84, 85]. RoboBees previously used a piezoelectric bimorph actuator for power and a pair of smaller actuators to provide adjustment to each wing for maneuvering flight [86-88]. More recently, flight with independent wing actuators has been demonstrated [89, 90]. RoboBees are notable as the first at-scale insect-style MAV flight, and also for demonstrating the efficacy of independent wing actuation as an approach for maneuvering and control.

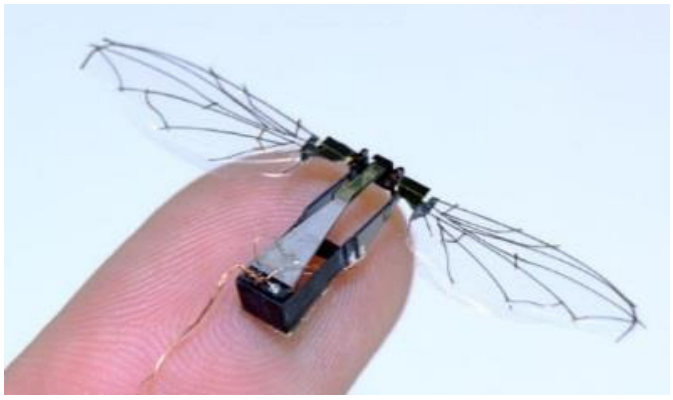

Figure 2.1: RoboBee insect-scale aerial vehicle [17]

The energetics [91] and a conceptual design [92] led to new size, weight, and power insights. New actuators [93] and power electronics [94] were developed to efficiently propel the RoboBees. The custom manufacturing process [17] helps in minimizing weight.

One commercial example which achieved flight by drawing inspiration from nature was the Smartbird, shown in Figure 2.2 on the right [95]. Festo's Bionic Learning Network created the Smartbird by copying the wing kinematics and deformations of a herring gull [96], an approach known as biomimicry. By implanting servo motors in the wingtips, active wing twisting is realized, providing improved control over the wing shapes during flapping. The same group is also responsible for creating the Bionicopter, a slowly flying and hovering FWAV which resembles a giant dragonfly, shown in Figure 2.2 on the left [29].

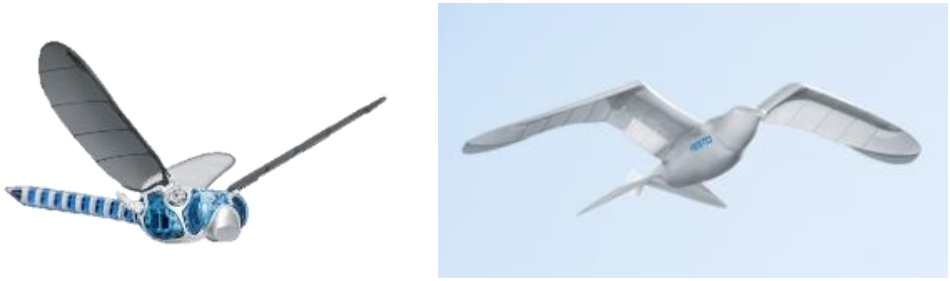

Figure 2.2: Festo Bionic Learning Network's Bionicopter (left) and Smartbird (right) [28, 29]

Another significant group working on the development of FWAVs is AeroVironment, who contributed to the first flight of a small electrically powered ornithopter in 1998 when the Microbat flew for nine seconds [35]. The Microbat used the popular crank-rocker mechanism to achieve flight, which saves weight but does not provide adjustable wing kinematics [97]. Years later, this approach was significantly advanced in response to a Defense Advanced Research Projects Agency (DARPA) project called Nano Air Vehicle. In response to the Nano Air Vehicle program AeroVironment created the Nano Hummingbird, shown together with the Microbat in Figure 2.3. The AeroVironment Nano Hummingbird flies with wings that beat between 20 and 40 times per second using a yoke-based flapping mechanism that is driven by a single motor and deflected by smaller control actuators, leading to a highly maneuverable flying vehicle with multiple degrees of freedom on wing kinematics and wing tension [34, 98]. The ability of the Nano Hummingbird to hover and maneuver is largely due to its expanded degrees of freedom, and represents an important achievement in maneuverability for a man-made vehicle.

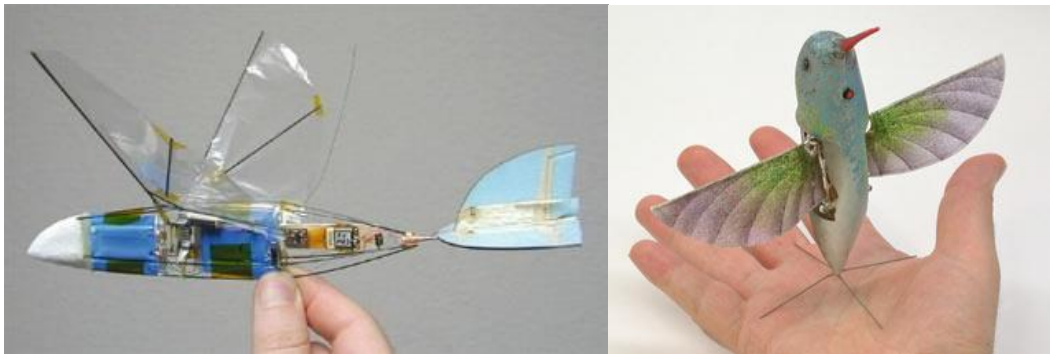

Figure 2.3: AeroVironment Microbat (left) and Nano Hummingbird (right)[34, 35]

A significant hobbyist-turned-commercial effort was the family of vehicles developed by Sean Kinkade, including several variants each of the Slow Hawk and Park Hawk, shown in Figure 2.4 on the left. These ornithopters have gained significant popularity and have been used in some research efforts as flying test beds [25, 37]. Regrettably, these ornithopters are only available through resale, as the inventor Sean Kinkade passed away in early 2013. Japanese inventor Kazuhiko Kakuta has modified a Slow Hawk 2 flapping mechanism to provide asymmetric flapping and thrust production via an adjustable mechanism part shown on the right in Figure 2.4, but tests have shown limited success [36].

Figure 2.4: Sean Kinkade's Park Hawk and Slow Hawk ornithopters (left) and a Slow Hawk 2 modified with articulated wing turning (right) [36, 37]

Several efforts in flapping wing flight with controllable wing motions have come from academic groups, in addition to the private and commercial efforts. Researchers at the University of Delaware have studied the energetic requirements of the flapping wing system and built several prototype flying vehicles, shown in Figure 2.5 [15, 16]. The same group has developed a method for designing a spherical 4R mechanism that can approximate desired wingbeat kinematics, even complex three-dimensional patterns, thus providing favorable performance for unusual gait kinematics in a lightweight package [99]. This group has also developed mechanisms capable of passive wing rotation subject to spring loads [100] and a mechanism that is capable of asymmetric in-phase flapping [101], which flaps both wings with one actuator and slides the mechanism left and right with a second actuator, leading to an asymmetry in the range of motion of each wing. They have also developed a strategy for wing optimization including the path and the topology of reinforcement [102]. However, the group has

yet to include the differential flapping mechanism into their freely flying flapping wing aerial vehicle.

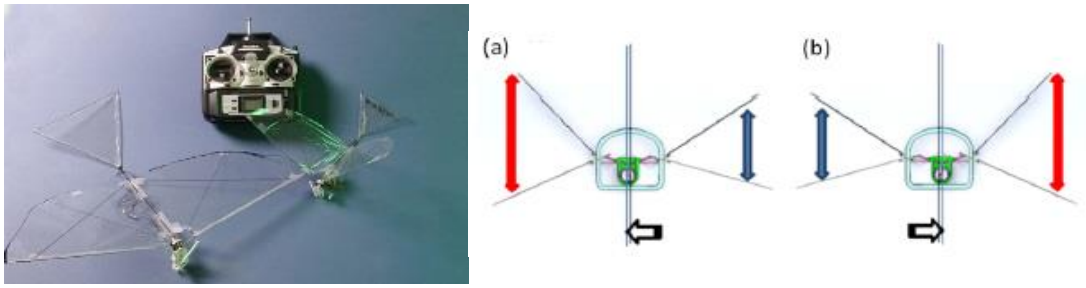

Figure 2.5: Two prototype FWAVs [13] (left) and a variable asymmetric amplitude flapping mechanism concept (right) designed at the University of Delaware [15, 16]

Wing folding has been demonstrated as a possible means of augmenting aerodynamic force production. The University of Illinois' Aerospace Robotics and Control group have demonstrated perching on a target by altering the orientation of the wings in a coordinated manner, which demonstrates how a wing-based steering approach may enhance maneuverability in FWAVs [20, 103]. The group has conducted some impressive demonstrations of precision perching maneuvers by using a VICON tracking system to provide position feedback to the vehicle. A multi-exposure picture of one test flight is shown in Figure 2.6. More recently, the same group has studied bat-style flight using their BatBot flapping wing aerial vehicle that provides several degrees of freedom to control flexible membrane wings [104-106].

Figure 2.6: Wing-based steering used to perch from the University of Illinois' Aerospace Robotics and Control Group [20]

Passive wing folding in response to upstroke aerodynamic loads has been demonstrated by the University of Maryland as a strategy for trading aerodynamic lift for static lift, which could enable reduced flight speeds and enhance maneuverability [11]. A bat wing developed by Brown University that is capable of active wing folding is shown in Figure 2.7. A significant drawback associated with this approach is the increased engineering and functional complexity associated with wing articulation. Both active and passive approaches tend to reduce thrust production by using wing folding.

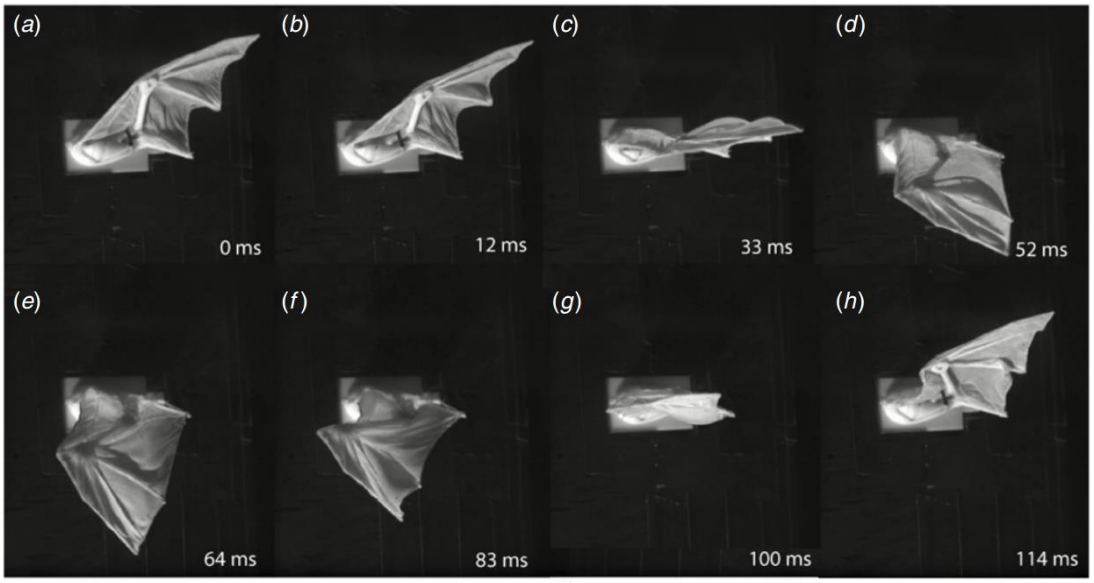

Figure 2.7: Articulated bat wing developed at Brown University to study the effects of changing flapping kinematics [27]

A more general summary of flapping wing aerial vehicles that don't use independent wing control, including exploration of different flapping mechanisms, wing styles, and flight capabilities, is available in [97]. That discussion is mainly focused on vehicles of a similar size scale that have demonstrated at least one successful test flight.

2.2 Flapping Wing Aerial Vehicle Development at the University of Maryland Advanced Manufacturing Laboratory

Along with others at the University of Maryland's Advanced Manufacturing Laboratory, I have developed several bird-inspired FWAVs as research platforms and as practical flying prototypes capable of transmitting live video, flying with morphing

wings, and lifting large payloads [12-19]. A manufacturing process that concurrently optimizes injection mold design of drive components and their functionality was demonstrated in the Small Bird vehicle in 2008 [10]. To explore the performance of a variety of vehicle and wing designs, a custom testing apparatus was created to characterize force production of flapping wing vehicles [107]. Subsequently, a Big Bird platform was developed with enhanced payload capacity, improved outdoor flight dynamics, and the ability to lift a camera and transmitter [11]. This design also incorporated passive wing folding to provide decreased reliance on forward speed for lift generation through an asymmetry in wing area during upstroke and downstroke. Next, a Jumbo Bird was developed with substantially increased payload capacity and endurance, solar cells integrated into the wings, and some new techniques for experimental characterization of performance [108, 109]. These FWAVs are shown in Figure 2.8.

Figure 2.8: University of Maryland Advanced Manufacturing Laboratory's Small Bird, Big Bird with folding wings, and Jumbo Bird (left to right) [10-12]

More recently, several variants of the Robo Raven FWAV described in the remainder of this dissertation have been developed to explore new design directions. The Robo Raven III explores the feasibility and performance of wings that incorporate multifunctional flexible solar cells that harvest solar energy and augment aerodynamic force production [3, 110-114]. Robo Raven IV includes a GPS-enabled autopilot for flight stabilization and waypoint navigation, and has demonstrated several precision maneuvering strategies [2, 115-117]. Robo Raven V uses multi-modal propulsion where flapping is augmented by propellers for additional thrust to carry much larger sensors and explore the interaction between the wings and propellers [1, 118, 119]. These versions of the Robo Raven are shown in Figure 2.9.

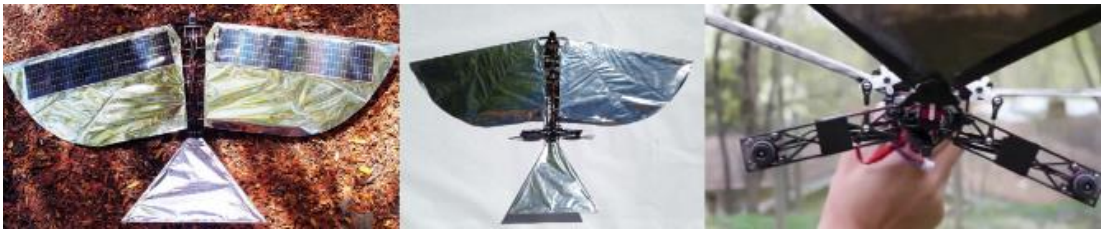

Figure 2.9: Robo Raven III, Robo Raven IV, and Robo Raven V (left to right) [1-3]

2.3 Experimental Characterization of Flapping Wing Aerial Vehicles

The interdependence of wing deformations, flapping kinematics, and force production create significant challenges in modeling for flapping wing aerial vehicles. This has led many researchers to pursue experimental techniques for performance characterization under varying conditions. One of the most popular strategies for experimental

investigation of FWAVs is optical wing shape reconstruction. By tracking markers or specified locations on the wing surface, a three-dimensional point cloud can be used to provide insight into how wing design impacts loading and wing deformation. Researchers at the University of Maryland used a point grid on the wings to track deformation during the wingbeat using high speed photography as shown in Figure 2.10 [12]. The wing deformation was related to lift and thrust production by tracking the volume encapsulated by the deformed wing. In addition a sensitivity analysis was conducted to establish the relationship between manufacturing variability and aerodynamic performance.

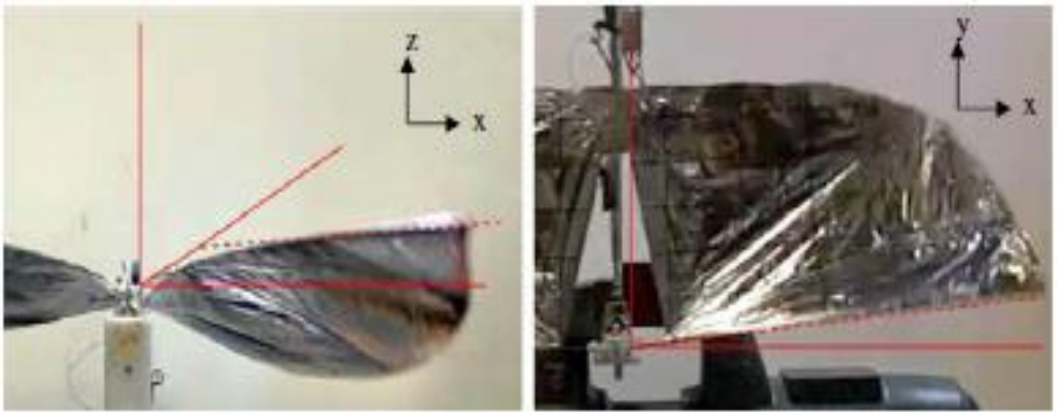

Figure 2.10: Point grid wing shape reconstruction technique conducted at University of Maryland Advanced Manufacturing Laboratory [12]

Similar experiments have also been conducted by University of Maryland researchers using a VICON motion capture system to record the deformation of flapping wings equipped with reflective markers while also recording forces on a load cell as shown

in Figure 2.11. These experiments were focused on capturing the required parameters for a quasi-steady aerodynamic model to predict flight forces.

Figure 2.11: Combined VICON and load cell testing conducted at University of Maryland Morpheus Laboratory [25]

An alternative to VICON is the digital image correlation (DIC) technique that tracks consecutive images of a wing with an applied speckle pattern to provide a dense point cloud. This technique has been used by Wu et al. to demonstrate the dependence of force production on the wing deformation properties [22]. This study also explored the

relationship between aerodynamic and inertial loads by using an evacuated chamber, as shown in Figure 2.12.

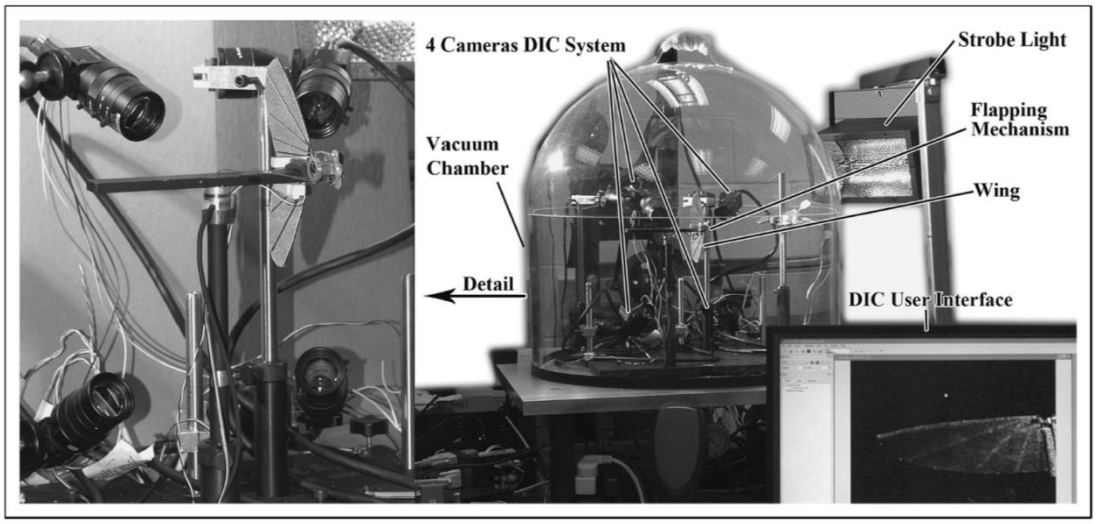

Figure 2.12: Digital image correlation study of flexible wings conducted at the University of Florida [22]

A similar approach to DIC is photogrammetry, which reconstructs 3D coordinates of markers by coordinating multiple cameras focused on a target area as shown in Figure 2.13 [120]. Shkarayev et al. collected wing shape data using the photogrammetry technique and performed computational fluid dynamics (CFD) simulations to reveal the importance of added mass effects and passive downstroke ratio adjustment to force production [23].

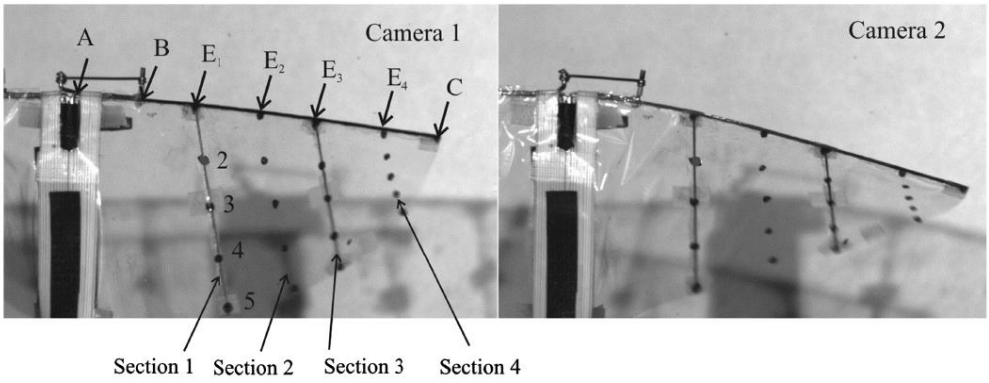

Figure 2.13: Photogrammetric wing shape reconstruction technique conducted at the University of Arizona [23]

Another method for characterizing performance is focused on wake visualization, which provides insight into circulation and unsteady effects. Hubel and Tropea used a wind tunnel equipped with a force balance to record loads and particle image velocimetry (PIV) to perform flow visualization of the wake as shown in Figure 2.14 [19]. Their study showed that PIV results have excellent agreement with force balance results at lower reduced frequencies, but higher reduced frequencies show diminished accuracy due to unsteady effects including delayed stall.

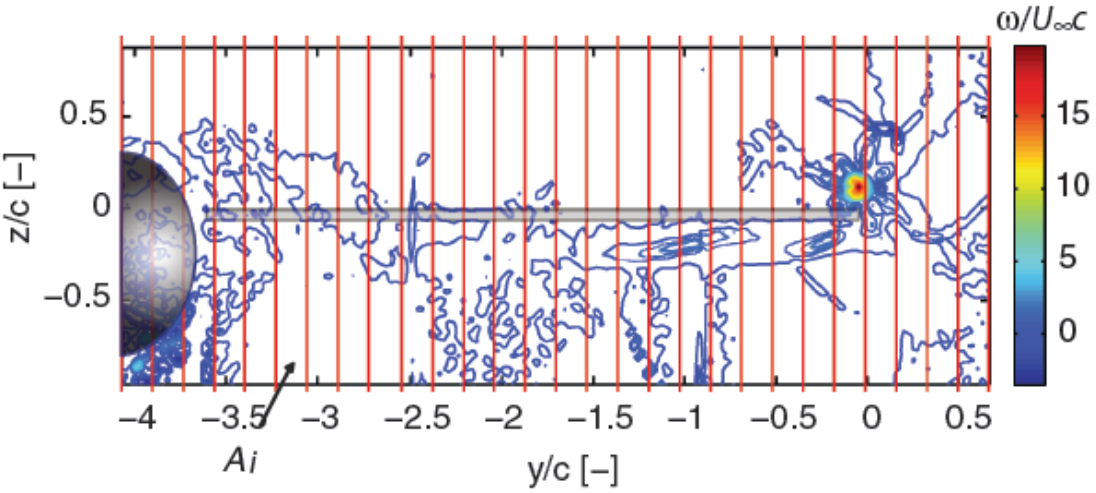

Figure 2.14: PIV wake imaging results conducted at Technische Universitat Darmstadt [19]

PIV studies have also been undertaken by researchers in the development of the Delfly, with a focus on 3D wake reconstruction techniques and correlation to the measured forces produced during varying reduced frequency conditions [26]. The dual camera stereo PIV approach shown in Figure 2.15 was used to generate a series of wake images at varying reduced frequency, which showed well-organized structures that exhibit interaction that is dependent on reduced frequency.

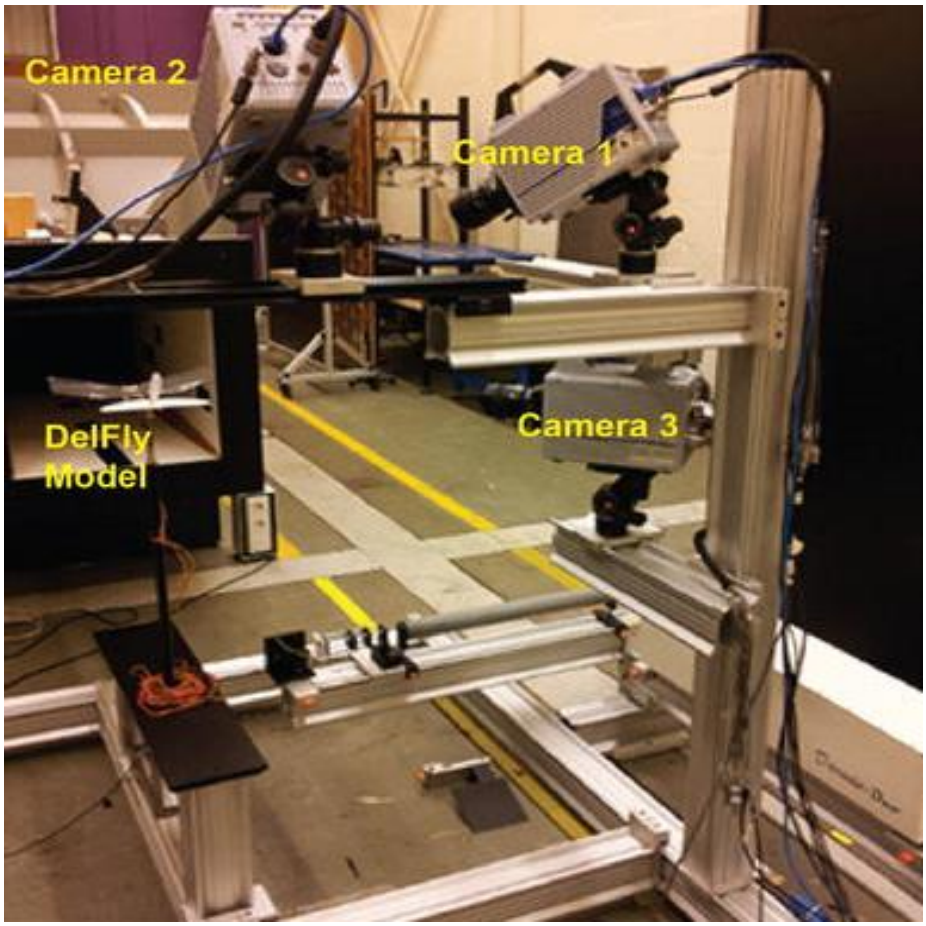

Figure 2.15: Stereo PIV wake reconstruction of the Delfly flapping wing aerial vehicle conducted at TU Delft [26]

BYU's fluids imaging group has used synthetic aperture PIV (SAPIV) to visualize time-resolved flow structures in a 3D volume of fluid by creating focal stacks with an array of cameras as shown in Figure 2.16 [24]. Their study investigated a painted lady butterfly and a tethered mechanical flapper, and showed that SAPIV is able to generate reasonable estimates of flapping forces by extracting flow field information from the leading edge vortex and trailing edge vortex. By using a refocusing algorithm, SAPIV

is able to mitigate the effects of flow occlusion due to the body of the vehicle blocking the view of some of the cameras.

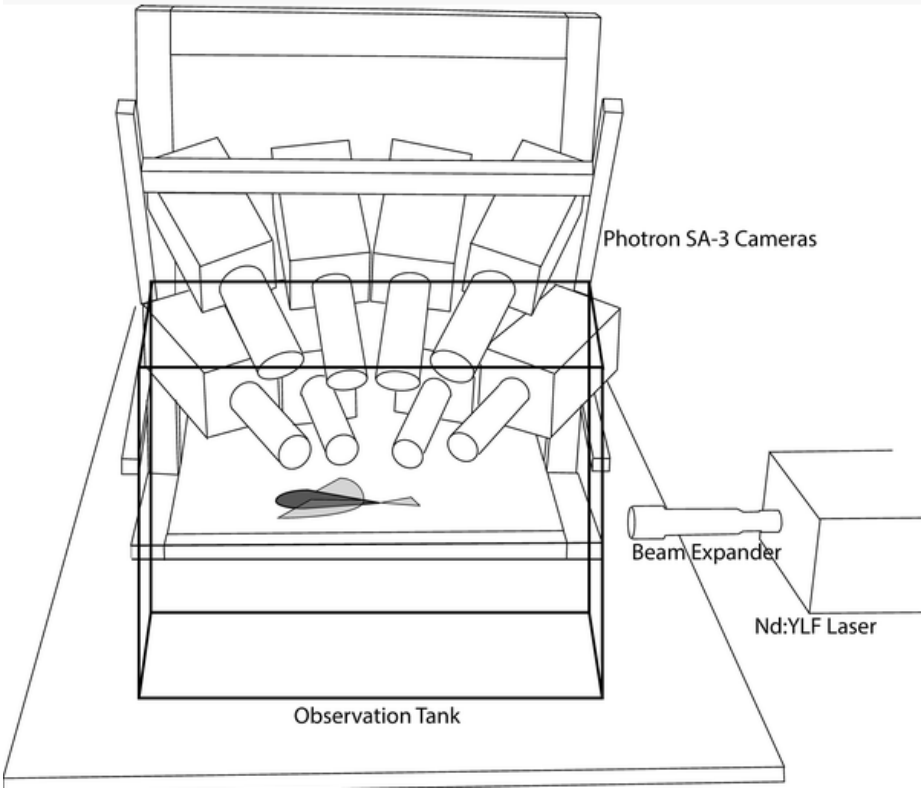

Figure 2.16: SAPIV experimental setup used by BYU to measure 3D time-resolved flow structures [24]

Another technique for resolving 3D flow structures is tomographic PIV, which uses a laser sheet that is scanned through several slices of the flow. Thomas et al. describe this strategy in detail and use the setup shown in Figure 2.17 to capture the formation of a wingtip vortex that stabilizes the flow over the wing [21]. The results collected with

this approach show that the tip vortex has an important role in stabilizing the flow and reduces wing-wake interactions.

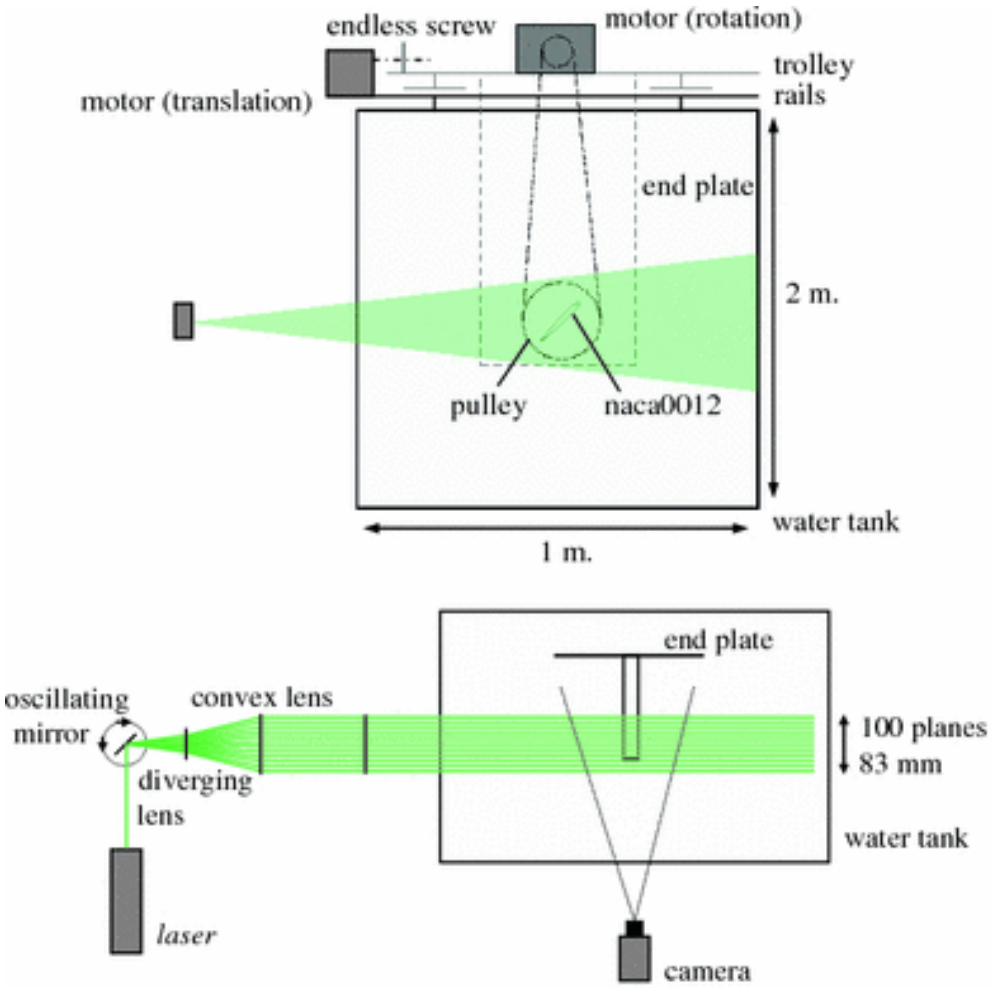

Figure 2.17: Tomographic PIV setup used to construct 3D time-resolved flow structures [21]

As an alternative or an addition to flow field visualization techniques, several researchers have characterized force production for a variety of flapping conditions and wing designs using load cell testing, either with or without a wind tunnel [11, 12, 19, 27, 107, 121-125]. The direct measurement of force production under varying test conditions provides an excellent means of comparative study for a variety of technologies, including folding wings, changing wing kinematics, and varying wing stiffness. The main drawback associated with load cell testing is the rigid mount that constrains motion of the body in response to flapping forces in an unnatural way.

The developers of the Delfly conducted a notable study that compared the results of load cell testing to an estimate based on a visual reconstruction of the flight path using VICON to infer flight forces, which found that there is information loss associated with the rigid load cell mounting due to interference with the natural body motions [126]. In addition, several sources of error were explored including the mounting position to the load cell, the sampling rate, and the selection of data filtering frequency. This study underscores the importance of careful experimental design in hardware testing, as it provides a comprehensive treatment of the error sources in a typical load cell test.

Several flight-enabling technologies have been the focus of research to understand how they may impact overall performance. A key technology that has been researched due to the potential for weight savings is a flexible membrane wing, since passive deformations may achieve desired wing shapes without requiring the extra weight of

additional actuation and control hardware [22, 127, 128]. In addition, suitably flexible wings demonstrate a favorable stall behavior whereby the camber is automatically reduced in response to flow separation. The results in [127] and [23, 128] show a dependence of the wing lift slope and drag on the compliance, however with conflicting results that are likely due to the particular flow structures on each wing tested. However, each study provides valuable insight into the system-level trades associated with vehicles using membrane wings, where an appropriate balance between lift and drag as well as stall behavior is desired. An additional topic of research, from both a biological and man-made perspective, is the effect of the tail on flight [103, 129-132] Depending on the particular style of flight chosen, the tail is able to alter the aerodynamics over the wings and body to reduce drag, generate lift, and improve maneuverability.

A final research of area that potentially may offer useful data is to equip a flying vehicle with instrumentation and collect data in-flight. To date, there is only one attempt at this approach for flapping wing aerial vehicles beyond the current scope of work, developed at the University of Maryland Morpheus Laboratory [133]. This effort provided vehicle attitude and wing tracking, but lacked measurement of power consumption, airspeed, altitude, position, and suffered from data storage issues related to processing power and timestamp synchronization.

2.4 Aerodynamic Modeling of Low Speed Avian Flight

Aerodynamic models for flapping wing aerial vehicles are diverse, as a natural consequence of the breadth of flight styles that are possible with flapping wings. Broadly, flapping may be categorized into two primary categories, hovering and cruising flight. Hovering flight is characterized by a large body inclination angle, low airspeed, rapid flapping, and hence a high reduced frequency and highly unsteady aerodynamic effects. Conversely, cruising flight is achieved with a relatively flat body pose, high airspeed, and steady lift generation due to airflow over a cambered airfoil. In nature, as well as with man-made vehicles, the natural trend is for smaller wings operating at lower Reynolds numbers to exhibit hovering flight, while larger wings exhibit cruising flight. Models have been developed to capture both extremes of flight. Here, models are explored that are intended for the cruising style of flight in the lower speed transition regime, which exhibits aspects of both cruising and hovering. The challenge posed by this regime is to determine which aspects of cruising and hovering flight models are appropriate for application to the quasi-steady aerodynamics exhibited in slow flight.

Blade element theory is a popular tool for aerodynamic analysis, owing to its conceptual and computational simplicity in describing forces. The model is so named because it was initially used as a tool for analysis of propeller and rotor blades. The model considers integrates span-wise segments from root to tip at each time step to find the overall force and moment production. In a study conducted with Aerovironment

that analyzed a large pterosaur model, DeLaurier used this method to predict the effect of wing twist on lift and thrust productivity [134]. This model uses a modified Theodorsen function to capture unsteady normal force production and also accounts for dynamic stall behavior and leading edge suction. An important requirement in implementing this modeling approach is accurate specification of many parameters, including the coefficient of drag, the stall angle of the airfoil, the leading edge suction efficiency, and the dynamic twist angle of the wings. Depending on the usage scenario, another potential issue with this approach is the assumption of an elliptical wing planform in the calculation of downwash. Despite these challenges, the method is widely used due to the simplicity of the equations which results in a low cost of computation. Several interesting extensions to the blade element model have been explored to improve its accuracy or applicability in different scenarios. One common extension is to combine blade element and classical helicopter momentum theory to produce a more accurate estimate of induced velocity [135]. This method was implemented by Yang to analyze the Robo Raven flapping wing aerial vehicle by performing iterative solution of the momentum equations combined with blade element analysis based on a DIC wing shape reconstruction [136]. The Morpheus group at University of Maryland combined blade element theory with membrane theory developed for the analysis of sails to analyze flapping wings equipped with VICON markers for deformation tracking as shown in Figure 2.18 [25]. Each of these analyses showed significant gaps between predictions and experimental results, but offered

some general insight into the magnitude of forces produced during flapping for preliminary engineering analysis.

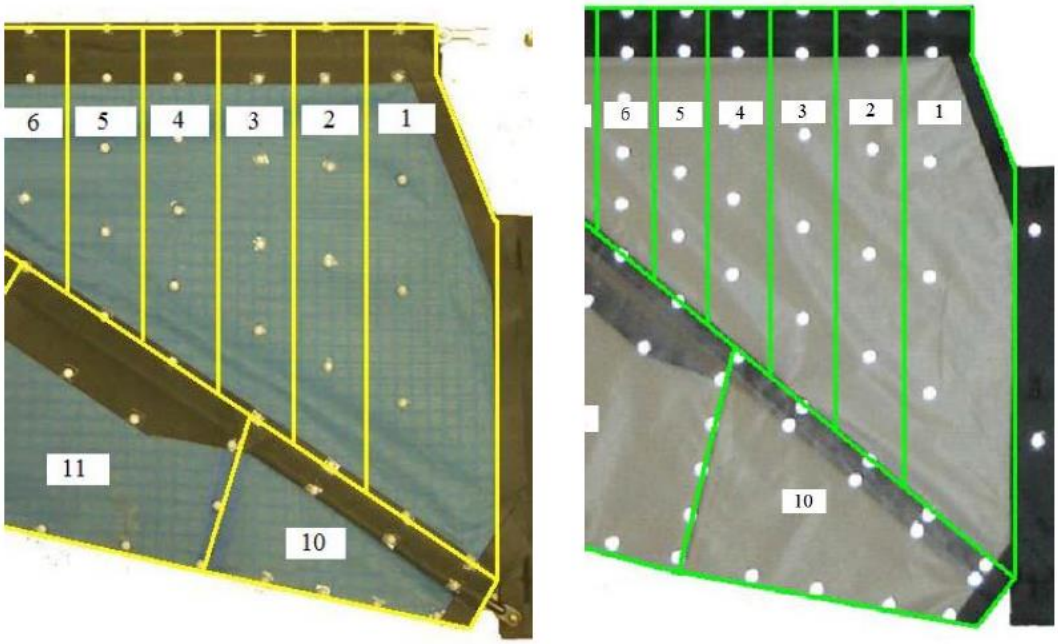

Figure 2.18: Blade elements used to discretize flexible flapping wings by the University of Maryland Morpheus Laboratory [25]

The difficulty of correctly predicting aerodynamic coefficients motivated the application of lifting line theory to flapping wings, which solves for the distribution of circulation over the wings. This modeling framework was originally applied to flapping wings by Pennycuick [137], with some modifications by Tucker [70, 138, 139]. The vortex ring modeling approach by Rayner extends the theory to provide a more detailed description of the wake that assumes the downward wingbeats shed a series of planar elliptical vortex rings with the shape and spacing determined by wingbeat kinematics

and wing shape [140, 141]. The nature of the vortex structure for low speed flight in transitional regime aerodynamics has been visualized and shown to exhibit a clear ring structure consistent with this claim, as shown in Figure 2.19 [14].

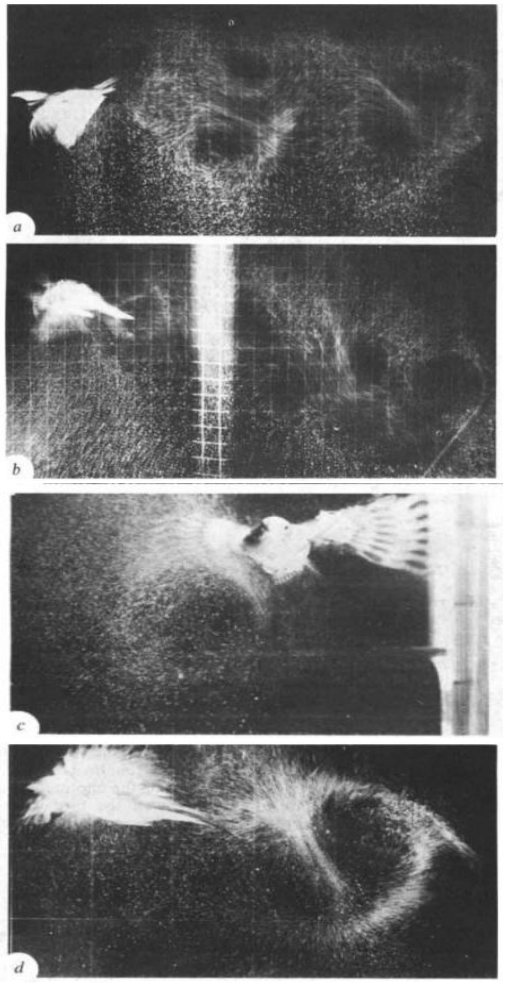

Figure 2.19: Wake visualization of a chaffinch [14]

The vortex ring approach calculates profile drag with a blade element strategy and parasite drag with either a flat plate model or an allometric relation [70, 142]. Induced

power is then computing by solving for the vortex momentum and angle of inclination necessary to sustain flight during one downstroke period. Finally, the power required for flight is computed by determining the self-energy and interactive energy of the vortex rings. The approach yields acceptably accurate predictions of flight power for animals in the limited validation studies that have been performed [66, 143]. A drawback of this approach is the lack of consideration for force production in the upstroke. Simulation-based optimizations of the Rock Pigeon in varying flight conditions have shown that this is unlikely to be a realistic condition in animal flight [144]. Spedding has shown that in higher speed flight, a continuous undulating vortex structure is formed that he calls the 'concertina' wake, as shown in Figure 2.20.

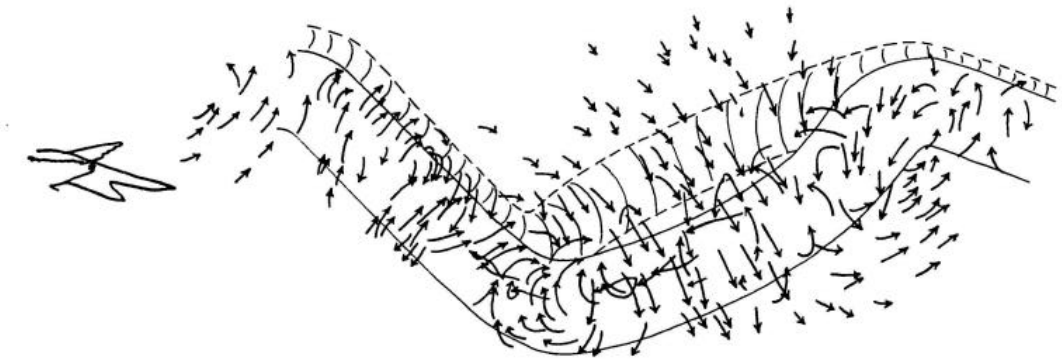

Figure 2.20: Concertina wake structure formed by a kestrel in cruising flight [18]

A numerical approach to solution of the lifting line equations is presented by Phlips, East, and Pratt [145]. This approach considers unsteady force production for a rigid wing that does not exhibit twist. The vortex wake is modeled and compared to the

approaches of Pennycuick and Rayner to establish the strengths and weaknesses of each modeling approach.

An alternative to the analytical methods previously discussed is numerical solution of both the fluid and structural domains in tandem, an approach commonly known as fluid-structure interaction (FSI). Examples of this technique applied to insect-scale flight are widespread, however avian-scale flight is much less frequently studied using this strategy. Ruck and Oertel conducted a broad study of avian flight spanning reduced frequencies of 0.22 to 1.0 and Reynolds numbers of 16,000 to 50,000 [146]. The results from the simulation were then validated with a series of wind tunnel tests conducted on a flapping model, revealing the wake structure contains an increasingly active upstroke component with smaller reduced frequency, accompanied by elongation of the vortex rings described by Rayner's model. An alternative to FSI with somewhat reduced complexity is to ignore the structural coupling and only solve for the aerodynamics using a vortex lattice method (VLM). VLMs cover a lifting surface with a lattice of vortex panels and use numerical solution techniques to obtain a prediction of force production. The principles of these techniques are described in detail in [147] including the significant challenges associated with practical applications of the method including panel discretization strategy and code implementation. Fritz and Long conducted a broad study of this technique with a focus on biological and man-made flapping wing flight analysis that demonstrated the effectiveness of this technique in a variety of aerodynamic conditions [148].

A strategy for alleviating the complexity of full-fidelity numerical solution of flapping wing problems is reduced order modeling. This strategy uses a surrogate model that has reduced complexity while retaining most of the accuracy of classical methods. Stanford and Beran developed a reduced order model based on proper orthogonal decomposition of wing structural deformation modes with a focus the inertial loads of a flexible MAV wing structure [149]. The developed strategy is used to optimize the wing thickness for tip deflection reduction and shows good agreement with the full-order model. Gomez, Bryant, and Garcia developed a low-order phenomenological model they call the Bryant-Gomez-Garcia model to evaluate the effects of translation, rotational lift, and dynamic stall [150]. Their study seeks to capture the relative contributions of each effect by using influence factors to greatly reduce required computational complexity in generating aerodynamic predictions, however their study is limited to fruit fly-sized analysis and is therefore focused on the low Reynolds number range of $O(10^3)$ where unsteady aerodynamics are more important.

2.5 Research Summary and Gap Analysis

Several researchers have explored flapping wing flight by constructing flying prototypes that are capable of free flight [151]. These vehicles have provided valuable insight to researchers, however traditional FWAV designs suffer from limitations in research usefulness due to compromises intended to improve their flight performance. One of the major challenges in FWAV design is a limited weight budget. The simplest

strategy for maximizing available payload is to use wings with passive compliance coupled with a single powerful motor to drive a flapping mechanism. This approach minimizes the number of actuators, but necessarily imposes constraints on the ability to customize wing shapes and kinematics, which reduces available payload and potentially prohibits free flight [101]. Despite the additional weight required, customizable wing control that can be arbitrarily programmed will offer researchers an improved capability to explore design tradeoffs, given that cruising flight is still possible with this approach.

Experimental strategies for characterization of FWAVs are focused primarily on wind tunnel testing and wing tracking strategies in a stationary arrangement. The results provided by this approach are different than free flight conditions. The rigid fixture used in these tests does not allow the vehicle to move in response to wingbeats, resulting in loss of information, particularly in the lift forces and moments. While instrumented flight may offer a solution to this problem, to date there has not been a demonstration of a freely flying FWAV equipped with all the required sensors to characterize free flight from a system perspective.

Modeling strategies used for FWAVs at avian scale in low speed cruising flight typically provide either a highly tractable solution strategy or excellent accuracy, but not both. This tradeoff creates difficulty in using an aerodynamic model in design tradespace studies and often forces designers to use many experimental trials to

converge on a reasonable solution. A major reason for the lack of high quality model predictions is the separate consideration of the wings and drive system. Such an approach does not account for important interactions that impact overall vehicle performance. A system-level model is needed for design studies that includes these component interactions and balances rapid solution generation times with reasonable accuracy. This model must be validated using experimental data to ensure the description of physics and prediction results are reasonably accurate over the desired range of design parameters.

Chapter 3: Preliminary Design Efforts

3.1 Research Roadmap

Throughout this dissertation, an approach for modeling flapping wing aerial vehicles will be developed that combines tractability with suitable accuracy. The main challenge in modeling flapping wing aerial vehicle performance is to ensure that model predictions are appropriately capturing real-world effects that arise due to component interactions. In order to capture these effects, first experimental methods will be developed that are used to characterize important features of each vehicle component. Next, models will be developed that adopt data collected during these experimental trials. Finally, component models will be assembled together such that functional constraints arise which mirror real effects that are observed, thus improving the predictive accuracy of the overall modeling framework.

Prior to engaging with this plan of experiment, modeling, and finally coupled modeling, it is necessary to understand what interactions matter, how components may work together in a baseline design, and what a reasonable parameter space might be that enables practical flight operations. Since flapping wing aerial vehicles may span a broad range of styles, just as natural fliers do, this preliminary work is required to bound the problem space to some basic concept of operations, a generalized vehicle architecture, and at least broadly, identify the rough operational parameters to be explored. Therefore, a key task to initialize the remainder of the experiment and

modeling that is planned is to develop a baseline design that may be used to idenitfy these crucial pieces of information that will allow for more focused analysis to take place. It is with this driving motivation that the development of the Robo Raven I platform was undertaken. The process that led to realization of that platform follows in the remainder of this chapter. In Chapter 4, the experimental techniques necessary to derive important operational characteristics of each vehicle component are developed, including the motors, battery, and wings, as well as an in-flight instrumentation system. Chapter 5 presents modeling approaches for each vehicle component that capture functionality while adopting empirical data observed in the previous chapter. Chapter 6 presents a strategy for improving the prediction of wing kinematics by coupling component models to enforce physically realistic wing motions. Finally, Chapter 7 couples all component models to perform system-level predictions that account for the interactive effects between components that were initially observed in the Robo Raven I platform and further explored in Chapter 4 during instrumented flight testing.

3.2 Robo Raven I Design Objectives and System Decomposition

As discussed in the Introduction, efforts have been made in developing smaller platforms that have the capability to move their wings in tandem. However, a gap remains in avian flight with independent wing control. This led to the high-level objective to build a FWAV that can be used to learn about the effect of changing wing kinematics. In addition, coupling between actuators, wings, and body led to the need for a modular design capable of accepting a variety of candidate parts for experiments.

This modular approach enables data collection that facilitates construction of a system-level model that describes important interactions' effect on vehicle performance. Preliminary laboratory experiments and the prior work performed at the University of Maryland [109] led to the following requirements:

1. Software-programmable wing motions to enable new gait kinematics without hardware redesign.
2. Synchronize wing motions when needed. This enables switching between normal flight and experimental kinematics in the same flight.
3. Minimize weight to achieve a climb rate of at least 0.5 m/s to enable a powered climb to a safe altitude prior to beginning experimental gait kinematics testing.
4. Turning radius at least as small as 10 m for inside flight and flying outdoor in cluttered fields with trees and obstacles.
5. Remotely control the flight from a distance of at least 500 m.
6. Land unpowered at glide speed from a height of 3 m without sustaining structural damage.

Initially, bio-inspiration was used to anchor the preliminary design to a known feasible solution. The namesake of the Robo Raven, the Common Raven *Corvus Corax* was chosen with properties summarized in Table 3.1. The Common Raven was selected for several reasons. Ravens possess a versatile flight envelope including flips, rolls, inverted flight, and aggressive maneuvers [152]. Due to their adaptability they have a wide distribution of geography and climate [153]. Finally, ravens are highly intelligent

and inquisitive, so they made an excellent choice as an inspiration for both the physical design and the guiding philosophy of subsequent research activities [55, 56].

Table 3.1: Properties of the Common Raven, *Corvus Corax* [56]

Parameter	**Value**
Total Mass	0.69-2.00kg
Length	0.63m
Wingspan	1.00-1.50m
Average Chord	0.21m
Aspect Ratio	2.77
Flight Speed	9.80-12.50m/s

The identified requirements led to a system decomposition containing the required major components and the relationships among them, shown in Figure 3.1. This system decomposition was the basis for component selection and integration for the Robo Raven.

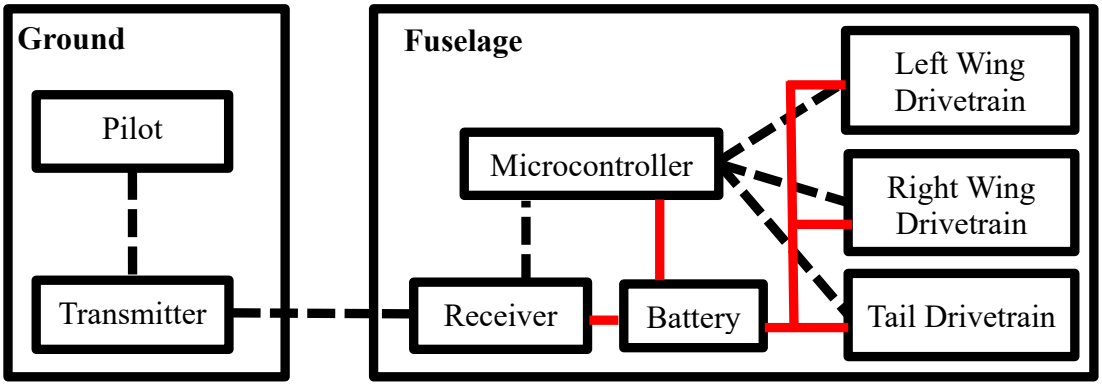

Figure 3.1: Functional decomposition of Robo Raven. Dotted black lines denote signal flows, solid red lines denote energy flows.

3.3 Actuator Selection

The initial focus of the Robo Raven was on achieving free flight to provide a platform to build upon for more advanced capabilities. Since power density is a key design factor for FWAVs and the actuators tend to be the major contributor to vehicle mass, the first design decision was to identify the type of actuators to be used. The design of custom actuators was beyond the scope of this dissertation, so the process began by selecting a commercially available actuator for the wing drive component. The vehicle sizing and associated flapping bandwidth needs limited feasible choices to slower, more powerful actuator types. At this size and loading scale, electric motors are certainly the most popular actuator choice, but some alternatives exist. Popular choices include electrostatic actuators, bimetal bending actuators, piezoelectric cantilevers, shape

memory alloys, and dielectric elastomers [154]. Of these choices, only dielectric elastomers offer acceptably high efficiency of operation. However, the very high operating voltage presents integration challenges and requires additional voltage step-up electronics on-board. Therefore, a pair of electric motors were used with one powering each wing to achieve the desired objective of programmable flapping kinematics. Electric motors must be paired with a flapping mechanism to provide reasonable speeds of operation and sufficient torque. In addition, motors require integration with power electronics that control motor speed and direction to generate the necessary drive signals. Finally, to provide precisely controlled programmable kinematics, feedback control loop must be integrated into the system to correct errors between desired position and actual position during the flapping motions. Together each of these actuator components leads to increased weight, part count, complexity, and integration difficulty. To avoid the challenges associated with matching all of those components and designing the required hardware and software, commercially available servos were chosen for wing actuation, due to their high power output, programmable motions, and integrated packaging including the motor, drive train, speed controller, and position feedback controller.

The unique approach of using a separate actuator for each wing increases weight relative to traditional FWAV designs due to redundant drivetrain parts and smaller, less efficient motors [151]. For these reasons, available payload was expected to be much smaller than would be possible with the coupled wing approach explored in prior efforts

[10, 12, 107, 108, 151, 155]. Light weight was a key requirement for all aspects of the design. Therefore, it was important to identify servos that offered the most favorable combination of high power output and low total weight to maximize the likelihood of achieving flight in the prototype vehicle. In pursuit of this goal, a survey of commercially available servos was conducted in a likely size range to identify a candidate for further testing.

Typically, servo manufacturers will quote a maximum speed under no load and a maximum torque at stall. A nearly linear relationship exists between these two points for small electric motors of the class used in servos [156]. A figure of merit was generated for each servo that seeks to capture potential power output available for driving wings. For each servo, half the maximum speed was multiplied by half the maximum torque. This expected power output was then divided by the mass of the servo to provide a simple power to weight measurement. The servos providing the highest power to weight ratio were deemed the most likely candidates for achieving flight in a prototype vehicle, and were benchmarked for a more detailed performance estimate. The survey of servos is listed in Table 3.2 [157-163]. The Radiopost 5005s and Futaba S9352HV were chosen for further evaluation based on their high figure of merit values, indicating a strong power to weight ratio and greater likelihood of achieving flight.

Table 3.2: Market survey of candidate servos

Make	**Model**	**Torque [N-m]**	**Speed [rad/s]**	**Power [W]**	**Mass [kg]**	**FOM [W/kg]**
Radiopost	5005s	3.241	14.96	12.1	0.059	205.5
Futaba	S9352HV	2.158	17.45	9.4	0.072	130.8
Integy	XQ-S4618D	2.903	10.47	7.6	0.060	126.7
Dynamixel	EX-106+	10.486	7.32	19.2	0.154	124.7
MKS	DS 660	2.834	13.09	9.3	0.075	123.6
Futaba	S9353HV	2.158	17.45	9.4	0.077	122.3
Hobby King	HK47902TM-HV	0.824	34.91	7.2	0.061	117.8
KO Propo	KO-30103	3.080	9.52	7.3	0.066	111.7
MKS	HV787	0.828	34.91	7.2	0.066	109.4
Hitec	HS-7940TH	1.568	17.45	6.8	0.068	100.6
Savox	SC-1273TG	1.569	16.11	6.3	0.063	100.3
Savox	SC-1268SG	2.550	9.52	6.1	0.062	97.9
Savox	SC-1267SG	2.055	11.64	6.0	0.062	96.4
JR	Z9100HVS	1.624	17.45	7.1	0.074	96.2
Hitec	HS-7945TH	2.255	10.47	5.9	0.065	90.8
Hobby King	HK47903TM-HV	3.040	6.98	5.3	0.060	88.4
Hobby King	HK47179TM-HV	1.157	17.45	5.0	0.061	82.8

3.4 Software Development

Selection of a servo as the actuation system enables the realization of programmable kinematics by replacing a traditional motor connected to a flapping mechanism with a software analog. Instead of using hardware to convert rotation of the motor into flapping action, programming executed by a microcontroller is used to provide the servo controller with time-varying angular positions for each wing, which are then achieved through the action of the position error feedback controller. The Arduino Nano built by Gravitech was selected for this task due to its integration of several input and output pins, voltage regulation, and many pre-existing code libraries [164]. The desired software functionality requires development of several layers that work together. First, the pilot commands must be interpreted. The radio receiver encodes this information as a series of six pulses between 1000-2000μs based on the commanded position for each channel, separated into 20ms frames as shown in Figure 3.2. These pulses are parsed by the microcontroller by locating the start of a new data frame, sequentially timing the width of the high time for each channel's pulse using an interrupt subroutine, and storing the value in memory until the next data window, resulting in a 50Hz refresh rate for commanded kinematics.

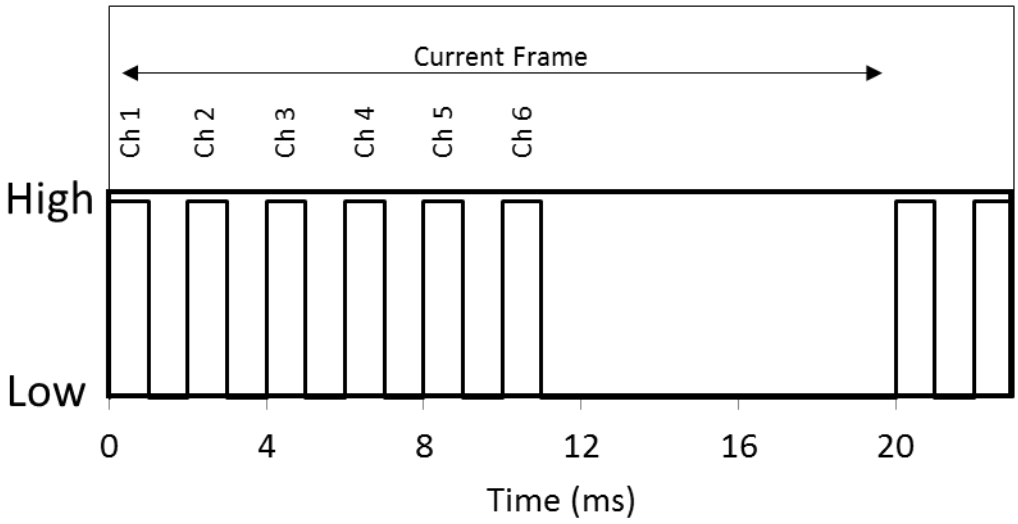

Figure 3.2: Pulse position modulation scheme used to encode pilot commands

The pilot commands are mixed based on a series of pre-programmed rules set up to establish flapping modes that are selectable by the pilot. The purpose of these rules is to create a fly-by-wire mode of control to ease cognitive burden on the pilot and maintain expandability for testing new flapping gaits. The flapping motions programmed include variable flapping rate and amplitude, tail-only steering, asymmetric wing amplitude variation, up-down flap speed asymmetry, average dihedral shifting, and flap-bounding. In addition to mixing pilot commands, transitions between wing motions at each time step are timed and coordinated to prevent discontinuous position changes. Position command continuity prevents abrupt wing motions that upset vehicle stability and drain battery power. Finally, the mixed position commands are output at the same 50 Hz rate to each of the wing drive servos and the

tail servo. Final position control is then left to each servo's on-board feedback controller, which effectively minimizes the effect of variable asymmetric loading due to wind gusts and other disturbances. Several additional blocks of code are also included that record data from on-board sensors. This data collection functionality will be described in greater detail in Chapter 5.

A priority in the development of the flapping code was avoidance of floating point operations, which are more demanding on the selected microcontroller, since it lacks a hardware floating point unit. Preliminary testing revealed that floating point operations create unpredictable jitter in the desired output rate of 50 Hz to the servos, resulting in unacceptable flapping dynamics. Since the baseline flapping motion chosen was a sinusoidal profile, exclusion of floating point operations presented a challenge. To avoid floating point operations while providing smooth sinusoidal motion, the direct digital synthesis (DDS) approach was implemented. The DDS approach uses a hardware clock to sum values that are recorded on the throttle input channel at a known frequency. These values are stored in a 16-bit number. Immediately prior to sending updated position commands to each wing drive servo, the 16-bit throttle counter is bit-shifted to an 8-bit number, then mapped to a 256 entry lookup table containing the sinusoidal motion primitive used for baseline flapping motion. This approach provides efficient operation, high resolution for varying throttle positions, and thus ensures smooth flapping action across the entire range of throttle inputs. Testing revealed this approach is capable of executing at approximately 75 kHz on the chosen Arduino Nano,

well above the frequency required to reach a 50 Hz output refresh rate. By comparison, directly computing the sinusoidal flapping motion with floating point operation resulted in highly unstable flapping motions due to a non-deterministic code execution rate.

3.5 Platform Integration

With the drive motors and microcontroller selected, a compatible lithium polymer battery and radio receiver were selected to complete the wing drive electrical system. In addition a light weight tail servo was chosen to finalize the electronics for the initial Robo Raven design. The tail subassembly shown in Figure 3.3 is a direct drive rudder-type control surface that is inclined to provide a stabilizing moment to counteract the wing forces.

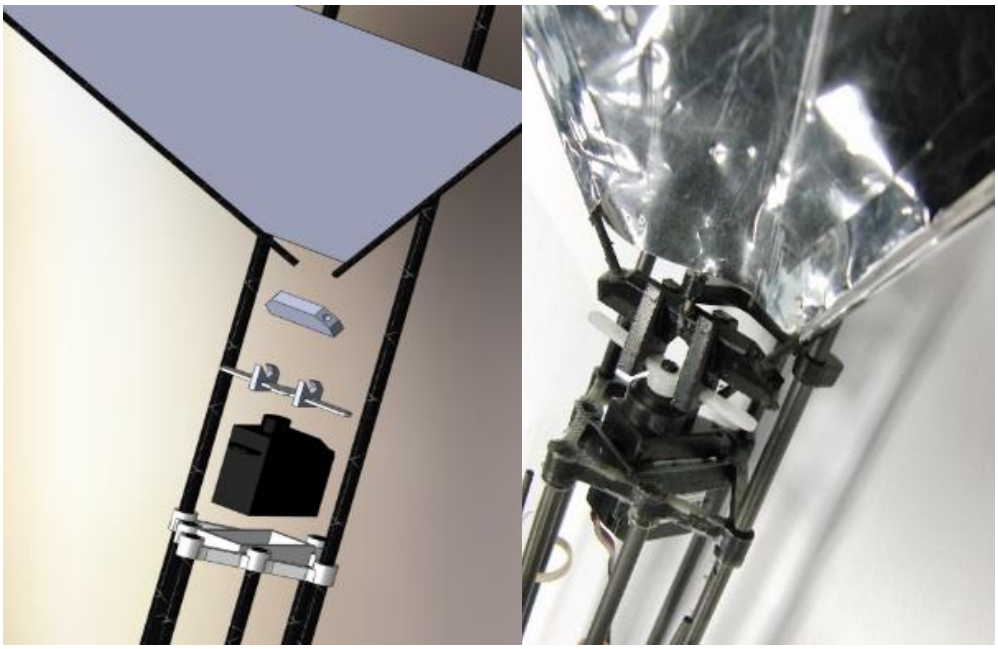

Figure 3.3: Exploded view of tail subassembly (left) and as-built tail (right)

The fuselage consists of a carbon fiber skeleton that minimizes both mass and projected surface area for improved flight performance. At the front is the housing for the drive servos. The servo housing is 3D printed with the fused deposition modeling technique to precisely fit the motors while providing maximum cooling and keeping mass to a minimum. The wings are mounted to the servos using adapters that the wings slide into, and then slip over the metal horns that are driven by the servo output. These are locked to the drive motors and fuselage with a nose piece that absorbs off-axis loads to the motors created by force oscillations from the wings in both the lift and thrust directions.

The nose piece also provides crash protection for the more delicate servo frame and fuselage. An exploded view of the fuselage is shown in Figure 3.4.

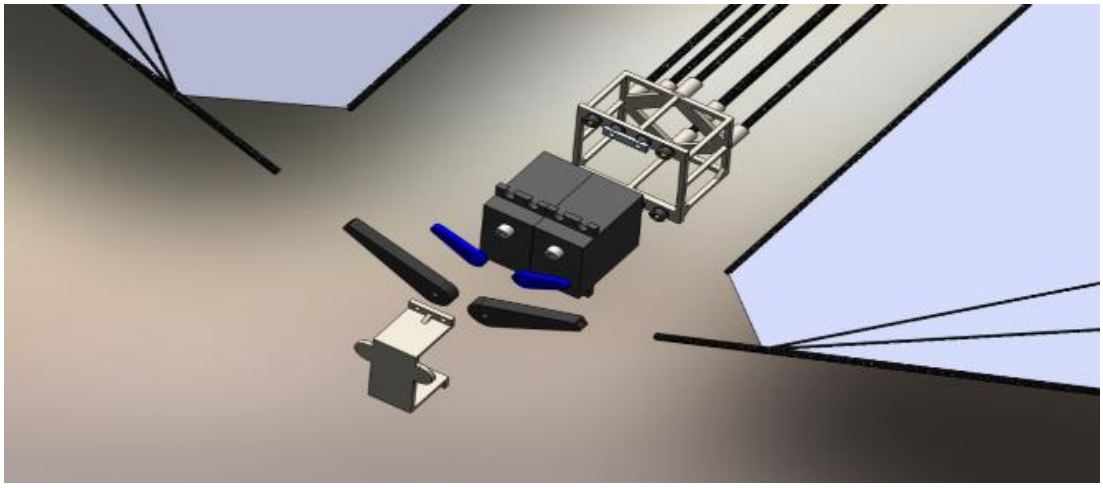

Figure 3.4: Exploded view of nose piece, wing mounts, servo horns (blue), servos, servo housing, and carbon fiber fuselage (left to right). Wings are shown on edges.

Weight minimization was achieved for the servo housing by using finite element analysis (FEA) to remove material from non-critical regions of the part. A sample FEA stress calculation is shown in Figure 3.5 indicating a maximum stress of 4.5 MPa when

subjected to a 1kg crash load, well below the 71.6 MPa yield stress of the ULTEM 9085 build material [165].

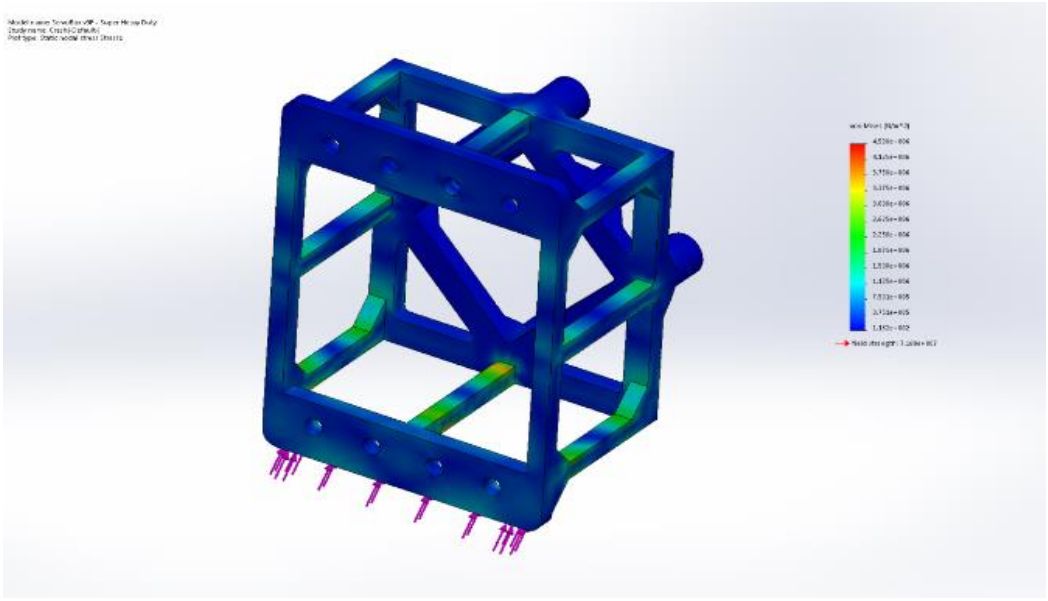

Figure 3.5: FEA stress calculation for servo frame

A summary of each component included in the initial Robo Raven prototype is included in Table 3.3.

Table 3.3: Mass summary of Robo Raven prototype

Component	**Mass (g)**
2 Futaba S9352HV Drive Servos	136.0
Tail Servo	7.8
Arduino Nano Microcontroller	6.0
Interconnect Wiring	19.8
Turnigy Nanotech 2 Cell 370mAh Lithium Polymer Battery	27.0
Spektrum AR6110E 6ch 2.4GHz Radio Receiver	3.0
Tail	8.0
Servo Mounting Frame	16.4
Fuselage	30.0
Foam Crash Protector	5.0
Assembly Fasteners	5.3
2 Wings	26.0
Total	**290.3**

3.6 Wing Design

The wings used by the Robo Raven use lightweight materials and passive deformation to achieve desired shape changes during flapping. The wings are constructed from 1 mil Mylar foil and carbon fiber stiffeners according to the template shown in Figure 3.6. The variables *S*, *C*, *t*, and θ refer to semispan, maximum chord, carbon fiber stiffener thickness, and orientation angle relative to the leading edge, respectively. The general design for these wings was varied across several configurations as summarized in Table 3.4 to determine how spatial stiffness distribution affects lift and thrust production.

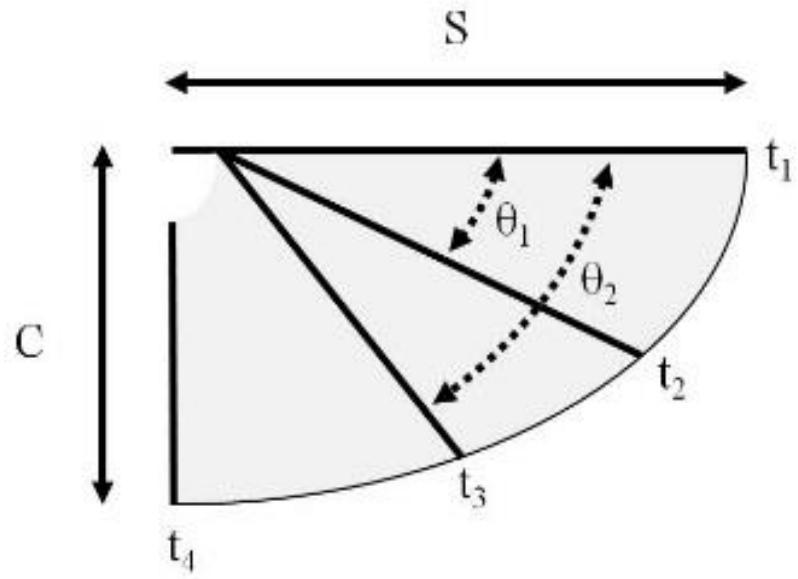

Figure 3.6: Wing design template developed in [12]

Table 3.4: Wing designs evaluated

Design	**θ_1**	**θ_2**
A	20°	40°
B	27.5°	40°
C	20°	47.5°
D	20°	32.5°
E	12.5°	32.5°
F	12.5°	47.5°

Each wing design was evaluated using a combination of high speed video footage and a wind tunnel equipped with a six degree of freedom load cell to measure flapping forces. Peak force results collected during load cell testing for each wing are summarized in Figure 3.7. Wing A was selected due to superior lift and thrust performance.

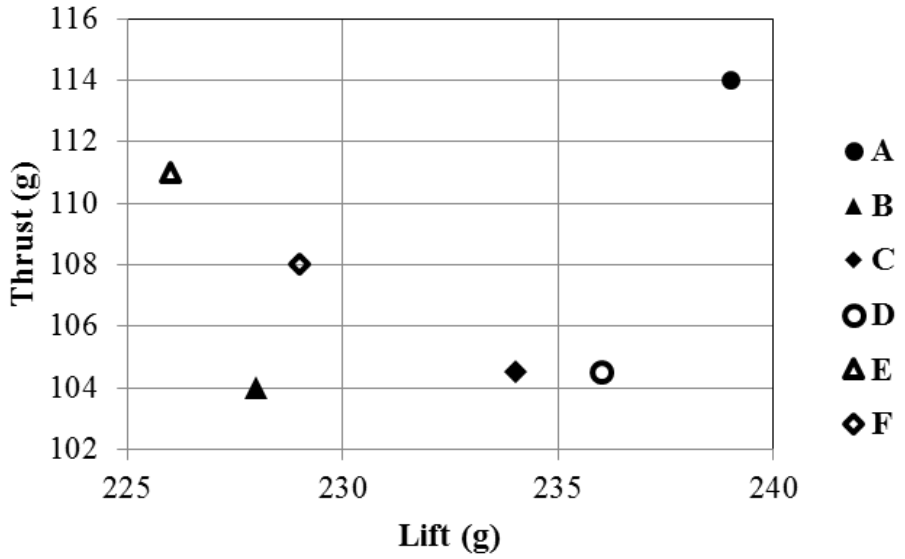

Figure 3.7: Load cell results for the wing designs in Table 3.4

High speed images of each wing were captured during each load cell trial to help explain the reasons for varying performance across the designs. Results from testing Wing A are shown in Figure 3.8.

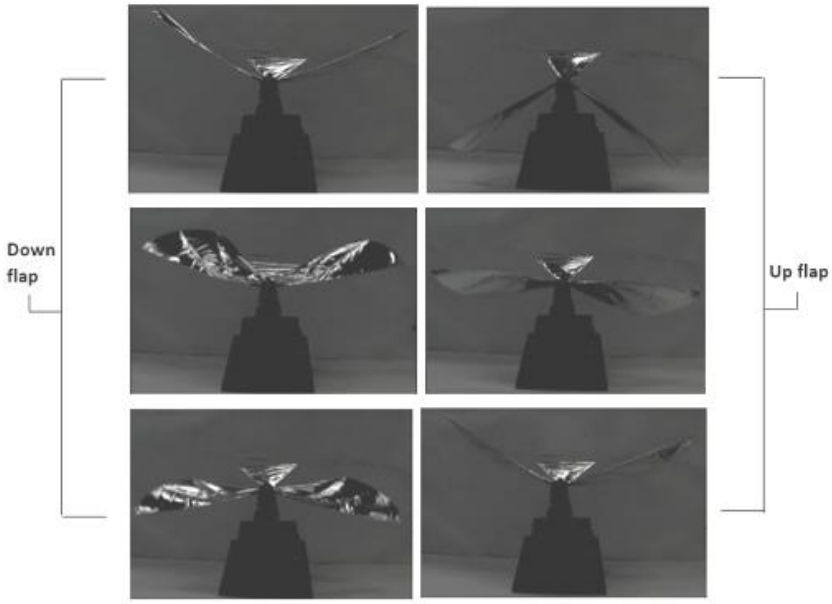

Figure 3.8: High speed images captured during Wing A testing

The superior lift and thrust of the A design is attributed to the deformed volume, which was the largest for this spar arrangement. The importance of this metric was established by conducting an optical characterization study that mapped deformation properties to force production [12]. During that study a sensitivity analysis was also performed to determine the dependence of wing performance on manufacturing errors and demonstrate the repeatability of performance across multiple sets of wings.

After establishing the spatial distribution of stiffeners, the next step was to perform initial wing sizing to ensure compatibility with the drive motors. The strategy for initial sizing was to build a series of wings with the ‘A’ design shown in Figure 3.7 and varied area, then drive them up and down at full speed using the Futaba S9352HV servos,

identified earlier in this chapter. The angular velocity was recorded by using high speed video capture during each trial. The servos possess an approximately linear relationship between peak torque and no-load speed operating points and therefore have a parabolic power curve with peak output at approximately 50% of the no-load speed. Therefore, initial wing sizing was intended to match this speed as closely as possible, thus maximizing the mechanical power output from the motors. This approach yielded wings with the properties described in Table 3.5.

Table 3.5: Wing design used on Robo Raven

Parameter	**Value**
S	605.8mm
C	362.0mm
t_1	3.18mm
t_2	1.37mm
t_3	1.02mm
t_4	1.65mm
θ_1	20°
θ_2	40°

Significant deformations are experienced by the wings during flapping due to aerodynamic and structural loads. The deformations cause the projected length of the chord at the wing root to reduce due to camber increase and the leading edge spar to

deform aft in response to drag forces. To counteract these effects and to maintain sufficient tension for proper airflow, it was necessary to use a compliant connection between the wing and the fuselage. Rubber bands looped through the root chord spar every two inches maintain appropriate tension in the wings and prevent deformations from causing shape discontinuities that reduce lift and thrust production. The completed wing is shown in Figure 3.9.

Figure 3.9: Compliant wing based on Table 3.5 parameters

3.7 Design Summary and Testing

The finalized design is shown assembled in Figure 3.10 equipped with the components listed in Table 3.3. Initially, the prototype Robo Raven was programmed with variable flapping rate control up to 4Hz and tail-based passive steering. This configuration led to a coupling between flap rate, flight speed, and climb rate, as well as a passive rudder-type steering achieved by shifting the tail left and right.

Figure 3.10: Assembled Robo Raven prototype

A series of flight tests were conducted to establish performance capabilities of the initial Robo Raven prototype. These tests demonstrated the first successful free flight of an avian-scale flapping wing aerial vehicle with independently controlled and actuated wings. A summary of the flight testing of the Robo Raven is shown in Table 3.6. The flight dynamics are well-aligned with flying animals of a similar size class, as indicated by the Strouhal number which describes the nature of vortex shedding from the wings. The value of 0.395 falls into the expected range of 0.2-0.4 exhibited by a broad range of animals [76, 166].

Table 3.6: Flight test results of the Robo Raven

Parameter	**Value**
Flap Rate	4.0 Hz
Flap Amplitude	100°
Angle of Attack	20°
Climb Rate	0.53 m/s
Reynolds Number	124,000
Strouhal Number	0.395
Minimum Turning radius	6.1 m

Following the initial flight testing trials, several new wing-based maneuvers were tested to leverage the independent wing control capabilities afforded by the Robo Raven. The first maneuver tested was a button-hook turn, shown in Figure 3.11. This maneuver is initiated by commanding one wing to move to a 40 degree dihedral and the other to move to a 40 degree anhedral. The resultant force asymmetry creates a lateral instability, resulting in rapid yaw and roll that is much more aggressive than would be possible with only rotating the tail. The button-hook maneuver allows for a turning radius of 2.4 m which is smaller than the tail-based minimum turning radius of 6 m. It takes 2.1 s to complete a full 180° turn with this control, and Robo Raven drops

about 3 m during the turn. This altitude loss is expected due to the lost lift and thrust associated with non-flapping wings.

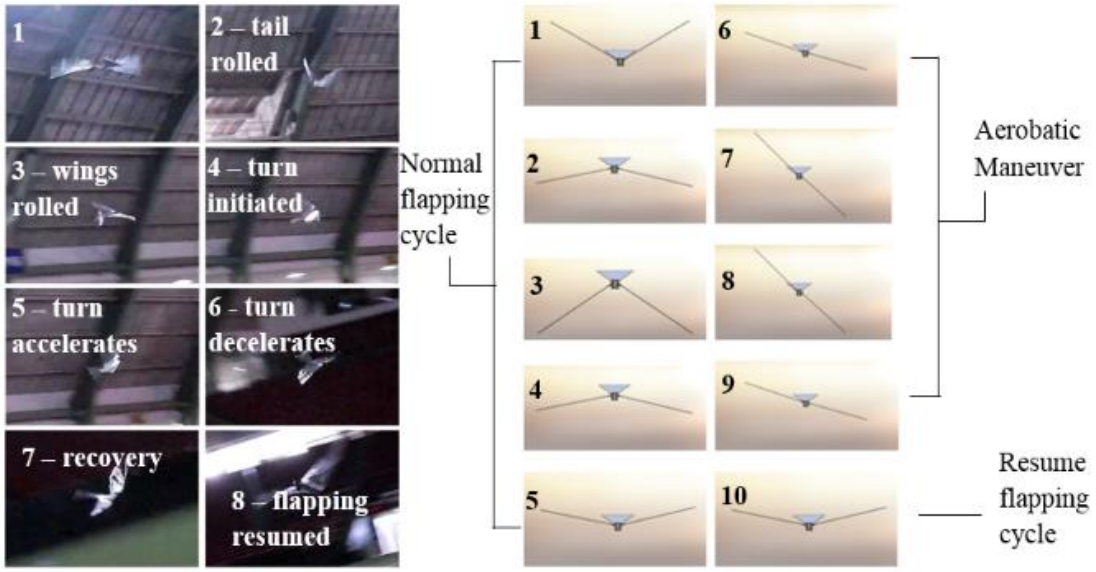

Figure 3.11: Buttonhook turn maneuver (left) and CAD representation of motion sequence (right)

The next maneuver tested was a back flip, as shown in Figure 3.12. This aerobatic maneuver is initiated by commanding both wings to rapidly move below the fuselage to a 40° anhedral which initiates the backwards roll as the body heaves in response to the flapping motion. Moving the center of lift below the center of mass creates a force imbalance, aided by the drag of the elevated tail surface, both of which further accelerate the roll. After the fuselage has pitched beyond the vertical, flapping is resumed to establish vehicle stability and complete the transition back to cruising flight.

This maneuver takes 1.7 seconds to complete. The backflip maneuver is a useful capability because if the flare-up is terminated at the proper moment, a delayed stall can be generated and controlled with small wing adjustments [20, 167]. This is analogous to flying animals' pre-landing flare-up maneuver used to precisely locate their bodies prior to grasping a suitable object for perching or landing.

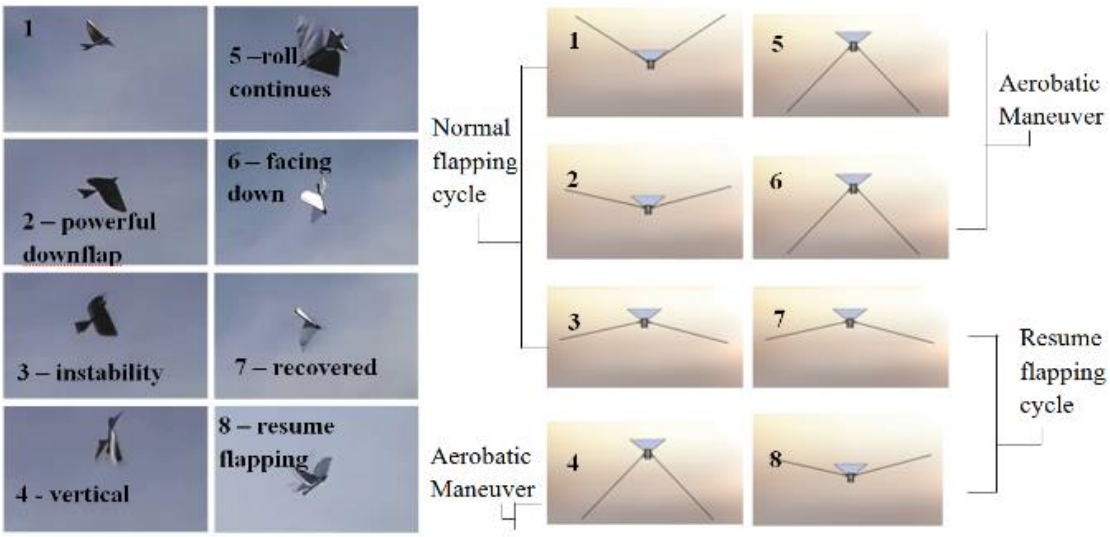

Figure 3.12: Back flip maneuver (left) and CAD representation of motion sequence (right)

The third maneuver tested is a dive motion, shown in Figure 3.13. This maneuver is initiated by moving both wings to a 40 degree dihedral and holding for as long as the dive command is received. When in this position, the vehicle exhibits passive stability

so that it maintains constant orientation in yaw and roll, while increasing dive angle and airspeed. Flapping is resumed at the end of the dive to continue cruising flight.

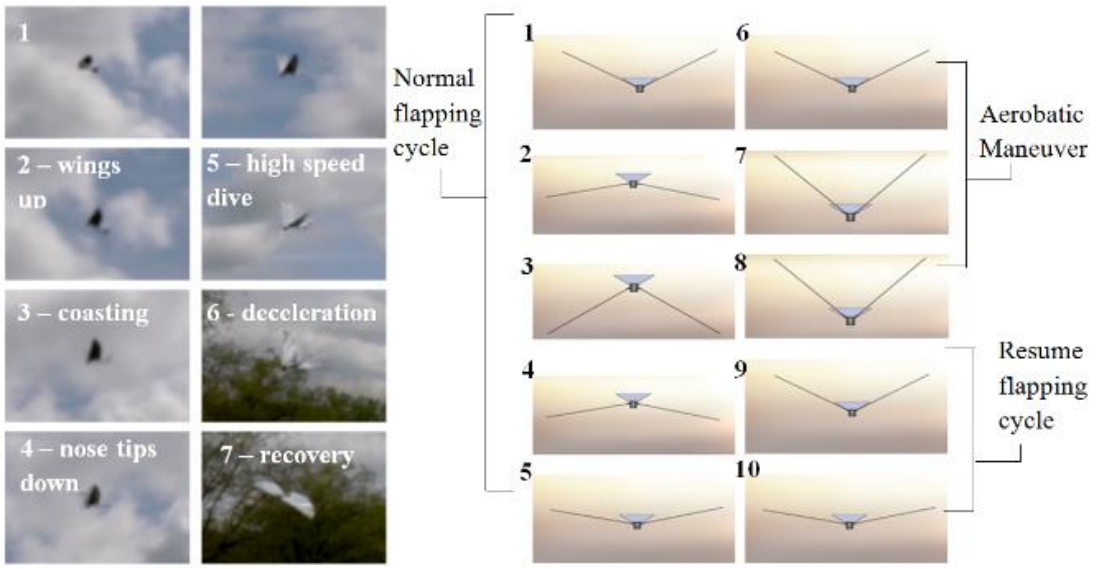

Figure 3.13: Dive maneuver (left) and CAD representation of the motion sequence (right)

The prototype described in this chapter is named the Robo Raven I, and is the baseline design for a series of complimentary research endeavors which includes the vehicles described in Chapter 2.2. Subsequent chapters will describe the experimental and modeling processes used to build an understanding of component interactions, with the objective of realizing models that predict component performance, and in composition predict vehicle performance. The vehicle used to validate these experiments and models is named the Robo Raven II and is derived from the insights gained through

these modeling and experimental efforts, applied to the Robo Raven I baseline vehicle design.

Chapter 4: Development of Experimental Characterization Techniques

4.1 Servo Motor

Several candidate servos were identified in Chapter 3.3 and the performance was estimated using a basic formulation for figure of merit that sought to capture a rough power to weight ratio. Now, a generalized process is developed for evaluation of this class of actuators for two reasons. First, the process yields a structured approach for motor selection based on validated empirical data rather than rough estimation strategies that rely on manufacturer claims alone. Second, the process reveals useful insights including areas where current capabilities are lacking and where further research and development may provide benefits. This leads to a clearer picture of the actuator trade space, and helps vehicle designers ensure component selections are trusted to perform as intended.

The characterization process begins with benchmarking to validate the linear performance assumptions made during actuator candidate selection. Servo benchmarking began with disassembly to determine the gear reduction from the drivetrains, determined by counting gear teeth. The disassembly also provided insight into the functionality of the servos. Inspection of the parts revealed that a position measurement via a potentiometer is supplied to an onboard microcontroller, which regulates the servo velocity in response to position error feedback. The velocity is driven with a rapidly switching (pulse width modulation) PWM power supply

operating at 300 Hz. This is an important feature of these servos as it provides a lower bound on sampling rate for subsequent power testing to ensure the high speed switching effects are captured.

With the motors disassembled, the next step was to measure the electromechanical performance of the servos. A testing approach was developed as shown in Figure 4.1.

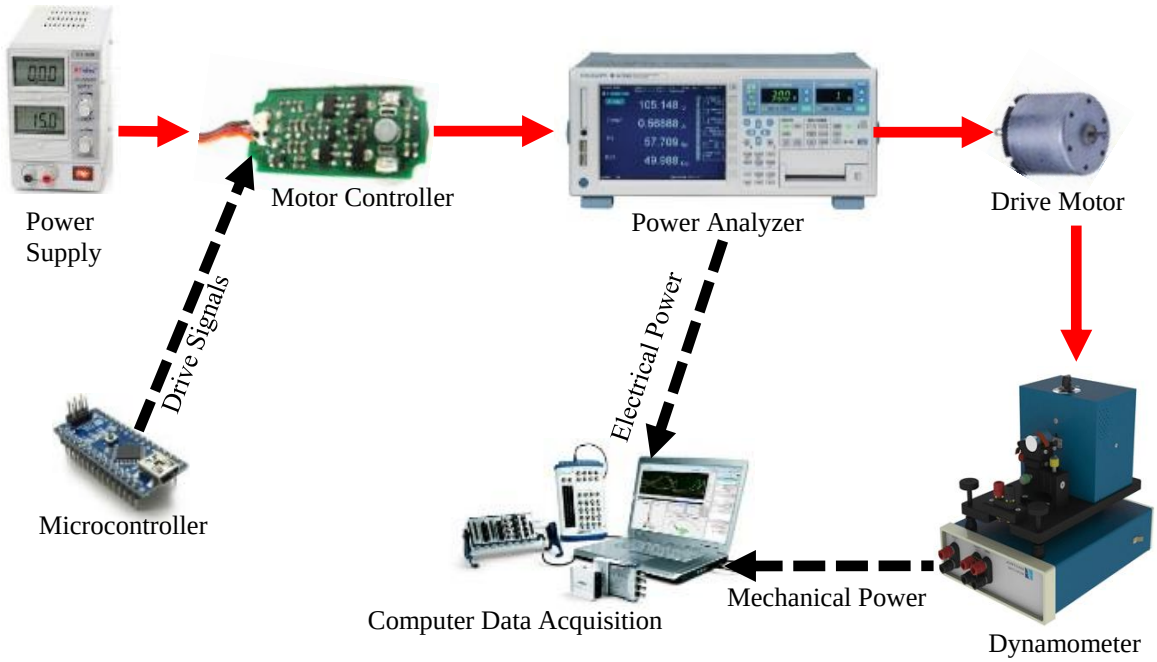

Figure 4.1: Motor testing experimental setup. Red solid lines denote power flows, black dashed lines denote signal flows.

The power supply provides the system with a user-selectable voltage with no limit on the supply current. Testing begins by supplying an angular position command to the

motor controller in the form of a PWM signal somewhere in the range of 1000-2000 microseconds. This range corresponds to the limits of rotation by the servo in each direction. Internally, the servo converts this PWM signal into an analog voltage. By disconnecting the potentiometer from the output shaft of the servo and turning its wiper to a value that is not close to the commanded position, the controller can be forced to drive the motor at full velocity, since it is trying to correct a perceived large position error. Unlike typical hobby-grade servos, the selected Futaba S9352HV and Radiopost 5005s servos are digitally controlled, resulting in non-linear feedback in response to measured position errors. This effect was evaluated with a series of characterization tests, shown in Figure 4.2.

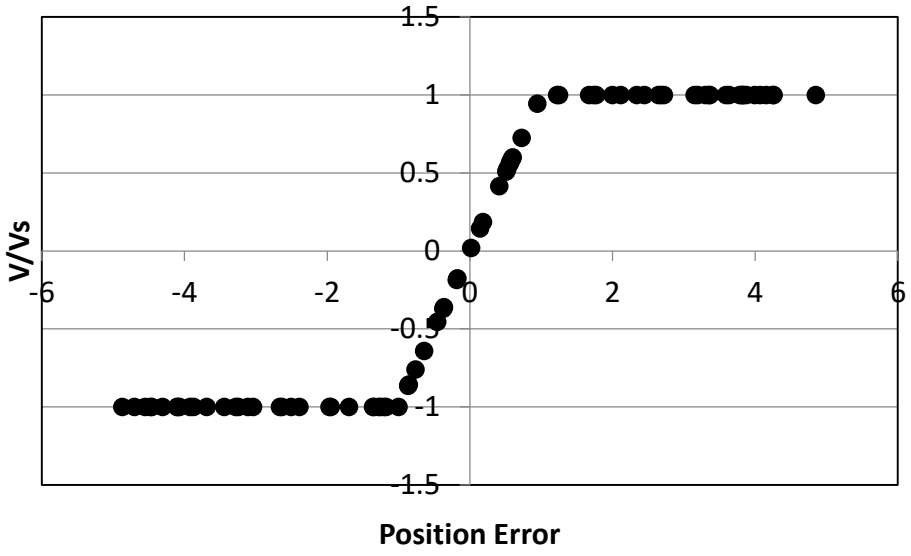

Figure 4.2: Voltage applied relative to supply voltage as a function of the measured position error

Load testing with the dynamometer is conducted by connecting the output shaft of the motor to the load spindle on the dynamometer and commanding a full power rotation achieved via potentiometer deflection away from the control point. Once the drive motor has been commanded to run at full velocity, it is allowed to accelerate to its maximum free-run speed under an unloaded condition. Once this condition has stabilized, the dynamometer applies a magnetic brake that gradually ramps up a resisting torque. The dynamometer used for this testing was a Magtrol Microdyne [168]. This dynamometer has a maximum torque limit of 4 mN-m and is a hysteresis type, which means that the load is ramped up then ramped down, which creates a hysteresis loop. The difference between the ramp-up and ramp-down are averaged to compensate for the effect of the motor's inertia either boosting or reducing the torque measurement. This approach is shown in Figure 4.3 with recorded torque and speed data plotted up to the torque limit along with a regression forecasting the remainder of the operating envelope for a preliminary test of the Futaba 9352HV at a nominal voltage of 6.0 Volts. The effect of motor inertia is evident in the spread between the two loading directions, however the prediction has excellent accuracy and effectively removes this inertial offset.

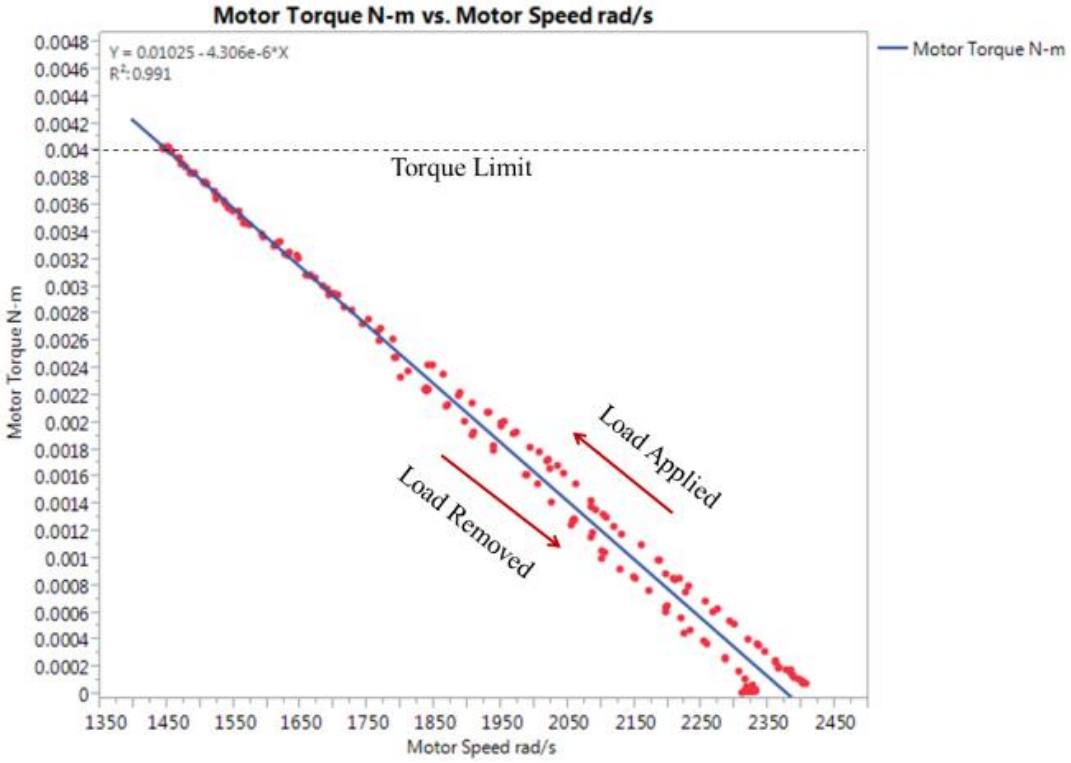

Figure 4.3: Hysteresis effect due to motor inertia

Each test generates a set of mechanical and electrical data including voltage, current, revolutions per minute (rpm), and torque. From this data, additional measures are generated including electrical power input as the product of voltage and current, mechanical power output as the product of torque and angular velocity, and electromechanical efficiency as the quotient of input and output power.

The servo figure of merit defined in Chapter 3.3 depends on an assumption of a linear relationship between two critical operational points: stall torque and maximum speed under no load. Therefore, early testing was focused on verifying the linear assumption

by measuring the torque as a function of motor speed. The torque-speed results also provide a direct strategy to validate manufacturer performance claims.

In Figure 4.4, a Futaba 9352HV test is shown, conducted at a nominal voltage of 7.40. This value is selected because high voltage servos of this class are designed to be operated in conjunction with a two cell lithium polymer battery, with a typical voltage of 7.40. Since the dynamometer is directly measuring torque and speed at the motor output, the results are scaled to final drive values based on the gear ratio determined during benchmarking. The test is truncated at the dynamometer torque limit of 4 mN-m at the motor output. This value scales to the plotted maximum value of about 0.70 N-m for the final drive.

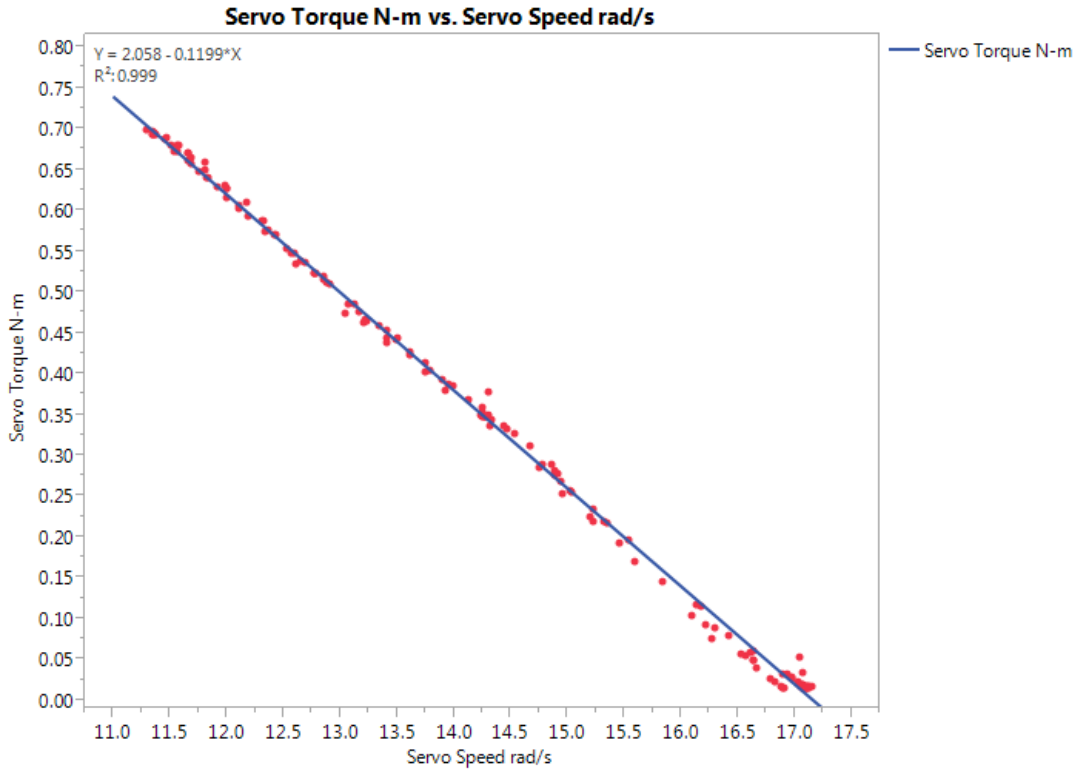

Figure 4.4: Performance verification for Futaba S9352HV servo at 7.40 Volts

In Figure 4.5, the Radiopost 5005s has been tested at the same nominal 7.40 Volts. Similarly, the results are scaled to final drive based on the gear ratio measured during benchmarking. In both the Futaba and Radiopost test results, the line of fit contains two variables. The constant represents the final drive stall torque, and the scaling factor represents the speed constant, which describes how speed reduces with loading and may be used to solve for the no-load speed.

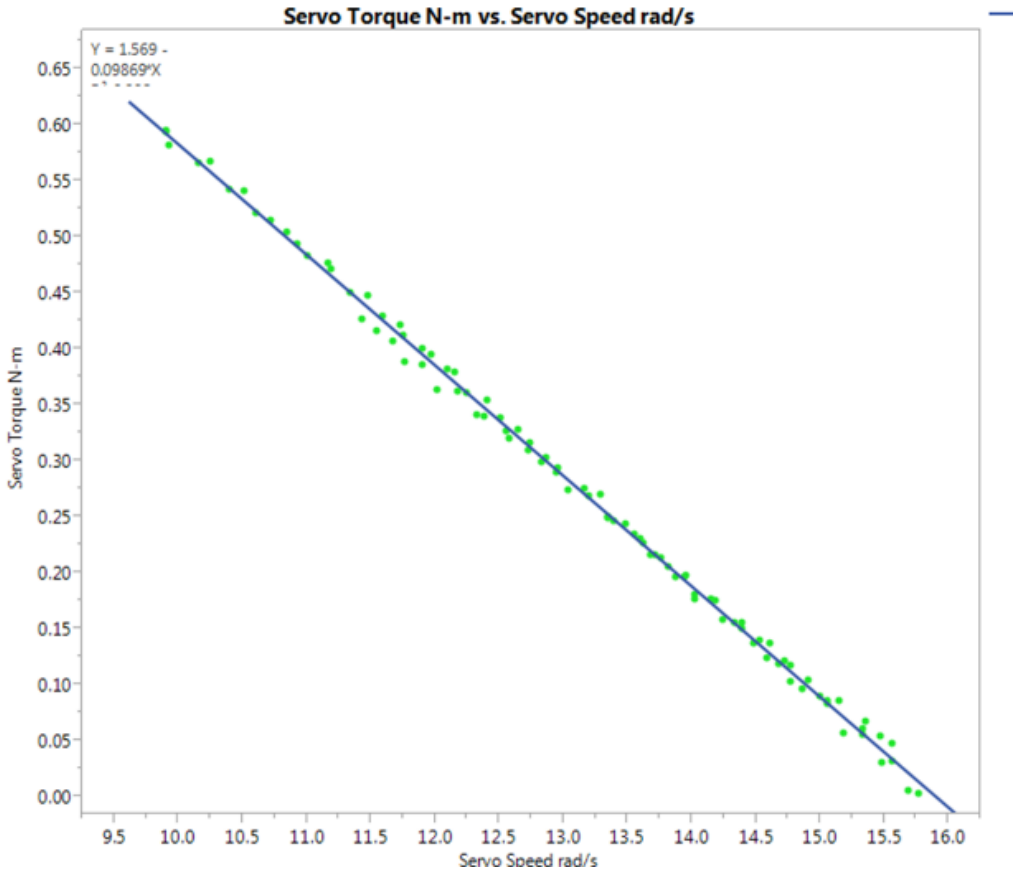

Figure 4.5: Performance verification for Radiopost 5005s servo at 7.40 Volts

The excellent correlation of the linear regression for each of the plotted torque-speed results reveal that the assumed linear relationship between the two critical operating points was valid. Following this assumption, the power curves are plotted for each servo in Figure 4.6. The Futaba has an apparent performance advantage, with a peak power output almost 50% greater than the Radiopost. Therefore, in applications requiring increased lift and thrust and hence greater power output, the Futaba servo is potentially a better candidate. Conversely, applications with reduced power

requirements may benefit from the lighter weight and reduced power consumption of the Radiopost servos for more efficient battery power usage.

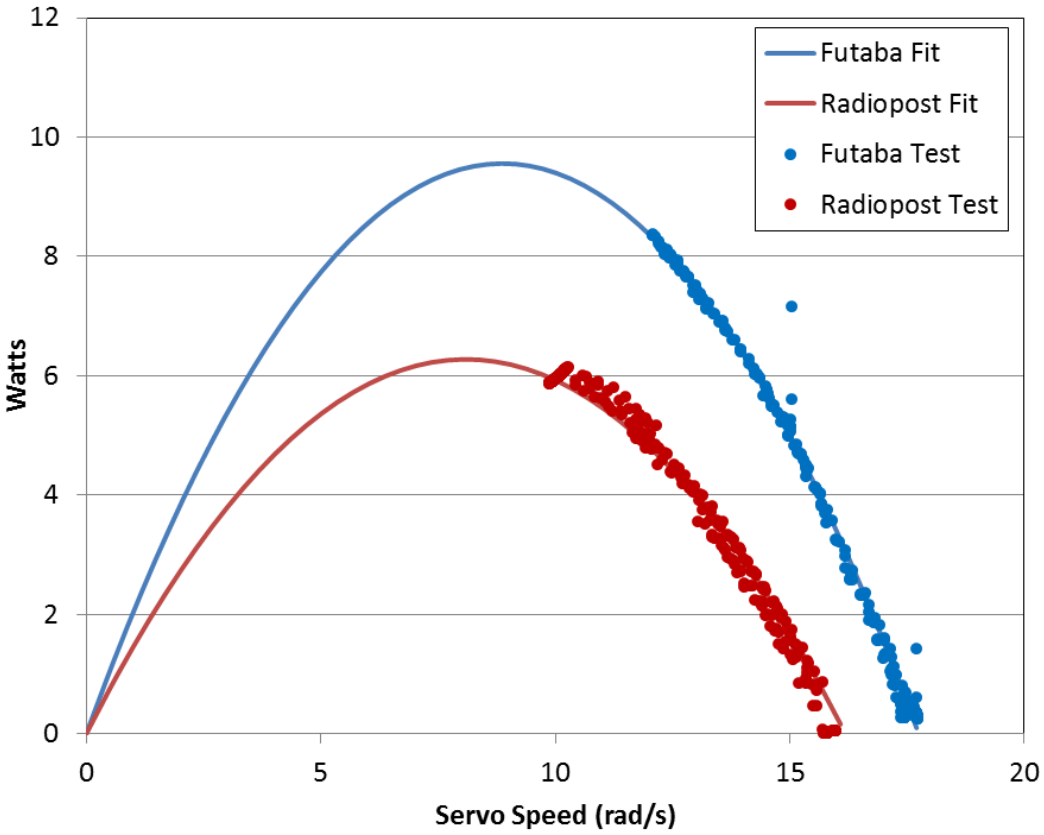

Figure 4.6: Power output comparison between two candidate servos tested at 7.40 nominal voltage

Another important performance metric is the efficiency, defined as the mechanical power output divided by the electrical power input. The peak efficiency happens at a higher speed than peak power output, which creates a region of reasonable performance trades for the motor between about 50% and 75% of the maximum free-run speed. The

Futaba servo dominates the performance of the Radiopost servo under all operating conditions, while the Radiopost servo has smaller mass and reduced energy consumption. A summary of the endurance for each servo derived from the 7.40 Volt verification test is shown in Figure 4.7.

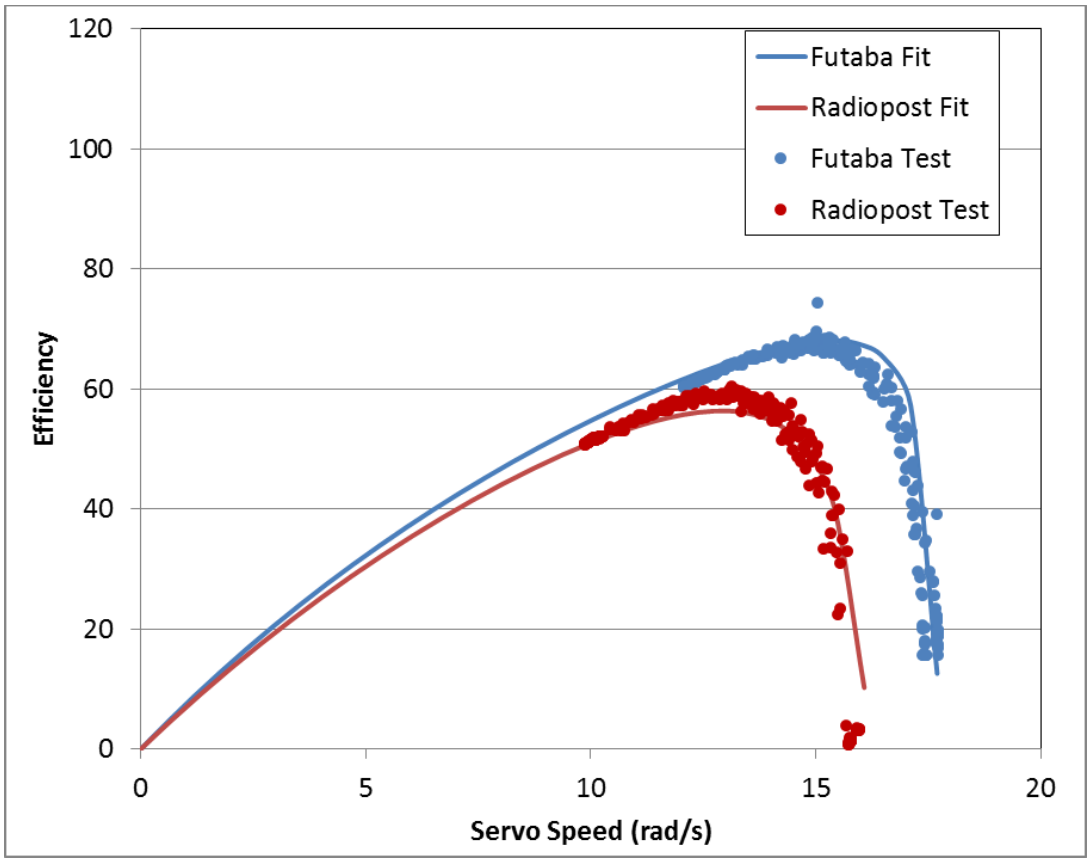

Figure 4.7: Electromechanical efficiency comparison between two candidate servos tested at 7.40 nominal voltage

The testing performed thus far does not provide the required granularity in operational conditions that will be encountered throughout a battery discharge cycle, where voltage

will gradually reduce. A series of experiments were conducted to construct a map of motor electromechanical performance for all feasible operational conditions to address this issue. The testing matrix consisted of a series of torque ramping tests, conducted at several voltage intervals providing coverage of the range of reasonable operational voltages for the actuators. The results collected for the Futaba servo are plotted in Figure 4.8. Following the same approach, results were collected for the Radiopost servo, plotted in Figure 4.9. The data shown in each plot is raw data collected prior to correction for motor inertia so it still exhibits hysteresis. The torque and speed are scaled to final drive values using the gear ratio for each servo respectively. For each labeled test index, a nominal (starting) voltage is selected, then ramp loading is applied.

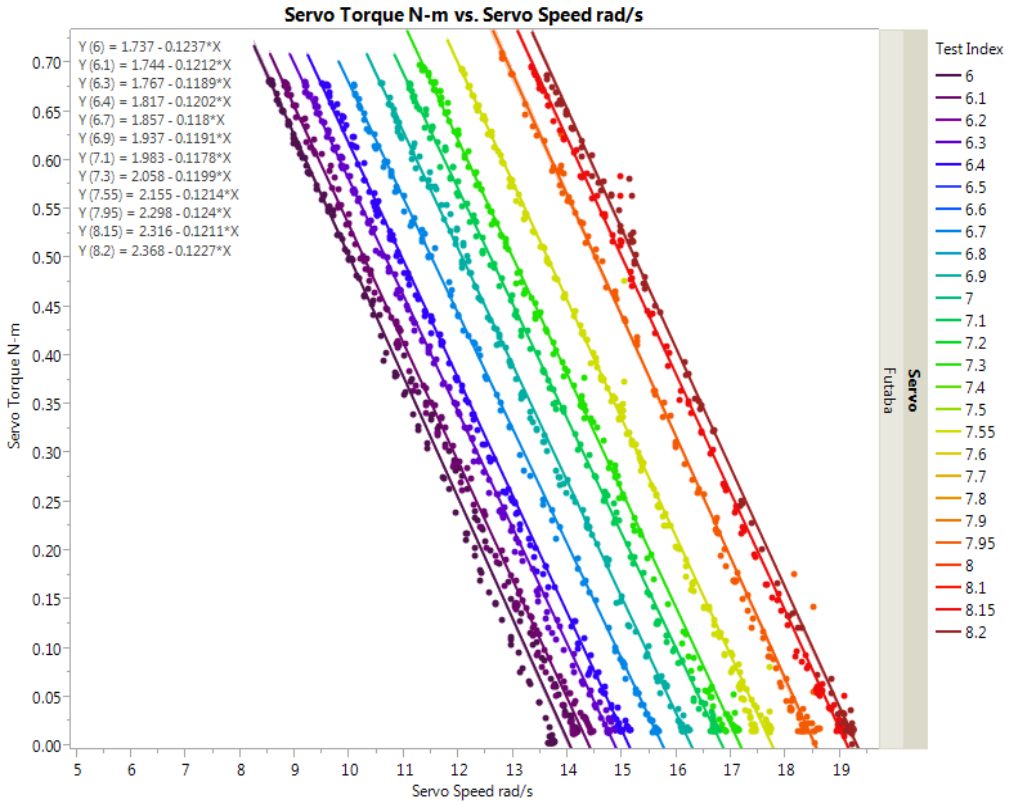

Figure 4.8: Futaba S9352HV performance map test results

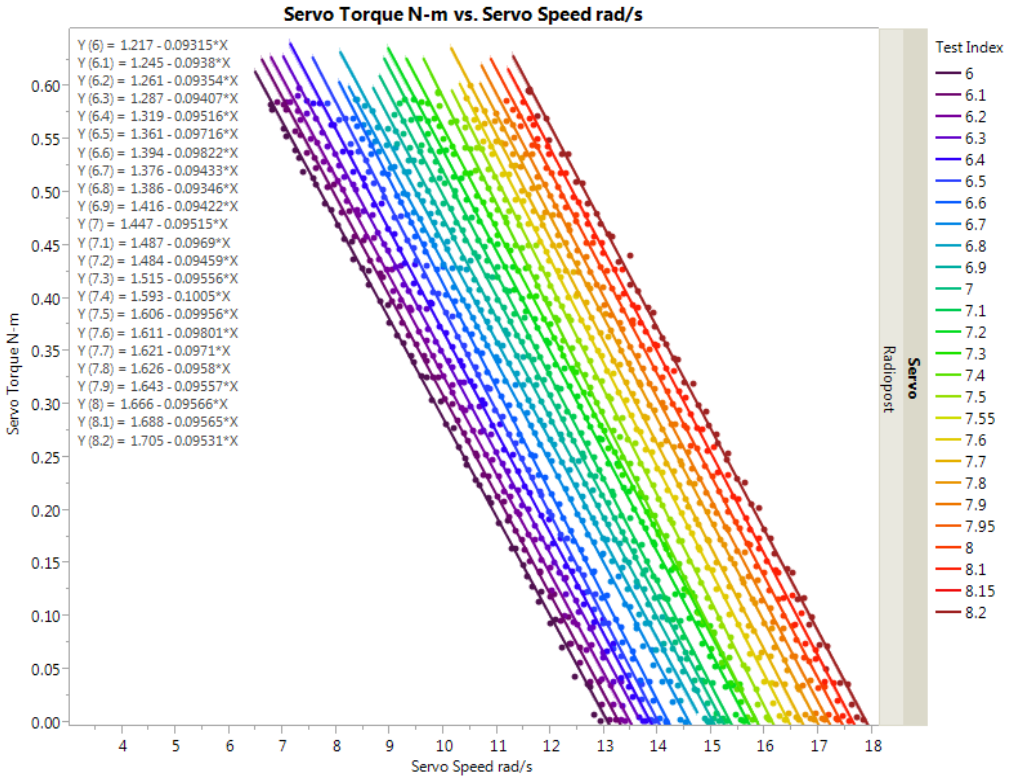

Figure 4.9: Radiopost 5005s performance map test results

Notably, each servo exhibits little inter-test variation in the slope relating speed reduction to increased torque loading, suggesting a linear torque relationship that is invariant of applied voltage. To verify this effect a linear regression model was set up using JMP software. For both the Futaba and Radiopost amps were a reliable predictor of output torque. The results for each servo (final drive) and motor only are plotted together in Figure 4.10. An interesting result arises due to the difference in gear ratios. While the final drive results are quite similar for each as shown in the bottom plot, the

Radiopost motor tested in isolation is more efficient at producing torque per amp supplied.

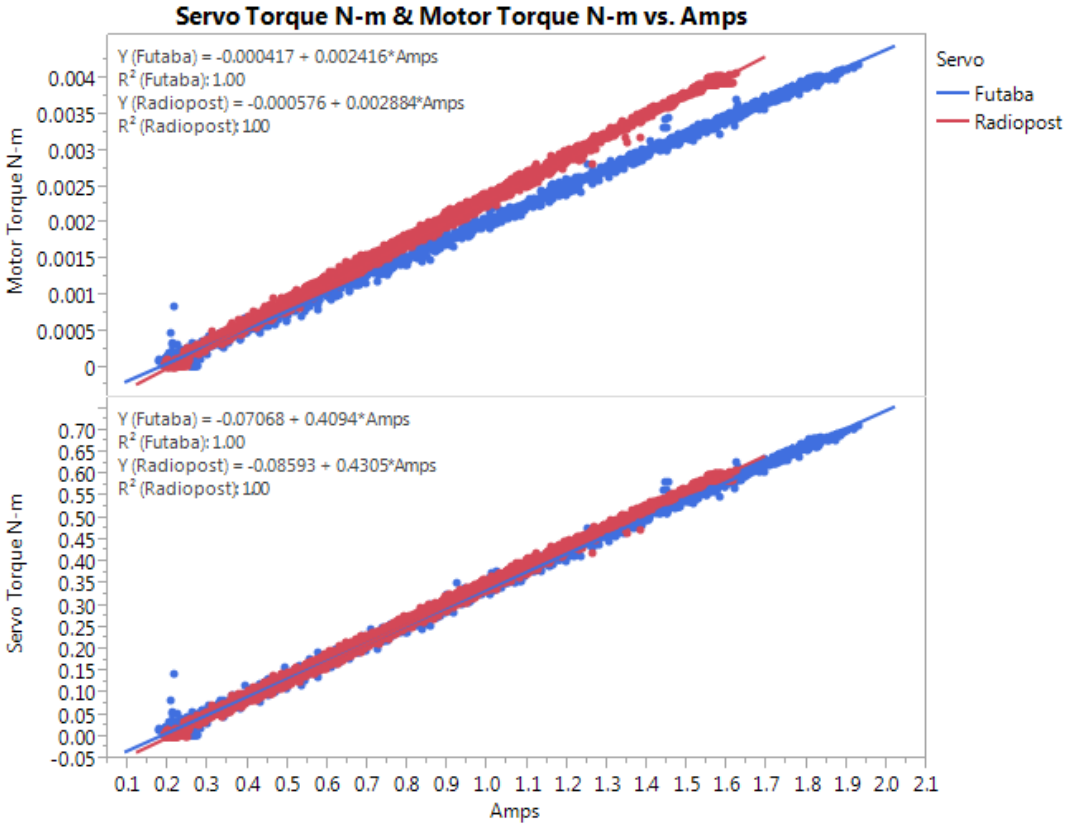

Figure 4.10: Torque production as a function of amperage

A summary comparison of the tested results for each servo is shown along with manufacturer performance claims in Table 4.1. The Futaba stall torque and free-run speed are 4.6% and 3.4% less than the manufacturer's claims, respectively. The Radiopost stall torque and free-run speed are 51.6% less and 6.3% greater than the manufacturer's claims. The resulting discrepancies are factored into new power and

figure of merit calculations in Table 4.1, resulting in a significant change and re-ranking of the two candidate actuators.

Table 4.1: Results of experimental performance verification

		Futaba S9352HV	**Radiopost 5005s**
Mass (kg)	Initial	0.072	0.059
	Tested	0.072	0.059
Stall Torque (N-m)	Initial	2.158	3.241
	Tested	2.058	1.569
Free Run Speed (rad/s)	Initial	17.45	14.96
	Tested	17.16	15.90
Power (W)	Initial	9.41	12.12
	Tested	8.82	6.24
Figure of Merit (Power/mass)	Initial	130.8	205.5
	Tested	122.5	105.8

In the power and efficiency results shown in Figure 4.6 and Figure 4.7, the Futaba servo exhibits performance that dominates the Radiopost servo. In addition, the re-ranking of the figures of merit shows the Futaba to be a superior performer. While in this case it presents favorable performance, the approach presented for building a model in this section is generalizable to other servo models that may offer superior performance in

the future, but the results collected here underscore the need to verify claimed performance prior to making final component selections in any practical design setting.

4.2 Lithium Polymer Battery

As has been shown in the previous section, an essential determining factor in the motor performance is the voltage supplied and the current availability. While the dynamometer testing performed so far was conducted with a power supply that provided programmable voltage input and sufficient current across all conditions, real flight operations are conducted using relatively small lithium polymer batteries. A key characteristic of these batteries is a voltage sag effect that is associated with high discharge rates. As this is expected to manifest in terms of the motor performance and ultimately the wing performance, it is important to experimentally evaluate candidate batteries to ensure the component model is valid.

The experimental setup used for battery characterization is shown in Figure 4.11. This setup records voltage and current while applying variable loading intended to exercise a battery that is to be characterized. Measured signals are recorded using a National Instruments CompactDAQ 9188 chassis. Current measurements below 5A RMS are recorded using a NI-9227 current input module. For higher currents than 5A RMS (pictured in the figure), the device under test is connected to a Y-harness that routes the positive branch through an Allegro Microsystems ACS723 hall effect sensor that

converts current into a voltage signal. This signal as well as the voltage from the device under test are recorded with a NI-9205 voltage input module. A variable load is supplied by a Sparkfun KIT-14449 variable load kit for applying controlled loading conditions, or to a servo motor or other article capable of drawing sufficient power to exercise the device under test appropriately. Samples are collected at up to 50kHz during testing to ensure transient effects associated with rapid pulse loads are captured to enable characterization of transient effects in the battery voltage.

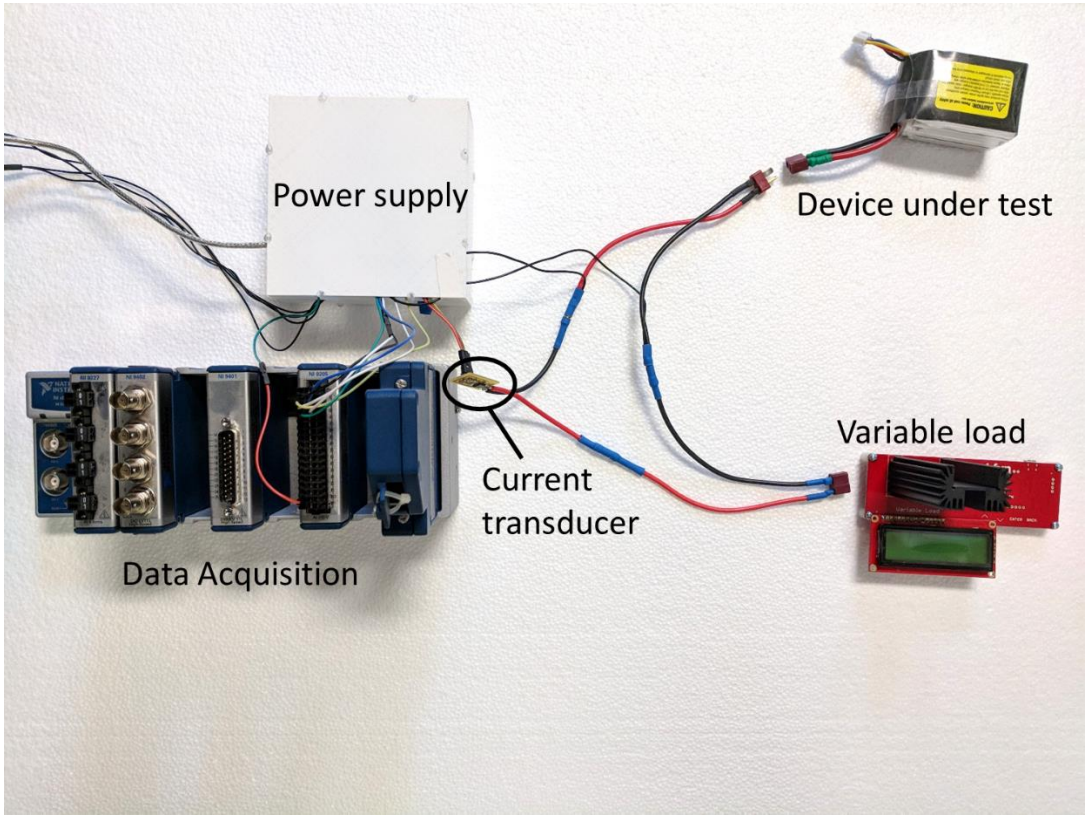

Figure 4.11: Experimental setup used to characterize lithium polymer batteries

A data collection trial used to verify the functionality of the data collection system is plotted in Figure 4.12. The results are collected using a Robo Raven flapping at 4.0 Hz to apply the variable load. The plot shows a complete battery discharge cycle, where the short timescale spread in the data is associated with the large spike loads from each wingbeat, and the longer timescale loss of voltage is associated with the reduction in the state of charge for the battery under test.

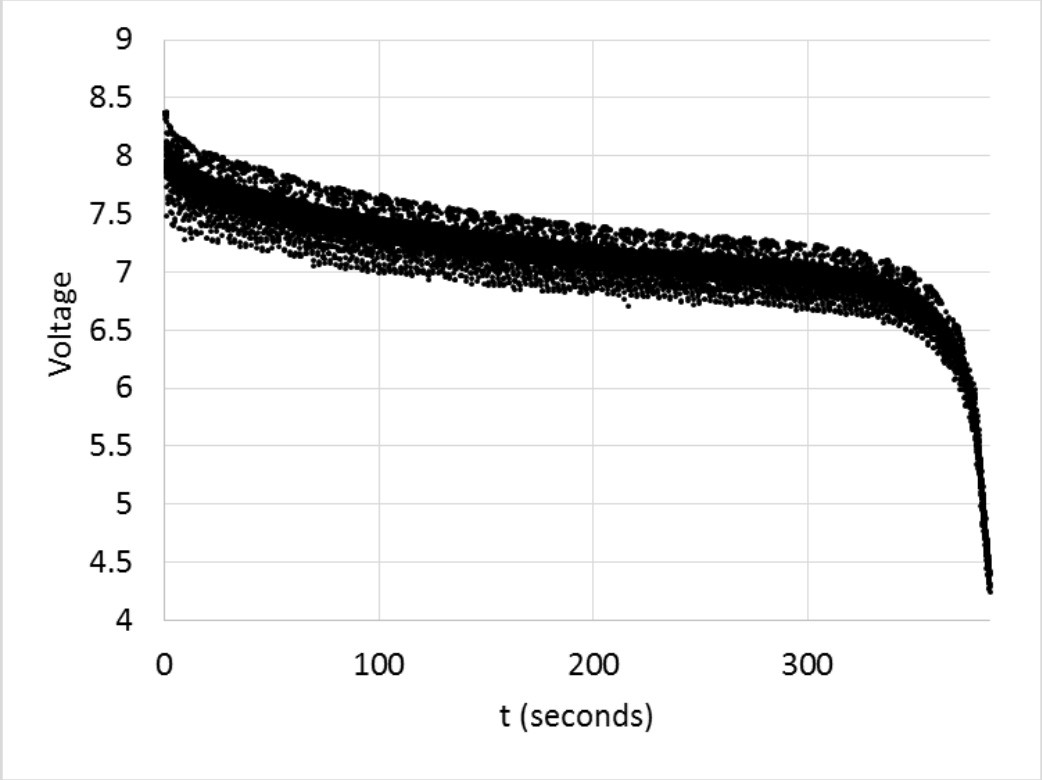

Figure 4.12: Data collected using battery characterization experimental setup

4.3 Load Cell Test Stand

In order to support the simultaneous selection of motors, flapping gait, and wing sizing, information about the force productivity associated with varying component selections is required. In addition, details about how the components interact under varying conditions is useful to describe the ways that constraints on the system-level performance may arise. Therefore, load cell testing of flapping wings is used to collect this data.

A new experimental setup has been developed for this study that provides the necessary measurements to understand how wing size and flapping affect system performance. The servo motors are powered with a Powerwerx SPS-30DM 30 Amp power supply with programmable voltage level. A US Digital E5 optical shaft encoder mounted to one of the drive motors is used to provide angular position tracking of the leading edge spar of the wing. This encoder is fitted with a 500 count per revolution disk. Forces and torques are measured using a six-axis ATI Mini40 transducer with a resolution of less than 1/50 N. Signal conditioning hardware is used to improve the quality of the measurements. Calibration trials revealed the typical resolution to be approximately 1/100 N during most tests. Software installed on the data collection computer converts the raw voltages from the load cell to Cartesian coordinates and standard units. Voltage and current are measured at the drive motor during each trial, synchronized with the load cell measurements. All signals are recorded by a data collection computer, connected with an Ethernet connection to a National Instruments ConpactDAQ chassis

equipped with NI 9227, NI 9402, and NI 9205 modules that provide current measurement, counter input, and analog voltage input, respectively. The load cell, motor, and wing assembly is secured to an extruded aluminum frame to provide the necessary spacing from the ground to fit the larger wings tested in this study. The motors and wings under test are secured to the frame using 3D printed ABS plastic parts. The assembled test stand is shown in Figure 4.13.

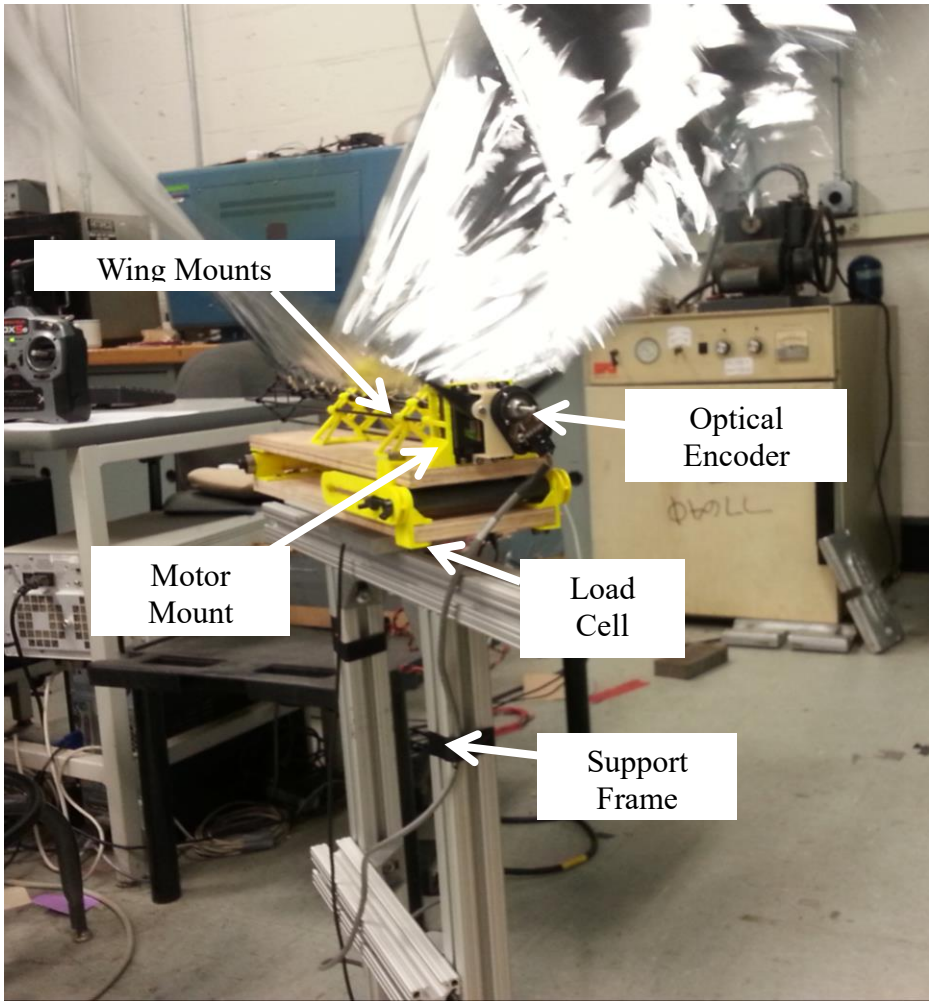

Figure 4.13: Load cell test stand

Four wings following the baseline design described in the Robo Raven I preliminary design efforts chapter were constructed for load cell testing. Each wing maintains constant spar orientation and size, while scaling the size up to 200% relative to the baseline. For the remainder of this section these wings are referred to as designs A, B, C, and D, as shown in Table 4.2.

Table 4.2: Wings tested using load cell test stand

Wing	**Mass (g)**	**Span**	**Chord**	**Area**
A	12.7	20.75 in	12.25 in	254.2 in^2
B	19.4	24.50 in	14.00 in	343.0 in^2
C	21.0	26.25 in	15.50 in	406.9 in^2
D	25.4	30.00 in	17.00 in	510.0 in^2

A total of 84 separate testing trials were conducted providing coverage of each of the wings A, B, C, and D, flap rates from 1.0 to 4.0 Hz in 0.5 Hz steps, and voltages of 6.70, 7.40, and 8.00. Each trial consisted of 10 seconds of data collection at a steady flapping condition and voltage, with 1 kHz sampling. Data channels directly recorded include timestamp, three forces, three torques, voltage, current, and angular position of the wings. In addition, five derived quantities are added to each data file including torque, input power, output power, motor efficiency, and angular velocity.

The resulting data set consists of 12.6 million data points, which creates a challenge in data visualization and interpretation. Each flap exhibits slight variability due to interactions between the flexible wings, the rubber bands used to secure the wings to the fuselage, and vibrations that are induced in the structure of the test stand. The stability of the wing angle tracking measured with an optical encoder is stable across each data set collected. A snapshot of nine flap cycles is plotted together in Figure 4.14.

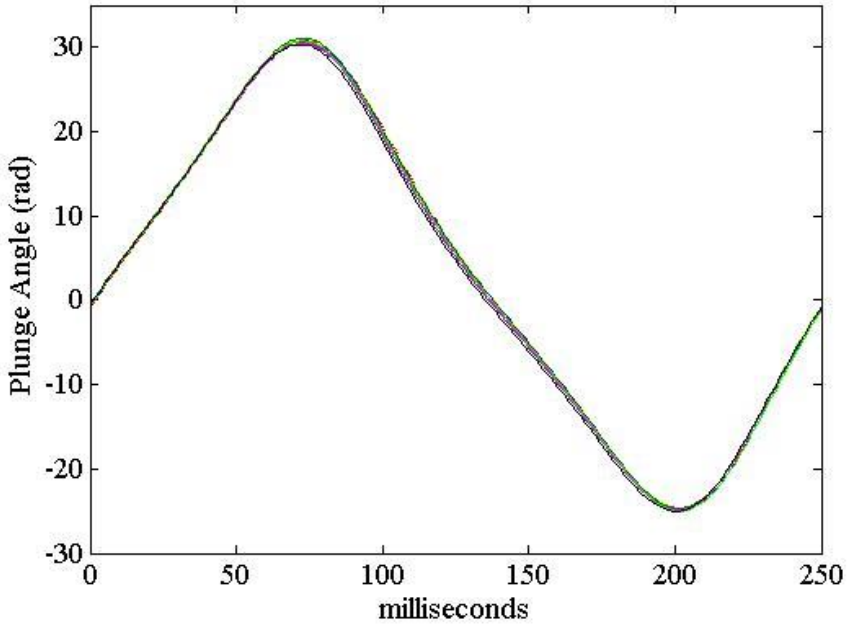

Figure 4.14: Ensemble of nine flap cycles recorded with optical encoder on test stand

The variability of the encoder signals have an average standard deviation of 0.28° leading to repeatable encoder signals in each test, as shown in Figure 4.15. Due to this intra-cycle stability, the optical encoder is used as the basis for subsequent post-processing steps.

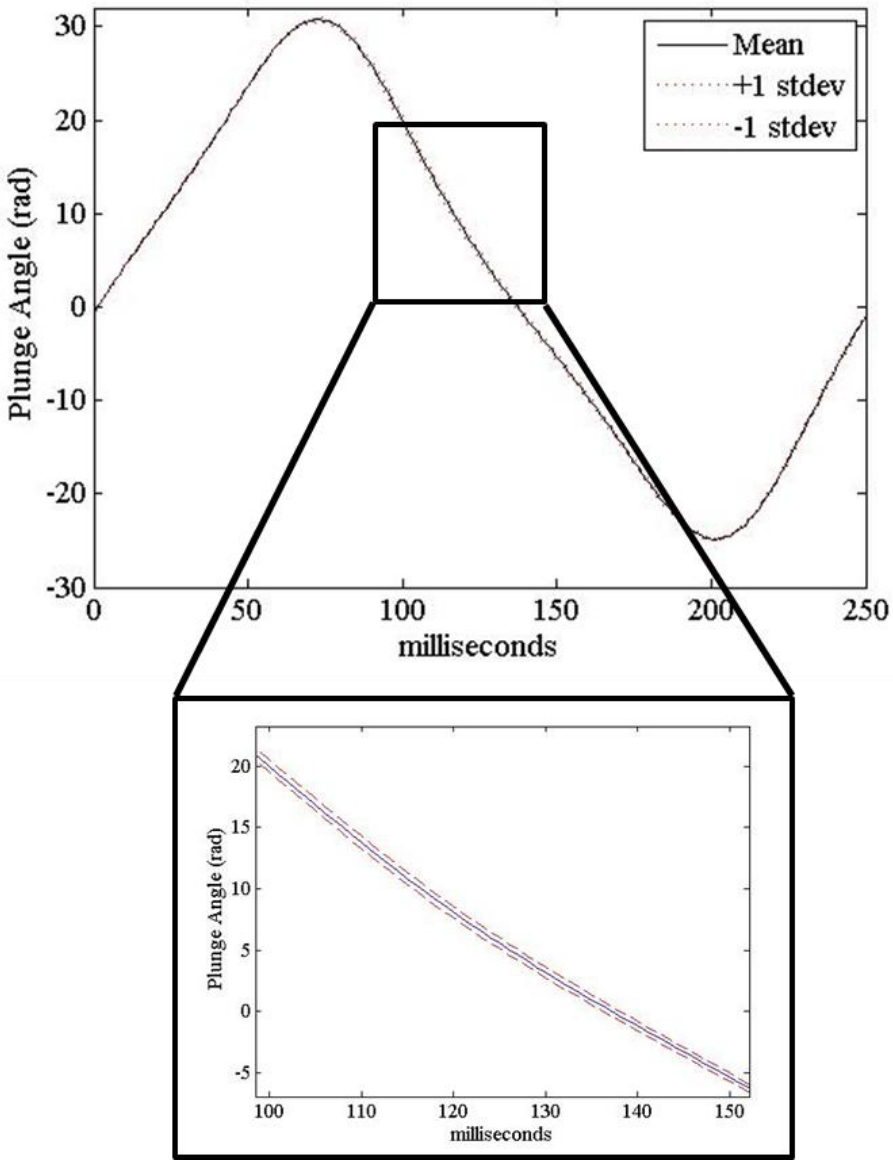

Figure 4.15: Optical encoder repeatability analysis

A custom post-processing script is used to remove these effects from each test. First, the script performs cycle detection using the optical encoder data that tracks angular position of the wings. Second, each flapping cycle is stacked to build up a repetitive

data set across each data channel. Third, low-pass filtering with a cut-off frequency of 40 Hz (ten times the highest tested flapping frequency) is applied to the data. Fourth, outliers are detected and rejected from the final data set. Finally, the stacked and filtered data is collapsed into a single cycle-averaged result that provides excellent clarity and improves differentiation between varying test conditions. This approach is shown for a single data collection trial in Figure 4.16, with the cycle detection in the top plot, the stacked and filtered results for thrust production in the middle plot, and the final collapsed result shown in the bottom plot.

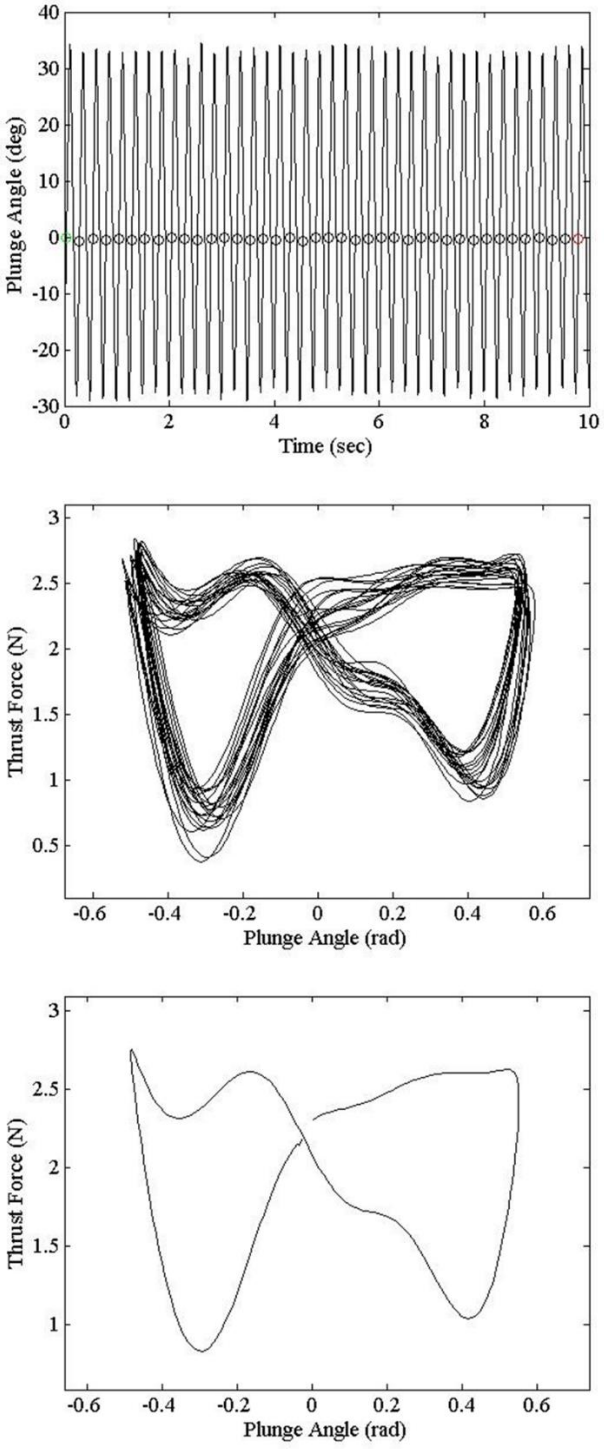

Figure 4.16: Data post-processing procedure

After applying the post-processing to the data set, several averaged results are calculated to derive insight into component interactions. A key result from the data set is the thrust production across each wing size and flapping rate. The averaged results for thrust are plotted in Figure 4.17. Increased wing area adds thrust productivity for all wing sizes tested. Flap rate exhibits a clear peak at moderate flapping rates followed by a decline at higher flapping rates.

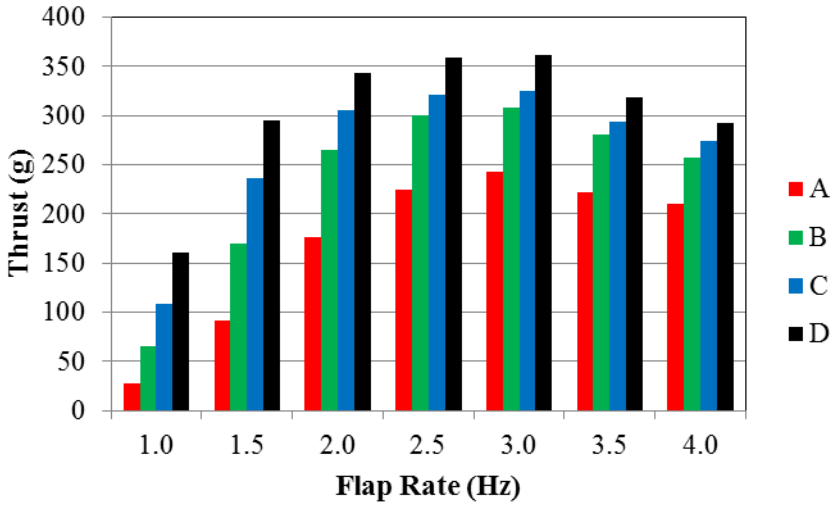

Figure 4.17: Thrust production results from load cell testing

The lift results shown in Figure 4.18 exhibit an increase in productivity with wing area and flap rate until higher flapping rates are reached. Near the 2.5 – 4.0 Hz range, lift productivity is saturated and settles within a narrow range regardless of wing size or flapping rate. This result appears to indicate a motor limitation is affecting the results by limiting the power in more demanding conditions of flapping. In particular, at the

4.0 Hz flapping rate, the A wings are exhibiting greater lift than the D wings, which is a highly non-intuitive result and deserving of further investigation into the motor-wing interaction that takes place under these conditions.

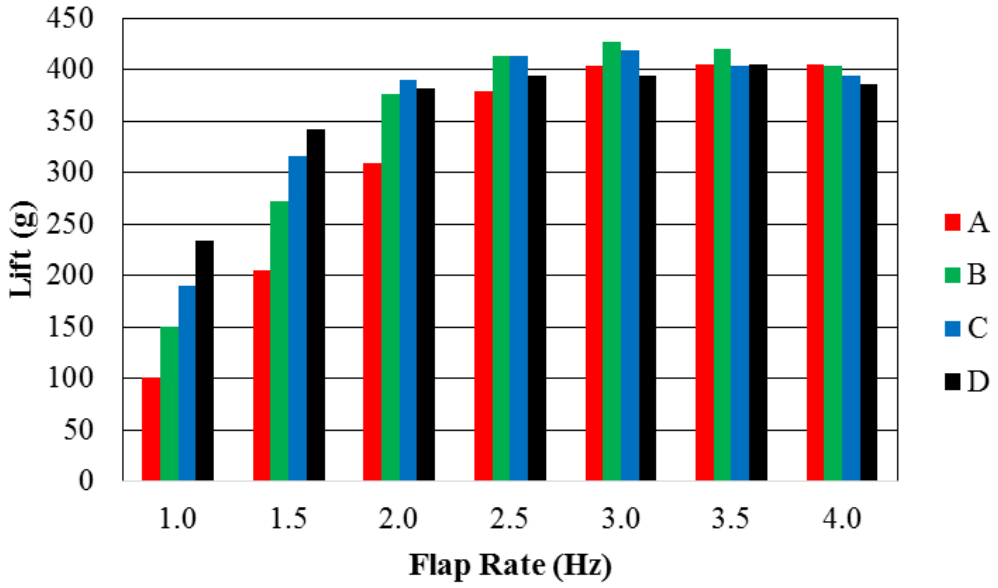

Figure 4.18: Lift production results from load cell testing

A plot of the power input for each test condition is shown in Figure 4.19. The power input reaches a clear peak that closely tracks the lift production. This appears to offer an explanation for the mechanism of lift production, however thrust production is not well-explained by the power input to the motors.

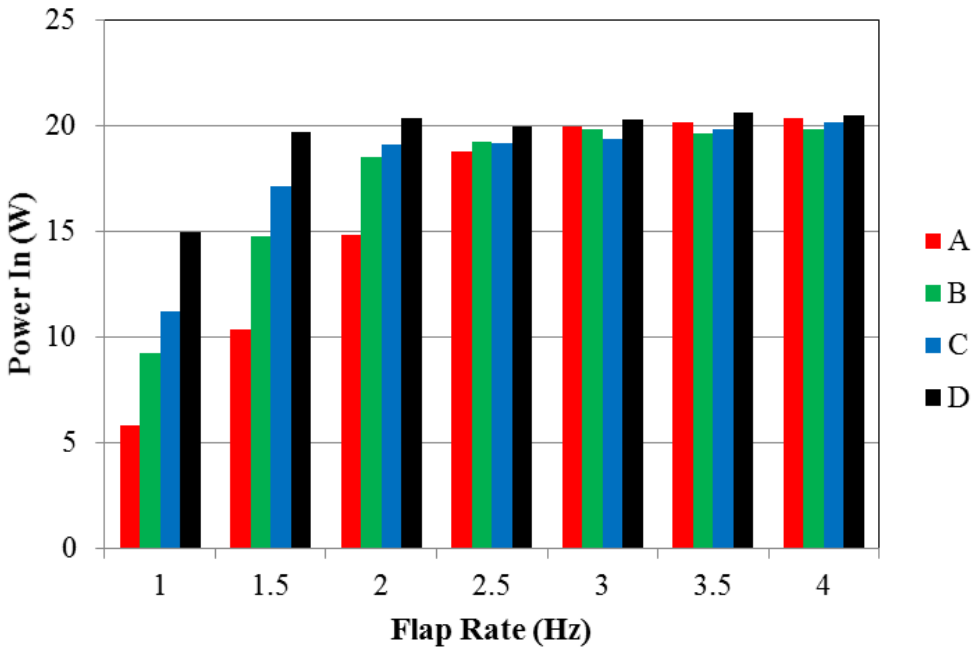

Figure 4.19: Motor power input results from load cell testing

The peak in thrust production is not coincident with the power input characteristics shown in Figure 4.19. Therefore, to explain the thrust production mechanism, exploration of the motor-wing interactions is needed. This interaction will be explored in the following section and used to construct a model based on the observed wing dynamics. However, for the purposes of initial design decisions including wing sizing, flap rate selection, and motor selection, the load cell testing offers insight into the target operational regime. By combining the results of the thrust production in Figure 4.17 with the motor power output predicted in Equation 4, a wing figure of merit may be generated that provides insight into the effectiveness of a given wing size and flapping rate at converting motor output power into useful aerodynamic force. This result is

plotted in Figure 4.20. At lower flapping rates, the larger wings exhibit more aerodynamic productivity, due to Reynolds number scaling. However, at higher flapping rates, the inability of the large wings to operate in the efficient speed range of the motor causes a drop in the computed figure of merit.

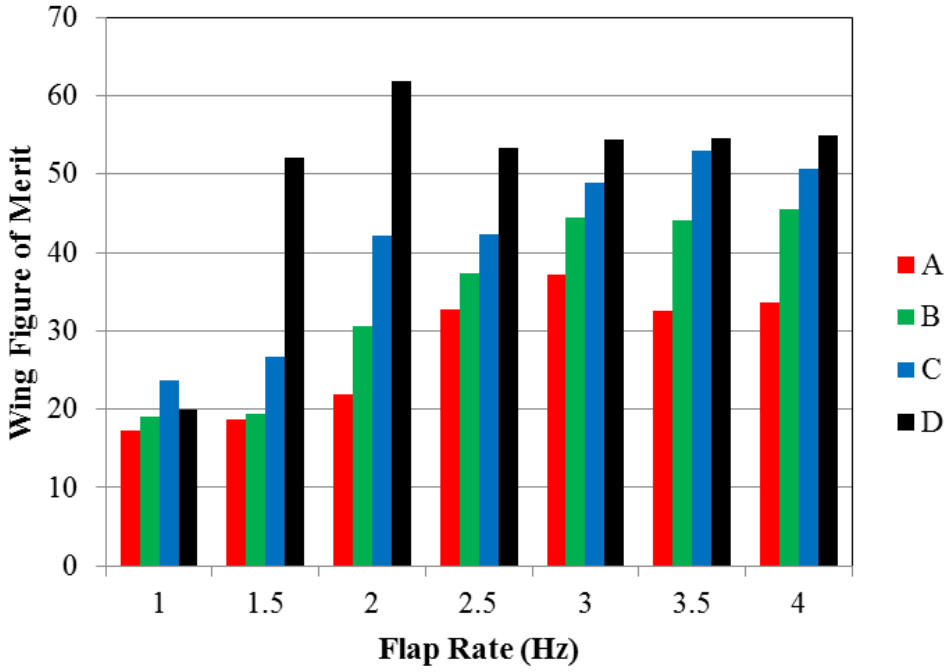

Figure 4.20: Figure of merit for conversion of motor output power to thrust force by wings

By considering the thrust productivity relative to the input power instead of the output power, a basic system-level figure of merit is generated that captures the overall ability of the system to convert stored energy into useful aerodynamic forces. The results for the system-level figure of merit are plotted in Figure 4.21. This plot shows a clear trend

of superior performance by the larger wings, as expected based on the wing-level figure of merit results in Figure 4.20. The lift results collected are only a static result corresponding to the intensity of lift produced in a laboratory setting. This limitation is why only the thrust production was used to generate the initial figure of merit predictions for the preceding results.

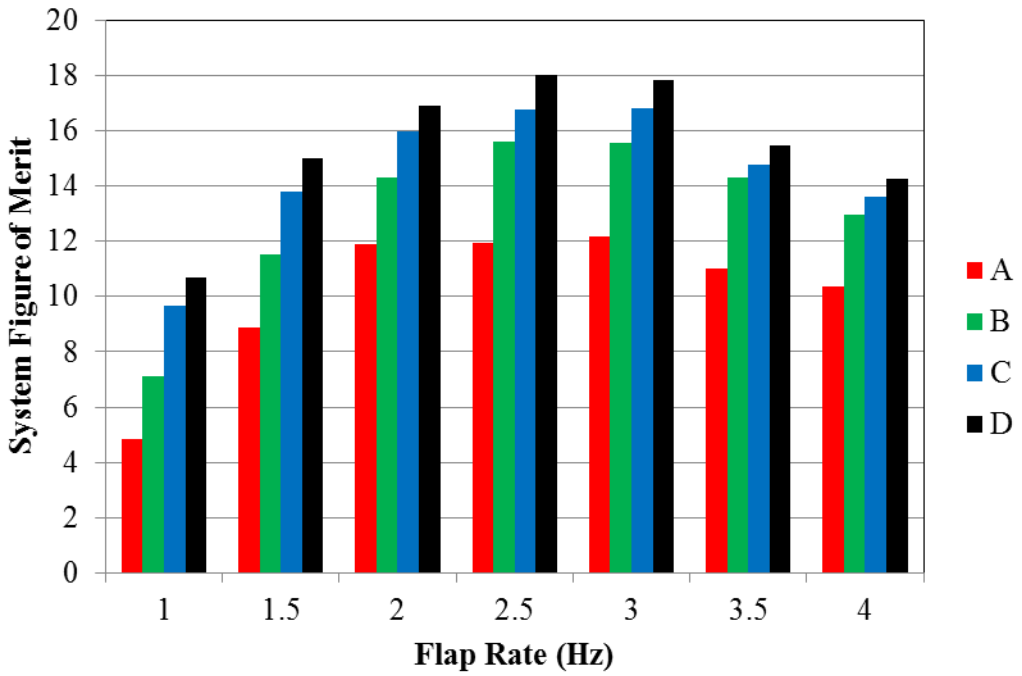

Figure 4.21: Figure of merit for conversion of stored energy into thrust force by motor-wing system

A summary of important results collected on the test stand is shown in Table 4.3. By setting up the tradeoffs between wings and motors, the boundaries on system feasibility begin to emerge. For each wing considered, the motor efficiency is a concern, as each

motor must dissipate over 7 W, resulting in substantial heating during extended testing. For each wing the reported power stroke velocity is captured during the mid-stroke when the wing has completed pronation or supination. This power stroke result provides a more realistic estimate of the operational condition resulting from a given wing size, since larger wings exhibit a twist-softening effect that increases flapping speed during wing rotation. This effect will be explored in the following section in more detail.

Table 4.3: Summary load cell results

Wing	Wing Mass (g)	Power Stroke Velocity (°/s)	Peak Power Draw (W)	Mean Motor Efficiency	Thrust (g)
A	12.7	577.9	13.62	52.42	220
B	19.4	531.7	15.05	48.57	270
C	21.0	484.9	15.85	44.72	295
D	25.4	439.5	17.61	40.86	320

4.4 In-Flight Instrumentation

The previous section has presented an experimental characterization methodology to explore component feasibility, investigate interactions, and combine into a system-level figure of merit to describe overall system performance. The approach is generalizable to a variety of component choices and operational conditions, but it suffers from a lack of specific information about aerodynamic performance because the

tests are conducted in a laboratory environment. A key challenge associated with collection of aerodynamic data for flapping wing aerial vehicles is to ensure that the data acquisition system that does not obstruct the natural functionality of the vehicle. Wind tunnels do not meet this requirement in the case of FWAVs. The rigid mounting fixture required to use a load cell in a wind tunnel prevents the natural heaving motions of the vehicle that arise in reaction to flapping forces. By obstructing these motions, wind tunnels may hide the true performance and dynamics of the vehicle.

A data collection system is preferred that retains the free-flight characteristics of the vehicle. The impact of such a system will be directly related to both size and weight, as these will introduce unwanted drag and gravitational forces. Thus miniaturization is a crucial requirement for a successful system. The data collection system must provide data that is compatible with the previously developed methods of vehicle performance characterization. Therefore, voltage and current are necessary to highlight motor performance. In addition, wing angle tracking is necessary, which can be differentiated to provide an estimate of wing angular velocity. Finally, vehicle dynamics must be captured by tracking position, attitude, airspeed, and altitude. Incorporating all of these measurements provides a more complete energetic picture of flight that is not subject to the information loss associated with wind tunnel testing.

The sensor selections that provide a complete picture of the in-flight performance depend on the models that will ultimately be used once enough experimental data has

been collected. Hence, it is useful to begin with an exploration of the variables that impact system performance in terms of a simplified aerodynamics and energetics model. For this purpose, the simple quasi-steady aerodynamic model based on the strip theory proposed in [20] and presented in the previous chapter is useful, since it is well-suited to accepting experimental data, and provides a clear picture of the variables that have a strong impact on performance. This model discretizes the wing spatially into span-wise strips, and discretizes the wing kinematics temporally into normalized time steps. Therefore, two pieces of information are required. First, an accurate description of chord as a function of span is necessary. Second, precise measurements of the wing kinematics are required.

The first point has already been addressed by the standardized wing design template established in the previous chapters. As was demonstrated during load cell testing, realized kinematics vary significantly from commanded kinematics. To address the need for precise wing kinematics, an optical encoder has been selected to measure the position of the wing's main spar at high frequency during flight tests. This encoder is mounted directly to the output drive of the servo motor used for wing flapping as shown in Figure 4.22. The encoder provides tracking of the true angular orientation of the wing, since loading causes a deviation between the commanded kinematics and actual wing motions, particularly in the presence of a moving airstream that increases loads beyond static conditions.

Figure 4.22: Front view of instrumented Robo Raven FWAV showing optical encoder and Pitot tube

Another important variable considered in the quasi-steady strip theory is airspeed, which effects lift, thrust, and efficiency due to wake interactions resulting from the Strouhal number and reduced frequency [76]. By combining the measurements of the optical encoder with an accurate airspeed measurement, this important non-dimensional parameter may be measured in a free-flight condition. Hence, a pitot tube was included, mounted on the front of the vehicle as shown on the left of Figure 4.22. The static and dynamic pressure ports on the pitot tube are connected to opposite sides of a high sensitivity differential pressure sensor via small silicone hoses.

The lift and thrust production are important outputs from any aerodynamic model, yet are challenging to measure in a freely flying vehicle. For these forces, it is necessary to infer information about lift and thrust by measuring vehicle mass prior to flight, then looking at the vehicle orientation, airspeed, and altitude gain or loss while flying. To provide information about the vehicle orientation, several sensors are combined in an Attitude Heading Reference System (AHRS). The AHRS consists of sensors and a microcontroller working together. An accelerometer, gyroscope, and magnetometer together in XYZ triads provide acceleration, roll rates, and compass readings, which are fused using a direction cosine matrix that eliminates drift errors in the readings to provide excellent stability in estimation of the attitude and heading. To provide the altitude readings needed to check if lift forces are greater than vehicle weight, a high sensitivity barometer is used.

Thus far, the sensors identified have addressed the wings and aerodynamics, however the motors and energetics of the system are equally important in determining overall system performance, as was described in the motor modeling chapter. The motor model is heavily dependent on both the current draw and the instantaneous battery voltage. Due to the tight weight restrictions on the Robo Raven FWAV, small capacity batteries must be used, which when combined with high power draw result in transient effects in the instantaneous current and voltage. Because of this, real-time high-rate measurement of both voltage and current is necessary to account for high discharge

rates. Therefore, an analog to digital converter and a hall-effect sensor are required that are capable of handling the large power consumed by the Futaba S9352HV servos.

The required voltage, current, and angular velocity measurements create a challenging situation for a typical microcontroller to handle simultaneously. The first challenge comes from the need to measure voltages that may be as large as 8.5 Volts, since the Robo Raven II currently uses a two-cell lithium polymer battery. Microcontrollers are typically only rated for 1.8-5.5 Volts, so a step-down is necessary to avoid damage. The second challenge comes from the need to measure angular velocities at over 1000 degrees per second with high precision. This necessarily imposes a high sampling rate and therefore clock speed on the microcontroller responsible for tracking wing position. Making this problem worse, the measurement of current and voltage must take place at high speeds to keep up with the switching rate of the digitally controlled servos. The particular digital servos used here modulate a PWM drive current at 300 Hz. If the position error accumulates to even one degree, maximum torque is applied. During the course of typical operation, the practical effect of this control system is rapid switching of torque between full-off and full-on current. Hence, if even a few samples by the current sensor are missing these switching effects due to slow sampling rates, measurement errors begin to accumulate. Another challenging aspect of these coupled problems is the fact that all readings are to be taken synchronously. This is a task that microcontrollers are not well suited to, as a typical microcontroller uses a successive approximation sample and hold approach to perform analog to digital conversions

[169]. In short, this means the microcontroller is blocked while collecting samples from a sensor.

The accuracy of the data recorded improves in trustworthiness if there is an extra layer of redundancy built in. Therefore, a GPS was also included to provide information for comparing to the other sensors to check if there was drift, systematic or random errors, or other unexpected behaviors from the sensor suite.

With the necessary sensors identified for a free-flight test, the next step was to identify a strategy for storing data. There are basically two options, either transmitting the data via a radio or modem, or storing the information on-board for subsequent download. Due to the limitations of available payload on the Robo Raven platform, the lightest solution was sought that could maintain sufficient data throughput to keep up with all the sensors' outputs. Therefore, a microSD card was chosen due to simplicity and reliability combined with large storage capacity.

Identification of the particular sensors to be used depends on knowledge of the ranges of measurement, sampling rates required, communication busses used, and inter-system compatibility constraints. The sampling rate was chosen as 50 Hz to provide a good balance between development complexity and density of data to be used in any subsequent modeling efforts. Furthermore, the standard Robo Raven flight control system must also be integrated into the sensor suite to provide command and control

functionality to the pilot. The identified sensors to be used in the vehicle are listed in Table 4.4.

Table 4.4: Sensors used on Robo Raven II instrumented FWAV

Sensor	**Model**	**Voltage**	**Range**
Voltage	ATMEGA328P	5.0	0-5.5V
Current	ACS723	5.0	±10A
Optical Encoder	E2-500	5.0	N/A
Accelerometer	ADXL345	3.3	±16 g
Magnetometer	HMC5883L	3.3	±8 gauss
Gyroscope	ITG-3200	3.3	±2000°/sec
Diff.Pressure (pitot)	HSCMRRN001ND2A5	5.0	±1” H_2O
GPS	PA6H - MTK3339	3.3	< 3m
Data Logging	OpenLog	3.3	Up to 1M Baud

The ATMEGA328P microcontrollers chosen are incompatible with the range of voltages to be measured, therefore a high impedance voltage divider circuit was introduced to the ADC port used for system voltage monitoring that cuts voltage in half.

To maintain a 50Hz sample rate for the current and voltage measurements, it was necessary to sample at a minimum of 15,000 Hz, where during every 1/300 second window corresponding to a PWM control signal from the servo, 50 samples were collected by the microcontroller. Bench top testing revealed that the analog to digital conversions were too computationally demanding to be performed by a non-dedicated processor, therefore a separate processor is devoted to performing these high speed window averages for power measurement. After each windowing operation, the averaged result is merged with the other channels from the sensor suite at a synchronized time step.

The encoder chosen contains a 500 count per revolution disk that uses an x4 quadrature to read position (two offset square waves, all edge changes trigger a count). A minimum sampling rate of 5,556 Hz is necessary to guarantee no counts will be missed. The encoder measurements are less demanding since the microcontroller only needs to detect an edge change, therefore it shares the same microcontroller that runs the main command and control functions which are on the traditional Robo Raven. In addition, the main microcontroller collects samples from the pressure sensor connected to the pitot tube and altitude readings from the barometer. Since these components do some on-board processing before generating a reading, they are less demanding on the processor resources.

AHRS sensor fusion is performed by an additional dedicated microcontroller since it requires both analog to digital conversions and floating point math, which is highly demanding for a low-end microprocessor such as the ATMEGA328P that lacks a dedicated floating point processor.

The data logging is handled by an OpenLog, which consists of an ATMEGA328P microcontroller running the open source software available at [170] connected to a microSD card. This system provides multi-channel data logging at a programmable sample rate.

The GPS is a complete standalone data logging system, consisting of an MTK3339 chipset connected to a second OpenLog system. This provides a totally separate data collection path for comparison after testing with typical accuracy of +/- 1m.

Due to the number of sensors required to complete the sensor suite, plus supporting circuitry including voltage regulation and signal routing, many interconnections are required between sensors and microcontrollers. A diagram showing the circuit architecture is shown in Figure 4.23. In the diagram, white boxes are microcontrollers, gray boxes are external hardware, and green boxes are sensors. Yellow connections are UART connections, blue lines are SPI connections, and green lines are I^2C connections. In addition to these connections, there is a separate network of connections made

between the raw battery voltage to a 5.0 V linear regulator and 3.3 V linear regulator, with power and ground routed to the appropriate devices as listed in Table 4.4.

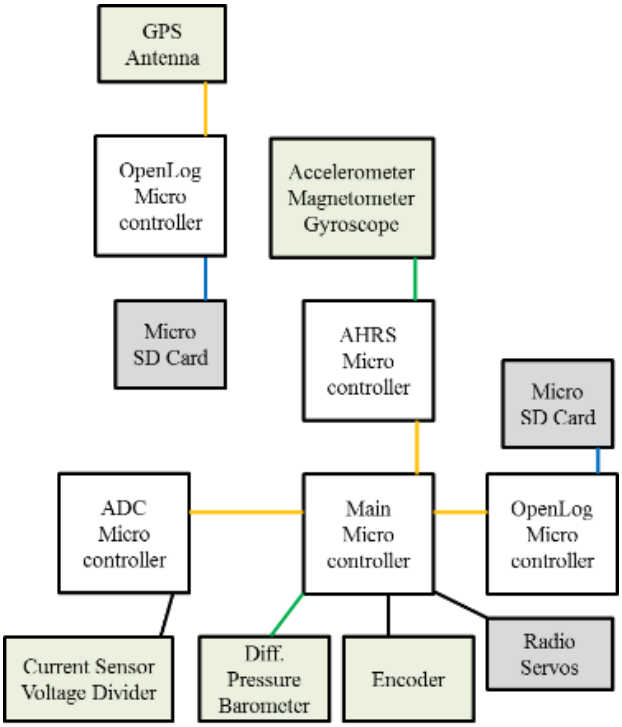

Figure 4.23: High level functional diagram

The number and complexity of connections shown in Figure 4.23 necessitated the integration of the components into a printed circuit board (PCB). The schematic design and board design were completed using EAGLE software. The board design is shown in Figure 4.24. Fabrication of the PCB was completed by an external fabricator, and assembly and soldering was completed by surface mount soldering of the components. The completed custom printed circuit board (PCB) is shown in Figure 4.25. The mass of the board is 7.5 grams. The two large wires soldered to the middle of the board are

power connections for a lithium polymer battery. All voltage regulation and routing takes place on the board.

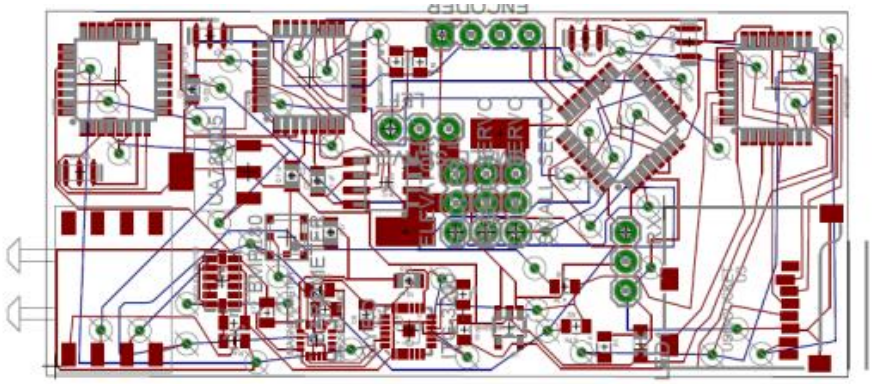

Figure 4.24: Circuit board routing generated from EAGLE schematic

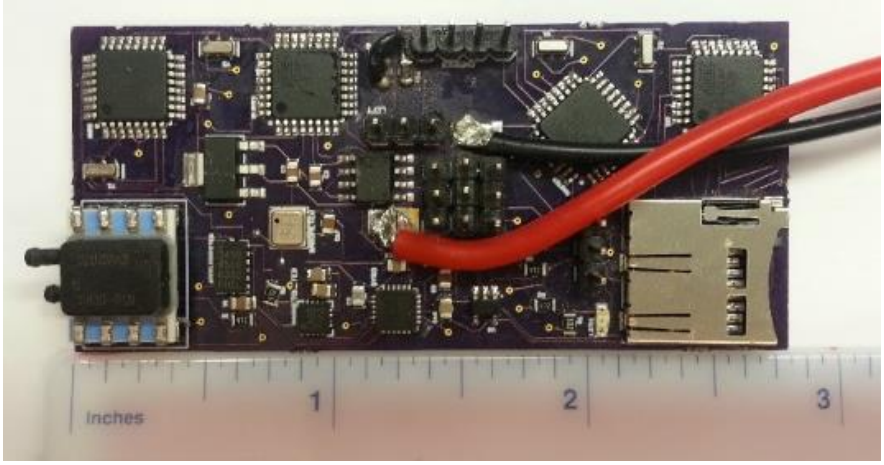

Figure 4.25: Custom PCB used in Robo Raven II flight tests

After the assembly of the board, calibration of the sensors was conducted to convert sensor values into standard units and establish measurement precision for each data channel. The results of calibration are listed in Table 4.5.

Table 4.5: Sensor calibration results

Sensor	**Precision**
Voltage	4.9 mV
Current	20 mA
Encoder	0.18 degrees
Airspeed	0.2 m/s
Altitude	0.3 m
GPS Position	3 m
Yaw, Pitch, Roll	0.2 degrees

After sensor calibration was completed, several tests were conducted to evaluate the data collection capabilities of the instrumented vehicle. First, a static test was performed by holding the vehicle still and slowly ramping up flapping speed to see how the power draw and flap amplitude change with increasing flap rate for each wing size, shown in Figure 4.26.

By combining the data from the voltage sensor, current sensor, and optical encoder with the motor model presented earlier, the torque is shown as a function of the plunge speed of the wings. As was noted in prior testing, this data exhibits a fairly linear increase in torque as plunge speed increases until the servo is saturated due to excessive loading and slack effects, at which point all the wings converge to a common point of shallow quick flaps without significantly reduced lift production due to excessive wing rotation.

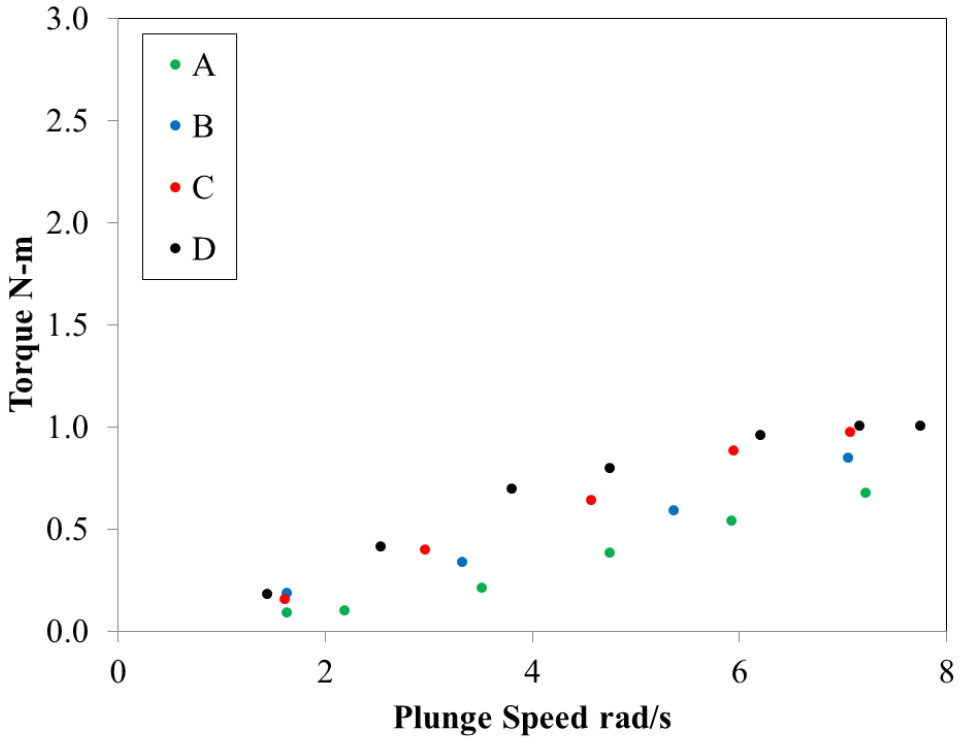

Figure 4.26: Static testing results from instrumented FWAV

Since this check was well-correlated to prior results observed in [123, 124] free flight testing was started. In each test flight, the vehicle was hand-launched from a height of 3 meters and flown in steady level flight with 4.0 Hz flapping before landing. In Figure 4.27, the results of one flight test trial for Wing C are shown.

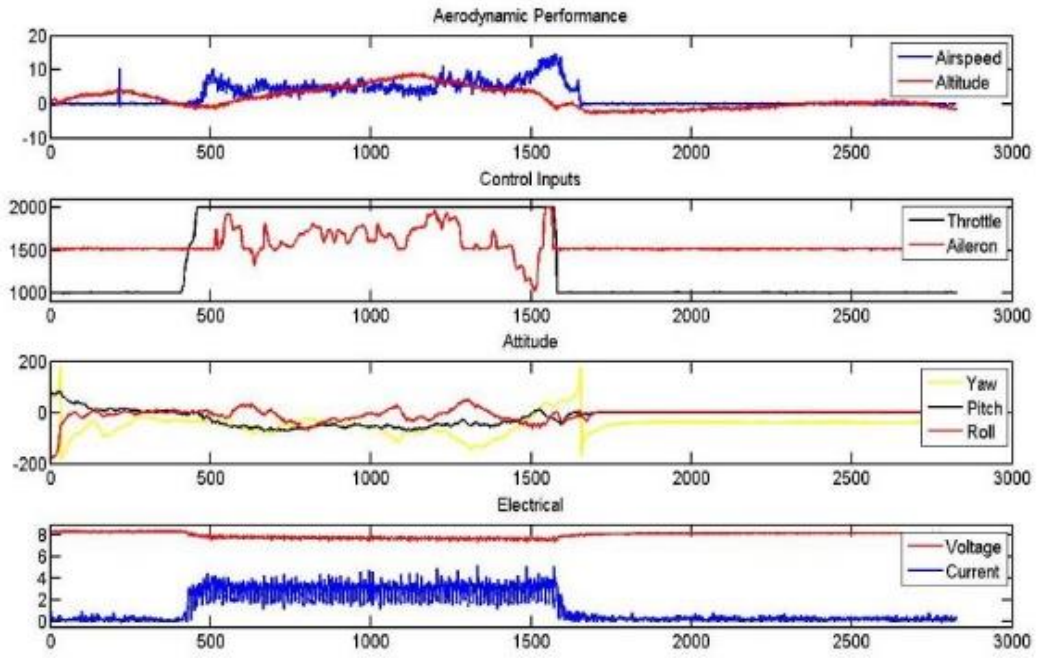

Figure 4.27: Flight test results

In the first row are the airspeed and altitude recorded by the pitot tube and differential pressure sensor and the barometer. In the second row are the pilot commands issued during flight. In the third row are the yaw, pitch, and roll values computed by the AHRS. In the fourth row the voltage and current are shown, with a slight discharge noticeable from the start to the finish of the flight, followed by a minor voltage recovery after the flight is stopped. The test flight begins at approximately t=500ms. Powered

flight takes place until t=1600ms, when a gliding landing takes place. Note that the sign is reversed on the pitch measurement, so a negative value indicates nose up orientation. In the altitude plot, the large ramp up leading to the launch time is due to a climb up to a stage for an elevated launch position.

A total of 112 flight test trials were conducted spanning a range of operational conditions as summarized in Table 4.6. Following each test trial, the recorded data is post-processed to remove regions of the flight that contain noisy or undesired data, which may be caused by strong wind gusts, turns required to avoid obstacles during flight, unexpected mechanical errors, motor overheating, or excessive battery discharge. The data collected by the 112 flight testing trials have been reduced to 12 particularly high quality tests in the results presented for the remainder of this section, due to an observed strong dependence of the vehicle performance on weather conditions. Across the testing, the center of gravity was varied to provide a range of performance data, leading to the spread in inclination angle and flight speed. In all trials climb, descent, and turning were minimized to ensure that data collected had minimal non-cruising conditions that would hide the periodically steady cruise behavior that was sought.

Table 4.6: Robo Raven II flight testing data ranges

Parameter	**Value**
Flap Rate (f)	4.0 Hz
Flap Amplitude (A)	0.873 rad (zero-peak)
Angle of Attack (β)	0.349-1.047 rad
Flight Speed (V)	2.0-8.0 m/s
Total Vehicle Mass (M)	0.395 kg
Aspect ratio	2.01
Wing Span (b)	0.67 m
Wing Area (S)	26.25 $m^2$10E-2
Wing Root Chord (c_0)	0.39 m

One of the first results explored was the behavior of the test flights with respect to the inclination angle. Figure 4.28 shows the dependence of the rate of climb on the inclination. The data show a definite peak in climbing performance at a moderate angles corresponding to the minimum power flight speed. At very low angles and at very high angles climb rate suffers due to increases in the parasite drag and induced power, respectively. Figure 4.29 shows the change in airspeed with inclination. In both of the figures shown, the ability to maintain steady flight was degraded at the extremes of the range tested due to a power deficit.

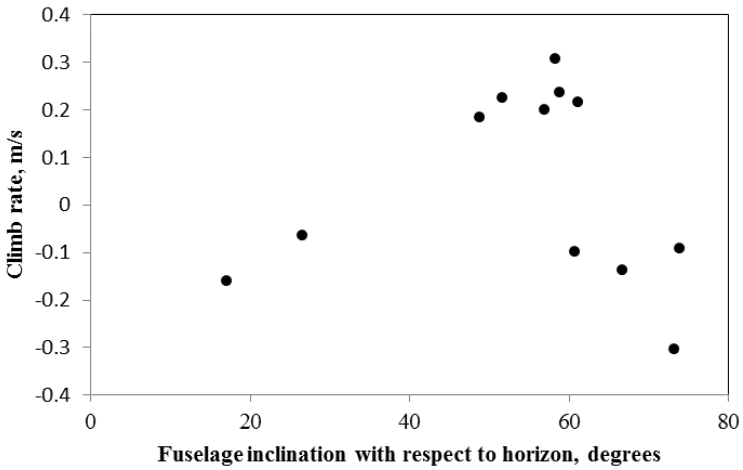

Figure 4.28: Climb rate dependence on inclination angle

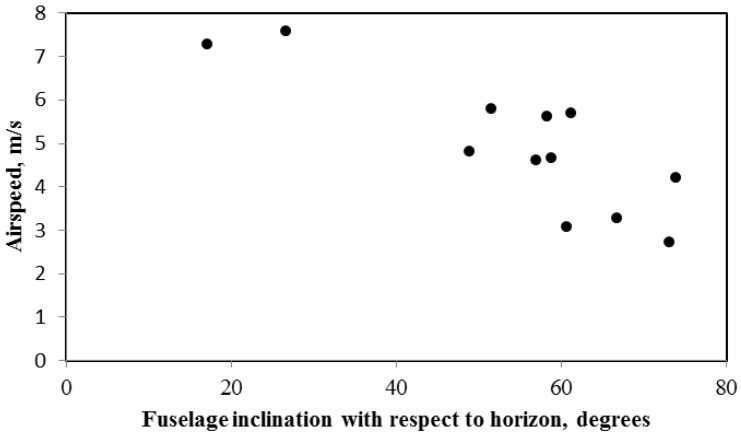

Figure 4.29: Airspeed dependence on inclination angle

The overall results were compiled to establish performance averages for each wing design. While the results are highly variable due to weather conditions, vehicle center of gravity, and random variation, over many trials the results converge to reasonable trends. The results are compiled in Table 4.7.

Table 4.7: Flight testing results

Parameter	**Wing A**	**Wing B**	**Wing C**	**Wing D**
Climb Rate (m/s)	0.489	0.758	0.851	0.395
Angle of Attack (rad)	0.879	0.839	0.390	0.585
Airspeed (m/s)	5.54	4.80	6.42	7.75
All-up weight (kg)	0.312	0.329	0.329	0.359
Flap Amplitude (rad)	1.137	1.062	1.049	1.032
Mean Current (A)	2.54	2.85	2.93	3.26

The trends observed in the in-flight results reinforce the results of the load cell testing conducted in the previous section. Wing C offers the best lifting ability, which translates into superior climb performance. While wing D was showing strong performance in the static laboratory testing, the added loading associated with a moving airstream during cruise appears to have bogged down the motors too much and pushed the desirable design range to a smaller wing.

In addition to level flight testing, a series of maneuvering tests are conducted to evaluate the effectiveness of two strategies for turning. First, a tail-based strategy is tested where the tail angle is simply deflected away from the vehicle centerline to initiate a yaw. Second, a combined wing and tail-based strategy is used that adds flap amplitude asymmetry to the tail maneuver. By reducing the amplitude of the wing on the inside of a turn, the thrust is imbalanced and the turn performance is increased. In total nine trials of each maneuver have been completed so far. By pre-programming the maneuver timing in the flight control software, the turn is always initiated at the same point in the flapping kinematics and maintained for the same amount of time to ensure a time-synchronous averaging approach may be used to improve signal-to-noise ratio. The results of the maneuver tests are plotted in Figure 4.30. The first 0.25 seconds exhibit a favorable performance across yaw, pitch, and roll, with a rapid direction change in yaw and minimal disturbances in pitch and roll, which upset airspeed and stability, respectively. Beyond 0.5 seconds a steady spiraling effect takes over with nearly constant rate of change in yaw, relatively stable roll that tracks flapping, and a linear decrease in pitch as the vehicle accelerates into a dive caused by the loss of lift due to roll. The results shown in this plot provide an indication that non-linear active maneuvering effects may be harnessed to maintain flight stability in highly gusty conditions and to enhance maneuverability. This strategy for control and maneuvering is superior to passive drag-based strategies that are typically employed by airplanes' control surfaces because it of the unique nature of FWAVs combining the lifting and control surfaces into the wing together.

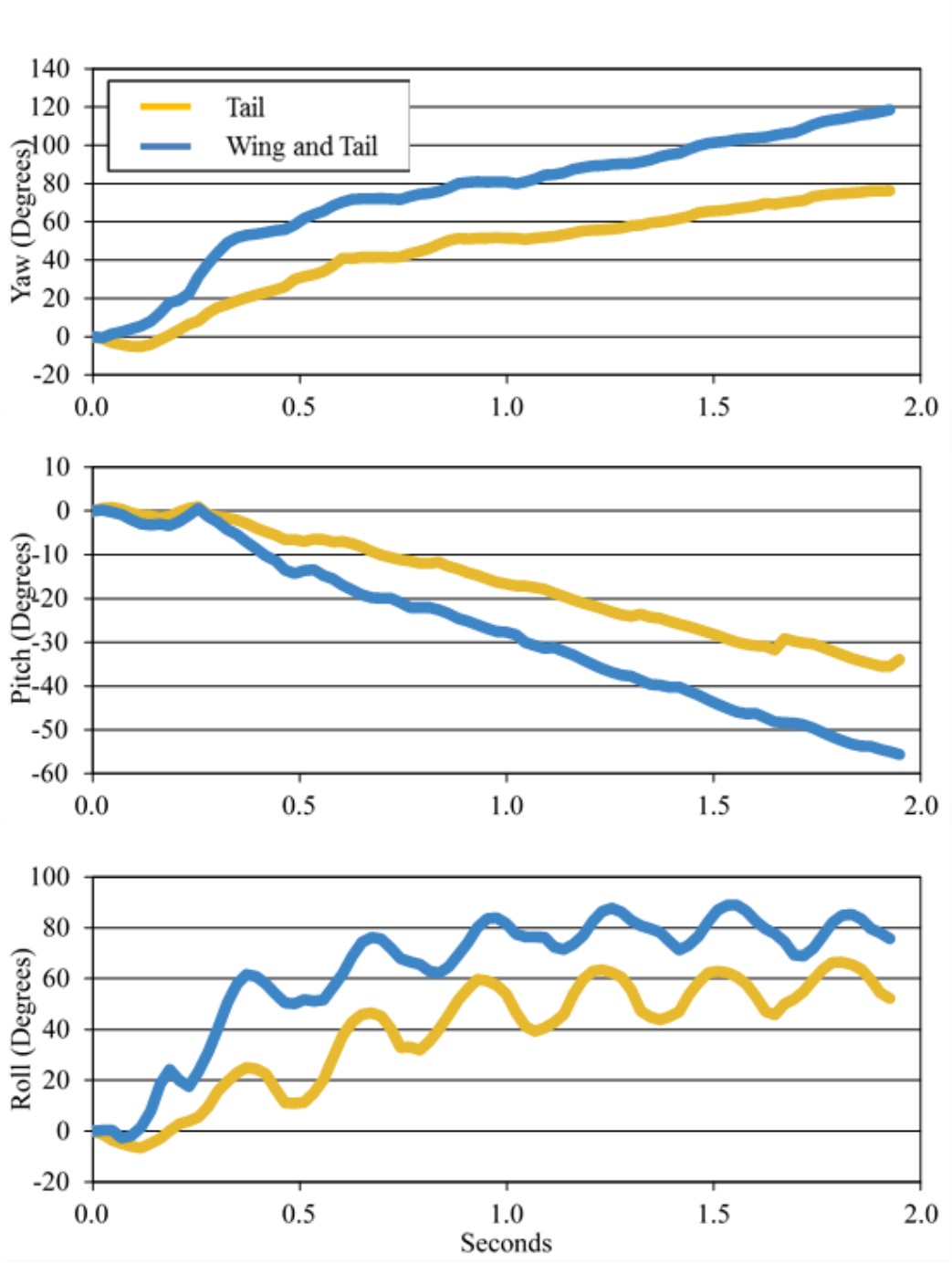

Figure 4.30: Turn performance testing results

Chapter 5: Component Modeling

5.1 Servo Motor Steady Modeling

A motor model is required that describes the relationships between electrical input parameters and mechanical outputs. In addition, a motor component model may be used to build system-level design insight in conjunction with models for other important system components including the wings and energy source. At the heart of each servo under test is a small electric motor. The equivalent form of the motor is shown in Figure 5.1, where L indicates armature inductance, R indicates internal resistance, and E indicates a battery-opposing electromotive force (EMF) that is induced in response to motor rotation as a function of angular velocity.

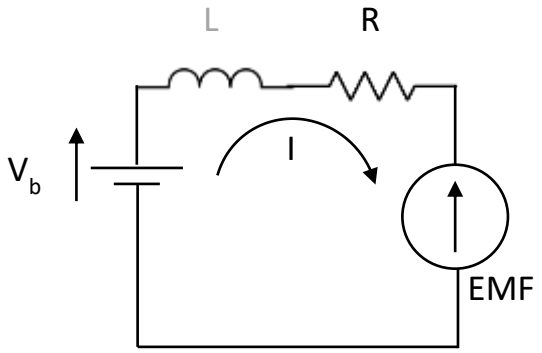

Figure 5.1: Equivalent form of a small electric motor

The general form of the electric motor model shown in Equation 1 is the starting point for the motor model. The inductance term is neglected in this model due to the small size of the motors used.

$$V_b = L\frac{dI}{dt} + IR + EMF \quad (1)$$

While the model in Equation 1 provides insight into the functionality of the motor, it is not yet complete because explicit formulations of torque and angular velocity are lacking. Therefore some additional relationships are required. From the dynamometer testing results, the torque model in Equation 2 is developed. The first constant relates the torque production to current supplied, and the second constant captures a static loss that is associated with the switching electronics and microcontroller used to power the motor, which manifests as a zero offset. This relationship provides excellent predictions for torque, with R^2 over 0.998 across each data set and a RMS error of 10.146e-3 N-m for the Futaba data and 8.128e-3 N-m for the Radiopost data.

$$\tau = K_\tau I + K_{\tau 2} \quad (2)$$

In addition to the torque model, a speed model is required to fully characterize the performance. From the experimental performance maps, two effects are evident that suggest the form of this model. First, the nominal battery voltage, referred to as the test index in the plots, is responsible for determining the free-run speed. This effect may be observed by the linear increase in the zero torque points for each test case. For each curve plotted, the bottom right point represents the free-run speed. Second, regardless

of the nominal voltage, the motor angular velocity exhibits a linear decrease as the torque load is increased. This slope indicates the production of the back-EMF related to current draw, as predicted in Equation 1. Since the speed is dependent on the voltage as well as the torque which is in turn dependent on the current, both voltage and current must be known to extract the motor speed. A two-dimensional response surface with the form shown in Equation 3 is used to set up the speed model.

$$\frac{d\theta}{dt} = K_I I + K_v V + K_s \qquad 3$$

The response surface parameters are solved using JMP software. For the Futaba servo, R^2 is 0.996 and RMS error is 15.80e-2 rad/s, and for the Radiopost servo, R^2 is 0.999 and RMS error is 9.13e-2 rad/s. The values of the coefficients of Equation 2 and Equation 3 are listed in Table 5.1.

Table 5.1: Motor speed and torque model regression coefficients

Parameter	**Futaba S9352HV**	**Radiopost 5005s**
K_I	-3.093	-4.394
K_V	2.385	2.274
K_S	0.261	0.219
K_T	0.409	-0.071
K_{T2}	0.431	-0.086

Equation 2 and Equation 3 provide explicit formulations of torque and speed as functions of voltage and current. The final step remaining in constructing a motor performance model is to extend these results to include power and efficiency predictions. The mechanical power output of a small electric motor is simply the product of torque and angular velocity. By merging the results of the torque and angular velocity models, a non-linear response surface is generated for output power that captures the non-linear nested relationship between voltage and current, as shown in Equation 4. The values for each of the parameters are listed in

Table 5.2.

$$P_{out} = C_A + C_B I + C_C V + (I + C_D)\big((V + C_E)C_F\big) + (I + C_D)\big((I + C_D)C_G\big) + (V + C_E)((V + C_E)C_H \quad (4)$$

Table 5.2: Parameters for servo power model in Equation 4

Parameter	**Futaba S9352HV**	**Radiopost 5005s**
C_A	-4.688	-4.308
C_B	4.646	3.983
C_C	0.677	0.634
C_D	-0.936	-0.884
C_E	-6.877	-6.997

C_F	0.919	1.060
C_G	-1.270	-2.043
C_H	-0.070	0.017

The response surface exhibits excellent accuracy in power predictions. The Futaba model has R^2>0.992 and RMS error of 0.232 Watts, and the Radiopost model has R^2>0.998 and RMS error of 0.083 Watts. Given that the Futaba and Radiopost servos are capable of producing 11.4 Watts and 7.2 Watts, the RMS errors in the prediction amount to 2.04% and 1.15% of the maximum power output. The improved accuracy of the Radiopost model is attributed to the greater density of experimental data collected in the performance map.

An efficiency prediction is set up as simply the ratio of output power to input electrical power, as shown in Equation 5.

$$\varepsilon = \frac{P_{out}}{VI} \qquad 5$$

The models constructed for power and efficiency are functions of the voltage and current. These are useful for describing the operational conditions of the motor given an electrical measurement. However, it is also useful to describe the power and efficiency in terms of the servo speed, which provides guidance for selection of

flapping kinematics. The model form given in Equation 6 is derived from the performance map results obtained in Figure 4.8. Each test trial corresponding to differing battery voltage shifts the starting point, then each trial has a constant slope of torque relative to the rotational velocity. The values of each of the parameters are listed in

Table 5.3. This equation can describe if the torque loads arising from the current plunge rate and wing and vehicle trim properties are feasible with respect to the actuator capabilities, given the voltage that is supplied to the motor that depends on state of charge and some dynamic loading behavior that will be discussed later in this chapter.

$$\tau = V_{batt} C_{V\tau} + C_{2\tau} - \omega C_{\omega\tau} \qquad 6$$

Table 5.3: Parameters for servo torque model in Equation 6

Parameter	**Futaba S9352HV**	**Radiopost 5005s**
$C_{V\tau}$	0.2956 N-m/V	0.2259 N-m/V
$C_{2\tau}$	-0.0815 N-m	-0.1276 N-m
$C_{\omega\tau}$	0.1207 N-m-s/rad	0.0932 N-m-s/rad

Finally, power output is given by the product of torque and angular velocity as shown in Equation 7.

$$P = \omega(V_{batt}C_{V\tau} + C_{2\tau} - \omega C_{\omega\tau}) \quad (7)$$

This model is exercised across the range of reasonable battery voltages for a two cell lithium polymer battery and across all reachable speeds at a full battery state of charge and no-load condition. Model results are shown in Figure 5.2 for the Radiopost servo and Figure 5.3 for the Futaba servo. For each plot, there is a clear peak in power around the 50% speed point, which suggests a target for flapping kinematics that will be explored in the next section. In the lower right corner of each plot the blue regions represent unreachable conditions due to battery discharge reducing the performance envelope.

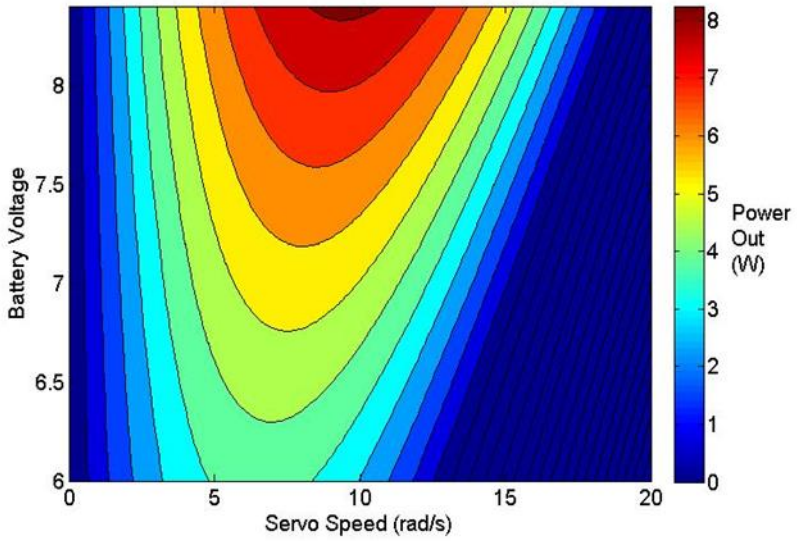

Figure 5.2: Radiopost 5005s power model

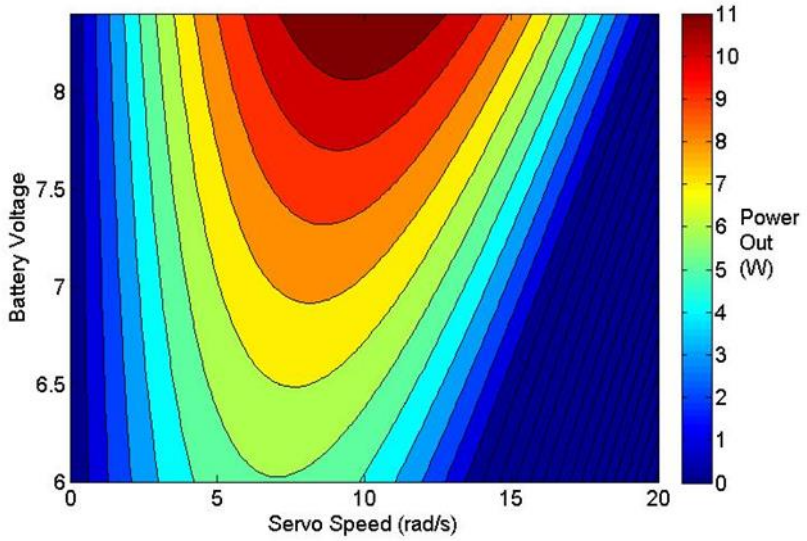

Figure 5.3: Futaba S9352HV power model

In addition to the power model just presented, the efficiency model shown in Equation 5 is reformulated in terms of motor speed and battery voltage by incorporating explicit expressions for the current and voltage that depend on these variables. Equation 8 lists the current expression, and Equation 9 lists the voltage expression. These equations capture the effect of induced EMF with increasing motor rotational velocity as well as the effect of battery discharge. Parameters for each equation are listed in Table 5.4.

$$I = C_{VI}V_{batt} + C_{2I} - \omega C_{\omega I} \quad (8)$$

$$V = C_{VV}V_{batt} + C_{2V} - \omega C_{\omega V} \quad (9)$$

Table 5.4: Parameters for Equations 8 and 9

Parameter	**Futaba S9352HV**	**Radiopost 5005s**
C_{VI}	0.7528	0.5326
C_{2I}	-0.2384 A	-0.1653 A
$C_{\omega I}$	0.2951 A-s/rad	0.2226 A-s/rad
C_{VV}	0.9086	0.9373
C_{2V}	0.0795 V	0.0170 V
$C_{\omega V}$	0.0349 V-s/rad	0.2542 V-s/rad

The efficiency models are plotted in Figure 5.4 and Figure 5.5. In each plot, the sharp boundary on the right represents the limit of feasible space by the servo. Clearly higher speeds are more efficient from a motor standpoint, however a power penalty is incurred to reach the most efficient range of operation.

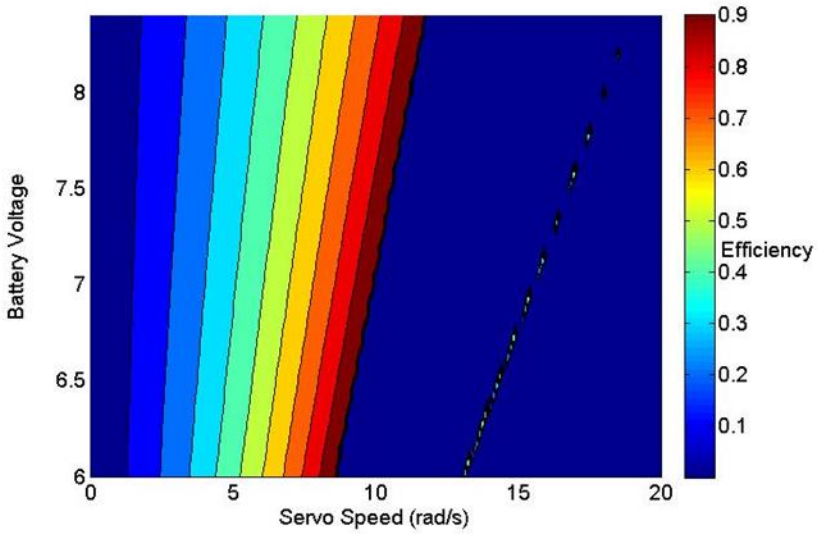

Figure 5.4: Radiopost 5005s efficiency model

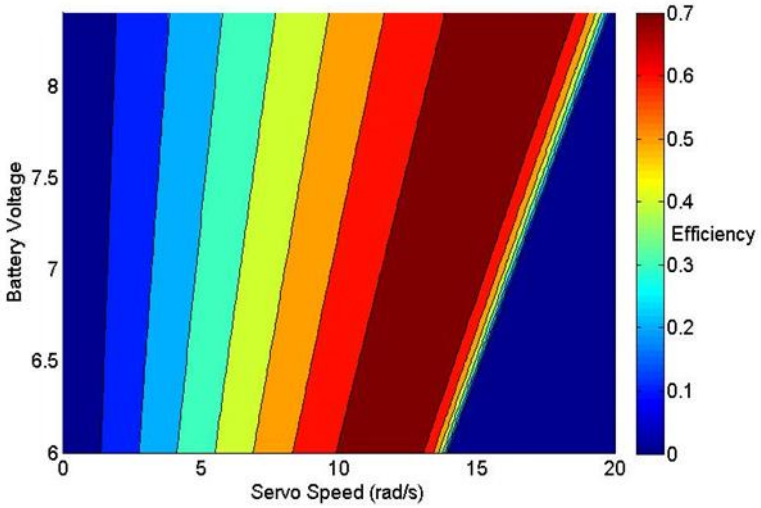

Figure 5.5: Futaba S9352HV efficiency model

At this stage it is worthwhile to make a comment regarding the generality of this modeling approach. In general, if experimental data has not yet been collected, such as

in a preliminary design effort, it may be reasonable to approximate motor performance using manufacturer published data for maximum torque and maximum rotational velocity at reference voltages, which is typically provided at levels of 5.0 V and 7.4 V for a high voltage servo. However, detailed mission analysis ultimately requires more granular motor characterization to fully understand the impact of variable battery voltage, as well as to verify that actual performance is modeled with sufficient accuracy.

Summary results of the developed torque model are plotted in Figure 5.6 across the typical range of voltages observed during instrumented flight testing in the previous chapter. Similarly, the developed power output and electromechanical efficiency are plotted together over the same range of voltages in Figure 5.7. These plots highlight two important results for the motors. First, the power output is reduced in the course of a discharge cycle. This loss in power production will have important implications in determination of interactive motor-wing performance constraints since a sizing analysis necessarily must account for a moving target with respect to the available motor bandwidth. Second, with regard to more generalized design efforts, the ideal operational range for the motors, framed by the peaks in power and efficiency respectively, shifts with voltage, making the selection of an appropriate wing somewhat more challenging. The ideal speed for power production starts at 12.9 rad/s and ends at 6.6 rad/s. Similarly the ideal efficiency speed starts at 16.5 rad/s and ends at 12.1 rad/s. This plot is a valuable snapshot of the performance of the motor component in isolation,

and provides detailed information about how system functionality may be expected to degrade in a practical usage scenario. This is a necessary improvement for a more accurate system-level analysis, and shows a much broader range of operational conditions than simpler models that only capture the performance of the drive motor at a nominal voltage level [123].

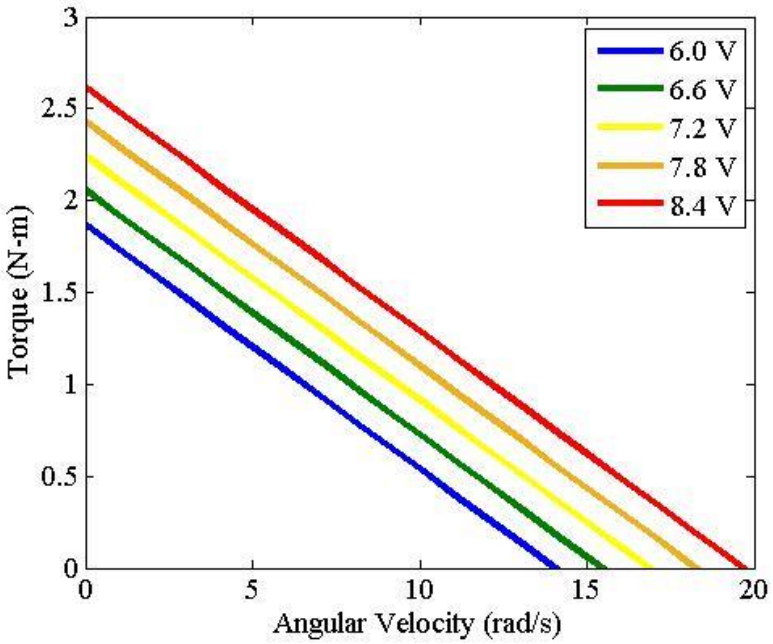

Figure 5.6: Torque-Speed bandwidth for Futaba S9352HV servo in steady state operation

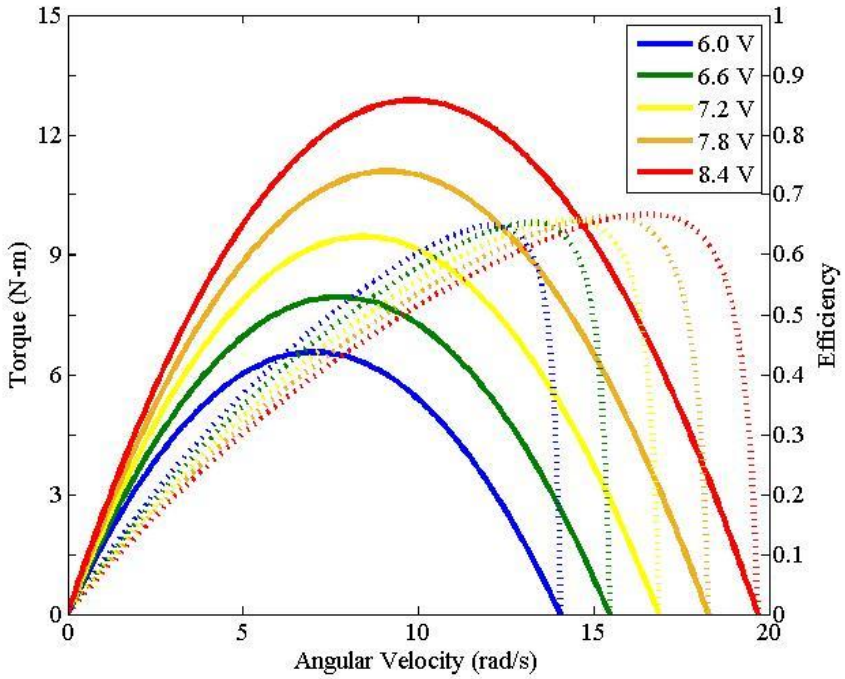

Figure 5.7: Power and efficiency contours for Futaba S9352HV servo in steady state operation

5.2 Servo Motor Dynamic Modeling

From the experimental motor characterization, a steady-state torque output model has been developed that describes the bandwidth of the servo in terms of the available torque, given a rotational velocity and input voltage. In addition, a power output model and an electromechanical efficiency model have been developed. This approach provides accurate predictions in constant testing, but does not account for losses that arise due to the inertia and friction of the geartrain. An unloaded test of the S9352HV

servo moving in a 4.0 Hz sinusoid with amplitude 45° is conducted to explore these dynamic losses that arise. The power input and angular acceleration are plotted together in Figure 5.8.

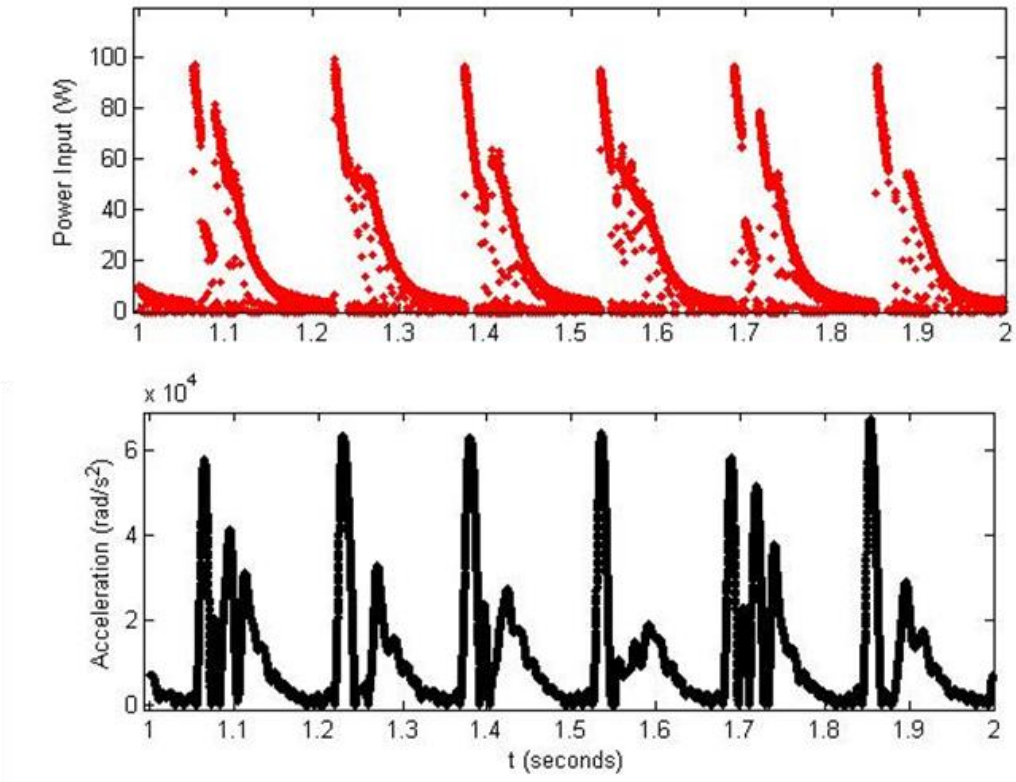

Figure 5.8: Power input (top) and angular acceleration (bottom) during an unloaded test of a Futaba S9352HV servo

These dynamic loads place large power demands on the motors, the mean power consumption measured during this test is 17.41 W, therefore a dynamic model that accounts for losses associated with acceleration of the motor is required, particularly in

this application that necessitates aggressive accelerations at each stroke reversal in cruise, and during any dynamic maneuver that is performed.

In order to characterize the dynamic power losses, a frequency sweep from 1 Hz to 4 Hz is performed while recording voltage, current, and wing plunge angle via an optical encoder at the wing root. The recorded encoder signal is twice differentiated and low pass filtered using a Savitzky-Golay smoothing filter to reduce signal quantization noise [171]. The resulting acceleration magnitude signal is plotted together with the encoder signal measured during the test in Figure 5.9. The measured electrical power resulting from actuator acceleration is plotted in Figure 5.10 together with the second order fit from the following equation that captures the power losses arising from geartrain acceleration:

$$P_{gear} = K_{P\theta 2}\ddot{\theta}^2 + K_{P\theta 1}\ddot{\theta} + K_{P0} \qquad 10$$

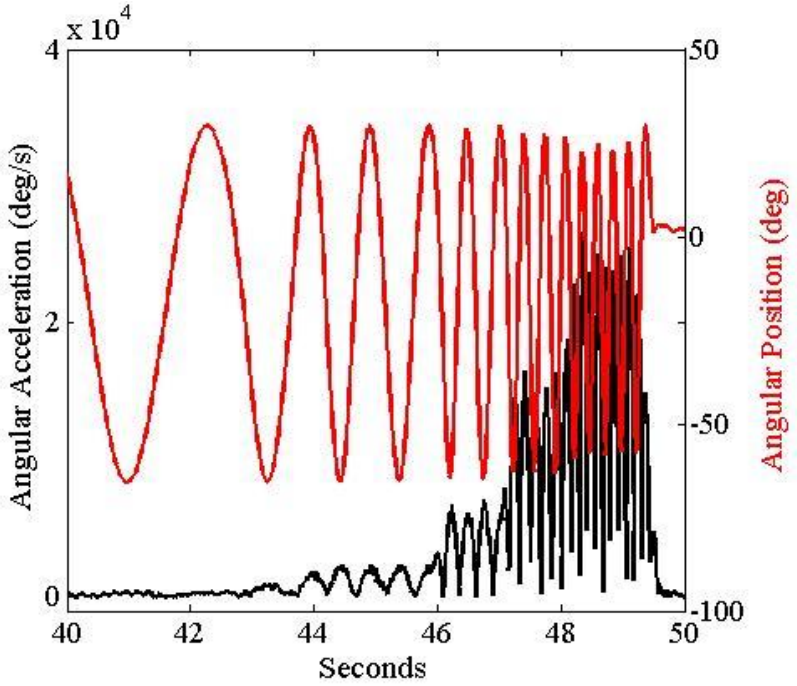

Figure 5.9: Frequency sweep test data used to estimate geartrain losses

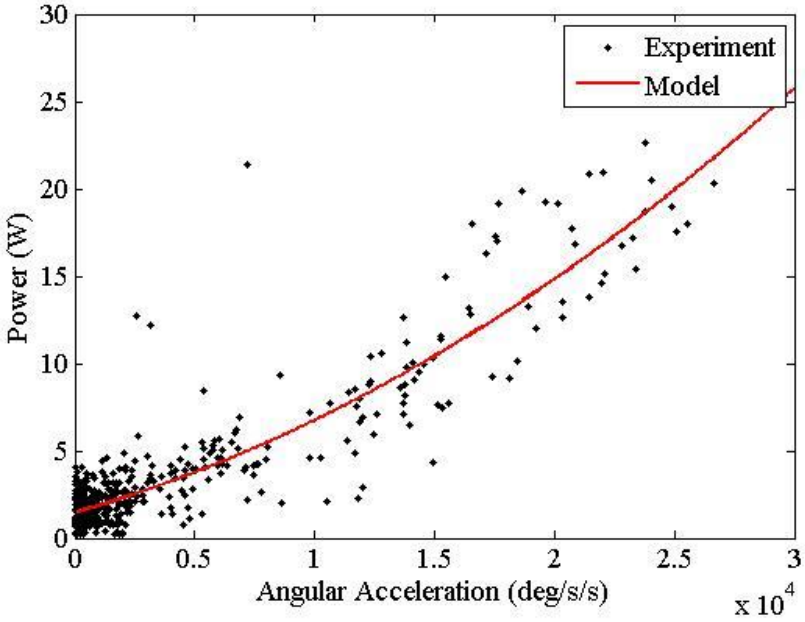

Figure 5.10: Power requirements for unloaded acceleration of servo geartrain

Values for each of the empirical constants used in the equations in this section are listed in Table 5.5.

Table 5.5: Empirical constants for dynamic geartrain power model

Description	**Variable**	**Value**
geartrain power loss 2nd order term	$K_{P\theta 2}$	1.4166E-8
geartrain power 1st order term	$K_{P\theta 1}$	3.8494E-4
geartrain power loss null offset	$K_{P\theta 0}$	1.5065

The effects of using this model are explored by applying this dynamic model to data collected during a flapping test conducted on the test stand developed in the previous chapter. Test conditions were a Wing C design flapping at 4.0 Hz. The model comparison is shown in Figure 5.11 Overlaid on the experimentally measured input power are results from the dynamic model developed in this section as well as the steady state power model from the previous section. The dynamic model has an RMS error of 5.53 W across a flapping cycle, while the static model has an RMS error of 6.72 W. Thus the dynamic model implementation provides a 17.7% reduction in error, and also offers improved tracking of the effects associated with stroke reversal, where loads become much more demanding.

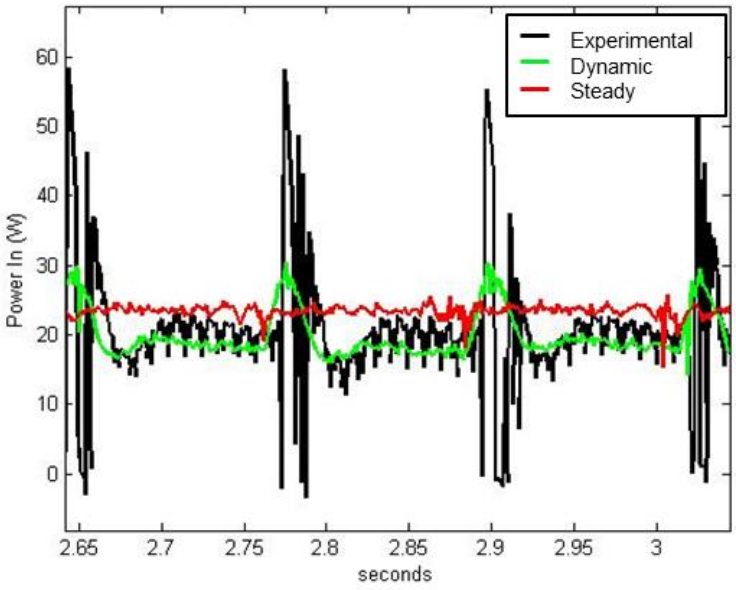

Figure 5.11: Effect of geartrain dynamic model on power prediction

5.3 Lithium Polymer Battery Modeling

A central piece in a comprehensive system model of flapping wing flight is the lithium polymer battery used to provide power. Typically, it is desirable to select a battery that offers maximum system endurance while meeting other constraints. As shown in Figure 5.6, a shift in the available motor bandwidth is experienced during the discharge cycle. Therefore, a real-world mission termination is more likely to be attributed to lost motor bandwidth at some intermediate state of charge, rather than full battery discharge. In order to accurately estimate how battery selection impacts system performance, an experimentally validated battery model is adopted that captures all relevant features of battery health, environment, and usage conditions, including run

time, multiple time-scale current-voltage characteristics, and derating effects related to rapid discharge [172]. The approach relies on some experimental characterization to set appropriate values for empirical constants, which is necessary due to variation between battery chemistries, manufacturers, and other conditions that cannot be ignored while retaining sufficient accuracy in predictions. This model uses a nonlinear relationship to provide a mapping from state of charge (SOC) to open circuit voltage, as follows:

$$V_{OC} = -1.031e^{-35 \cdot SOC} + 3.685 + 0.2156 \cdot SOC - 0.1178 \cdot SOC^2 + 0.3201 \cdot SOC^3 \quad (11)$$

The SOC value is updated throughout the simulation process using the coulomb counting approach, which uses the time integral of current draw $I(t)$ divided by the battery capacity Q_{lipo} to track state of charge as follows:

$$SOC = 1 - \int_0^t \frac{I(t)}{Q_{lipo}} dt \quad (12)$$

The current-voltage behavior during discharge of the battery is then modeled by generalizing the framework presented in [172] to allow for variable battery capacity, as follows:

$$V(t) = V_{OC} - \int_0^t \left(\frac{I(\tau)}{Q_{lipo}}\right)^{K_1} \left(K_2 e^{\left(\frac{-\tau}{K_4}\right)^{K_3}}\right) d\tau \quad (13)$$

This equation captures the discharge associated with slow timescale effects with the first term that denotes open-circuit voltage. The fast timescale effects are described by the convolution of a nonlinear discharge-rate term and a battery plant model with exponential decay. The K parameters are tuned to capture current-dependent derating in usable capacity, as well as the time-dependent voltage changes associated with rapidly changing current. These effects are quite important in flapping wing analysis, which contains both high discharge rates and rapidly changing cyclic loading conditions. Model tuning is necessary to ensure the model is properly capturing the particular make and model of batteries chosen for this application. This procedure is completed by generating a data set that captures a complete discharge process using the test stand shown in Figure 4.13.

A two-cell lithium polymer battery pack with 370 mAh capacity is used in a stationary flapping test and the recorded current draw during this test is then used as an input into the battery model in Equation 13. The model parameters are then identified to provide a close fit to the data, with the result shown in Figure 5.12.

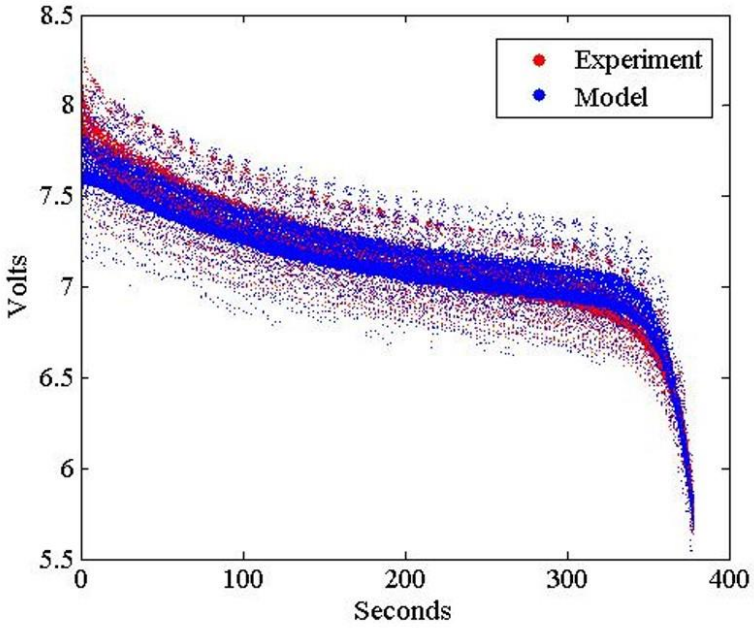

Figure 5.12: Comparison of battery model to experimental data

A comparison using a simple coulomb counting approach is plotted in Figure 5.13 to help demonstrate the benefits of the modified approach that incorporates dynamic effects. The key difference is that the large loads associated with wingbeats aren't causing a voltage drop, leading to instantaneous errors. In addition, the lack of a dynamic component to the battery capacity model causes errors in the state of charge estimation. At the conclusion of the test the coulomb counting approach predicts a remaining SOC of 46.9% which will result in errors if this approach is used to estimate endurance of any practical system.

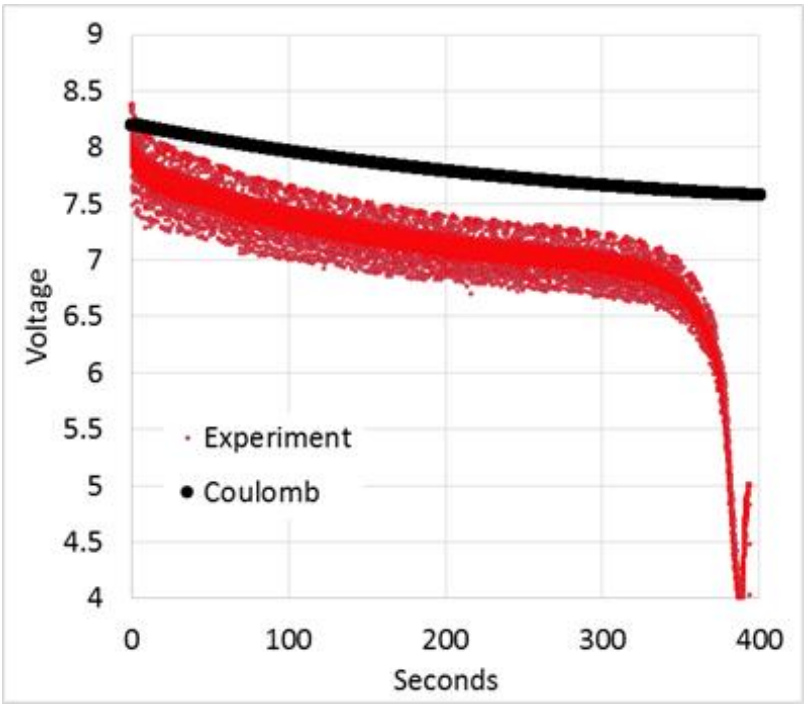

Figure 5.13: Coulomb counting used to estimate battery voltage during a bench test

As a validation check, an additional test was performed containing random motor speeds and loads, intended to exercise both the fast and slow timescales, and also highlight any areas in the battery model that may not be accurately capturing the behavior appropriately. This test is plotted in Figure 5.14, along with a basic version of the model that only performs coulomb counting with no modifications related to the fast and slow timescale dynamics of the battery voltage. The dynamic model achieves RMS error across the test of 0.016 V, while the much simpler coulomb counting approach exhibits RMS error across the test of 0.1127 V.

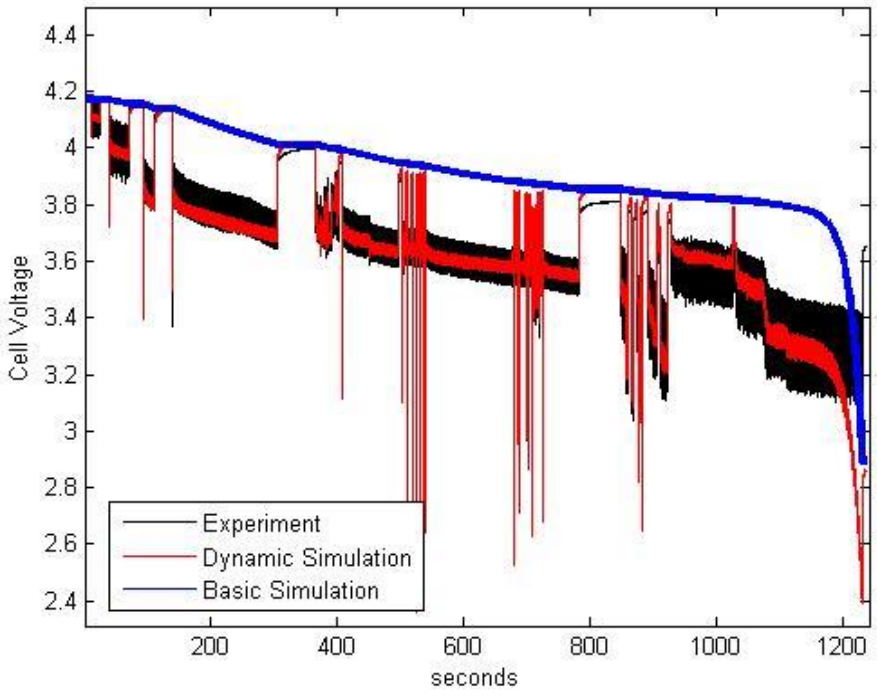

Figure 5.14: Battery model validation

Values for the empirical constants appearing in the equations for this section are listed in Table 5.6.

Table 5.6: Empirical constants for battery model

Description	**Variable**	**Value**
battery model empirical parameter	K_1	0.7
battery model empirical parameter	K_2	1.93
battery model empirical parameter	K_3	2.5E-4
battery model empirical parameter	K_4	0.4

5.4 Wing Aerodynamic Modeling

A key tool used to understand flapping wing flight is aerodynamic modeling, which provides insight into the interaction between the four forces of flight: lift, thrust, drag, and weight. With appropriate modeling, it is possible to understand the relationships and constraints that arise between vehicle components. Furthermore, in certain models, it may be possible to explore the underlying physics of achieving flight, to explore the suitability of a particular style of flight in achieving a given objective. The aerodynamic model is an essential tool in designing a man-made FWAV because it provides insight into the requirements for powered flight, which may be used to concurrently perform component selection, wing sizing, and flapping gait design.

In part due to the breadth of flapping wing flight styles, aerodynamic models for flapping wings have several general forms that are more or less applicable to a particular style of flight. The selection of an appropriate power model is a key decision in realizing predictions that are realistic, and in capturing the physical effects that are enabling flight. Here, the scope is limited to avian cruising flight, primarily for Reynolds numbers on the order of 10^5.

In Chapter 3, the Robo Raven flapping wing aerial vehicle was presented, which provides an example of a feasible combination of vehicle design and operational characteristics, with the capabilities of sustained cruising and climbing flight as well as controllable maneuvers. Arriving at that vehicle design was an exhaustive effort

focused mainly on experimental trials and prior experience in flapping wing aerial vehicle development. In many cases, a designer may not have a baseline design to learn from, or may wish to generate a new design with significantly different parameters from prior vehicles. In this case, it is necessary to rely on modeling to establish a reasonable combination of vehicle design and operational characteristics.

5.4.1 Simplified Aerodynamic Modeling with Vortex Ring Method

Early stage design work benefits from a simulation approach with lower fidelity and higher throughput to enable broad exploration of the trade space, which contains a large number of parameters. Therefore, blade-element modeling is a popular tool to explore design performance. While this modeling approach has been shown to be capable of providing some reasonable predictions about flapping wing aerial vehicle performance [134, 173], it requires a substantial amount of tuning and adjustment to achieve acceptable results. The major drivers of model uncertainty are airspeed, body pose, and resulting power requirements, all of which are challenging to prescribe simultaneously. Therefore, without experimental data to rely on for model validation, this style of model is difficult to implement in practical scenarios.

To overcome this difficulty and provide the required inputs to the blade-element model, a vortex-based model may be used as an alternative. Vortex-based models are reasonably easy to formulate and don’t rely on knowledge of the lift and drag

coefficients. When correctly configured, they provide useful insight into feasible conditions for airspeed and body pose, and how the power required varies according to these inputs. In vortex theory, the induced power increases the kinetic energy of the vortex wake. The momentum of the wake balances the weight of the bird and overcomes drag forces.

There are several distinct gait models summarized in Figure 5.15 that correspond to the circulation model used to represent the flow around the lifting surface. The present scope is limited to avian flight, thus the two models of greatest interest are the continuous and continuous in downstroke circulation models, which are ascribed to avian flight. In experimental studies, both the vortex ring gait and the continuous vortex gait have been observed in flying animals. The vortex ring gait corresponds to lower aspect ratio wings and lower flight speeds, along with larger wingbeat amplitudes. A ring vortex is shed at the end of each downstroke which sustains flight but the upstroke provides little useful lift. The continuous wake results in an undulating vortex filament shed from each wingtip, and is typical of higher aspect ratio wings in faster cruising flight, along with smaller wingbeat amplitudes.

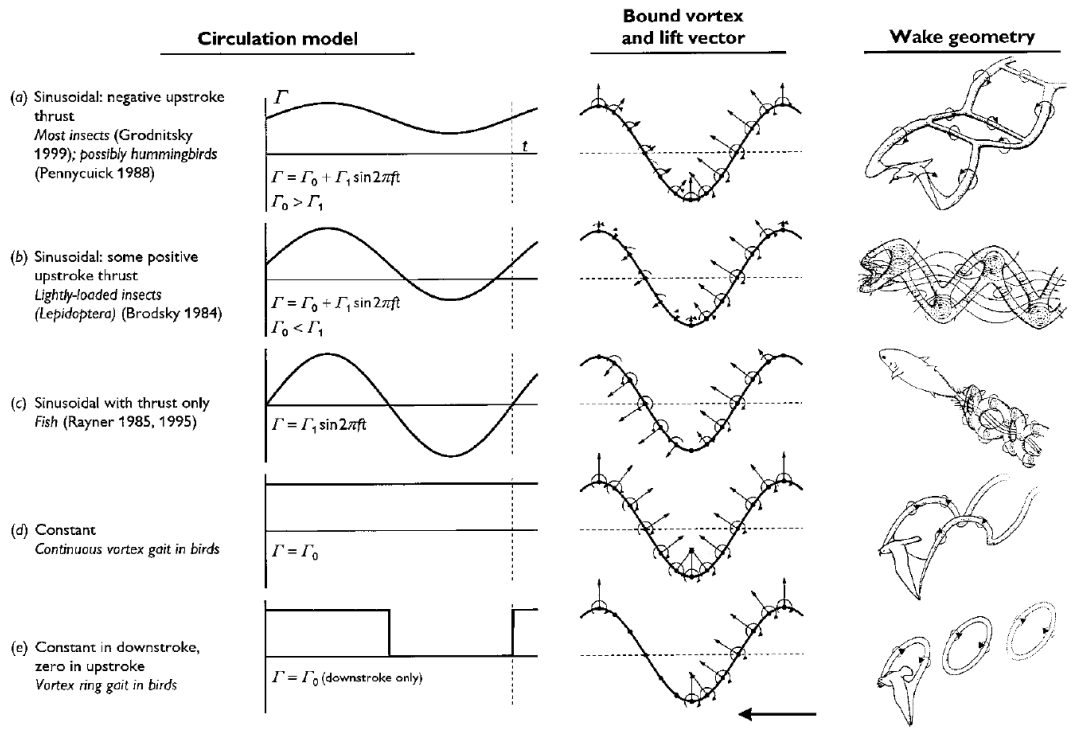

Figure 5.15: Circulation models and associated vortex and wake visualizations [143]

Several additional criteria must be considered when selecting a modeling strategy relating to the style of lift and thrust generation. The key criteria are the usage of wingspan variation in the continuous vortex model to avoid the production of negative lift on the upstroke, the wing aspect ratio, and the flight speed, as summarized in Figure 5.16. Given that the Robo Raven baseline design is incapable of this functionality in its current version, and instead relies on large angle of attack flight with passive wing twisting, the upstroke is expected to provide little to no contribution to lift. Therefore, the continuous on downstroke vortex model is selected. As will be seen later in experimental validation data, this assumption is somewhat valid, but requires some

further refinement. In the most general terms, the selection of an appropriate circulation model is important to maximizing predictive accuracy, and requires an understanding by the vehicle designer of the size scale, the anticipated nature of the wing functionality, and the rationale for making this selection.

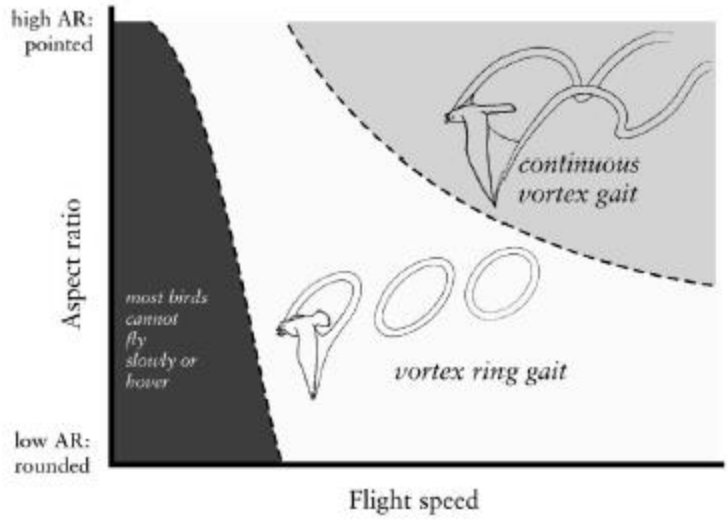

Figure 5.16: Avian circulation model selection criteria [143]

5.4.1.1 Model Specification

The fundamental assumption of the vortex ring modeling approach is that at the end of each downward wingbeat shed vorticity rolls up into a planar ring that is inclined relative to the horizontal as shown in Figure 5.18. Each ring has sufficient momentum Q and angle of inclination ψ to balance weight, parasite drag, and profile drag. Hence, this approach relies on estimates of the parasite drag and profile drag. Parasite drag is assumed to take the form shown in Equation 14. Natural mass scaling suggests a range

of reasonable values for the flat plate area of the fuselage, A_{fp} [139, 142]. For a man-made vehicle like the Robo Raven II parasite drag is not necessarily expected to agree with natural scaling due to the lack of a streamlined body. Therefore, flat plate area was directly determined to be 22.58E-3m^2 by creating a CAD model of the Robo Raven fuselage. The parasite drag is resolved into horizontal and vertical components such that a body inclination above horizontal will provide lift.

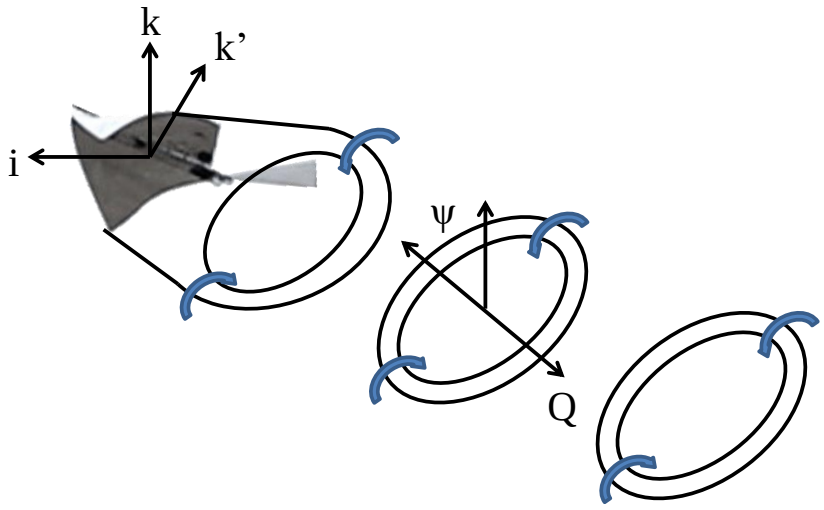

Figure 5.17: Vortex ring conceptual diagram

$$D_{par} = \frac{1}{2}\rho A_{fp} V^2 \qquad 14$$

The profile power is computed using a blade element strategy that depends on wing geometry and velocity. The wing geometry is described by $c_0\bar{c}(\zeta)$, where c_0 is the chord at the wing root and $\bar{c}(\zeta)$ is the normalized wing shape as shown in Equation 15.

$$\bar{c}(\zeta) = \begin{cases} 1 & for \quad 0 < \zeta < \frac{1}{2}, \\ 4\zeta(1-\zeta) & for \quad \frac{1}{2} < \zeta < 1 \end{cases} \qquad 15$$

The wing motion is sinusoidal, therefore the velocity of a wing strip as it moves through the air is given by Equation 16, where V is the airspeed, θ(t) describes the time-dependent sinusoidal path of the wings, γ is the angle of inclination of the stroke plane relative to the $-\hat{\imath}$ direction, and radial position along the wing is bζ where b is the semi-span, following the convention for wing chord described by Equation 15.

$$U(\zeta) = V\hat{i} - b\zeta\dot{\theta}(t)(\cos(\theta(t))\sin(\gamma)\hat{k}) \qquad 16$$

From Equation 16 the magnitude of velocity U is given by Equation 17.

$$|U| = (V^2 + 2Vb\zeta\dot{\theta}(t)\cos(\theta(t)\cos(\gamma) + b^2\zeta^2)^{1/2} \qquad 17$$

The profile drag is given by Equation 18 which adopts a similar form as was used in Equation 14 for estimation of the parasite drag. T is the period of a flapping cycle and

τ is the downstroke fraction, and the coefficient of drag at zero lift C_{D0} is estimated as 0.02 as outlined by Rayner [141]. The $d\zeta$ integral is doubled to account for the contribution to profile drag from each wing.

$$D_{pro} = -\frac{b}{T}\int_0^{\tau T} dt \int_0^1 2(-\frac{1}{2}\rho c_0 \bar{c}(\zeta) C_{D0} |U| U(\zeta)) d\zeta \qquad 18$$

Given estimates of the parasite and profile drag, the momentum balance for each vortex is set up in Equation 19. This equation is fundamental for establishing the induced power, as it states that the strength of circulation Q and angle of inclination ψ of each vortex ring formed during a wingbeat are sufficient to balance the weight and drag forces, thus sustaining flight.

$$|Q|(\sin(\psi)\hat{i} + \cos(\psi)\hat{k} = T(Mg\hat{k} - D_{par} - D_{pro}) \qquad 19$$

A convenient consequence of this formulation is that the model will only converge on a limited range of airspeeds. Thus, the model will automatically identify when airspeed is too low for feasible flight, and also will identify when airspeed to too high to use the vortex ring gait and a concertina gait would be more appropriate, in both cases due to a lack of model convergence. Equation 19 sets up Q and ψ as functions of the airspeed and wingtip kinematics. By eliminating ψ all the variables become solvable as a function of the airspeed. This problem is handled by first finding the angle of the path

traced by the wingtip during a downbeat. The angle between the wingtip path and the horizontal is given by ψ_1 as shown in Equation 20. The flapping amplitude is given by A, therefore the numerator is simply the vertical motion of the wingtip during a downbeat based on the flapping kinematics, and the denominator is the horizontal motion of the wingtip plus the motion associated with the forward airspeed during the same downstroke period.

$$\psi_1 = \arctan\left(\frac{b\sin(\frac{1}{2}A)\sin(\gamma)}{b\sin(\frac{1}{2}A)\cos(\gamma) + \frac{1}{2}V\tau T}\right) \qquad 20$$

Next the distance is found that is traversed due to the downward self-convective velocity of a vortex loop during the downbeat period. During the downstroke, the motion created by the self-convective velocity Us0 of the vortex ring causes the starting point of the vortex to migrate downward, away from the wingtip path described in Equation 20, while the ending point is coincident with the wingtip path. The resulting angle is described by the angle ψ_0 in Equation 21, where the numerator is the distance traveled by the vortex ring perpendicular to the wingtip path during a downstroke period, and a0 is the radius of the vortex ring shed at the end of the wingbeat.

$$\psi_0 = \arctan\left(\frac{1}{2}\tau T U_{s0} / a_0\right) \qquad 21$$

A derivation of the self-convective velocity U_{s0} and radius a_0 are omitted here but details are provided by Rayner in [141]. For the purposes of this study, the objective is to obtain a relationship between the airspeed and the power required for flight, which requires a realistic model to for $\gamma(V)$, or how the angle of wingtip inclination varies with increasing flight speed. This is realized by iteratively solving the system of equations that follows from Equation 19 until the solution converges to compatibility with the predicted vortex orientation, given in Equation 22. Satisfying the constraint of Equation 22 ensures that the wingtip path, flight speed, and forces resulting from drag as well as vortex size and strength are self-consistent. The resulting effect of enforcement of Equation 22 is easily observable in most flying animals. As flight speed increases, the body pose tends to shift closer to horizontal to direct more momentum rearward.

$$\psi = \psi_1 - \psi_0 \tag{22}$$

Once Equation 22 is satisfied, the parasite power P_{par} is computed as the product of the parasite drag and airspeed, and the profile power is similarly computed as the product of the profile force and velocity, as shown in Equation 23.

$$P_{pro} = -\frac{b}{T}\int_0^1 d\zeta \int_0^{\tau T} 2[U(\zeta)\cdot(-\frac{1}{2}\rho c_0 \bar{c}(\zeta) C_{D0}|U|U(\zeta))]d\zeta \tag{23}$$

The induced power is computed as a combination of two sources, the self-energy of the most recent vortex loop E_s and the mutual energy E_m of interactions between prior loops in the chain, as described in Equation 11. Details of the calculation approach for mutual energy and a derivation of the circulation of the vortex ring κ and the radius a_r are available in [140]. In this case, four terms of mutual interaction are enough to achieve less than a 1% change in self-energy.

$$P_i = \tfrac{1}{2}\rho\kappa^2 a_r (E_s + E_m)/T \qquad 24$$

In addition to the parasite, profile, and induced power components, the inertial power is computed for each wing. Due to the complex geometry and mass distribution of the wing, a CAD model is created to determine the mass moment of inertia J about the primary flapping axis for wing C. The resulting value is 27.371E-4 kg-m2. The inertial power required per wing is calculated as the rate of work against the inertial torque as shown in Equation 12, using the root mean squared velocity and acceleration of the wing.

$$\overline{P}_{iner} = J\ddot{\theta}_{RMS}(t)\dot{\theta}_{RMS}(t) \qquad 25$$

Finally, the total power requirement is computed as the sum of the converged results for parasite, profile, and induced power, as well as the inertial power for each wing as shown in Equation 26.

$$\overline{P}_{total} = P_{par} + P_{pro} + P_i + 2\overline{P}_{iner} \quad 26$$

Equation 26 provides a prediction of the power required to fly based on the vehicle dimensions and mass as well as the flight velocity and flapping kinematics. As defined in Equation 22, the model converges to a realistic body pose by balancing the wake momentum against the drag force for a given airspeed. The usefulness of this model depends on the validity of the assumptions that have been made about the nature of the flow circulation resembling vortex rings. Hence, the next step is to compare flight testing data to model predictions to establish bounds on the inputs to the model, generate power predictions, and finally to explore the feasibility of the model predictions in a real-world application.

5.4.1.2 Model Validation

Model validation is performed using the experimental flight testing equipment presented in Chapter 4 to collect relevant data in cruising flight. Flight tests provide data to validate the vortex ring model and evaluate its effectiveness in making power predictions as well as in estimating a set of reasonable parameters describing cruising

flight. Finally, the differences between the model predictions and flight test data are discussed to explore the effectiveness of the model in providing design insight. Overall, the vortex ring modeling approach will be shown to offer valuable insight in performing initial design parameter specification due to a minimal reliance on prescribed parameters as would typically be necessary to implement a more common blade-element model.

The vortex ring model was set up with the parameters listed in Table 4.6 to generate power predictions for a range of feasible flight speeds. The results of this prediction are shown in Figure 5.19 compared to flight testing data. In the middle of the range of airspeeds tested, the model is providing acceptable estimation of the measured power. At the extremes of the range tested, the prediction accuracy degrades, for reasons that will be explored in the following chapter.

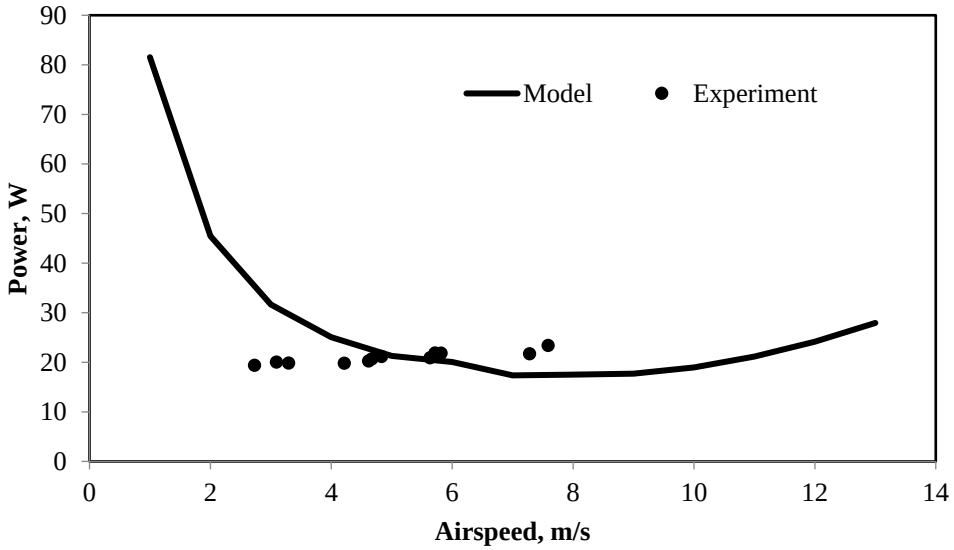

Figure 5.18: Comparison of power predicted and power measured by flight testing

The peak power can vary significantly relative to the mean power required for flight. This effect is plotted in Figure 5.20 for one of the flight test trials. The spike in power around the beginning of the downstroke is 38.8 W, which is 71% larger than the mean power of 22.6 W. An interesting result from this plot is the large difference in the mean downstroke power of 25.2 W and the mean upstroke power of only 19.5 W. The difference between these two values is noteworthy but the magnitudes are close enough to suggest that the assumption of an aerodynamically inactive upstroke is unlikely to be entirely accurate, and that some modification to the model is necessary to capture the upstroke power more accurately.

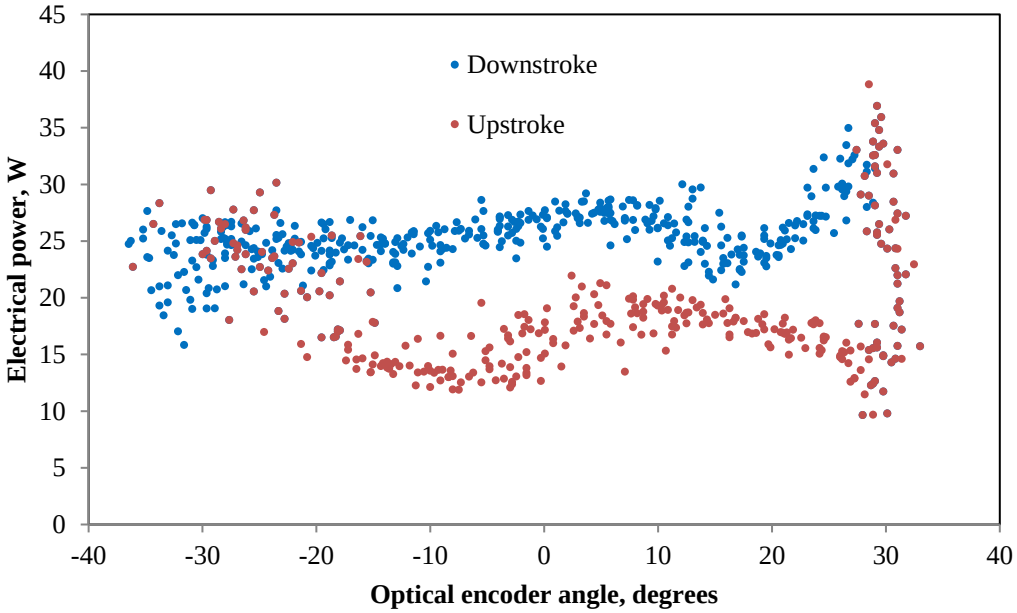

Figure 5.19: Power variation within flapping cycle

The vortex ring model generates fairly accurate predictions of average power required for flight. However, one of the goals of this modeling approach was to adapt it to a prescriptive design scenario, where vehicle performance is specified in the absence of pre-existing test data. Clearly several key effects must be properly accounted for to realize this vision. First, the cycle variation in power required must be accounted, because ultimately the drive motor must supply the peak power demanded by the wing design and flapping kinematics or else performance will suffer. Second, the upstroke contribution to aerodynamic force must be properly captured, likely through a hybrid formulation of the vortex ring and continuous vortex gait that covers the transition region. Third, the power required to climb must be accounted, as this is a significant

part of any practical flight. A final limitation on this model validation study in particular was the tight power budget allotted for test flights used to collect validation data. Despite efforts to miniaturize all sensors as much as possible, nearly every flight test trial was conducted at maximum power and level or positive climb rates were difficult to achieve. This led to a low rate of acceptable data sets relative to the number of flight testing trials (10.7%) and is likely responsible for the relatively flat shape of the experimental results plotted in Figure 5.19. A more extensive study of how the power requirements depend on wing kinematics, wing size, climb rate, airspeed, and angle of attack requires a higher power margin, hence a new version of the Robo Raven II must be developed with increased power density of the drive motors, when they become available.

5.4.2 Strip Theory Aerodynamic Modeling for Flapping Wings

The forces produced by flapping wings during flight depend primarily on the interaction between commanded flapping motions, power system bandwidth, and wing flexibility. These effects were shown in the previous section, in particular Figure 5.20, where the instantaneous conditions were unsteady throughout the wingbeat. Therefore, an aerodynamic model of the wing is required that for each time step in the flapping cycle, couples to the battery and actuator models to ensure the forces acting on the wings balance the torque generated by the drive motor at the corresponding angular velocity.

A suitable aerodynamic modeling approach for this purpose is the classic strip theory method, adapted to flapping wing flight. This modeling approach is widely used in flapping wing flight owing to its simplicity, ability to account for varying trim conditions, computational efficiency, and basic ability to account for unsteady aerodynamics, as would be expected due to cyclic wing heaving motions and rotations.

The modified strip theory approach developed by DeLaurier is adopted as a model baseline for the prediction of flapping wing performance [134]. The modified strip theory model discretizes the wings into chordwise strips from the root to the tip, computes quasi-steady forces on each strip due to wing and body motions, and sums the forces to determine the total wing force.

Wing chord is defined in Equation 27 as a function of normalized span location ζ with the root chord defined as c_0 and chord shape defined as $\bar{c}(\zeta)$. This wing design is derived from an experimental characterization and manufacturing sensitivity analysis that established a wing baseline with a favorable blend of lift and thrust production [12].

$$c_0\bar{c}(\zeta) = \begin{cases} 1\ for\ 0 < \zeta < \frac{1}{2} \\ 4\zeta(1-\zeta) for\ \frac{1}{2} < \zeta < 1 \end{cases} \quad 27$$

The wing motions in plunge and twist are defined using sinusoids with a phase offset. The parameters *A* and β are used to control the amplitudes of plunge and twist per unit span, respectively:

$$h = -Aycos\phi \quad (28)$$

$$\dot{h} = Ay\omega sin\phi \quad (29)$$

$$\ddot{h} = Ay\omega^2 cos\phi \quad (30)$$

$$\theta = -(\beta y)\sin(\phi) \quad (31)$$

$$\dot{\theta} = -(\beta y)\omega\cos(\phi) \quad (32)$$

$$\ddot{\theta} = (\beta y)\omega^2\sin(\phi) \quad (33)$$

Strip-wise normal force is computed as the sum of circulatory and added mass forces. Circulatory force is computed as shown in Equation 34, where the flight speed is given as U and the relative flow velocity at the quarter chord inclusive of the wing's motion and downwash is given as $\hat{V}_{0.25c}$, semispan is y_0, spanwise location is y, and the normal force coefficient is C_n.

$$dN_c = \frac{\rho U\hat{V}_{0.25c}}{2} C_n(y)cdy \quad (34)$$

The normal force coefficient is computed as shown in Equation 35 using as a function of the apparent angle of attack, calculated as a combination of the mean angle of the chord relative to the flapping axis $\bar{\theta}_w$, the mean angle of the flapping axis relative to the incoming airstream $\bar{\theta}_a$, the zero lift line α_0, and the relative angle of attack induced by the wing's motion and finite-span wake effects α'.

$$C_n(y) = 2\pi(\alpha' + \alpha_0 + \bar{\theta}_a + \bar{\theta}_w) \quad 35$$

The α' angle describes the relative angle of attack at the ¾ chord location and is given in Equation 36, where the downwash is given by $\frac{w_0}{U}$, the unsteady wake effects are accounted for by the coefficient of α, and the angle of attack arising from wing motion is given by α as shown in Equation 42. The wing's motion includes the plunge velocity given by $\dot{h}$, the twist given by θ, and the velocity of the incoming airstream given as U.

$$\alpha' = \left[\frac{ARC'(k)}{(2 + AR)}\right]\alpha - \frac{w_0}{U} \quad 36$$

$$\alpha = \frac{\dot{h}\cos(\theta - \bar{\theta}_a) + \frac{3}{4}c\dot{\theta} + U(\theta - \bar{\theta})}{U} \quad 37$$

In Equation 36, the coefficient of the angle of attack is calculated using a modified three-dimensional Theodorsen function to account for finite-span unsteady vortex

wake effects [174, 175]. The possibility exists to extend the model by adopting a more accurate modeling approach to estimate the downwash such as an extended lifting line approach [176, 177], however the approximate form used here provides sufficient accuracy and superior computational tractability.

The relative flow velocity at the quarter chord is given in Equation 38 is calculated using the wing kinematics in plunge and twist, given by h and θ respectively, as well as the relative angle of attack induced by the wing's motion and finite-span wake effects α'.

$$\hat{V}_{0.25c} = \{\left[Ucos\theta - \dot{h}\sin(\theta - \bar{\theta}_a)\right]^2 + \left[U(\alpha' + \bar{\theta}) - \tfrac{1}{2}c\dot{\theta}\right]^2\}^{1/2} \qquad 38$$

In addition to the circulatory normal force, the added mass effect adds additional normal force, computed as shown in Equation 39. The overall normal force in Equation 42 is then given by the sum of the contributions from the circulatory and added mass normal forces

$$dN_a = \frac{\rho\pi c^2}{4}(U\dot{\alpha} - \frac{1}{4}c\ddot{\theta})dy \qquad 39$$

$$dN = dN_c + dN_a \qquad 40$$

The chordwise forces are computed as the sum of cambered wing drag, leading edge suction, and viscous friction drag as shown in Equations 41, 42, and 43. In these equations, the leading edge suction efficiency η_s is set to 0.98 following the example calculation provided in DeLaurier's presentation of these equations. The V_x term is the flow speed tangential to the current strip, approximated using the first bracketed term of Equation 38.

$$dD_{camber} = -2\pi\alpha_0(\alpha' + \bar{\theta})\frac{\rho U\hat{V}_{0.25c}}{2}cdy \tag{41}$$

$$dT_s = \eta_s 2\pi\left(\alpha' + \bar{\theta} - \frac{1}{4}\frac{c\dot{\theta}}{U}\right)^2\frac{\rho U\hat{V}_{0.25c}}{2}cdy \tag{42}$$

$$dD_f = C_{df}\frac{\rho V_x^2}{2}\,cdy \tag{43}$$

The flow is assumed to be fully turbulent, so the friction drag coefficient is calculated as a function of the Reynolds number using Hoerner's approximation shown in Equation 44 [178].

$$C_{df} = \frac{0.89}{(\log(Re))^{2.58}} \tag{44}$$

Drag due to the tail is computed as an inclined flat plate, with the tail inclined relative to the fuselage:

$$dD_{tail} = C_{Dtail}\frac{\rho U^2}{2}A_{tail}\sin(\theta_{tail} - \theta_{body}) \quad (45)$$

Total force in the chordwise direction is computed as:

$$dF_x = dT_s - dD_{camber} - dD_f - dD_{tail} \quad (46)$$

The baseline modified strip theory model used thus far determines if flow separation occurs following a helicopter analysis methodology that is unsuitable for the flapping wing case now examined. Therefore, an enhanced dynamic stall criterion is adopted from the model by Kim, Lee, and Han for large amplitude flapping [179] and based on experimental data collected by Scherer in characterizing oscillating airfoils [174]. The dynamic stall condition is defined in Equation 47 with the dynamic stall correction factor defined in Equation 48 as a function of both plunging and pitching. The static stall angle α_{stall} is specified as 0.227 rad in both the positive and negative directions.

$$\alpha_{dyn} = \xi_{max}\alpha_{stall} \quad (47)$$

$$\xi_{max} = \begin{cases} 1 + \dfrac{\left|tan^{-1}[\dot{h}\cos(\theta - \bar{\theta}_a)/V_x]\right|}{|\alpha_{stall}|} + \dfrac{0.51\dfrac{\theta}{|\dot{\theta}|}\sqrt{\dfrac{c|\dot{\theta}|}{2U}}}{\alpha_{stall}}, & \alpha_{dyn} \geq 2\alpha_{stall} \\ 2, & \alpha_{dyn} < 2\alpha_{stall} \end{cases} \quad (48)$$

The method of force application is dependent on flow condition at each time step. The attached flow condition is presented in Equation 62. As the flow transitions from attached to a dynamic stall and then poststall, the method of force application is altered according to the diagram in Figure 5.20.

$$\left|\alpha' + \bar{\theta} - \frac{3}{4}\frac{c\dot{\theta}}{U}\right| \leq \alpha_{dyn} \qquad 49$$

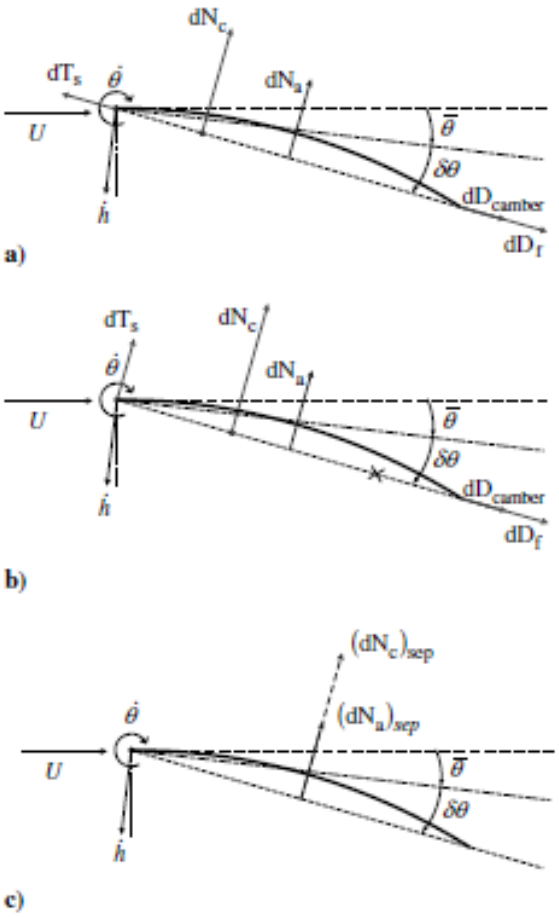

Figure 5.20: Sectionwise forces during a) attached flow, b) dynamic stall, and c) poststall from [179]

With attached flow, circulatory forces act at the quarter chord point, added mass acts at the half chord point, and chordwise forces act along the wing chord. In the case of dynamic stall, the leading-edge suction force shifts to the wing normal direction and the circulatory force moves to the 1/3 chord location. Finally in separated flow conditions, all chordwise forces vanish and all normal forces act at the half chord point.

The forces in the stall regimes are calculated as follows. The added mass in separated flow is assumed to be half the value calculated for attached flow. The circulatory normal force during flow separation arising due to crossflow drag is presented in Equation 50, with the poststall normal force coefficient $(C_d)_{cf}$ chosen as 1.98 as suggested in [134]. The V_x term is again the flow speed tangential to the current strip, approximated using the first bracketed term of Equation 38. The velocity magnitude due to wing motion $\hat{V}$ is given by Equation 51.

$$(dN_c)_{sep} = (C_d)_{cf} \frac{\rho \hat{V} V_n}{2} c dy \quad (50)$$

$$\hat{V} = (V_x^2 + V_n^2)^{1/2} \quad (51)$$

The forces for each strip in the normal and chordwise directions are resolved into lift and thrust forces at each time step based on the wing positions according to Equations 52 and 53.

$$dL = dN cos\theta + dF_x sin\theta \quad (52)$$

$$dT = dF_x cos\theta - dN sin\theta \quad (53)$$

The total lift and thrust are then calculated by integrating the spanwise strips according to Equations 54 and 55, where γ is the instantaneous dihedral angle and b is the span.

$$L(t) = 2\int_0^{b/2} \cos(\gamma) dL \tag{54}$$

$$T(t) = 2\int_0^{b/2} dT \tag{55}$$

The power on each spanwise strip for each instant is calculated using Equation 56 for attached flow and Equation 57 for separated flow, and the total power is calculated using Equation 58. The section's pitching moment due to apparent camber and apparent inertia moments dM_a is given by Equation 59, and dM_{ac} is the section airfoil's pitching moment about its aerodynamic center.

$$dP_{in} = dF_x \dot{h} sin(\theta - \bar{\theta}_a) + dN(\dot{h} cos(\theta - \bar{\theta}_a) + \frac{1}{4} c\dot{\theta}) + dN_a \frac{1}{4} c\dot{\theta} - dM_{ac}\dot{\theta} - dM_a\dot{\theta} \tag{56}$$

$$(dP_{in})_{sep} = dN_{sep}\left[\dot{h} cos(\theta - \bar{\theta}_a) + \frac{1}{2} c\dot{\theta}\right] \tag{57}$$

$$P_{in} = 2\int_0^{b/2} dP_{in} \tag{58}$$

$$dM_a = -\left[\frac{1}{16}\rho\pi c^3 \dot{\theta} U + \frac{1}{128}\rho\pi c^4 \ddot{\theta}\right] dy \tag{59}$$

The basic framework used for aerodynamic modeling and dynamic stall modeling has been presented here for completeness and to clarify where different aspects of each model have been utilized, especially with respect to the stall modeling. Highly detailed

treatments of the modified strip theory aerodynamic model as well as the dynamic stall corrections applied are available from the respective authors, including several illustrations depicting the terms in the equations used and experimental validation studies [134, 179].

5.4.3 Improved Wing Motion Prediction with Strip Theory Coupled to Motor Model

In the previous sections, a vortex ring model has been used to provide an estimation of the expected power consumption in cruising flight, and the model has been validated for certain conditions using an on-vehicle instrumentation system. The predictions did provide insight into the intra-flap variation in loads encountered, therefore a logical next step is to extend to a modeling approach that accounts for the evolution of a broad variety of vehicle conditions within each flapping cycle, including the effects of specific trim or flapping motions that may not conform to the model assumptions used in the previous section.

Accounting for these effects is possible using a modeling approach originally intended for propeller analysis, strip theory. This approach divides the lifting airfoils into spanwise strips, assumes quasi-steady aerodynamics at each time step, and generates performance estimates by integrating across span and time variables. Accurate modeling with strip theory requires a good description of the airfoil shape as well as accurate specification of the flow conditions that the airfoil is exposed to. In contrast

with the continuous rotation of a rigid propeller, the periodic plunging of flexible flapping wings necessitates some modifications to the traditional strip theory model to account for the unsteady conditions encountered. This unsteadiness gives rise to a challenge in the application of this modeling approach to flapping wings, as the model must properly account for the wing shapes during the flapping cycle at each time step.

Traditionally, flapping wings modeled with strip theory have kinematics that are specified in plunge and twist as sinusoids with a phase offset. Here, a new model for the aerodynamics and dynamics of flapping wings is developed to improve motion predictions beyond a simple sinusoidal specification. Unlike previous work, drive motor constraints on torque and speed are included. This enables the wing motion to be computed by enforcing feasible motor bandwidth at each time step instead of simply prescribing plunge and twist motions. The deflection properties of the wing spars are captured in a dynamic model that is used to improve correlation between experimentally measured flapping dynamics and the modeled flapping dynamics. This approach addresses the need for a simultaneous consideration of motor bandwidth and flapping loads, since their interaction will have strong effects on overall flapping wing performance. A strip theory modeling framework modified for flapping wings is used to predict aerodynamic loads, and therefore is dependent on experimental validation data to tune the model parameters. Using experimental data collected with the instrumentation suite already presented, model parameters are tuned to enforce feasible operational conditions. The model predictions show that flapping motions realized in

flight testing deviate from commanded sinusoidal motions due to interactions between the drive motors and wing loads. The new model for wing motions is coupled to the strip theory aerodynamic model to determine the improvement in prediction accuracy that can be achieved by including component interactions to enforce realistic wing motions with respect to drive motor constraints.

The strip theory aerodynamic model is a valuable tool for making predictions in an efficient way as several operational characteristics may be varied relating to the vehicle trim, wing properties, and flapping motions. However, the model is only useful if the parameters that describe the vehicle are sufficiently accurate. Ultimately, it is desired to make predictions about how the motor and wings will perform when considered together. Therefore, a wing component model is required that captures the important interactive effects between wing design, flapping motions, and force production. At present, models used to describe flapping wings such as [134] do not appropriately capture the interaction between flapping motions and wing compliance and loads. In particular, two key deficiencies exist. First, sinusoidal flapping is frequently assumed, with plunge and twist motions modeled using only a few parameters including plunge amplitude A and spanwise twist amplitude β.

While sinusoidal flapping motions are a reasonable approximation and lead to simplified expressions for wing motions, this assumption does not consider the retarding effect of wing loads interacting with drive motors that have finite bandwidth.

When the wing loading is considered together with the motor capabilities, the realized motion is augmented based on the wing size and motor bandwidth and no longer may be assumed to be sinusoidal. The second deficiency in existing models is the static wing shape specification, which assumes a constant linear wing twist and does not accurately describe the behavior of a flexible wing that deforms in response to flapping and structural loads. Accounting for these deficiencies will improve the aerodynamic model quality by ensuring real-world effects are appropriately considered in performance predictions.

In Figure 5.21 the plunge motions are shown for each wing while flapping at 4.0 Hz. A counter-intuitive effect takes place during pronation and supination where the larger wings are able to reach higher speeds and reduce the phase gap relative to the smaller wings. Following these portions of the flap cycle, the power stroke exhibits the expected behavior of larger wings falling behind the smaller wings due to larger loading arising from flapping a greater surface area. In addition, the motions measured for each wing are different than the pure sinusoidal motion that is commanded. The dynamic deformation of the wing spar structure in response to loading will be explored in this section to provide more a more accurate representation of flapping motions in the aerodynamic model.

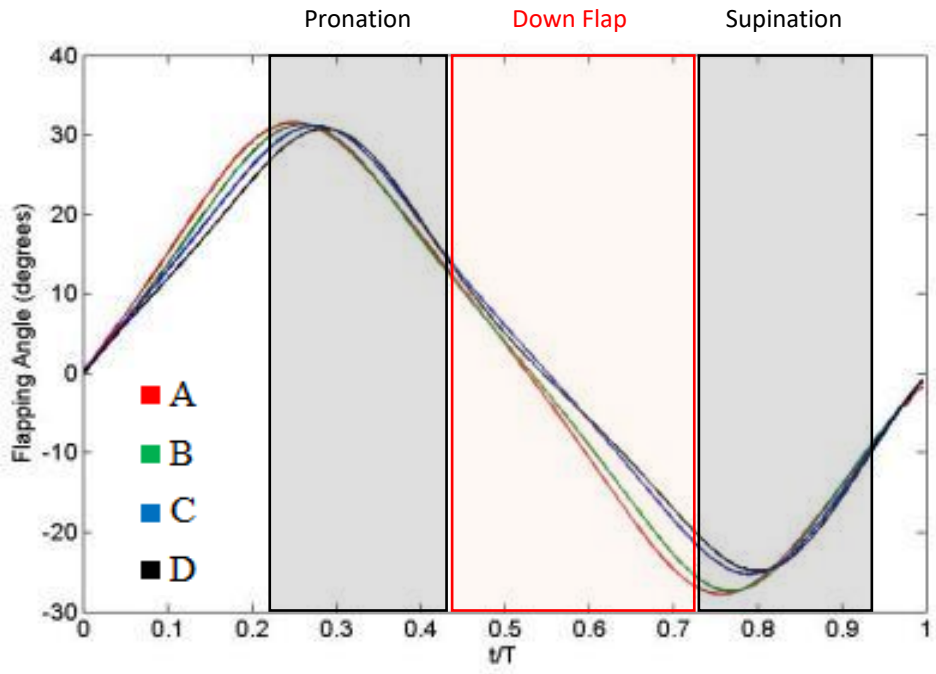

Figure 5.21: Wing angle tracking during load cell testing

The wing deformation has two separate modes that depend on flapping velocity and wing stiffness. The first is the primary bending mode, which consists of the wing spars flexing perpendicular to the wing surface in response to loading. The second is a twisting mode relative to the primary leading edge spar that occurs during stroke reversal. The bending mode controls drag which causes a torque load at the motor that scales linearly with flapping velocity and wing size, and remains in phase with the flapping velocity. To illustrate this effect, the torque required by the motor to drive each wing design at varying steady state angular velocity was recorded to establish the relationship between wing size and drag. A regression for each wing design is plotted

in Figure 5.22. The coefficients describing the relationship between wing size, flapping velocity, and torque required are listed in Table 5.7. Overlaid on the plot is the bandwidth for the Futaba S9352HV servo, which bounds a region of feasible operation for each wing size. Any operational conditions that fall below and to the left of this line are reachable by a given wing design.

Table 5.7: Torque required for each wing design in steady state plunge motion

Wing	**Area m^2**	**Torque Constant N-m-s/rad**
A	16.40E-2	59.45E-3
B	22.13E-2	11.27E-2
C	26.25E-2	14.39E-2
D	32.90E-2	20.02E-2

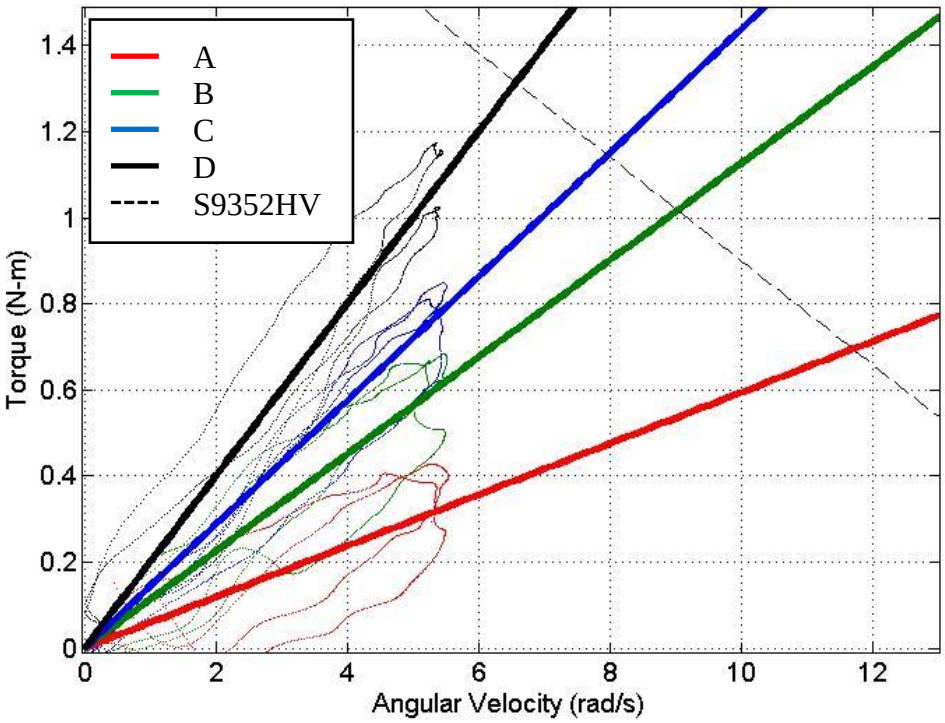

Figure 5.22: Torque required to flap each wing design from Table 5.7

In Figure 5.23, the angular velocity is plotted for wing D at the 1.0 Hz and 4.0 Hz flapping rates. The angular velocities corresponding to commanded kinematics are plotted as solid lines while the measured angular velocities are plotted as dots. The overlaid dashed lines are the torque limitations for the wing as shown in Figure 5.22. Two important effects may be observed in this plot. First, the motor is able to exactly reach the commanded kinematics as long as torque is maintained below the motor bandwidth. This is clear in the 1.0 Hz flapping condition where the commanded and actual motions are indistinguishable. However, as the commanded kinematics become more demanding, the motor bandwidth creates a limit on the reachable angular velocity.

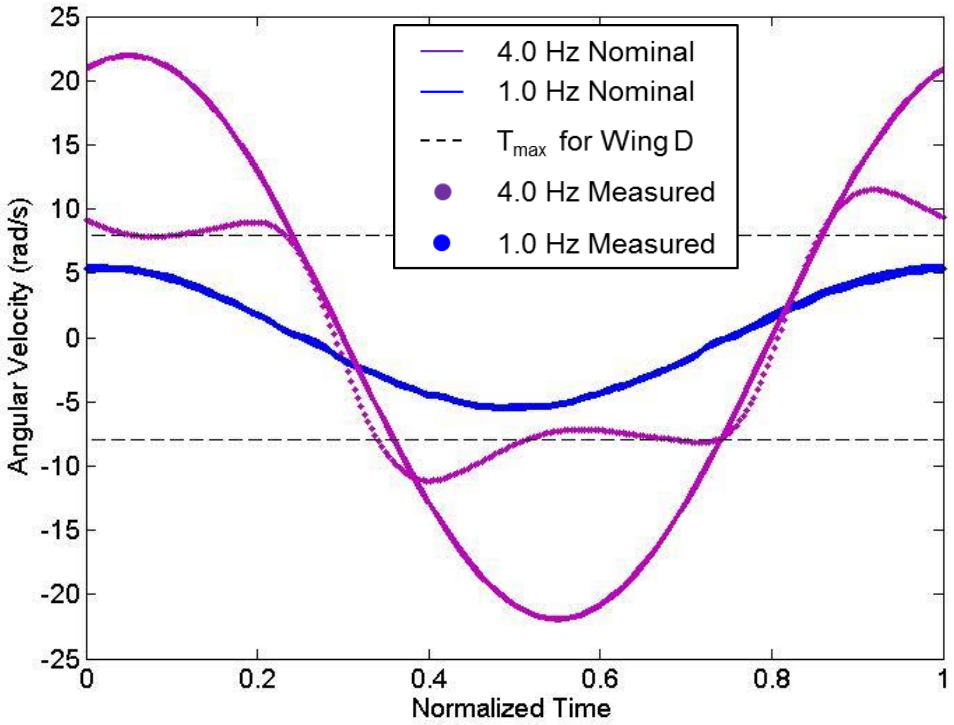

Figure 5.23: Comparison between actual and commanded angular velocity for wing D

In Figure 5.24, wing D angular velocity test results are shown for a range of flapping rates. At flapping rates below 1.5 Hz, there is a smooth sinusoidal velocity profile because the kinematics are not sufficiently demanding to exceed motor bandwidth. Beyond 1.5 Hz, the motor bandwidth limit is reached, however the angular velocity is not strictly limited by the theoretical maximum speed dictated by motor bandwidth. The angular velocity exhibits an overshoot effect that causes higher flapping velocity for brief periods. High speed videography was used to investigate the underlying

physical reason for this effect. A series of snapshots from one flap cycle are shown in Figure 5.25.

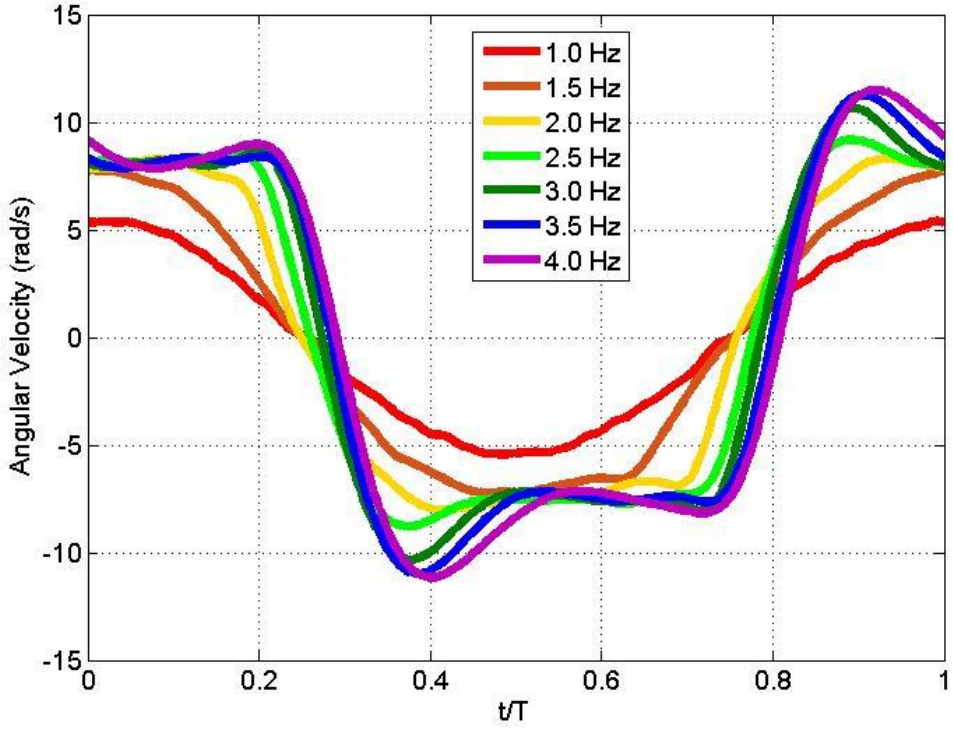

Figure 5.24: Angular velocity for D wings across flap rates

In the video snapshots, the flapping motion starts with the top row moving from left to right, then the bottom row moving from left to right. An upstroke is in progress in the top left frame. Moving along the top row, the upstroke is completed by the drive motor and hence the directly mounted primary wing spar reaches its apex in the fourth frame. On the fifth frame through the seventh frame, the wing is rotating as stored elastic energy is released, which aids the beginning of the downstroke by reducing torque

requirements temporarily. It is this rotational effect that augments the flapping velocity and causes the overshoot effect observed in Figure 5.23.

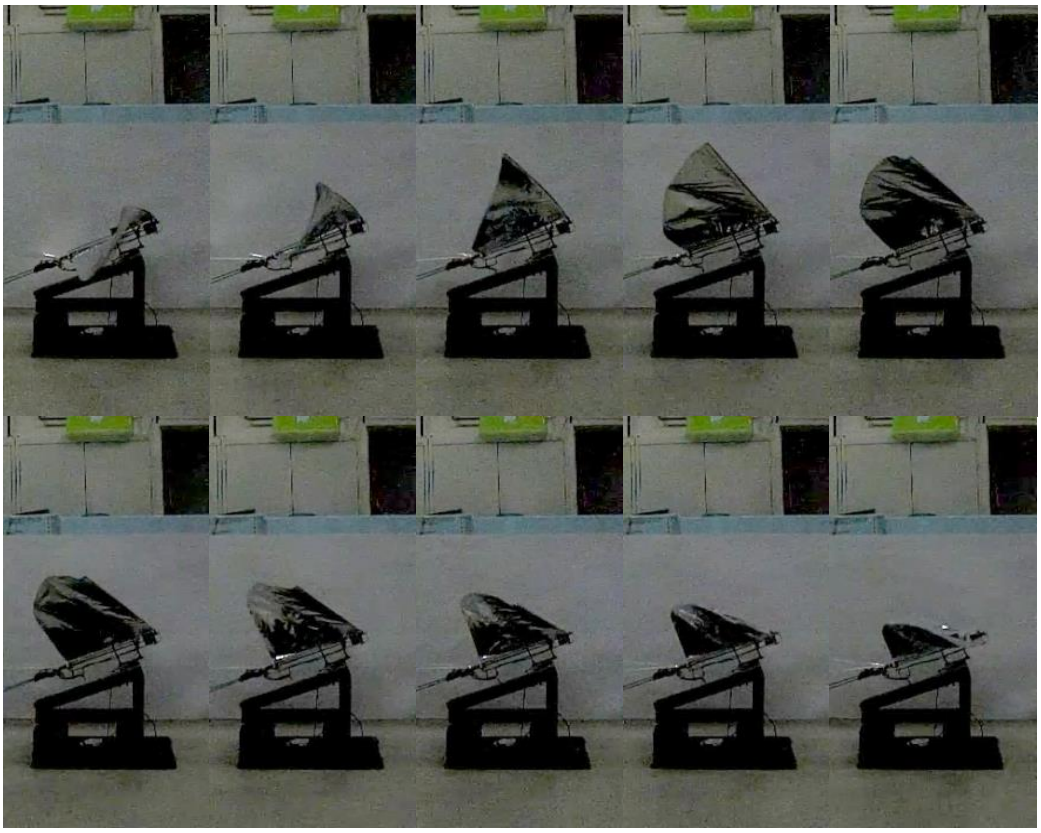

Figure 5.25: Images from high speed videography of wing D flapping at 4.0 Hz

The angular velocity results for each tested flapping rate are shown in Figure 5.24. Evidently the twisting effect causes overshoot that depends on flapping frequency. This becomes important when the wing stroke reversal rate approaches the natural wing twisting dynamics. Once these two effects begin to overlap the torque requirements are

reduced because the wing is exhibiting dynamic twisting and releasing stored elastic energy that aids the stroke reversal.

The twist dynamics are accounted for in the wing model by introducing several corrections to the nominal kinematics. To set up these corrections, first a notional wing system model is constructed as shown in Figure 5.26. In this model the two axes are defined as the primary flapping axis $\hat{f}$ and the wing twist axis $\hat{t}$. The two generalized coordinates that describe wing motion are θ_f and θ_t, which are the angle of the primary spar at the leading edge of the wing relative to the horizontal and the wing twist angle relative to the plane that includes the leading edge spar and the flapping axis. The energy system of the wing is modeled using torsion dampers attached to the flapping axis and the twist axis, a torsion spring attached to the twist axis, and a rotational inertia J with components in the flap and twist axes. Functionally, the effect of this model framework is that the wing plunging motion exhibits a dependence on the interaction between the flap rate, the wing size, and the twist stiffness.

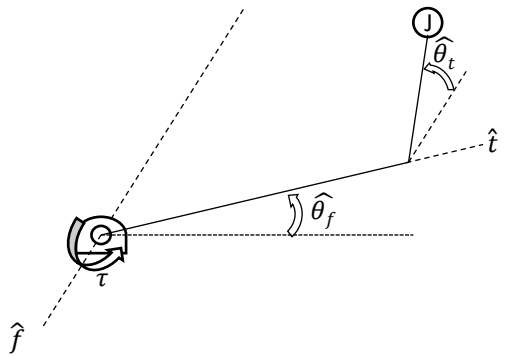

Figure 5.26: Wing energy system model

Using this model framework, the wing plunge rate is increased by the twist dynamics based on the interaction between wing natural frequency and flapping rate. As the flapping rate overlaps the wing natural frequency, the amount of twist will increase resulting in higher velocity peaks in plunge. To capture this effect, the wing natural frequency is described using an empirical relationship based on the wing design used. The primary structure resisting wing twist is the bending deformation of the spars in the chord-wise direction, therefore the twisting stiffness is modeled as proportional to cantilevered beam bending as described in Equation 60. Since each wing uses constant spar sizes of the same carbon fiber material, the elastic modulus and second moment of area terms are lumped together with the constant K_t to capture bending physics and the empirical constant of proportionality together.

$$K_t = \frac{3EI}{L^3} C \tag{60}$$

Combining the mass of each wing listed in Table 4.2 with the empirical stiffness relationship results in the wing natural frequency in Equation 61.

$$\omega_{n\hat{t}} = \sqrt{\frac{K_{\hat{t}}}{m}} \tag{61}$$

The twist is modeled as a damped vibratory system with damped natural frequency given by Equation 62.

$$\omega_{d\hat{t}} = \omega_{n\hat{t}}\sqrt{1-\zeta^2} \tag{62}$$

The solution for the homogeneous displacement response is shown in Equation 63.

$$\theta_{\hat{t}}(t) = \theta_0 e^{-\zeta\omega_{n\hat{t}}t}\cos(\omega_{d\hat{t}}t) + \frac{\dot{\theta}_0 + \zeta\omega_{n\hat{t}}\theta_0}{\omega_{d\hat{t}}} e^{-\zeta\omega_{n\hat{t}}t}\sin(\omega_{d\hat{t}}t) \tag{63}$$

The initial twist condition θ_0 is estimated using high speed photography to determine the wing twist for each wing tested as a function of flapping rate. A snapshot of this testing is shown in Figure 5.27.

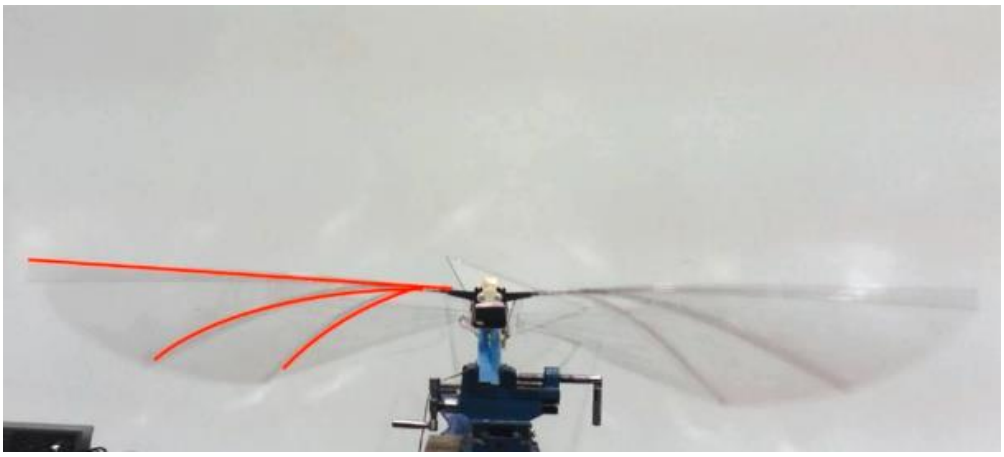

Figure 5.27: High speed photography used to characterize wing twist amplitude

The damping ratio ζ is estimated in Equation 64 as a function of flap rate per wing using the percent overshoot observed in Figure 5.24 following the relationship in Equation 64 [180], where the overshoot is measured by comparing the peak plunge rate achieved during pronation to the steady state plunge rate limit after velocity ringing settles. The results of damping ratio calculations are compiled in
Table 5.8 below for each wing size tested.

$$\zeta = \sqrt{\frac{(ln\frac{PO}{100})^2}{\pi^2 + (ln\frac{PO}{100})^2}} \quad (64)$$

Table 5.8: Wing twist damping ratio results

Wing	$\dot{\theta}_{max}$ (rad/s)	$\dot{\theta}_{ss}$ (rad/s)	% Overshoot	ζ
A	9.49	9.47	0.20	0.96
B	10.38	9.37	10.80	0.58
C	10.96	9.12	20.18	0.45
D	11.48	8.41	36.50	0.31

In the following figures, the plunge angle and wing twist augmentation model is plotted for each of the four tested wings along with the commanded and experimentally measured angular velocity for wing D at 4.0 Hz flapping. The early inaccuracy in the model is due to a brief transient effect that settles quickly and results in a much closer fit to actual flapping conditions by accounting for the interaction of the wing stiffness, twisting, and flapping kinematics. A summary of the error properties of the model is presented for each wing in Table 5.9.

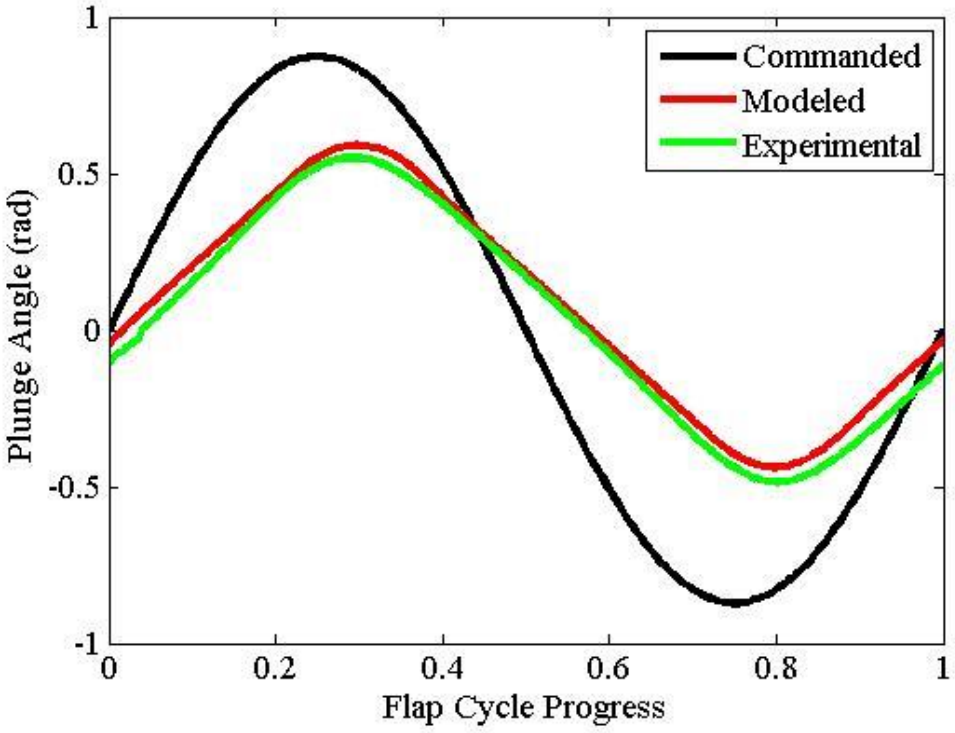

Figure 5.28: Augmented plunge angle model for wing A

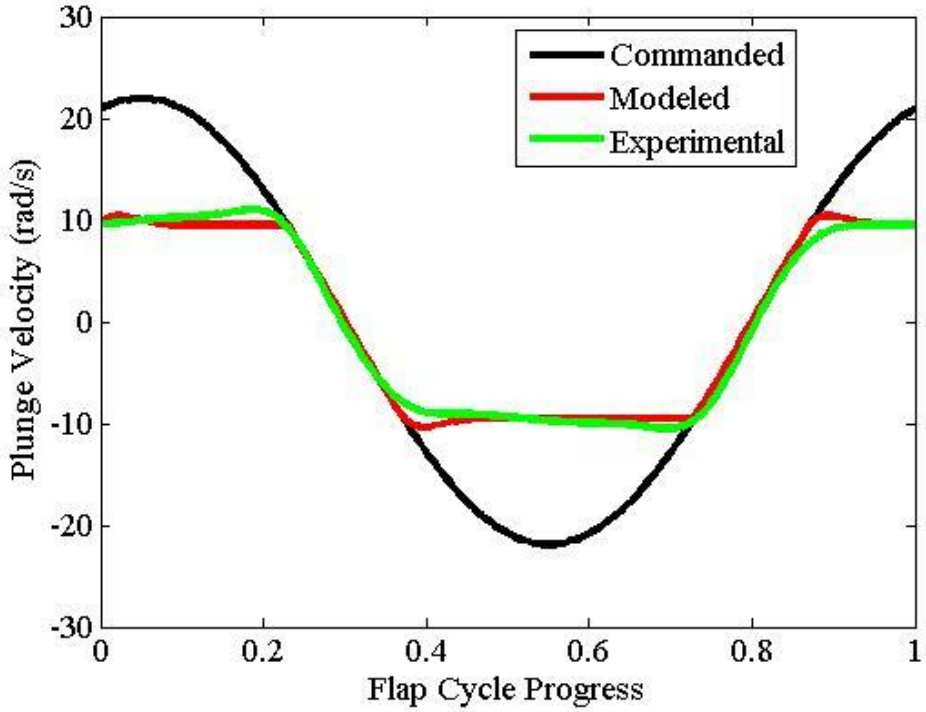

Figure 5.29: Augmented plunge rate model for wing A

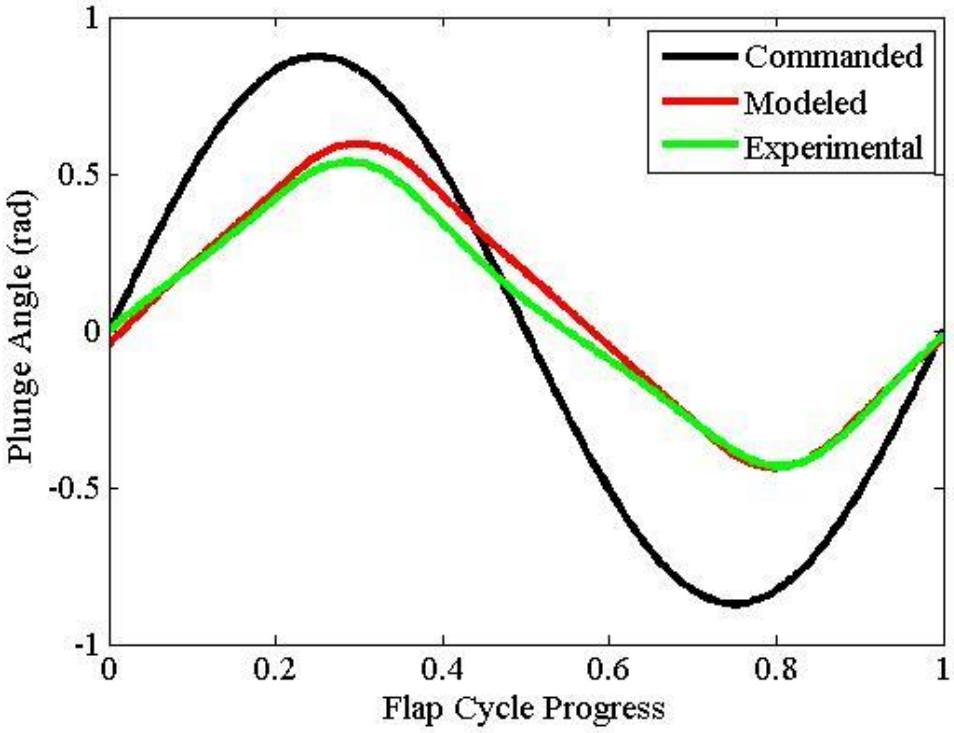

Figure 5.30: Augmented plunge angle model for wing B

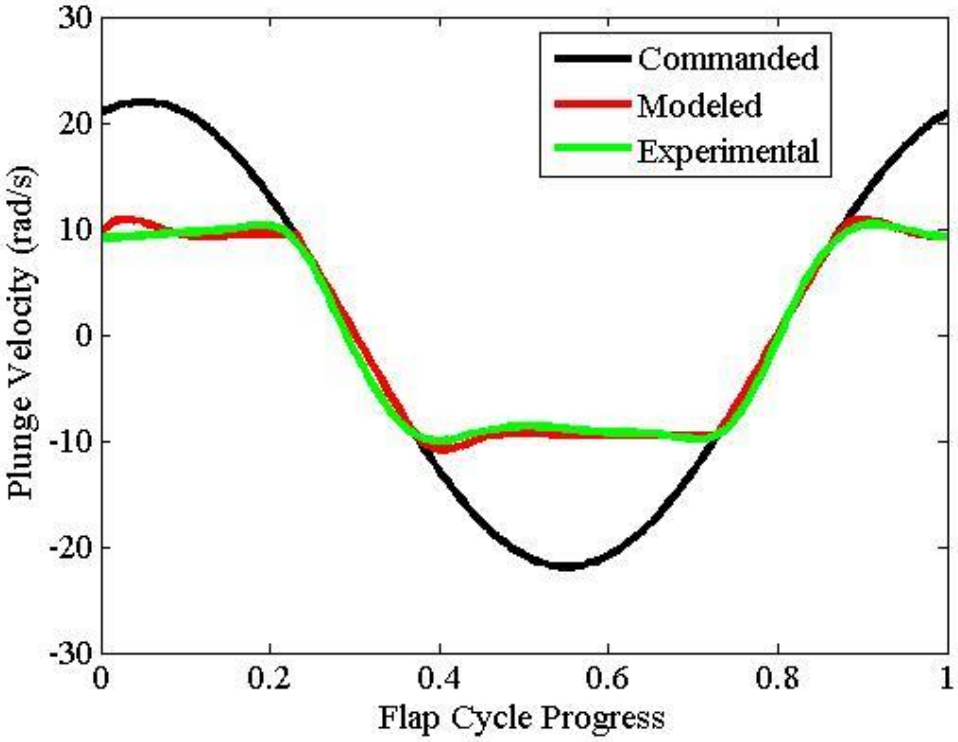

Figure 5.31: Augmented plunge rate model for wing B

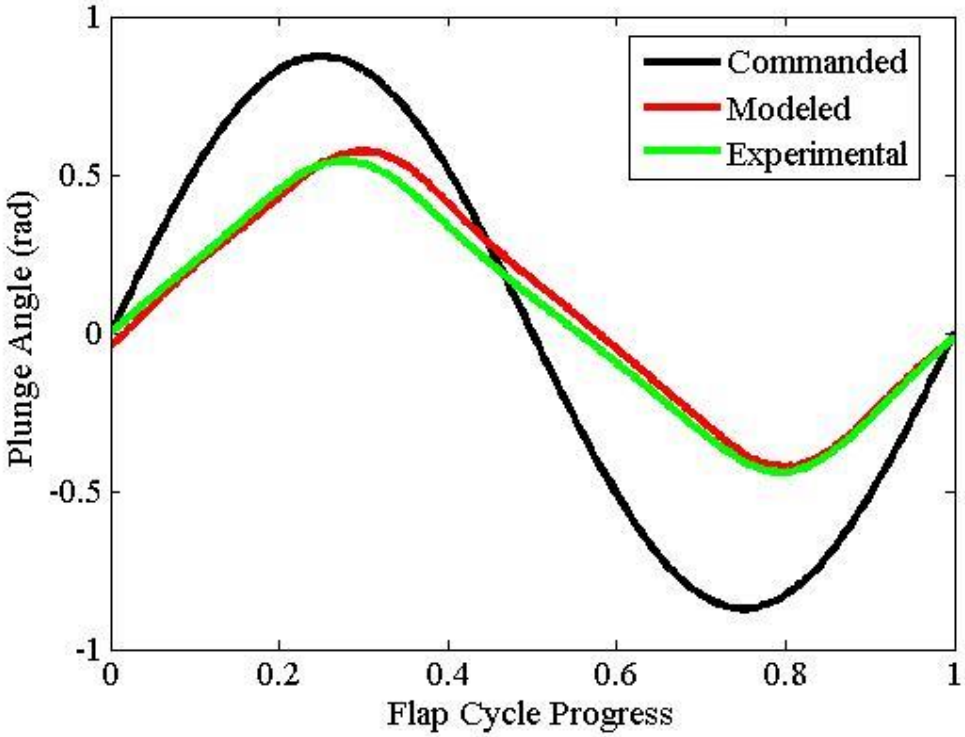

Figure 5.32: Augmented plunge angle model for wing C

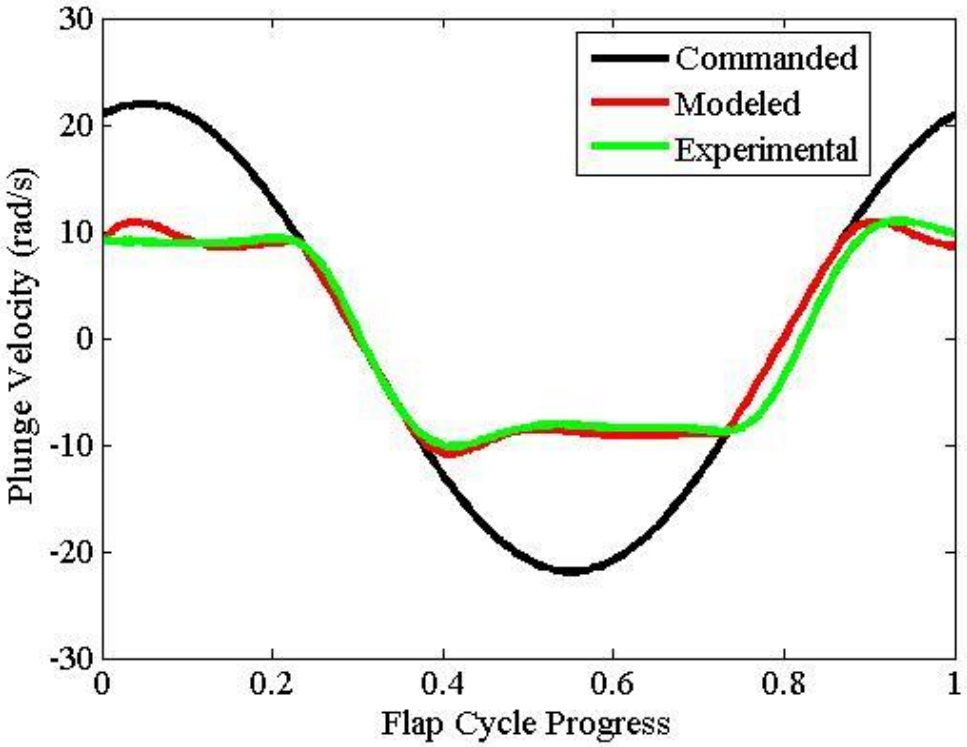

Figure 5.33: Augmented plunge rate model for wing C

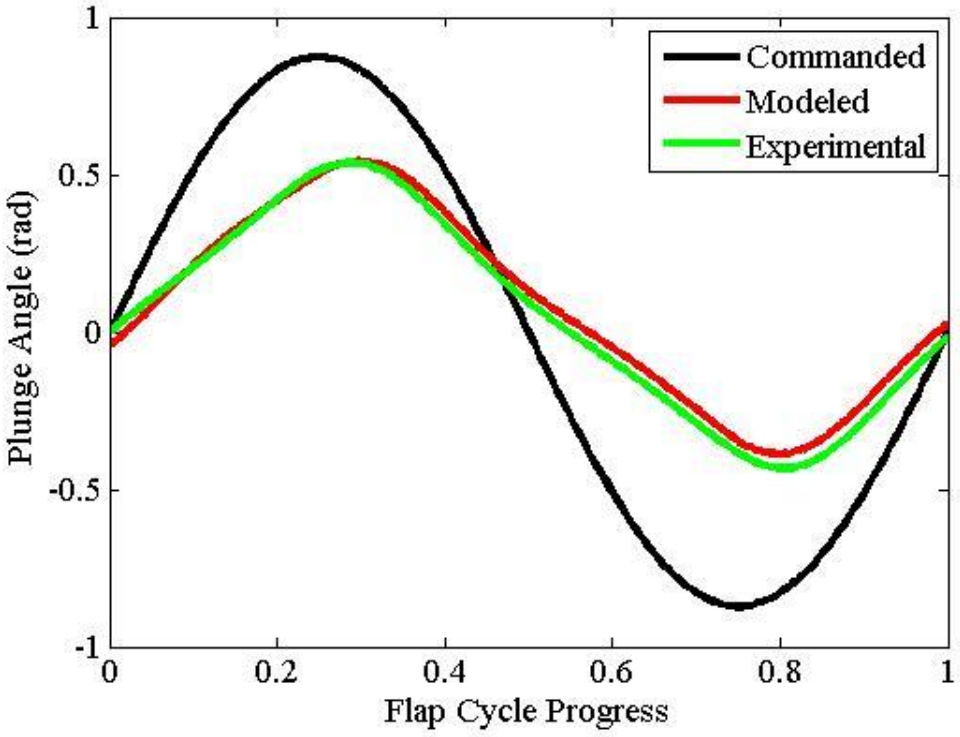

Figure 5.34: Augmented plunge angle model for wing D

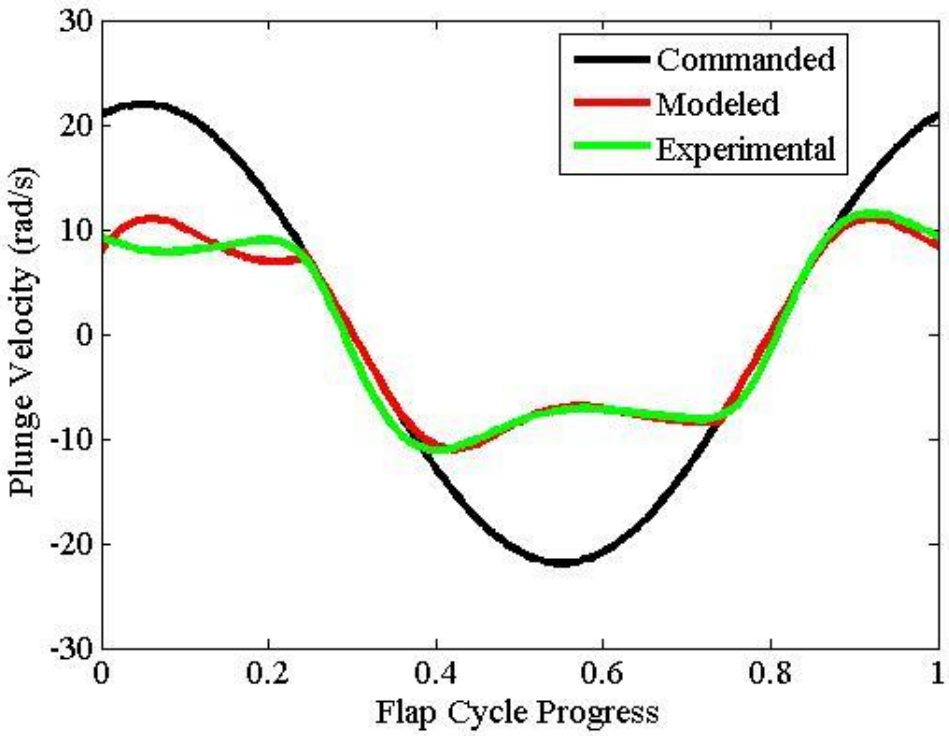

Figure 5.35: Augmented plunge rate model for wing D

Table 5.9: Error comparison in modeled plunge kinematics

	Model Result			
	RMS Position Error (rad)		RMS Velocity Error (rad/s)	
	Commanded	Experimental	Commanded	Experimental
Wing A	0.318	0.046	7.365	0.823
Wing B	0.325	0.048	7.692	0.748
Wing C	0.316	0.039	8.114	0.916
Wing D	0.325	0.037	8.378	1.143

The flapping wing system is modeled by creating a linkage between the strip theory model and the motor torque model to perform feasibility checking at each time step as shown in in Figure 5.37. This is realized by computing the aerodynamic loads and flapping speeds associated with nominal flapping profile, mapping the loads to a torque and angular velocity bandwidth for the drive motors, and using feedback control to correct the flapping profile until feasible motor operation is achieved. If the loads are either too large to be driven at the current speed or less than what the motor is capable of, the plunge rate is reduced and forces recomputed until the solution converges to agreement between the two models, which prevents violation of the feasibility constraint. In this way, the modeling approach is a reflection of the digital control system used by the drive servo to minimize position error. This approach is a new strategy to modeling wing dynamics in flapping wing air vehicles, since wing motions are predicted at each time step by considering the interactions between the motors and wings. In contrast, the traditional strategy has been to design a flapping mechanism which follows specified flapping kinematics and to represent the same kinematics exactly in the modeling without corrections due to motor loading conditions or wing dynamics.

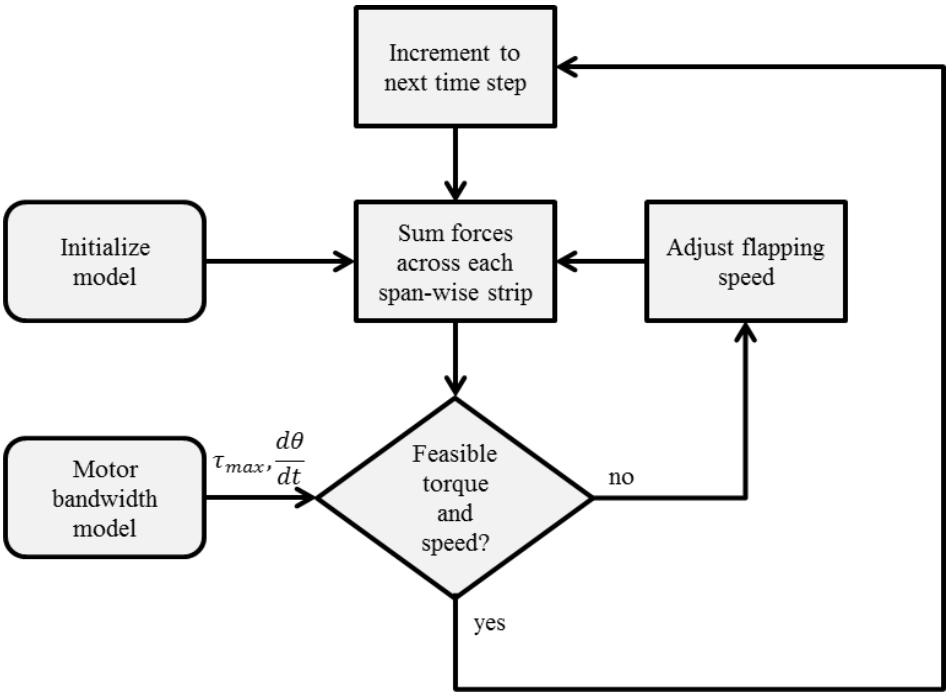

Figure 5.36: Strip theory model feasibility checking

Each of the typical flight conditions corresponding to wings A through D were modeled using the aerodynamic code combined with the wing twist model and motor constraints to establish model capabilities in describing real flight conditions. The flight testing parameters were entered into the aerodynamic model to check the ability of the model to describe known flight-worthy conditions, and to identify areas requiring tuning. A comparison of the flight test results to the modeled results both with and without the kinematic corrections is shown in Table 5.10.

Table 5.10: Comparison of model results to flight testing data

	Flight Testing				Coupled Model (Developed in this paper)				Kinematics Only			
	A	**B**	**C**	**D**	**A**	**B**	**C**	**D**	**A**	**B**	**C**	**D**
Avg. Lift (N)	-	-	-	-	2.50	3.08	3.19	3.31	2.51	4.03	4.75	6.42
Avg. Thrust (N)	-	-	-	-	1.16	1.15	1.37	2.19	1.16	2.88	3.95	7.15
Avg. Power (W)	13.6	15.1	15.9	17.6	12.9	18.3	20.0	22.1	13.0	29.8	39.9	70.9
Avg. Torque (N-m)	0.99	1.05	1.06	1.17	0.70	1.02	1.15	1.31	1.43	2.30	2.70	3.64
Max. Plunge Rate (rad/s)	14.69	14.04	13.60	12.61	16.69	15.02	12.96	11.56	20	20	20	20

In the comparison, lift and thrust data are not populated for the flight test results since these are not directly measurable from the instrumentation suite. In the coupled model results, the inclusion of wing dynamics and a motor feasibility constraint causes a size-dependent reduction in the power predictions. This results in model conditions that much more closely track the behavior exhibited during the flight testing trials. For comparison, the model results that specify flapping kinematics without any modifications may be thought of as estimating the requirements to drive a given wing at exactly the nominal flapping kinematics. The corrected data presents an estimate of the achieved performance given the interactions between the selected components. The

major reason underlying the improvement in the coupled model is the reduction in required motor bandwidth. The torque requirements necessary to achieve sinusoidal flapping kinematics are far beyond the capability of the motors selected, as shown by the discrepancy between commanded and experimental motions in the plunge plots for each wing shown in the previous section. In addition, the kinematics-only model prescribes the same sinusoidal flapping motion across each wing size, despite the large differences in loading that must be overcome by the motors as wing area increases. With the modified wing motion model, the plunge velocity is reduced to a feasible condition that places the operation of the motor within feasible bounds and ensures that modeled kinematics are more representative of real flight conditions.

Chapter 6: Performance Estimation Using Coupled Dynamic Component Models

6.1 Modeling Strategy Overview

In the previous chapter, it was demonstrated that by coupling the prediction of aerodynamics to constraints that are imposed by the drive motors, the accuracy of modeled wing kinematics may be improved. However, a few gaps remain to be addressed in that modeling approach. Primarily, it does not provide a strategy for simulating the evolution of vehicle properties throughout a flight, since it is solving for operational conditions only in a particular steady condition across one flap cycle. By expanding upon that approach to include the dynamic effects taking place in each vehicle component, the predictive utility and accuracy may be improved by including the ability to observe how the vehicle behavior changes throughout a flight, rather than only during a particular point in time.

This chapter develops a simulation framework that addresses this need and provides insight into design functionality by linking together aspects of previously developed work with dynamic component models. The focus is on the key components that dictate vehicle performance: (1) the actuator, (2) the battery, and (3) the wings. To this end, the flapping wing design problem is decomposed into key subproblems that are each important to the system-level performance, and are inherently coupled:

(1) Propulsion system selection and characterization

(2) Wing design and sizing

(3) Flapping frequency and amplitude selection

(4) Battery sizing

Using this decomposition makes the design problem more tractable, and highlights how the components are dictating system performance. First, the actuator selection is necessary to constrain the design space, based on knowledge of the desired vehicle performance attributes, comparison to some natural and man-made designs, and some simple motor power and efficiency criteria. This initial selection sets up several important design constraints that may be used to make subsequent design decisions, and since this component will generally be a discrete design, it is a logical starting point to the vehicle design. These procedures were presented in Chapter 4 and Chapter 5 as the servos were characterized using experimental and modeling techniques. Following the motor selection, the flapping profile and optimal wing design and sizing need to be determined for the characteristics of the motor. Too large of a wing will require more torque than the motor can produce at a given flapping frequency and amplitude, while too small of a wing will require flapping frequencies and amplitudes with associated angular velocities that are beyond the capabilities of the motor. Furthermore, to generate more torque and angular velocity typically requires a more massive motor drawing more power, which requires more massive power components, which in turn

requires the wing to be capable of generating enough lift to carry the mass in-flight for a given flapping profile. This defines part of the tradeoff space for the design problem. For proper wing design, the ability to make aeroelastic predictions across several design parameters is required to ensure compatibility between the motor choice and the wing and flapping motions. The results in the previous chapter highlighted how this interaction leads to performance augmentation that needs to be considered for accurate wing motion predictions. Together, these requirements led to the overall approach to systematic analysis of the design problem shown in Figure 6.1. Given some wing design for FWAVs that has a mass and stiffness distribution, an aeroelastic solver is initialized with a commanded plunge motion and trimmed flight condition. The aeroelastic solver uses a strip theory model to capture aerodynamics, and is modified with several unsteady terms that capture dynamic stall effects, apparent mass effects, and lift coefficient hysteresis effects. The solver provides estimates of forces and torques which are then corrected by a comparison to a drive system model containing two important effects. First, a motor model that contains the available motor bandwidth in terms of torque and speed, and second, a battery model that contains derating effects due to state of charge and high discharge rates that propagates into the motor model to update the available bandwidth. This inner loop is computed at each time step until convergence is obtained, then the expected charge depletion is used to update the battery model for the next time step. This procedure continues until the battery is sufficiently depleted to terminate the flight based on the reduction in available motor

bandwidth. Using this modeling framework, the components of the Robo Raven II are used to build up system-level performance estimates.

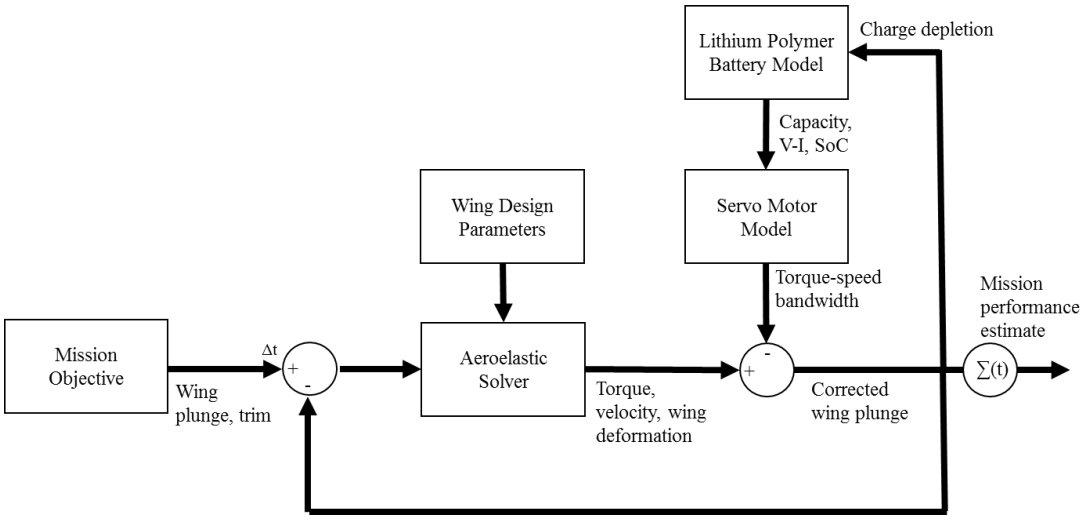

Figure 6.1: Proposed workflow for systematic analysis of flapping wing aerial vehicle performance analysis

6.2 Aeroelastic Model for Flapping Wings

The forces produced by flapping wings during flight depend primarily on the interaction between commanded flapping motions, power system bandwidth, and wing flexibility. Therefore, an aeroelastic model of the wing is required that couples to the battery and actuator models to ensure the forces acting on the wings balance the torque generated by the drive motor at the corresponding angular velocity. In Chapter 6, the importance of this concept was explored for a particular steady snapshot of flight conditions, and it was shown that actual wing kinematics and resultant forces differ

substantially from what would be expected from a prescribed sinusoidal wingbeat. By improving the kinematics of the wings, the predictive accuracy may be improved. However, that approach was based on observations of how the wings were moving and augmented wing motions using a simple spring-mass-damper approach, without providing a tight coupling between the forces and kinematics. In this chapter, that coupling is realized, such that the generality of the modeling approach may potentially be expanded beyond the range of wing designs that were physically observed thus far.

Here, the baseline aerodynamic modeling approach is again primarily adopted from the classic strip theory method, adapted to flapping wing flight. This modeling approach is widely used in flapping wing flight owing to its simplicity, ability to account for varying trim conditions, computational efficiency, and basic ability to account for unsteady aerodynamics, as would be expected due to cyclic wing heaving motions and rotations. Several key modifications will now be made to improve the predictions by enforcing drive system compatibility [181], while also adding more sophisticated unsteady aerodynamic predictions and a structural solver to compute elastic wing deformations in the loop using a boundary value problem solver, as detailed in [182]. These modifications are included to account for discrepancies between stiff and flexible wings as well as ideal and actual wing motions, and have been validated in a FWAV of similar scale and flight conditions [105].

The aerodynamic forces are calculated at each time step by solving for the normal and tangential forces as a function of the wing motions and deformations. The wings exhibit large deformations and extreme angles of attack during flight, therefore a lift model is required that can account for flow separation and post-stall behavior. The model presented in [183] and implemented for flapping wing flight in [184] offers one solution. In this approach, the coefficient of lift is calculated as:

$$C_L = \frac{\pi}{2}\sin[\alpha(1+\nu+2\sqrt{\nu})] \tag{65}$$

and the coefficient of moment about the aerodynamic center is calculated as:

$$C_{Mac} = \frac{\pi}{2}\sin[\alpha(1+\nu+2\sqrt{\nu})]\,[\frac{5+5\nu-6\sqrt{\nu}}{16}] \tag{66}$$

The sectionwise normal force and moment are then computed as:

$$dN = 0.5\rho V^2 c C_L + \frac{\pi}{4}\rho c^2[\ddot{\xi} + U\dot{\alpha} - (x_a - 0.25)c\ddot{\alpha})] \tag{67}$$

$$dM = 0.5\rho V^2 c^2 C_{Mac} + \frac{\pi}{4}\rho c^2\left\{U\dot{\xi} + \frac{(x_a-0.25)c\ddot{\xi}}{2} + U^2\alpha - c^2[\frac{1}{32} + (x_a-0.25)^2]\ddot{\alpha}\right\} \tag{68}$$

The terms that depend on the location of the aerodynamic center x_a account for added mass effects as detailed in [184]. In equation 65, the coefficient of lift depends on several tunable parameters that define the spatial and temporal characteristics of flow separation, as listed in Equation 69.

$$\tau_1 + \dot{\nu} = \nu_0(\alpha - \tau_2\dot{\alpha}) \tag{69}$$

This equation describes the movement of the flow separation position ν relative to the nominal position ν_0 using tunable time delays τ_1 and τ_2. For details about the derivation and usage of Equation 69 refer to [183].

Chordwise forces need to be calculated next. First, the leading edge suction force is computed as:

$$dT_s = \eta_s 2\pi(\alpha' + \bar{\theta} - 0.25\frac{c\dot{\theta}}{U})^2 \frac{\rho UV}{2} c dy \tag{70}$$

The chordwise drag induced by the flow's circulation around a cambered wing is computed as:

$$dD_{camber} = -2\pi\alpha_0(\alpha' + \bar{\theta})\frac{\rho UV}{2} c dy \tag{71}$$

Viscous chordwise drag is computed as:

$$dD_f = C_{df}\frac{\rho(Ucos\theta - \dot{h}sin(\theta - \bar{\theta}_a))^2}{2}cdy \quad (72)$$

Drag due to the tail is computed as an inclined flat plate, with the tail inclined relative to the fuselage:

$$dD_{tail} = C_{Dtail}\frac{\rho U^2}{2}A_{tail}\sin(\theta_{tail} - \theta_{body}) \quad (73)$$

Total force in the chordwise direction is computed as:

$$dF_x = dT_s - dD_{camber} - dD_f - dD_{tail} \quad (74)$$

Lift and thrust forces are calculated by resolving the normal and chordwise forces using the local angle of attack as:

$$dL = dNcos\theta + dF_x sin\theta \quad (75)$$

$$dT = dF_x cos\theta - dNsin\theta \quad (76)$$

The total lift and thrust forces are then calculated by integrating along the semispan at each instant, using flapping frequency normalized time units, as follows:

$$L(\phi) = 2\int_0^{b/2} \cos(\gamma)\, dL \tag{77}$$

$$T(\phi) = 2\int_0^{b/2} dT \tag{78}$$

$$\phi = \omega t \tag{79}$$

In order to calculate the structural deformations of the wings during each flapping cycle, the forces and moments are coupled to bending and twisting equations of motion as:

$$\begin{bmatrix} F_N \\ M \end{bmatrix} = \begin{bmatrix} \widetilde{m}_R & -\widetilde{m}_R x_e c \\ -\widetilde{m}_R x_e c & I_p \end{bmatrix} \begin{bmatrix} \dot{V}_N \\ \dot{\Omega}_c \end{bmatrix} + \begin{bmatrix} \eta\left(EI_b\dot{\xi}''\right)'' + (EI_b\xi'')'' - T\xi'' \\ -\eta\left(G\tilde{J}\dot{\theta}_s'\right)' - (GJ\theta_s')' \end{bmatrix} \tag{80}$$

In Equation 80, the normal force and local pitching moment are equated to a mass matrix multiplied by the accelerations plus a Kelvin-Voigt damping contribution controlled by the parameter η, as well as a wing tension term T. The wing tension *T* is a tunable parameter in this equation that may be used to explore the effects of varying wing stiffness, which offers an improvement over the more simplified modeling used in standard modified strip theory where a simple sinusoid is used to define wing twist, and spanwise bending is not considered. Suggested boundary conditions to apply in the solution of this system of equations are provided in [184].

The wing motions are initialized using a sinusoidal plunge profile representing commanded flapping, as was presented in Equation 28. The structural deformations set up by Equation 80 are then solved in the loop and used to modify the computed forces until convergence is achieved at each time step. The torque at each flapping cycle step ϕ is then computed as follows:

$$\tau = \int_0^{b/2} |y\, dN| \tag{81}$$

At each cycle step, if the torque and plunge velocity $\dot{h}$ violate the motor bandwidth constraint at the current battery voltage, the plunge acceleration is reduced, and the velocity and position are recalculated using successive integrations of the acceleration as shown in Equation 82, and the inner aeroelastic loop is re-run iteratively until convergence is achieved. The integrations are calculated using a trapezoidal rule implemented in MATLAB software.

$$h(\phi) = \int_0^{\phi-1} \dot{h}\, d\phi \tag{82}$$

The consequence of this formulation is to reduce flapping amplitude in response to increasing demands on the motors, as the commanded motions would result in infeasible loading conditions.

It is worth mentioning that this particular formulation for making kinematic corrections is somewhat customized for the Robo Raven II drive system, and will likely require modification for application by a typical flapping wing researcher who typically favor the much more efficient crank-rocker mechanism layout [151]. For a crank-rocker mechanism, infeasible loading conditions must be corrected with a reduction in the flapping phase step size $d\phi$. This change is required because the flapping amplitude remains constant as the motion ranges are locked in by the hardware design, for most typical examples [97]. Instead, the rate of traversal through the mechanically defined flapping path is retarded in response to excessive loading conditions. Put simply, the modeling approach must be chosen to maintain commanded flap rate in the Robo Raven II framework, and the modeling approach must be chosen to maintain hardware-designed amplitude in a standard design.

Throughout the simulation, it is necessary to enforce physically realistic flight conditions to ensure that the results remain reasonable. Especially in cases where little or no experimental data exists to tune the model parameters, this is a crucial check on the simulation. One means of performing this check is with the Strouhal number, defined as:

$$\sigma = \frac{Af}{U} \tag{83}$$

The Strouhal number describes the interaction of the vortices on the wings arising due to the relative magnitudes of forward and vertical wing velocities, and must remain within a narrow range of values to ensure efficient flight conditions. Here, selected bounds of 0.3 to 0.4 are enforced, chosen through an understanding of how the code functions. The upper limit on Strouhal number of 0.4 is selected because that is an approximate limitation on efficient operational conditions, as identified by biologists studying many species of flying and swimming animals [73, 76, 166]. Furthermore, in prior experimental trials with the Robo Raven, measurements have shown that typical cruising flights take place near a Strouhal number of 0.395. Flights in this regime are characterized by a large angle of attack, low velocity cruising flight with a high degree of stability and a tendency to self-level. At the lower end of the chosen subset of Strouhal numbers, some judgment was necessary to establish a reasonable bound since the same biological studies have shown animals that exhibit Strouhal numbers below 0.2. The trend in the simulation data indicated a sharp increase in predicted lift with lower Strouhal numbers, which is characterized by higher speed cruising, greater susceptibility to disturbances, and smaller flapping motions by stiffer wings. This style of flight will generally present greater demands on the pilot or flight controller to make course corrections, and require more control authority and precision to sustain straight and level flight. In previous experimental trials, attempts to push toward this operational regime result in unstable flights that cannot be sustained given the current design. This is likely due to the combination of light weight, large wing and tail surface

area, and single degree of freedom wings, which together necessitate a self-stabilizing design at lower speeds.

6.3 Simulation Results for Robo Raven II

The typical objective in wing sizing is to maximize lift, endurance, or find a favorable compromise between those two optima. Incorrect wing sizing results in a poor compatibility between the motor power band and the force productivity of the wings, and hence diminishes vehicle performance. To explore this relationship, the four wing designs A through D that have been studied in previous chapters are used with properties summarized in Table 6.1. These four wing designs are pervasive in this dissertation because they have been experimentally studied in detail in prior work, and are known to cover the entire feasible operational space of Robo Raven II given the current motor selection [124].

Table 6.1: Wing design parameters

Wing	Area (m^2)	Mass/wing (grams)	Semispan (m)	Chord (m)
A	0.117	12.7	0.508	0.292
B	0.176	19.4	0.622	0.357
C	0.202	21.0	0.667	0.383
D	0.264	25.4	0.762	0.438

The simulation framework is first used to perform battery sizing effects and generate initial estimates of performance for each of the four wing designs under consideration. Battery sizing is required to avoid two potential issues with the system design. First, in the case of a battery that is too small, motor current demands will drop voltage so far that flight becomes infeasible, despite the weight savings. Second, in the case of a battery that is too large, motor current will no longer induce significant voltage drops, however excessive mass will prevent flight. Making an appropriate selection for battery size is challenging because the battery performance, and therefore motor performance, depends on the state of charge, which is constantly decreasing during a flight. Therefore, the sizing decision must be made to provide maximum vehicle system-level performance through a favorable choice of component interactions. To explore these interactions, the simulation framework is used to generate a design tradespace across

battery capacities ranging from 400 mA-h to 1800 mA-h, in steps of 100 mA-h. In each simulation, flight conditions are calculated over a full battery discharge cycle. This approach provides a realistic estimate of vehicle performance, rather than a simplified calculation based on the quotient of battery capacity and a snapshot of power consumption. Trim conditions that provide maximum lift production are extracted, while also enforcing feasible bounds on both the Strouhal Number and the torque and plunge rate demanded by the drive motors.

The net lift predictions for wing A are plotted in Figure 6.2, calculated using the vehicle weight including the modeled battery capacity. No feasible solutions for a flying vehicle were found for this wing size, due to excessive motor bandwidth losses at the low end of evaluated battery capacities, and excessive weight with larger battery capacities. Some regions of the data that remain unchanging for significant portions of time are limited by simulation constraints on acceptable Strouhal Numbers, which enforce physically realistic flight conditions, despite the mathematics underlying the simulation suggesting that greater performance may be obtained. Wing A shows a monotonic decrease in lift production with larger battery capacity, indicating that the added mass of the battery is dominating the performance predictions.

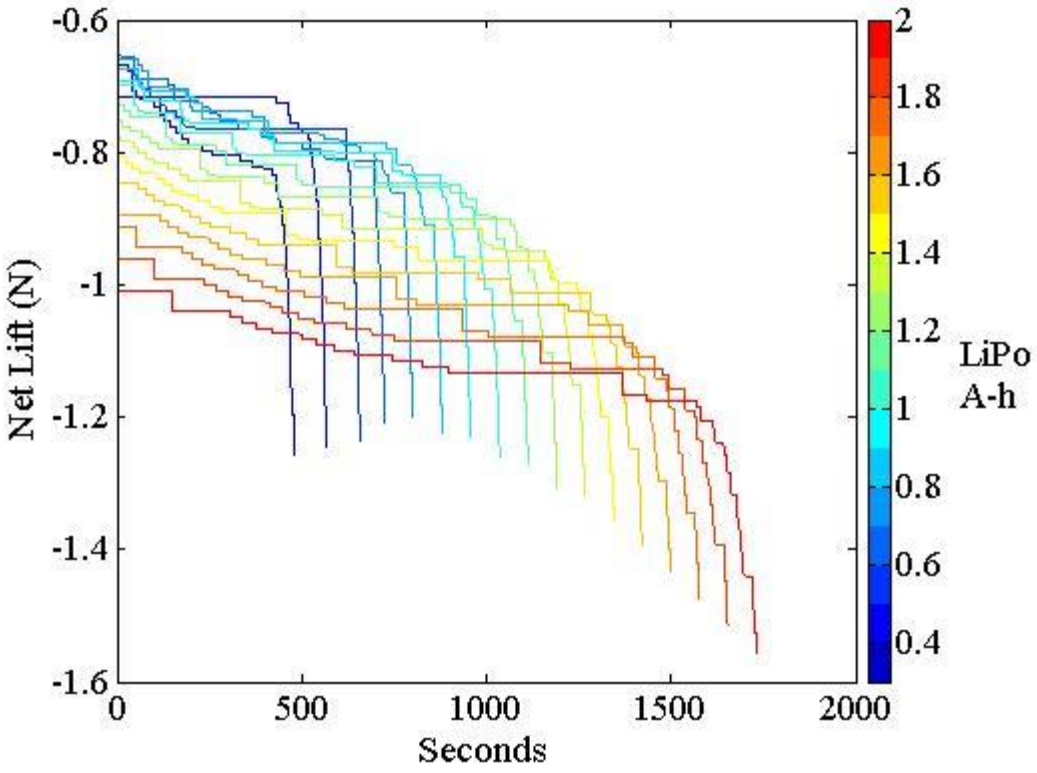

Figure 6.2: Wing A simulation results

The lift predictions for Wing B are plotted in Figure 6.3. This wing design is larger and presents greater loads to the drive motors, resulting in a voltage drop on the battery that alters the available torque and plunge rate more noticeably. In this plot, a tradeoff emerges between battery capacity and net lift production, as a result of the balance between the competing effects of voltage sag on small capacity batteries and added mass of large capacity batteries. Maximum instantaneous net lift of 0.32 N is obtained with a 1.3 A-h capacity, and maximum endurance of 777.3 seconds is obtained by a 1.4 A-h capacity.

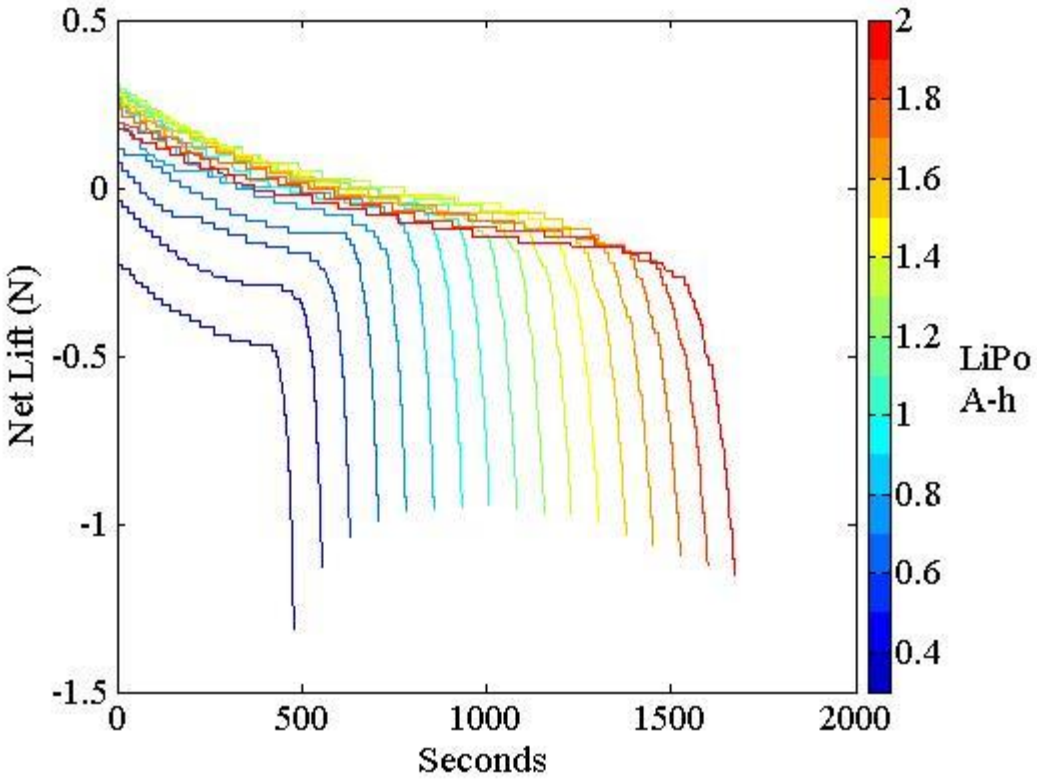

Figure 6.3: Wing B simulation results

Results for Wing C are plotted in Figure 6.4. Performance predictions for Wing C are similar to Wing B, but with a degradation in maximum lift production and endurance. This indicates a design which is optimal exists between wings A and C with respect to both lift production and endurance. For this wing design, maximum instantaneous net lift performance of 0.15 N is obtained with a 1.0 A-h capacity, while maximum endurance of 280.3 seconds is obtained with a 1.3 A-h capacity.

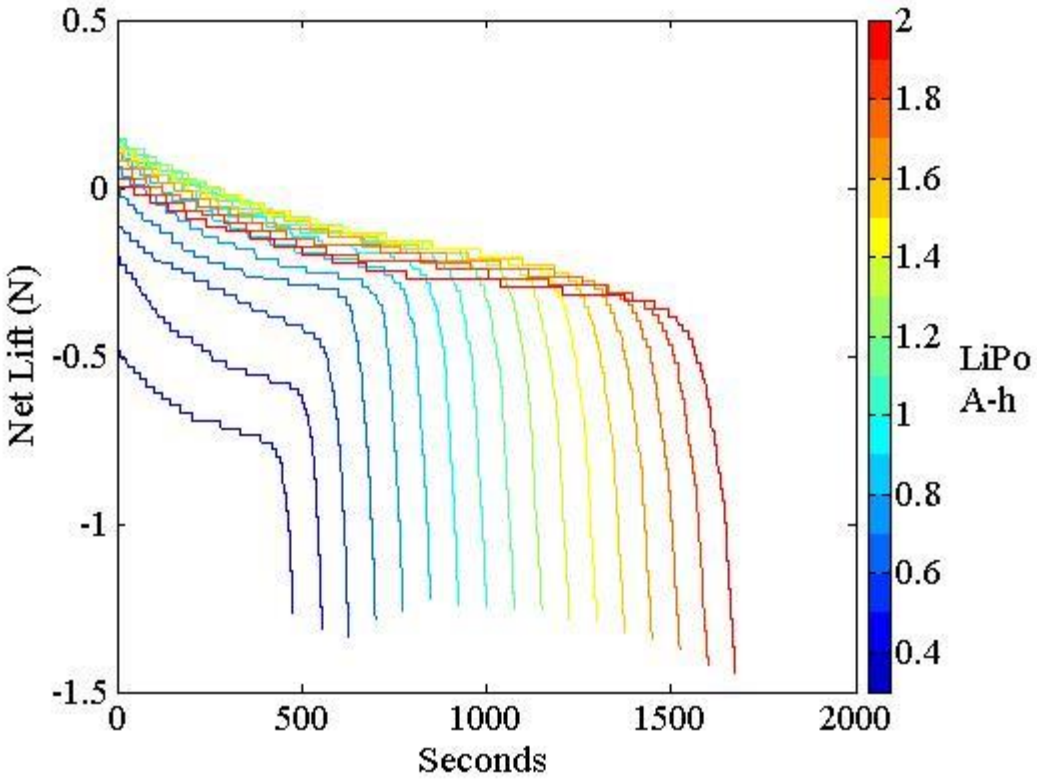

Figure 6.4: Wing C simulation results

Results for Wing D are plotted in Figure 6.5. The relatively larger surface area for this wing design presents excessive loading conditions to the motors, resulting in reductions in flapping amplitude, reduced thrust, and ultimately, reduced lift production. Due to the larger loading profiles of these wings, the heavier higher capacity batteries simulated present less of a penalty for added mass due to a reduction in voltage sag as compared to the smaller wings shown previously.

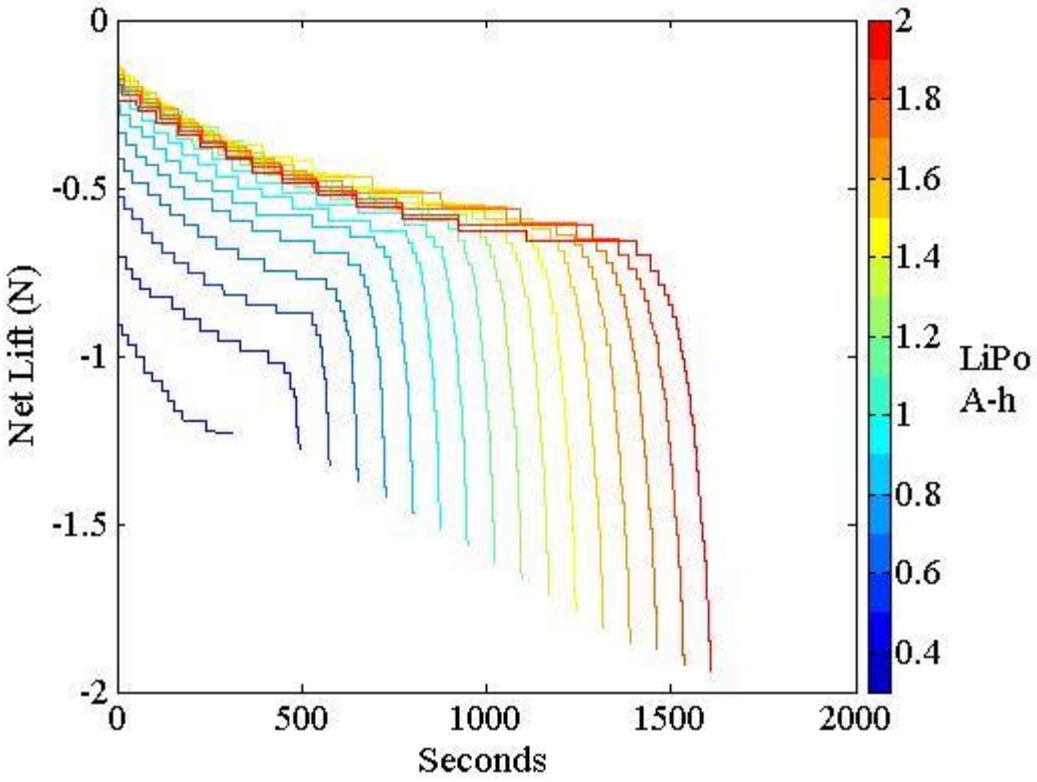

Figure 6.5: Wing D simulation results

In previous work, a major effort was devoted to experimentally characterizing the vehicle in laboratory and free flight scenarios, including lift measurement [12, 123, 124, 181, 185, 186]. Lift determination through flight testing relied on operator experience to set the trim during each trial in order to maximize lift production. For the Robo Raven, this is accomplished through variation in the tail angle of attack and movement of the center of gravity, which affects the airspeed, resulting in changes to the flight power, as discussed in [187]. Unfortunately, subtle changes to the center of

gravity and tail angle result in large effects on flight power. Meanwhile, variable weather conditions further complicate this process by making it difficult to differentiate between effects associated with vehicle trim and effects associated with wind gusts. Here, a simulation-based approach to wing and battery sizing has been shown as a means of reducing dependence on time-consuming experimental trials and operator experience. Next, it will be useful to determine how best to trim the vehicle, without conducting a huge number of flight tests, such that it is operating at the most efficient airspeed in terms of power consumption.

By simulating a Robo Raven with the same characteristics that were used in the battery discharge trials previously conducted, data may be generated that shows observe where there are opportunities to increase performance through minor adjustments to vehicle trim. The simulation is initialized with the same battery, motors, and wing C design used during the experimental trial shown in Table 6.1. The simulation is then run across a range of aerodynamically efficient Strouhal numbers, following the definition in Equation 83. The results for lift production are plotted in Figure 6.6, and the simulated Robo Raven with wing C has a baseline weight of 2.65 N, which includes all flight systems with no added mass. The gap in the data corresponding to Strouhal number of 0.320 appears because the code becomes unstable as it is no longer able to converge on feasible solutions due to limited motor power, hence this represents the highest lift production possible. This estimate offers close agreement with the experimentally

determined value of 3.39 N (346 grams-force), but also indicates that it may have been possible to achieve a slightly higher maximum payload with a faster vehicle trim.

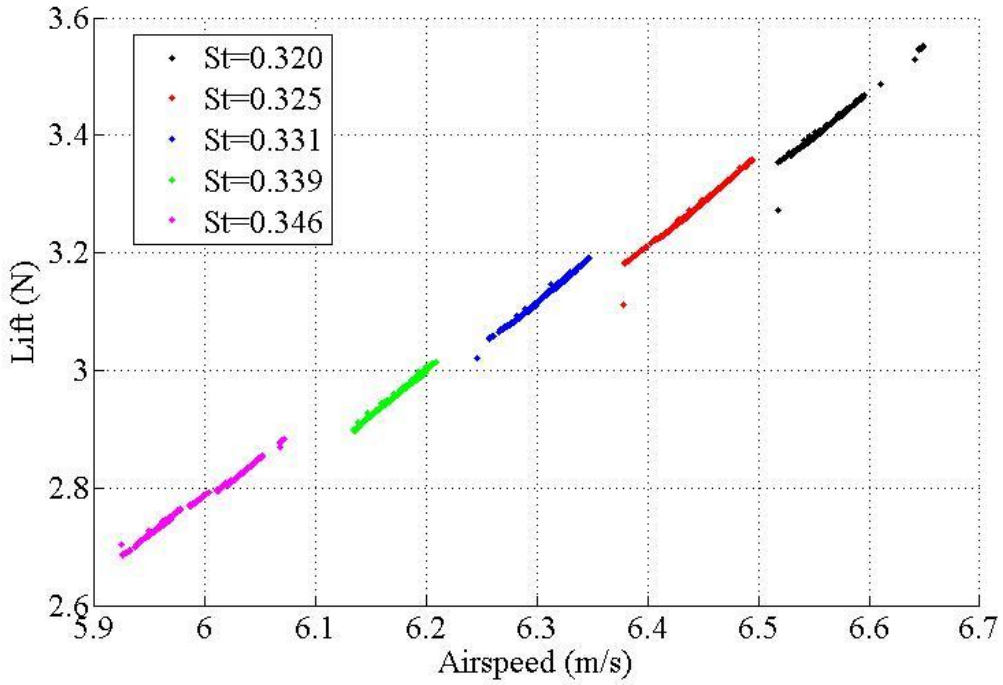

Figure 6.6: Simulated effect of changing trim conditions on lift productivity for Wing C

It is important to note that with the deformability of the wings, the actual amplitude in degrees changes with frequency as the torque exceeds the motor limitation. So, it ends up declining almost linearly at flapping frequencies of 2 Hz for the given flapping amplitudes employed for Robo Raven [123]. The resulting thrust will also change slightly, varying more linearly than quadratically with flapping frequency. So, the end

result may be that the change in flight velocity may match with the change in A*f*, so that the Strouhal number does not change as much with frequency. This effect can be very important, since a deformable wing combined with the torque limitation of the motor means that it is possible to maintain a Strouhal number that stays in the 0.2 to 0.4 range as you increase the frequency. A rigid wing would simply increase the Strouhal number linearly with velocity, so if there is not enough thrust generation as the flapping frequency increases to maintain forward velocity, the Strouhal number can exceed 0.4 and result in a loss in efficiency. Using model approximations for the thrust force generation with flapping frequency and amplitude for steady state flight, the Strouhal number can be approximated for the flapping profile of Robo Raven, where the flapping amplitudes never exceeds 50^o, as follows:

$$\frac{\sigma}{U} = \frac{\rho C_{D,p} b}{2 f k_F} \tag{84}$$

Where ρ is the density of air, b is the wingspan, $C_{D,p}$ is the drag coefficient for Robo Raven, and k_F is an empirically determined coefficient for a given wing design related to the drag force on the wing generated during flapping. Thus, Equation 84 can be used to determine how the wing design and flapping frequency will influence the slope of Figure 12. Note that the flapping amplitude, $\Delta\alpha$, will just influence the forward velocity, and therefore the Strouhal number, as follows:

$$U = f\sqrt{\frac{2k_F\Delta\alpha}{\rho C_{D,p}}} \quad (85)$$

6.4 Discussion of Simulation Results

The values for wing tension and sectional modulus used in Equation 80 must be properly selected to ensure the simulation generates realistic deformations in response to loading conditions. The effect of these values is explored in Figure 6.7, which shows bending deformation of the front spar in the plunge axis, normalized by span length such that a value of zero corresponds to the wing root and a value of one corresponds to the wingtip. Two surface plots are overlaid in this figure showing results from the structural boundary value problem solver for the bending deformation of Wing C, at a Strouhal Number of 0.32 and a fully charged battery. The plot with smaller deformation uses a value for sectional modulus derived from the material properties and dimensions of the carbon fiber stiffeners used in the wing construction [188]. The plot with the larger deformation is simulated with an order of magnitude decrease in section modulus. Each simulation is run with a wing tension of 0.1 N.

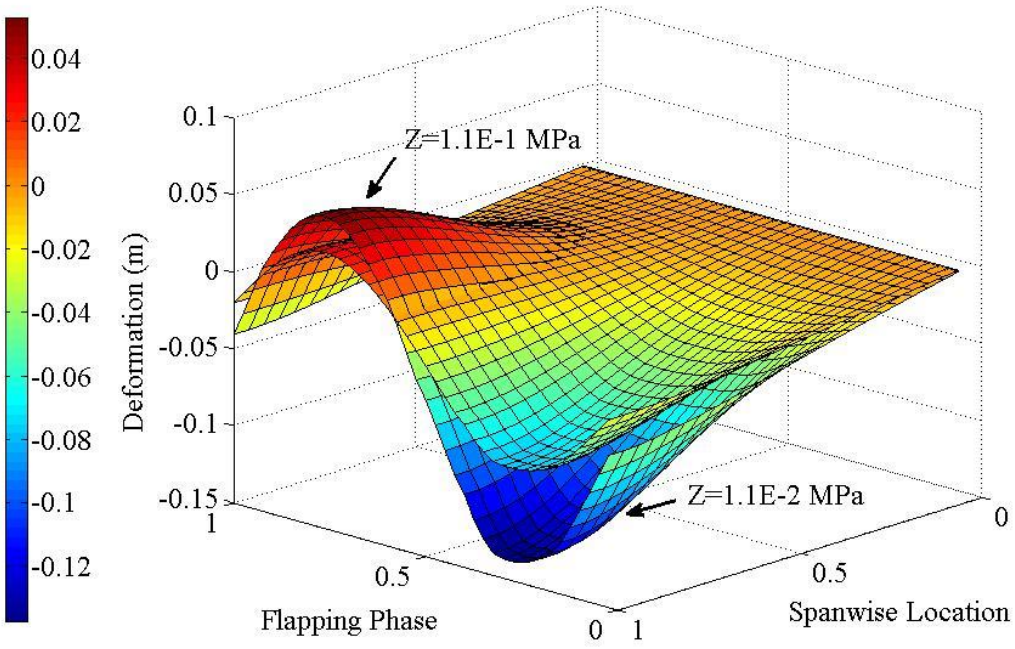

Figure 6.7: Wing C structural solver results for span-normalized bending deformation across one flapping cycle

In these simulations, there is little change to the character of the deformations, with only a reduction in the degree of deformations. However, the sensitivity of the lift predictions to changes in deformation are important. The reduced wing stiffness settings yield a predicted lift average across a flapping cycle of 3.36 N, while the increased stiffness settings result in a modestly smaller predicted lift of 3.23 N. Given the relative insensitivity of the lift force prediction to a substantial change in the wing stiffness properties, it is likely not necessary to set up a full aeroelastic solution to generate useful results, especially given the greatly increased computational cost

required to converge on a solution at each time step. Rather, the prescribed deformation baseline approach [134] modified with the highly simplified dynamic wing modeling approach presented in the previous chapter are typically sufficient for the purposes of generating useful design insight, given that the wings have structural modes that are sufficiently separated from flapping frequencies, which would typically be the case in practical wing designs. In addition, these simplified approaches avoid the complexity associated with measurement of wing stiffness, which is often non-trivial, and instead rely on direct observation of deformation magnitudes to tune the simulation parameters [12].

In contrast, the battery model appears to be an important aspect of a system level performance prediction, given that the force production of the wings is strongly related to the flapping motions, which depend greatly on available motor bandwidth. Replotting the highest performing Wing B results shown in Figure 6.3 in terms of time to discharge the battery to the threshold of usefulness, taken as 3.0 volts per cell, shows the initial tradeoff that must be considered when making a capacity selection. For lift maximization, the best strategy is to select a battery capacity that coincides with the edge of the linear portion of the curve, corresponding to the smallest possible battery that can support the discharge rate required to power the motors for cruising flight. Below this limit, rapid losses in performance occur due to capacity derating effects which offset the benefits of weight savings.

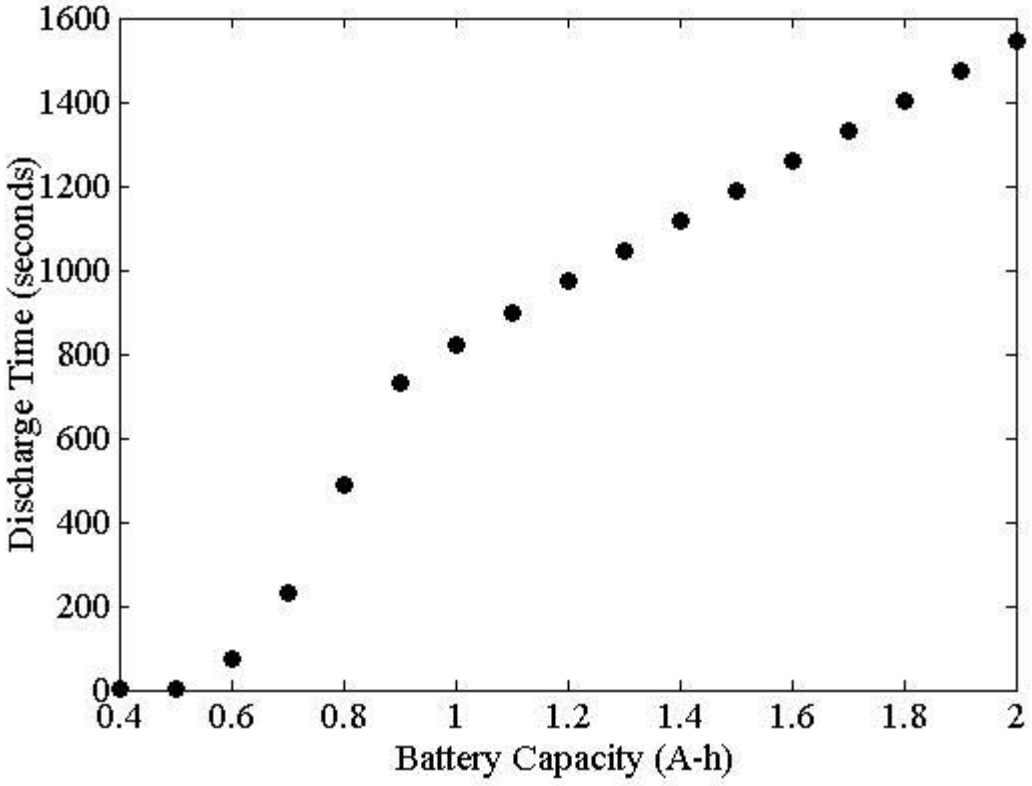

Figure 6.8: Time to discharge to 3.0 V/cell for Wing B across battery capacities

The simulation provides predictions for designing a vehicle to achieve maximum performance. Given the motor parameters are the input to initialize the simulation, the Wing B design demonstrates the highest lift production, as plotted in Figure 6.3. The simulation settings that resulted in the maximum lift production are summarized in Table 6.2, and serve as recommended initial conditions for design optimization, where the goal is defined as lift maximization. These values serve as the targets for flight at

the start of the flight, and will evolve throughout the battery discharge process as system conditions change.

Table 6.2: Recommended initial conditions for Robo Raven II lift maximization

Parameter	**Description**	**Value**
α	fuselage angle of attack	1.012E-1 rad
θ_{tail}	tail angle of inclination	5.236E-1 rad
U	airspeed	6.5 m/s
A	flapping amplitude	4.887E-1 rad
f	flapping rate	4.0 Hz
σ	Strouhal Number	0.3007

Similarly, by reconfiguring the simulation to seek lift production that exactly equals vehicle weight rather than seeking maximum lift, as was plotted previously, an additional result may be obtained for endurance maximization. The predicted endurance estimates across all simulated battery sizes are plotted in Figure 6.9. The data contains some numerical noise associated with the vehicle trim convergence, however the trend clearly indicates that moderate battery capacities will provide

maximum performance by balancing excessive discharge rates with excessive battery mass.

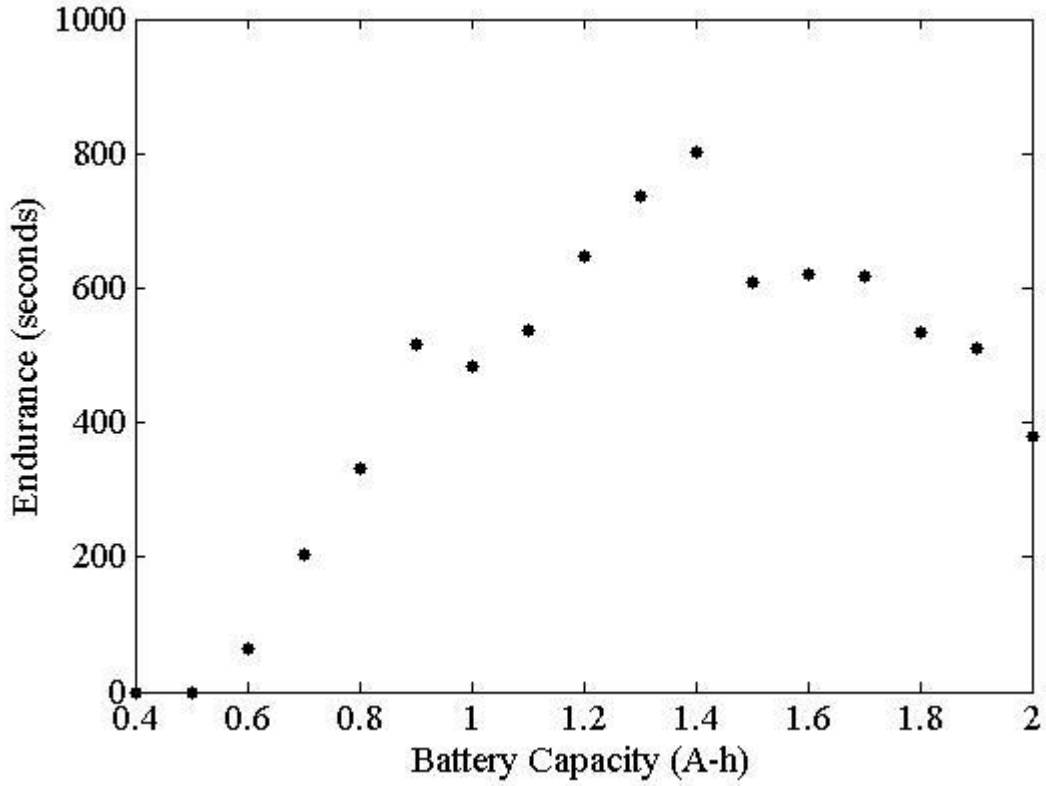

Figure 6.9: Wing B endurance estimates across battery capacities

6.5 Validation of System-Level Simulation

In the previous sections component models have been developed for the actuator, the battery, and the flexible wings that are coupled to produce system-level prediction performance for FWAVs. In order to ensure the predictions are reasonable, it was necessary to conduct some experimental validation of each component model prior to

inclusion in the system-level framework. The motor model has been both developed and validated following extensive dynamometer testing of the drive motors. The battery model was initially developed by considering all relevant conditions that impact performance, but only a subset of the most relevant conditions were retained for performance predictions, while battery health and environmental temperature where neglected. These effects were subsequently validated using experimental testing to ensure the model parameters were correctly capturing discharge behavior for the range of batteries considered here. Finally, the aeroelastic model was validated by integrating it with the other two component models to perform a system-level simulation. The aeroelastic model validation for the presented simulation framework is focused on two primary predictions. First, the flapping bandwidth arising from the motor model and current battery conditions, and second, the impact of changing Strouhal Number on flight performance. Together, these two predictions capture the performance of the drive component and the system-level flight performance that arises from variations in the vehicle parameters.

Several flight tests are conducted with the sensor suite presented in Chapter 4, with the goal of maintaining steady conditions in attitude, heading, and climb rate in order to provide a data set for model validation. The Robo Raven II is shown during one test trial in Figure 6.10. Following each trial, the data is post-processed to isolate stable cruising flight data. In addition, any test data containing significant turning, weather-

induced deflections, or other deviations from stable flight are removed from the trial data.

Figure 6.10: Robo Raven II in flight during data collection trials

The flapping bandwidth from a test flight with Wing C flapping at 4.0 Hz, 0.35 rad angle of attack, and 5 m/s airspeed is plotted together with simulated flapping of the same conditions in Figure 6.11. The predicted flapping amplitude is similar, with slight variation in plunge rate during the downstroke arising due to the tuning of the structural model. As mentioned before, the simplified approach to wing modeling of Chapter 6 appears to provide a potentially more favorable blend of tractability and accuracy, but

for the present study this is considered sufficiently accurate to validate the modeled wing plunge predictions [181].

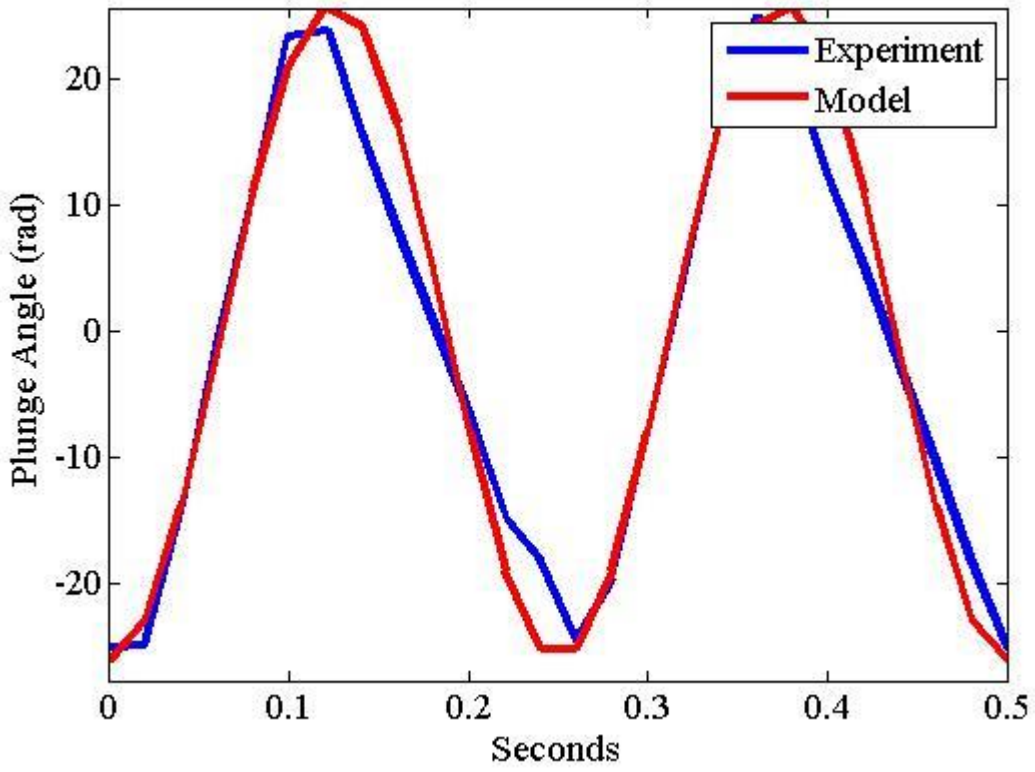

Figure 6.11: Experimental validation of plunge motions

An important model prediction is the lift production as flight conditions are varied. Since the on-board sensors are not capable of directly measuring lift production, a model is required that estimates lift force based on climb rate measurements and vehicle mass. For this purpose a model developed in prior work is adapted [2]:

$$L = mg + \frac{\rho}{2}(A_v cos\theta_p + A_h sin\theta_p)C_{Dy}V_y^2$$

The results of flight test trials are listed in Table 6.3. For each trial, the results have been averaged to reduce the effects of variation in vehicle trim. Experiments were not able to reproduce the theoretical maximum that is projected in Figure 6.3, which amounts to 3.922 N when including the contribution of vehicle weight, which is likely due to the need to make control corrections, weather variations, and a narrow trim and battery charge envelope that provides peak performance. However, in each experimental trial, the overall vehicle weight including batteries, wings, and sensors was 3.679 N, therefore the predictions for average lift are close to observed values during testing. The proximity of the predicted and experimentally observed values are considered sufficient to validate the modeled lift production.

Table 6.3: Experimental flight test results

Trial	**Strouhal Number**	**Airspeed (m/s)**	**Average Lift (N)**	**Average Power (W)**
1	0.386	6.15	3.82	43.6
2	0.401	5.70	3.68	42.0
3	0.446	4.71	3.67	37.4

To experimentally test the endurance predictions made in Figure 6.3, a bench test of a Robo Raven II was used while continuously applying dry ice to the motor housing for

cooling. This approach is necessary to avoid motor damage associated with extended full power flights. In this experiment an 850 mA-h lipo was used, which required 884 seconds to be discharged to a failure condition of below 3.0 V/cell. This value compares very well with the simulated lift in Figure 6.3 which sharply drops off between 858 and 933 seconds, for simulated lipo capacities of 800 and 900 mA-h, respectively. The accuracy of this prediction is considered sufficient to validate the modeled endurance estimates, however caution must be taken by system designers to consider external factors like motor overheating that have not been considered in the present framework.

6.6 Conclusions

This chapter presents a system-level simulation capability for FWAVs that relies on a buildup of coupled models for the following components: (1) the actuator, (2) the battery, and (3) the wings. First, dynamic component models are established that include the necessary effects for each component, and then appropriate linkages to couple these models are identified. Next, the component models are validated experimentally to ensure appropriate empirical constants, as well as correct model formulation. Finally, the overall system simulation is validated using the Robo Raven II custom flight data suite to record critical modeling parameters in-flight. The simulation captures important effects associated with component coupling, and for this reason offers valuable design insight that may be used for improved system-level performance. This simulation approach avoids issues associated with non-coupled

models by ensuring that across the entire flight, compatibility between components is enforced. By adopting this approach, the predicted flight endurance and lift production reflect interactions under real world conditions, whereas neglecting component interactions can lead to suboptimal designs.

This simulation approach may be used to make early design decisions when a lack of experimental data makes the initial specification of a feasible vehicle more challenging. Using the component models, it is possible to narrow down the design tradespace by collecting data on just the individual components, and then coupling them in the simulation. As a vehicle design is realized, the simulation can then be focused on a particular aerodynamic and structural regime by tuning parameters to enhance predictive accuracy and resolution. Since the prediction approach is ultimately based on several tunable parameters, this evolving approach is recommended to ensure suitable predictive accuracy while simultaneously reducing reliance on laborious experimental analysis.

While this simulation approach includes all relevant components in this modeling, it assumes ideal flight conditions. Bad weather and control corrections during flight will degrade endurance below the simulation predictions. Despite this limitation, the presented approach provides a substantially improved system-level prediction of flight performance relative to prior work, particularly for predicting the effects of changing vehicle components and flapping conditions to optimize flight, and should be useful to

flapping wing researchers, designers, and anyone interested in exploring how the components of a FWAV interact.

Chapter 7: Intellectual Contributions

7.1 Improved Accuracy for Component-Level Models

The baseline of the work performed in this dissertation was the early work in performing initial characterization of each of the important vehicle components. Each experiment was designed to highlight important features of the component functionality in steady and dynamic operation. By ensuring that each component was properly described using experiment, the structure of the chosen models was verified to match observed behavior, and tunable parameter values were identified to ensure model performance at the component level reflected observations. This approach led to error reductions in each of the three key vehicle subsystems of motors, wings, and battery, especially during dynamic loading conditions. This baseline for all subsequent work is essential in setting up proper linkages farther downstream in the modeling framework that is to be developed because of the importance of setting up concurrent component model constraints that enforce feasible operation throughout each simulation.

7.2 Efficient Determination of Feasible Operational Parameters for Flapping Wing Aerial Vehicles

A major challenge in flapping wing aerial vehicle design is the dynamic behavior of each component, which tends to be strongly dependent on the component choices and operational characteristics. Taken together, this presents a prohibitively large parameter space from a vehicle designer's perspective. Therefore, an efficient strategy

to determine feasible combinations of components and operational characteristics that requires a minimum of pre-specified vehicle properties was demonstrated based on the vortex ring modeling theory, with experimental validation performed using a custom in-flight instrumentation suite. This strategy captured cruising flight conditions of the Robo Raven platform in cruising flight with sufficient accuracy to enable initialization of a new design by bounding the parameter space to a reasonable range, thus enabling more focused design and prototyping to proceed, and facilitating more efficient design workflows.

7.3 Improved Scalability and Accuracy for Aerodynamic Modeling

Aerodynamic modeling with the lower fidelity strip theory methodology is highly dependent on correct specification of wing motions to obtain accurate results for lift, thrust, and power. The sinusoidal kinematics assumption has been replaced with a system of coupled component models that enforces feasible operations to ensure the strip theory model is more closely reflecting observed behavior. The resulting wing motions are shown to be accurate when compared to experimental results, which results in error reductions from the strip theory modeling with respect to lift, thrust, and power consumption. One of the most useful results of this work is the improvement in the scalability of the strip theory modeling that arises as a result of the component constraints. This helps to mitigate the need to re-tune the model parameters any time the simulation is run with different components, such as with larger or smaller wing area.

7.4 Improved Estimate of System-Level Measures of Performance

An important result in this work is the increased accuracy and granularity in the lift and endurance simulations presented in Chapter 6. Actual vehicles will suffer from a gradual degradation in functionality associated with changes to the vehicle state during a mission, and by simulating those effects, much more reasonable predictions of the vehicle may be realized. The improved ability to predict these system-level performance properties is directly attributable to the foundational work in developing and linking component models as a basis for the system-level model. By providing a time history of the operational characteristics of the vehicle during each simulation run, a much more detailed depiction of how the vehicle is functioning may be achieved when compared to a typical snapshot of performance that is provided in an aerodynamic code alone. This additional information that allows for exploration of how operational characteristics together with component choices build up to affect vehicle performance and entire mission effectiveness can directly inform the design trade space, leading to the possibility for future design optimization efforts to proceed.

7.5 Future Work

A key outcome of this dissertation is to inspire future work by others that may build upon the current results and allow realization of new capabilities in a variety of areas. The main objective addressed by this dissertation was to improve performance modeling through a buildup of component models that include constraints designed to enforce feasible conditions. A natural extension of this work will be to apply the

modeling framework in a new design effort. The procedure for a new design effort will depend upon the similarity of the new vehicle architecture to the Robo Raven II design that was explored in this work. Assuming that similar hardware choices are made, i.e. servos, flexible wings with thin film and spar structures, and lithium polymer batteries, the design process would proceed as follows. First, some rough estimation of vehicle capabilities is needed to reduce the design space. This will include approximation of the mass and vehicle size desired. This step may be performed in a two-stage process. First, inspiration from existing flying animals and FWAVs may be used to explore approximate trades to be made in this initial sizing. Second, a more detailed estimation of the performance properties may be performed using the vortex ring modeling approach presented in Chapter 5.4.1, which will provide a target range of values for airspeed, power output, and vehicle sizing. Given those initial estimates, identification of candidate components with compatible performance capabilities may be performed, as was done in Chapter 3. After suitable components have been selected, models must be constructed for each component. Each component model must capture the important performance properties that will give rise to the constraints between each component, as the component modeling must be performed in parallel with constraint modeling to ensure feasible conditions are enforced, as was explored in Chapter 5. Finally, the system-level performance may be simulated by composing the component models and associated constraints into a coupled framework as was presented in Chapter 6. The particular construction of the coupled simulation framework will depend on the mission objectives or performance properties that are sought by the designer, but in general the

goals of the simulation will be to aid component sizing for the wings and battery, as well as to reveal the impact of operational conditions through trim changes.

The process for vehicle design may change if a more innovative design is sought, for example if very different sizing is needed, or if totally different component choices are made. In the event that innovative design is sought, a more thorough effort will be needed, to include identification of the performance properties of each component through experimental characterization, as was presented in Chapter 4. This characterization will then be followed by selection of suitable modeling approaches that offer accuracy and tractability while retaining important properties that give rise to constraints in practical vehicle operation. Validating the performance of each component is a required step to ensure the system-level model will appropriately represent the functionality of the vehicle across a suitable range of component size choices and vehicle operational space. Following the extra work of component characterization and model validation, a similar effort could proceed in system-level modeling, with the added caveat that some system-level validation would be quite important to improve confidence in predictions, as was presented in Chapter 5.4.1.

Regardless of the novelty of a new design effort, a logical next step will be to perform vehicle optimization. Optimization efforts will require an iterative approach that relies on cycles of model tuning and testing to ensure accurate predictions. Since the underpinning aerodynamic models used in this dissertation are lower fidelity, it will be

important to perform an initial optimization, then conduct sensitivity testing in the neighborhood of the identified optimum to reveal where model assumptions may be inaccurate. The sensitivity of vehicle performance to relatively subtle changes in operation will necessitate the implementation of a control system that responds to disturbances. Since all flight testing conducted in this research was done through teleoperation, it was a major challenge to achieve ideal trim conditions for lift or endurance, particularly in the presence of unfavorable weather conditions. By including a controller that relies of state feedback and a model of how power consumption varies with vehicle operation, it will be possible to improve performance beyond the comparatively clumsy method of visually assessing vehicle state from the ground.

Researchers intending to adopt the modeling framework presented in this dissertation must carefully consider the limits where model predictions begin to break down. The limit of each component model should ideally be identified as a natural consequence of the experimental characterization procedure. Since the limits on the resulting models may not explicitly appear in the model, caution will be needed if a researcher uses a model presented here without also performing the experimental characterization steps. Particular focus will be needed on the aerodynamic model chosen, which must appropriately match the style of flight. For example, in the event that a vehicle is sized much smaller than the Robo Raven II, the unsteady aerodynamics must be appropriately captured to ensure lift predictions remain accurate. Similarly, if a vehicle flies at significantly higher airspeeds, the vortex ring model presented will break down

as a consequence of the wake model, as was discussed in Chapter 5.4.1, therefore a modification that more realistically captures the wake behavior is required for accurate predictions.

Chapter 8: Bibliography

[1] Holness, A., Bruck, H.A., and Gupta, S.K. Design of Propeller-Assisted Flapping Wing Air Vehicles for Enhanced Aerodynamic Performance. *ASME Mechanisms and Robotics Conference*, Boston, MA, August 2015.

[2] Roberts, L.J., Bruck, H.A., and Gupta, S.K. Modeling of dive maneuvers in flapping wing unmanned aerial vehicles. *IEEE International Symposium on Safety, Security, and Rescue Robotics*, West Lafayette, IN, October 2015.

[3] Perez-Rosado, A., Gupta, S.K., and Bruck, H.A. Mechanics of Multifunctional Wings with Solar Cells for Robotic Birds. *Mechanics of Composite and Multi-functional Materials*, 2016. 7: p. 1-10.

[4] *RQ-11B Raven*. http://www.army.mil/-images/2006/11/22/1023/army.mil-2006-11-22-114606.jpg.

[5] *ScanEagle*. http://www.usmc.mil/marinelink/image1.nsf/Lookup/2005417115454.

[6] *An operator wheeling out an RQ-7 Shadow 200 UAV*. http://www.militaryfactory.com/imageviewer/ac/pic-detail.asp?aircraft_id=326&sCurrentPic=pic1.

[7] *MQ-8B*. http://media.defenceindustrydaily.com/images/AIR_MQ-8B_Afghanistan_Maintenance_Ready_NAVAIR_lg.jpg.

[8] *MQ-1 Predator*. http://defense-update.com/images/predator050506-F-0000S-002.jpg.

[9] *MQ-9 Reaper*. http://www.wired.com/images_blogs/dangerroom/2011/09/Contract-crew-and-MQ-9-Reaper-62nd-Expeditionary-Reconnaissance-Squadron.-Kandahar-Nov.-5-2009-.jpg.

[10] Bejgerowski, W., Ananthanarayanan, A., Mueller, D., and Gupta, S. Integrated product and process design for a flapping wing drive mechanism. *Journal of Mechanical Design*, 2009. 131: p. 061006-1.

[11] Mueller, D., Gerdes, J., and Gupta, S. Incorporation of passive wing folding in flapping wing miniature air vehicles. *ASME Mechanisms and Robotics Conference*, San Diego, CA, August 2009.

[12] Gerdes, J.W., Cellon, K., Bruck, H.A., and Gupta, S.K. Characterization of the mechanics of compliant wing designs for flapping-wing miniature air vehicles. *Experimental Mechanics*, 2013. 53: p. 1561-1571.

[13] *University of Delaware Ornithopters Photo*. http://www.udel.edu/PR/UDaily/2004/Birds-Agrawal-5lg.jpg.

[14] Kokshaysky, N. Tracing of the wake of a flying bird. *Nature*, 1979. 279: p. 146-148.

[15] Madangopal, R., Khan, Z., and Agrawal, S. Biologically Inspired Design of Small Flapping Wing Air Vehicles Using Four-Bar Mechanisms and Quasi-Steady Aerodynamics. *Journal of Mechanical Design*, 2005. 127(4): p. 809-817.

[16] Madangopal, R., Khan, Z., and Agrawal, S. Energetics Based Design of Small Flapping Wing Air Vehicles. *IEEE International Conference on Robotics and Automation*, April 2004.

[17] Wood, R., Nagpal, R., and Wei, G.-Y. Flight of the Robobees. *Scientific American*, 2013. 308(3): p. 60-65.

[18] Spedding, G. The wake of a kestrel (Falco tinnunculus) in flapping flight. *Journal of Experimental Biology*, 1987. 127: p. 59-78.

[19] Hubel, T.Y. and Tropea, C. Experimental investigation of a flapping wing model. *Experiments in Fluids*, 2008. 46(5): p. 945-961.

[20] Chung, S.-J. *First-ever demonstration of autonomous bird-like robot perching on a human hand*. 2013, http://engineering.illinois.edu/news/article/2012-04-27-first-ever-demonstration-autonomous-bird-robot-perching-a-human-hand.

[21] David, L., Jardin, T., Braud, P., and Farcy, A. Time-resolved scanning tomography PIV measurements around a flapping wing. *Experiments in Fluids*, 2011. 52(4): p. 857-864.

[22] Wu, P., Ifju, P., and Stanford, B. Flapping Wing Structural Deformation and Thrust Correlation Study with Flexible Membrane Wings. *AIAA Journal*, 2010. 48(9): p. 2111-2122.

[23] Shkarayev, S., Maniar, G., and Shekhovtsov, A.V. Experimental and Computational Modeling of the Kinematics and Aerodynamics of Flapping Wing. *Journal of Aircraft*, 2013. 50(6): p. 1734-1747.

[24] Langley, K.R., Hardester, E., Thomson, S.L., and Truscott, T.T. Three-dimensional flow measurements on flapping wings using synthetic aperture PIV. *Experiments in Fluids*, 2014. 55(10): p. 1831.

[25] Roget, B., Sitaraman, J., Harmon, R., Grauer, J., Conroy, J., Hubbard, J., and Humbert, S. A computational study of flexible wing ornithopter flight. *26th AIAA Applied Aerodynamics Conference*, Honolulu, Hawaii, 2008.

[26] Percin, M., Oudheusden, B.v., Eisma, H., and Remes, B. Three-dimensional vortex wake structure of a flapping-wing micro aerial vehicle in forward flight configuration. *Experiments in Fluids*, 2014. 55(9): p. 1806.

[27] Bahlman, J.W., Swartz, S.M., and Breuer, K.S. How wing kinematics affect power requirements and aerodynamic force production in a robotic bat wing. *Bioinspiration and Biomimetics*, 2014. 9(2): p. 1-10.

[28] Festo. *SmartBird - bird flight deciphered*. 2018, http://www.festo.com/cms/en_corp/11369.htm.

[29] Festo. *BionicOpter - Inspired by dragonfly flight*. 2018, http://www.festo.com/cms/en_corp/13165.htm.

[30] *FPV Velcro Sandwich*. http://flitetest.com/articles/fpv-velcro-sandwich.

[31] *Arducopter: Flying High with an Open Source System*. http://mikrokopter.altigator.com/arducopter-flying-high-with-an-open-source-system-n-327.html.

[32] *DHL parcelcopter launches initial operations for research purposes*. 2 December, 2015, http://www.dhl.com/en/press/releases/releases_2014/group/dhl_parcelcopter_launches_initial_operations_for_research_purposes.html.

[33] *Amazon Prime Air*. 2 December, 2015, http://www.amazon.com/b?node=8037720011.

[34] AeroVironment. *Nano Hummingbird*. 2013, http://www.avinc.com/nano.

[35] Pornsin-Sirirak, T., Tai, Y., Ho, C., and Keennon, M. Microbat: A palm-sized electrically powered ornithopter. *NASA/JPL Workshop on Biomorphic Robotics*, Pasadena, CA, August 2001.

[36] Kakuta, K. *Slow Hawk 2 with Articulated Wings Turn System*. https://www.youtube.com/watch?v=1hEv6wFSEDo.

[37] Mazaheri, K. and Ebrahimi, A. Performance Analysis of a Flapping-Wing Vehicle Based on Experimental Aerodynamic Data. *Journal of Aerospace Engineering*, 2012. 25(1): p. 45-50.

[38] Taylor, J.W.R. and Munson, K., Jane's pocket book of remotely piloted vehicles: robot aircraft today. 1977: Collier Books.

[39] Department of Defense UAS Task Force Airspace Integration Integrated Product Team. Unmanned Aircraft System Airspace Integration Plan. March 2011, http://www.acq.osd.mil/sts/docs/DoD_UAS_Airspace_Integ_Plan_v2_(signed).pdf.

[40] *Professional Society of Drone Journalists*. 3 December, 2015, http://www.dronejournalism.org/.

[41] Boughtin, J., Drone Landscape Still Evolving as Realtor®, Other Commercial Use Grows. National Association of Realtors®.

[42] Gamerman, E. *Drones Invade Hollywood*. http://www.wsj.com/articles/drones-invade-hollywood-1427410534.

[43] *Parrot AR Drone*. http://ardrone2.parrot.com/.

[44] *DJI Phantom*. http://www.dji.com/products/phantom.

[45] *3DR Solo*. https://3drobotics.com/solo-drone/.

[46] *RMAX*. http://rmax.yamaha-motor.com.au/history.

[47] *Smart software uses drones to plot disaster relief*. https://www.newscientist.com/article/mg22029455.100-smart-software-uses-drones-to-plot-disaster-relief/#.Ux8sToWIzFM.

[48] *Air-chaeological drones search for ancient treasures*. https://www.newscientist.com/article/mg22329883-900-air-chaeological-drones-search-for-ancient-treasures/#.VC1hk_ldV8E.

[49] Lara, J. *Drones Might Save Lives in Chilean Beaches*. http://www.dronesrepublic.com/drones-might-save-lives-in-chilean-beaches/.

[50] *Unmanned Aerial Vehicle*. https://en.wikipedia.org/wiki/Unmanned_aerial_vehicle.

[51] Snow, C. *Diversity and Hype in Commercial Drone Market Forecasts*. http://www.suasnews.com/category/the-market/.

[52] Association for Unmanned Vehicle Systems International. The Economic Impact of Unmanned Aircraft Systems Integration in the United States. March 2013, http://www.auvsi.org/auvsiresources/economicreport.

[53] Banziger, G. *Ten-Engine Electric Plane Completes Successful Flight Test*. https://www.nasa.gov/langley/ten-engine-electric-plane-completes-successful-flight-test.

[54] Heinrich, B., Mind of the raven: investigations and adventures with wolf-birds. 1999, New York: HarperCollins Publishers Inc.

[55] Nature. *Ravens*. 12 August 2013, http://www.pbs.org/wnet/nature/episodes/ravens/introduction/1506/.

[56] Phoenix Zoo. *Common Raven*. 12 August 2013, http://www.phoenixzoo.org/visit/animal_news.aspx?ARTICLE_ID=100564.

[57] National Geographic. *Ruby-Throated Hummingbird*. 5 August 2013, http://animals.nationalgeographic.com/animals/birds/ruby-throat-hummingbird/.

[58] Tucker, V.A. Respiratory physiology of house sparrows in relation to high-altitude flight. *Journal of Experimental Biology*, 1968. 48: p. 55-66.

[59] Norberg, U., Vertebrate Flight. Zoophysiology. Vol. 27. 1990, New York: Springer-Verlag. 291.

[60] Videler, J., Avian Flight. Oxford Ornithology Series, ed. T R Birkhead FRS. 2005: Oxford University Press. 269.

[61] Bernstein, M., Thomas, S., and Schmidt-Nielsen, K. Power input during flight of the fish crow, corvus ossifragus. *Journal of Experimental Biology*, 1973. 58: p. 401-410.

[62] Pearson, O. The Metabolism of Hummingbirds. *The Condor*, 1950. 52(4): p. 145-152.

[63] Pennycuick, C.J. Span-ratio analysis used to estimate effective lift:drag ratio in the double-crested cormorant Phalacrocorax Auritus from field observations. *Journal of Experimental Biology*, 1989. 142: p. 1-15.

[64] Pennycuick, C. Predicting wingbeat frequency and wavelength of birds. *Journal of Experimental Biology*, 1990. 150: p. 171-185.

[65] Rayner, J.M.V. Form and function in avian flight. *Current Ornithology*, 1988. 5: p. 1-66.

[66] Rayner, J. and Ward, S. *On the power curves of flying birds*. 22 August 2013, http://www.fbs.leeds.ac.uk/staff/Rayner/Flight/publs/ioc/s31.1.htm.

[67] Schnell, G.D. and Hellack, J.J. Bird flight speeds in nautre: Optimized or a compromise? *The American Naturalist*, 1979. 113(1): p. 53-66.

[68] Thomas, S. Metabolism during flight in two species of bats, phyllostomus hastatus and pteropus gouldii. *Journal of Experimental Biology*, 1975. 63: p. 273-293.

[69] Tucker, V. Metabolism during flight in the laughing gull, larus atricilla. *American Journal of Physiology*, 1972. 222(2): p. 237-245.

[70] Tucker, V.A. Bird metabolism during flight: Evaluation of a theory. *Journal of Experimental Biology*, 1973. 58: p. 689-709.

[71] Videler, J., Groenewegen, A., Gnodde, M., and Vossebelt, G. Indoor flight experiments with trained kestrels II. The effect of added weight on flapping flight kinematics. *Journal of Experimental Biology*, 1988. 134: p. 185-199.

[72] Withers, P.C. and Timko, P.L. The significance of ground effect to the aerodynamic cost of flight and energetics of the black skimmer (Rhyncops Nigra). *Journal of Experimental Biology*, 1977. 70: p. 13-26.

[73] Linton, J. The physics of flight: II. Flapping wings. *Physics Education*, 2007. 42(4): p. 358-364.

[74] Rayner, J.M.V. A vortex theory of animal flight Part 2 The forward flight of birds. *Journal of Fluid Mechanics*, 1979. 91(4): p. 731-763.

[75] Rayner, J.M.V. A new approach to animal flight mechanics. *Journal of Experimental Biology*, 1979. 80: p. 17-54.

[76] Taylor, G., Nudds, R., and Thomas, A. Flying and swimming animals cruise at a Strouhal number tuned for high power efficiency. *Nature*, 2003. 425: p. 707-711.

[77] Azuma, A., The Biokinetics of Flying and Swimming. 2006: Springer Japan.

[78] Videler, J., Avian Flight. 2005: Oxford Ornithology Series.

[79] Tobalske, B. Biomechanics of bird flight. *The Journal of Experimental Biology*, 2007. 210: p. 3135-3146.

[80] Warrick, D., Dial, K., and Biewener, A. Asymmetrical force production in the slow maneuvering flight of pigeons. *The Auk*, 1998. 115(4): p. 916-928.

[81] Ol, M., Parker, G., Abate, G., and Evers, J. Flight Controls and Performance Challenges for MAVs in Complex Environments. *AIAA Guidance, Navigation and Control Conference and Exhibit*, Honolulu, HI, August 2008.

[82] Platzer, M., Jones, K., Young, J., and Lai, J. Flapping-Wing Aerodynamics: Progress and Challenges. *AIAA Journal*, 2008. 46(9): p. 2136-2149.

[83] *Robobees*. http://robobees.seas.harvard.edu/.

[84] Taha, H., Hajj, M., and Nayfeh, A. Flight dynamics and control of flapping-wing MAVs: a review. *Nonlinear Dynamics*, 2012. 70: p. 907-939.

[85] Doman, D., Oppenheimer, M., and Sigthorsson, D. Wingbeat Shape Modulation for Flapping-Wing Micro-Air-Vehicle Control During Hover. *Journal of Guidance, Control, and Dynamics*, 2010. 33(3): p. 724-739.

[86] *Robobees: A Convergence of Body, Brain, and Colony*. 20 November 2013, http://robobees.seas.harvard.edu/.

[87] Teoh, Z. and Wood, R. A Flapping-Wing Microbot with a Differential Angle-of-Attack Mechanism. *IEEE International Conference on Robotics and Automation (ICRA)*, Karlsruhe, Germany, May 2013.

[88] Finio, B. and Wood, R. Open-loop roll, pitch and yaw torques for a robotic bee. *IEEE/RSJ International Conference on Intelligent Robots and Systems*, Vilamoura, Algarve, October 2012.

[89] Chirarattananon, P., Ma, K.Y., and Wood, R.J. Adaptive control of a millimeter-scale flapping-wing robot. *Bioinspiration and Biomimetics*. 9(2): p. 025004.

[90] Ma, K.Y., Chirarattananon, P., Fuller, S.B., and Wood, R.J. Controlled Flight of a Biologically Inspired, Insect-Scale Robot. *Science*, 2013. 340(6132): p. 603-607.

[91] Karpelson, M., Whitney, J., Wei, G.-Y., and Wood, R. Energetics of Flapping-Wing Robotic Insects: Towards Autonomous Hovering Flight. *2010 IEEE/RSJ International Conference on Intelligent Robots and Systems (IROS)*, October 2010.

[92] Whitney, J. and Wood, R. Conceptual design of flapping-wing micro air vehicles. *Bioinspiration and Biomimicry*, 2012. 7: p. 036001.

[93] Wood, R., Steltz, E., and Fearing, R. Optimal energy density piezoelectric bending actuators. *Sensors and Actuators A: Physical*, 2004. 119: p. 476-488.

[94] Karpelson, M., Wei, G.-Y., and Wood, R. Milligram-Scale High-Voltage Power Electronics for Piezoelectric Microrobots. *IEEE International Conference on Robotics and Automation*, May 2009.

[95] *Festo Media Service*. https://www.festo.com/net/en_corp/SupportPortal/press.aspx?q=smartbird&tab=11.

[96] SmartBird. Festo. p. 1-8.

[97] Gerdes, J., Gupta, S., and Wilkerson, S. A Review of Bird-Inspired Flapping Wing Miniature Air Vehicle Designs. *Journal of Mechanisms and Robotics*, 2012. 4: p. 021003-1.

[98] Keennon, M., Klingebiel, K., Won, H., and Andriukov, A. Development of the Nano Hummingbird: A Tailless Flapping Wing Micro Air Vehicle. *50th AIAA Aerospace Sciences Meeting*, Nashville, Tennessee, January 2012.

[99] McDonald, M. and Agrawal, S. Design of a Bio-Inspired Spherical Four-Bar Mechanism for Flapping-Wing Micro Air-Vehicle Applications. *Journal of Mechanisms and Robotics*, 2010. 2(2): p. 021012.

[100] McIntosh, S., Agrawal, S., and Khan, Z. Design of a mechanism for biaxial rotation of a wing for a hovering vehicle. *IEEE/ASME Transactions on Mechatronics*, 2013. 11(2): p. 145-153.

[101] Park, J.-H., Yang, E., Zhang, C., and Agrawal, S. Kinematic Design of an Asymmetric In-phase Flapping Mechanism for MAVs. *IEEE International Conference on Robotics and Automation,* Saint Paul, MN, May 2012.

[102] Choi, J.-S., Zhao, L., Park, G.-J., Agrawal, S., and Kolonay, R. Enhancement of a Flapping Wing Using Path and Dynamic Topology Optimization. *AIAA Journal*, 2011. 49(12): p. 2616-2626.

[103] Paranjape, A., Chung, S.-J., and Selig, M. Flight mechanics of a tailless articulated wing aircraft. *Bioinspiration and Biomimicry*, 2011. 6: p. 026005.

[104] Ramezani, A., Chung, S.-J., and Hutchinson, S. A biomimetic robotic platform to study flight specializations of bats. *Science Robotics*, 2017. 2(3): p. eaal2505.

[105] Ramezani, A., Shi, X., Chung, S.-J., and Hutchinson, S. Bat Bot (B2), A Biologically Inspired Flying Machine. *IEEE International Conference on Robotics and Automation,* Stockholm, Sweden, 2016.

[106] Hoff, J., Ramezani, A., Chung, S.-J., and Hutchinson, S. Synergistic Design of a Bio-Inspired Micro Aerial Vehicle with Articulated Wings. *Robotics: Science and Systems,* June 2016.

[107] Mueller, D., Bruck, H.A., and Gupta, S.K. Measurement of Thrust and Lift Forces Associated With Drag of Compliant Flapping Wing for Micro Air Vehicles Using a New Test Stand Design. *Experimental Mechanics*, 2009. 50: p. 725-735.

[108] Cellon, K. Characterization of flexible flapping wings and the effects of solar cells for miniature air vehicles. University of Maryland Mechanical Engineering MS in Mechanical Engineering, 2010

[109] Gerdes, J. Design, analysis, and testing of a flapping-wing miniature air vehicle. University of Maryland Mechanical Engineering MS in Mechanical Engineering, 2010

[110] Perez-Rosado, A., Griesinger, A., Bruck, H.A., and Gupta, S.K., Performance characterization of multifunctional wings with integrated solar cells for miniature air vehicles, in *ASME Mechanisms and Robotics Conference*. Buffalo, NY.

[111] Perez-Rosado, A., Greisinger, A., Bruck, H.A., and Gupta, S.K. Performance characterization of multifunctional wings with integrated solar cells for

miniature air vehicles. *ASME Mechanisms and Robotics Conference,* Buffalo, NY, August 2014.

[112] Perez-Rosado, A., Bruck, H.A., and Gupta, S.K. Integrating solar cells into flapping wing air vehicles for enhanced flight endurance. *ASME Journal of Mechanisms and Robotics,* 2016. 8(10): p. 051006.

[113] Perez-Rosado, A., Gehlhar, R.D., Nolen, S., Gupta, S.K., and Bruck, H.A. Design, fabrication, and characterization of multifunctional wings to harvest solar energy in flapping wing air vehicles. *Smart Materials and Structures,* 2015. 24(6): p. 065042.

[114] Perez-Rosado, A., Bruck, H.A., and Gupta, S.K. Enhancing the Design of Solar-powered Flapping Wing Air Vehicles using Multifunctional Structural Components. *ASME Mechanism and Robotics Conference,* Boston, MA, August 2015.

[115] Roberts, L., Bruck, H.A., and Gupta, S.K. Autonomous loitering control for a flapping wing aerial vehicle with independent wing control. *ASME Mechanisms and Robotics Conference,* Buffalo, NY, August 2014.

[116] Roberts, L.J., Bruck, H.A., and Gupta, S.K. Modeling of dive maneuvers for executing autonomous dives with a flapping wing unmanned aerial vehicle. *ASME Journal of Mechanisms and Robotics,* 2017. 9(6): p. 061010-061010-11.

[117] Roberts, L.J., Bruck, H.A., and Gupta, S.K. Using a large two degree of freedom tail for autonomous aerobatics on a flapping wing unmanned serial vehicle. *ASME Mechanisms and Robotics Conference,* Charlotte, NC, August 2016.

[118] Holness, A.E., Bruck, H.A., and Gupta, S.K. Characterizing and modeling the enhancement of lift and payload capacity resulting from thrust augmentation in a propeller-assisted flapping wing air vehicle. *International Journal of Micro Air Vehicles,* 2018. 10(1): p. 50-69.

[119] Holness, A., Steins, E., Bruck, H.A., Peckerar, M., and Gupta, S.K. Performance characterization of multifunctional wings with integrated flexible batteries for flapping wing unmanned air vehicles. *ASME Mechanisms and Robotics Confere,* Charlotte, NC, August 2016.

[120] Walker, S., Thomas, A., and Taylor, G. Photogrammetric Reconstruction of High-Resolution Surface Topographies and Deformable Wing Kinematics of

Tethered Locusts and Free-Flying Hoverflies. *Journal of the Royal Society Interface*, 2009. 6(33): p. 351-366.

[121] Heathcote, S., Wang, Z., and Gursul, I. Effect of spanwise flexibility on flapping wing propulsion. *Journal of Fluids and Structures*, 2008. 24(2): p. 183-199.

[122] Gupta, S.K., Bejgerowski, W., Gerdes, J., Hopkins, J., Lee, L., Narayanan, M.S., Mendel, F., and Krovi, V., An Engineering Approach to Utilizing Bio-Inspiration in Robotics Applications, in *Biologically Inspired Design Computational Methods and Tools*, A. Goel, D. McAdams, and R.B. Stone, Editors. 2013, Springer-Verlag: London. p. 245-267.

[123] Gerdes, J.W., Roberts, L., Barnett, E., Kempny, J., Perez-Rosado, A., Bruck, H.A., and Gupta, S.K. Wing performance characterization for flapping wing air vehicles. *ASME Mechanisms and Robotics Conference,* Portland, Oregon, August 2013.

[124] Gerdes, J.W., Bruck, H.A., and Gupta, S.K. A Systematic Exploration of Wing Size on Flapping Wing Air Vehicle Performance. *ASME Mechanisms and Robotics Conference,* Boston, Massachusetts, August 2015.

[125] AM DeLuca, M.R., J Freeman, MV Oi. Flexible- and rigid-wing micro air vehicle: lift and drag comparison. *Journal of Aircraft*, 2006. 43(2).

[126] Caetano, J., Percin, M., Oudheusden, B.v., Remes, B., Wagter, C.d., Croon, G.d., and Visser, C.d. Error analysis and assessment of unsteady forces acting on a flapping wing micro air vehicle: free flight versus wind-tunnel experimental methods. *Bioinspiration and Biomimicry*, 2015. 10(5): p. 056004.

[127] Song, A., Tian, X., Israeli, E., Galvao, R., Bishop, K., Swartz, S., and Breuer, K. Aeromechanics of Membrane Wings with Implications for Animal Flight. *AIAA Journal*, 2008. 46(8): p. 2096-2106.

[128] Shkarayev, S. and Silin, D. Aerodynamics of Cambered Membrane Flapping Wings. *48th AIAA Aerospace Sceinces Meeting,* Orlando, Florida, January 2010.

[129] Thomas, A. On the aerodynamics of birds' tails. *Philos Trans Roy Soc Lond B Biol Sci*, 1993. 340: p. 361-380.

[130] Maybury, W., Rayner, J., and Couldrick, L. Lift generation by the avian tail. *Proc. R. Soc. Lond. B Biol. Sci.*, 2001. 268: p. 1443-1448.

[131] Maybury, W. and Rayner, J. The avian tail reduces body parasite drag by controlling flow separation and vortex shedding. *Proc. R. Soc. Lond. B Biol. Sci*, 2001. 268: p. 1405-1410.

[132] Hummel, D. Aerodynamic investigations on tail effects in birds. *Z Flugwiss Weltraumforsch*, 1992. 16: p. 159-168.

[133] Grauer, J.A. and Hubbard, J.E. Development of a Sensor Suite for a Flapping-Wing UAV Platform. *46th AIAA Aerospace Sciences Meeting and Exhibit*, Reno, Nevada, 2008.

[134] DeLaurier, J. An aerodynamic model for flapping-wing flight. *Aeronautical Journal*, 1993. 93: p. 125-130.

[135] Prouty, R., Aerodynamics of Hovering Flight, in *Helicopter Performance, Stability, and Control*. 1990, Robert E. Krieger Publishing Company: Malabar, Florida. p. 1-32.

[136] Yang, J. Conceptual Aerodynamic Modeling of a Flapping Wing Unmanned Aerial Vehicle. *Army Research Laboratory Technical Report*, 2013. ARL-TR-6747.

[137] Pennycuick, C., Mechanics of flight, in *Avian Biology*, D. Farner and J. King, Editors. 1975, Academic Press: London. p. 1-75.

[138] Tucker, V.A. Flight energetics. *Symposia of the Zoological Society of London*, 1975. 35: p. 49-63.

[139] Tucker, V.A., Energetics of natural avian flight, in *Avian Energetics*, R. Paynter, Editor. 1974, Nuttall Ornithological Club. p. 298-334.

[140] Rayner, J.M.V. A vortex theory of animal flight. Part 1. The vortex wake of a hovering animal. *Journal of Fluid Mechanics*, 1979. 91: p. 697-730.

[141] Rayner, J.M.V. A vortex theory of animal flight. Part 2. The forward flight of birds. *Journal of Fluid Mechanics*, 1979. 91: p. 731-763.

[142] Pennycuick, C. Power Requirements for Horizontal Flight in the Pigeon. *Journal of Experimental Biology*, 1968. 49(3): p. 527-555.

[143] Rayner, J.M.V. Mathematical modelling of the avian flight power curve. *Mathematical methods in the applied sciences*, 2001. 24: p. 1485-1514.

[144] Parslew, B. and Crowther, W.J. Simulating avian wingbeat kinematics. *Journal of Biomechanics*, 2010. 43(16): p. 3191-3198.

[145] Phlips, P., East, R., and Pratt, N. An unsteady lifting line theory of flapping wings with application to the forward flight of birds. *Journal of Fluid Mechanics*, 1981. 112: p. 97-125.

[146] Ruck, S. and Oertel, H. Fluid-structure interaction simulation of an avian flight model. *The Journal of Experimental Biology*, 2010. 213: p. 4180-4192.

[147] Anderson, J.D., Lifting-Surface Theory; Vortex Lattice Numerical Method, in *Fundamentals of Aerodynamics*. 1984, McGraw-Hill Book Company: New York.

[148] Fritz, T.E. and Long, L.N. Object-Oriented Unsteady Vortex Lattice Method for Flapping Flight. *Journal of Aircraft*, 2004. 41(6): p. 1275-1290.

[149] Stanford, B.K. and Beran, P.S. Cost reduction techniques for the design of non-linear flapping wing structures. *International Journal for Numerical Methods in Engineering*, 2011. 88: p. 533-555.

[150] Gomez, J.C., Bryant, M., and Garcia, E. Low-Order Modeling of the Unsteady Aerodynamics in Flapping Wings. *Journal of Aircraft*, 2015. 52(5): p. 1586-1595.

[151] Gerdes, J.W., Wilkerson, S.A., and Gupta, S.K. A review of bird-inspired flapping wing miniature air vehicle designs. *Journal of Mechanisms and Robotics*, 2012. 4(2): p. 021003.

[152] *Baby ravens play*. 15 August 2013, https://www.youtube.com/watch?v=DNjCwiaOiGU.

[153] National Geographic. *Common Raven*. 15 August 2013, http://animals.nationalgeographic.com/animals/birding/common-raven/.

[154] Karpelson, M., Wei, G.-Y., and Wood, R. A Review of Actuation and Power Electronics Options for Flapping-Wing Robotic Insects. *IEEE International Conference on Robotics and Automation*, Pasadena, CA, May 19-23 2008.

[155] Bejgerowski, W., Gerdes, J., Gupta, S., and Bruck, H. Design and fabrication of miniature compliant hinges for multi-material compliant mechanisms. *International Journal of Advanced Manufacturing Technology*, 2011. 57: p. 437-452.

[156] Harrington, A.M. and Kroninger, C. Characterization of small DC brushed and brushless motors. *Army Research Laboratory Technical Report*, 2013. ARL-TR-6389.

[157] *Servos & Parts*. 25 July 2013, 2013, http://www.hobbyking.com/hobbyking/store/__84__189__Servos_Parts-All_Servos.html.

[158] *Servos & Accessories*. 25 July 2013, 2013, http://www.servocity.com/html/servos___accessories.html.

[159] *ServoDatabase.com*. 25 July, 2013, http://www.servodatabase.com/.

[160] *Servo*. 25 July, 2013, http://www.rcmart.com/servo-c-1099.html.

[161] *Digital - Coreless*. 25 July, 2013, http://www.savoxusa.com/Savox_Coreless_Digital_Servos_s/36.htm?searching=Y&sort=13&cat=36&show=10&page=2.

[162] *Analog Servos & Digital Servos for RC Cars, Boats, Planes & Helicopters*. 25 July, 2013, http://www.integy.com/st_main.html?p_catid=98#.UgEr7W2sYyY.

[163] *Robotis MX/RX/EX Series DYNAMIXEL Robot Servos*. 25 July, 2013, http://www.trossenrobotics.com/c/robotis-dynamixel-robot-servos.aspx.

[164] *Arduino Nano*. https://www.arduino.cc/en/Main/ArduinoBoardNano.

[165] Stratasys. *ULTEM 9085 Spec Sheet*. 21 November 2013, http://www.stratasys.com/materials/fdm/ultem-9085.

[166] Nudds, R.L., Taylor, G.K., and Thomas, A.L.R. Tuning of Strouhal number for high propulsive efficiency accurately predicts how wingbeat frequency and stroke amplitude relate and scale with size and flight speed in birds. *Proc. R. Soc. Long. B*, 2004. 271: p. 2071-2076.

[167] Moore, J., Cory, R., and Tedrake, R. Robust post-stall perching with a simple fixed-wing glider using LQR-Trees. *Bioinspiration and Biomimetics*, 2014. 9(2): p. 025013.

[168] *Microdyne System*. http://www.magtrol.com/motortest/microdyne.html.

[169] *ATMEGA328P Datasheet*. http://www.atmel.com/devices/atmega328p.aspx.

[170] *OpenLog Hardware Datalogger*. https://github.com/sparkfun/OpenLog.

[171] Mathworks. *Savitzky-Golay filter design*. https://www.mathworks.com/help/signal/ref/sgolay.html?s_tid=gn_loc_drop.

[172] Chen, M. and Rincón-Mora, G.A. Accurate Electrical Battery Model Capable of Predicting Runtime and I-V Performance. *IEEE Transactions of Energy Conversion*, 2006. 21(2): p. 504-511.

[173] Zakaria, M.Y., Elshabka, A.M., Bayoumy, A.M., and Elhamid, O.E.A. Numerical aerodynamic characteristics of flapping wings. *13th International Conference on Aerospace Sciences & Aviation Technology*, Cairo, Egypt, 2009.

[174] Scherer, J.O. Experimental and Theoretical Investigation of Large Amplitude Oscillating Foil Propulsion Systems. *Hydronautics, Laurel, MD*, 1968: p. 13-14.

[175] Jones, R.T. The unsteady lift of a wing of finite aspect ratio. *NACA Technical Report 681*, 1940.

[176] Phillips, W. and Snyder, D. Modern Adaptation of Prandtl's Classic Lifting-Line Theory. *Journal of Aircraft*, 2000. 37(4): p. 662-670.

[177] Kuethe, A. and Chow, C.-Y., The finite wing, in *Foundations of Aerodynamics, 4th ed*. 1986, John Wiley: New York.

[178] Hoerner, S. Pressure drag. *Fluid-Dynamic Drag*, 1965: p. 3-16.

[179] Kim, D.-K., Lee, J.-S., and Han, J.-H. Improved Aerodynamic Model for Efficient Analysis of Flapping-Wing Flight. *AIAA Journal*, 2011. 49(4).

[180] Ogata, K., Modern Control Engineering (3rd Edition). 2009: Pearson.

[181] Gerdes, J.W., Bruck, H.A., and Gupta, S.K. Improving Prediction of Flapping Wing Motion by Incorporating Actuator Constraints with Models of Aerodynamic Loads Using In-Flight Data. *Journal of Mechanisms and Robotics*, 2017. Special Edition Selected Papers from IDETC2016.

[182] Shampine, L.F., Kierzenka, J., and Reichelt, M.W. *Solving Boundary Value Problems for Ordinary Differential Equations in MATLAB with bvp4c*. https://www.mathworks.com/matlabcentral/fileexchange/3819-tutorial-on-solving-bvps-with-bvp4c.

[183] Goman, M. and Khrabrov, A. State-Space Representation of Aerodynamic Characteristics of an Aircraft at High Angles of Attack. *Journal of Aircraft*, 1994. 31(5): p. 1109-1115.

[184] Paranjape, A.A., Chung, S.-J., and Hilton, H.H. Dynamics and Performance of a Tailless Micro Aerial Vehicle with Flexible Articulated Wings. *AIAA Journal*, 2012. 50(5): p. 11771188.

[185] Gerdes, J.W., Gupta, S.K., and Bruck, H.A. Instrumenting a Flapping Wing Air Vehicle System for Free Flight Measurement. *ASME Mechanisms and Robotics Conference,* Charlotte, North Carolina, August 2016.

[186] Gerdes, J.W., Holness, A., Perez-Rosado, A., Roberts, L., Greisinger, A., Barnett, E., Kempny, J., Lingam, D., Yeh, C.-H., Bruck, H.A., and Gupta, S.K. Robo Raven: A Flapping-Wing Air Vehicle with Highly Compliant and Independently Controlled Wings. *Soft Robotics*, 2014. 1(4): p. 275-288.

[187] Gerdes, J.W., Bruck, H.A., and Gupta, S.K. Validation of flight power modeling by direct measurement of a flapping wing aerial vehicle. *AIAA Atmospheric Flight Mechanics Conference,* AIAA Science and Technology Forum and Exposition, Grapevine, TX, 2017.

[188] *The Composites Store Material Data*. http://www.cstsales.com/material_data.html.